Development of two techniques for thermal characterization of materials: Scanning Thermal Microscopy (SThM) and 2ω method

Ali Assy

To cite this version:

Ali Assy. Development of two techniques for thermal characterization of materials: Scanning Thermal Microscopy (SThM) and 2ω method. Micro and nanotechnologies/Microelectronics. Université de Lyon, 2015. English. NNT : . tel-02141474

HAL Id: tel-02141474
https://hal.science/tel-02141474v1

Submitted on 27 May 2019

N° d'ordre: 2015ISAL0001 Année 2015

Thèse

Development of two techniques for thermal characterization of materials: Scanning Thermal Microscopy (SThM) and 2ω method

Présentée devant
L'Institut National des Sciences Appliquées de Lyon

Pour obtenir
Le grade de docteur

Formation doctorale : Énergétique
École doctorale : Mécanique, Énergétique, Génie Civil, Acoustique

Par

Ali ASSY

Soutenue le 03 Février 2015 devant la Commission d'examen

Jury MM.

	O. BOURGEOIS	Directeur de recherche CNRS (Institut Néel Grenoble)
	S. GOMES	Chargée de recherche CNRS (CETHIL Lyon)
Rapporteur	O. KOLOSOV	Researcher - Reader (Lancaster University)
	S. LEFEVRE	Maître de Conférences (INSA de Lyon)
	N. TRANNOY	Professeur (Université de Reims)
	R. VAILLON	Directeur de recherche CNRS (CETHIL Lyon)
Président	S. VOLZ	Directeur de recherche CNRS (Ecole Centrale Paris)
Rapporteur	J. WEAVER	Professeur (Glasgow University)

Laboratoire de recherche : Centre d'Energétique et de Thermique de Lyon (CETHIL)

INSA Direction de la Recherche - Ecoles Doctorales – Quinquennal 2011-2015

SIGLE	ECOLE DOCTORALE	NOM ET COORDONNEES DU RESPONSABLE
CHIMIE	**CHIMIE DE LYON** **http://www.edchimie-lyon.fr** Insa : R. GOURDON	M. Jean Marc LANCELIN Université de Lyon – Collège Doctoral Bât ESCPE 43 bd du 11 novembre 1918 69622 VILLEURBANNE Cedex Tél : 04.72.43 13 95 directeur@edchimie-lyon.fr
E.E.A.	**ELECTRONIQUE, ELECTROTECHNIQUE, AUTOMATIQUE** **http://edeea.ec-lyon.fr** Secrétariat : M.C. HAVGOUDOUKIAN eea@ec-lyon.fr	M. Gérard SCORLETTI Ecole Centrale de Lyon 36 avenue Guy de Collongue 69134 ECULLY Tél : 04.72.18 65 55 Fax : 04 78 43 37 17 Gerard.scorletti@ec-lyon.fr
E2M2	**EVOLUTION, ECOSYSTEME, MICROBIOLOGIE, MODELISATION** **http://e2m2.universite-lyon.fr** Insa : H. CHARLES	Mme Gudrun BORNETTE CNRS UMR 5023 LEHNA Université Claude Bernard Lyon 1 Bât Forel 43 bd du 11 novembre 1918 69622 VILLEURBANNE Cédex Tél : 06.07.53.89.13 e2m2@ univ-lyon1.fr
EDISS	**INTERDISCIPLINAIRE SCIENCES-SANTE** **http://www.ediss-lyon.fr** Sec : Samia VUILLERMOZ Insa : M. LAGARDE	M. Didier REVEL Hôpital Louis Pradel Bâtiment Central 28 Avenue Doyen Lépine 69677 BRON Tél : 04.72.68.49.09 Fax :04 72 68 49 16 Didier.revel@creatis.uni-lyon1.fr
INFOMATHS	**INFORMATIQUE ET MATHEMATIQUES** **http://infomaths.univ-lyon1.fr** Sec :Renée EL MELHEM	Mme Sylvie CALABRETTO Université Claude Bernard Lyon 1 INFOMATHS Bâtiment Braconnier 43 bd du 11 novembre 1918 69622 VILLEURBANNE Cedex Tél : 04.72. 44.82.94 Fax 04 72 43 16 87 infomaths@univ-lyon1.fr
Matériaux	**MATERIAUX DE LYON** **http://ed34.universite-lyon.fr** Secrétariat : M. LABOUNE PM : 71.70 –Fax : 87.12 Bat. Saint Exupéry Ed.materiaux@insa-lyon.fr	M. Jean-Yves BUFFIERE INSA de Lyon MATEIS Bâtiment Saint Exupéry 7 avenue Jean Capelle 69621 VILLEURBANNE Cedex Tél : 04.72.43 83 18 Fax 04 72 43 85 28 Jean-yves.buffiere@insa-lyon.fr
MEGA	**MECANIQUE, ENERGETIQUE, GENIE CIVIL, ACOUSTIQUE** **http://mega.ec-lyon.fr** Secrétariat : M. LABOUNE PM : 71.70 –Fax : 87.12 Bat. Saint Exupéry mega@insa-lyon.fr	M. Philippe BOISSE INSA de Lyon Laboratoire LAMCOS Bâtiment Jacquard 25 bis avenue Jean Capelle 69621 VILLEURBANNE Cedex Tél :04.72 .43.71.70 Fax : 04 72 43 72 37 Philippe.boisse@insa-lyon.fr
ScSo	**ScSo*** **http://recherche.univ-lyon2.fr/scso/** Sec : Viviane POLSINELLI Brigitte DUBOIS Insa : J.Y. TOUSSAINT	M. OBADIA Lionel Université Lyon 2 86 rue Pasteur 69365 LYON Cedex 07 Tél : 04.78.77.23.86 Fax : 04.37.28.04.48 Lionel.Obadia@univ-lyon2.fr

*ScSo : Histoire, Géographie, Aménagement, Urbanisme, Archéologie, Science politique, Sociologie, Anthropologie

Abstract

Two techniques to characterize the thermal properties of materials and to analyze the heat transfer at the micro/nanoscales have been studied and are presented in this manuscript.

The first technique is the Scanning Thermal Microscopy (SThM), an Atomic Force Microscopy (AFM)-based technique. Operating in its active mode, the AFM probe integrates a resistive element that is electrically heated. Used in AFM contact mode, it allows the localized thermal excitation of the material to be studied. The determination of the sample thermal properties requires the analysis of the probe thermal response through the modeling of the probe-sample system including its surrounding. With the help of a review of SThM studies, the current scientific questions and the analytical models used to analyze the probe-sample system are explored. Special attention is given to the probe-sample thermal interaction that conditions the tip-sample interface temperature. Reducing the probe size requires a more in depth study of the physics of the heat transfer mechanisms of this interaction. In this work, a new methodology for studying and specifying the heat rate exchanged between a probe and a sample through thermal conduction through water meniscus has been established. The methodology is based on the analysis of the dependence of force-distance curves on probe temperature obtained in ambient air. It was applied with samples of different thermal properties, surface roughness and wettability to three resistive probes different in size and heater configurations: Wollaston, KNT and doped silicon (DS) probes. Whatever the probe and the sample are, the contribution of water meniscus in the probe-sample interaction has been shown to be lower than the one of air. Moreover, for the Wollaston and KNT probes, the parameters of a model based on a description of the probe-sample system using a network of thermal resistances are identified from measurements performed under ambient and vacuum conditions. The thermal conductances at the solid-solid contact were determined for various samples. This allowed identifying the phonon transmission coefficient in the case of KNT probe and a nonmetallic sample. Experimental results and numerical simulations for measurements performed under ambient conditions have demonstrated that the thermal interaction parameters of the heat conduction through air strongly depend on the sample thermal conductivity. Improvements of the current calibration methodology for thermal conductivity measurement have been proposed. The variation of sample roughness during the calibration and measurements may be an issue. Moreover, the sensitivity to sample thermal conductivity for the Wollaston and KNT probes is shown to be strongly reduced for thermal conductivities larger than 10 and a few $W.m^{-1}.K^{-1}$ respectively.

The second technique developed in this thesis is a less local thermal analysis method. It operates by contact, requiring the implementation of the sample surface with a network of resistive wire probes. One wire of the network is heated by an alternating current at frequency f and has the role of heating source, continuous and at $2f$ frequency, for the sample. The other wires are sensors of temperature (method "2ω"). A 2D analytical model, based on the principle of thermal-waves, was developed to identify the effective thermal properties of anisotropic samples from experimental measurements with the technique. This model can be reduced to a simplified 1D model in the case of diffusive, homogeneous and isotropic materials. Finite element simulations and this model were used to design the experimental set-up and validate the method with pure silicon. The results obtained at sample temperatures ranging from ambient to 500 K are consistent with literature.

Keywords: thermal techniques, Scanning Thermal Microscopy, micro and nanoscale heat transfer, thermal conductance, thermal conductivity, phonon transmission coefficient, microresistors, water meniscus

Résumé

Deux techniques de caractérisation thermique des matériaux et d’analyse du transfert de chaleur aux micro- et nano- échelles ont été étudiées et sont présentées dans ce mémoire.
La première technique est la microscopie thermique à sonde locale (SThM). La pointe d’un microscope à force atomique intègre un élément résistif. Utilisée en mode contact, cette pointe, chauffée par effet joule, permet l'excitation thermique localisée de l’échantillon. La détermination des propriétés thermiques de l’échantillon nécessite l'analyse de la réponse de cette pointe avec un modèle du système sonde-échantillon et de son environnement. Un état de l'art général des études réalisées en SThM permet de poser les questions scientifiques actuellement traitées dans le domaine ainsi que les modèles utilisés pour analyser le système pointe-échantillon. Une attention particulière est accordée à l'interaction thermique sonde-échantillon. Sa compréhension nécessite d’être approfondie. L’étude ici présentée tient compte des propriétés thermiques, de la rugosité et de la mouillabilité de la surface de différents échantillons. Une nouvelle méthodologie est établie pour la spécification du transfert de chaleur échangée par conduction thermique au travers du ménisque d’eau formé au contact sonde-échantillon. Cette méthodologie est basée sur l'analyse de la dépendance à la température de la sonde des courbes de force-distance obtenues à l'air ambiant. Elle est appliquée à trois sondes de taille, forme et constitution différentes: la sonde Wollaston, la sonde KNT et une sonde en silicium dopé. Quels que soient la sonde et l'échantillon, la contribution du ménisque d’eau à l'interaction est montrée être inférieure à celle de l'air. Par ailleurs, pour les sondes Wollaston et KNT, les paramètres d'une modélisation, basée sur une description du système sonde-échantillon avec un réseau de conductances thermiques, sont identifiés à partir de mesures effectuées à l’ambiante et sous vide. La conductance thermique au contact solide-solide est déterminée pour différents échantillons. Cela a permis d’identifier le coefficient de transmission de phonons dans le cas de la sonde KNT et d’échantillons non-métalliques. Nos résultats expérimentaux et de simulations numériques pour les mesures effectuées sous air démontrent que les paramètres utilisés pour décrire la conduction thermique via l’air dépendent fortement de la conductivité thermique de l'échantillon. Aussi des améliorations de la méthodologie actuelle d'étalonnage pour la mesure de la conductivité thermique sont proposées. Il est en outre montré que la variation de la rugosité de l'échantillon lors de l'étalonnage et de mesures doit être prise en compte. La sensibilité à la conductivité thermique pour les sondes Wollaston et KNT est part ailleurs montrée fortement réduite pour les matériaux de conductivité thermique supérieure à 10 et quelques W.m^{-1}.K^{-1} respectivement.
La seconde technique développée est une méthode d’analyse thermique moins locale nécessitant l’instrumentation de la surface de l’échantillon avec un réseau de sondes résistives filiformes. L’un des fils du réseau, chauffé par un courant alternatif à la fréquence f, a le rôle de source excitatrice continue et à la fréquence $2f$ de l’échantillon. Les autres fils sont des capteurs de la température (méthode «2ω»). Un modèle analytique 2D, basé sur le principe des ondes thermiques et développé pour identifier les propriétés thermiques d’échantillons anisotropes est présenté. Ce modèle peut être réduit à un modèle simplifié 1D dans le cas de matériaux diffusifs, homogènes et isotropes. Des simulations par éléments finis et avec ce modèle ont été utilisées pour dimensionner le montage expérimental et valider la méthode sur un échantillon de silicium pur. Les résultats obtenus à des températures de l’échantillon variant de l’ambiante à 500 K corroborent ceux de la littérature.

Mots-clés: méthodes thermiques, microscopie thermique à sonde locale, transfert de chaleur aux micro- et nano-échelles, conductance thermique, conductivité thermique, coefficient de transmission des phonons, méthode à fils résistifs déposés, ménisque d’eau

Nomenclature

Abbreviation	***Term***
AFM	Atomic Force Microscope
ESEM	Environmental Scanning Electron Microscope
MD	Molecular Dynamics
NEMD	Non-Equilibrium Molecular Dynamics
SEM	Scanning Electron Microscope
SPM	Scanning Probe Microscope
SNOM	Scanning Near-Optical Microscope
SThM	Scanning Thermal Microscopy

Symbol	***Variable***	***Unit***
a	Thickness of the meniscus	m
A	Accommodation factor	
a_c	Radius of mechanical contact	m
b	Equivalent radius of the thermal exchange	m
b_w	Wire width	m
C	Heat capacity	$J.Kg^{-1}.K^{-1}$
C_p	Heat capacity at constant pressure	$J.Kg^{-1}.K^{-1}$
C_{pa}	Heat capacity of acoustic phonons	$J.Kg^{-1}.K^{-1}$
C_v	Heat capacity at constant volume	$J.Kg^{-1}.K^{-1}$
D	Diameter	m
d	Thickness	m
d_0	Density	$kg.m^{-3}$
d_s	Tip-sample separation distance	m
E	Young modulus	Pa
f	Frequency	Hz

F_N	Applied force	N
F_{ad}	Adhesion force	N
F_{cap}	Capillary forces	N
F_{po}	Pull-off forces	N
Gr	Grashof number	
G_{air}	Thermal conductance through air	$W.K^{-1}$
$G_{atom\text{-}atom}$	Thermal conductance of atom-atom contact	$W.K^{-1}$
G_c	Contact thermal conductance	$W.K^{-1}$
G_{ep}	Volumetric phonon-electron coupling constant	$W.m^{-3}.K^{-1}$
G_{eq}	Equivalent thermal conductance $G_{eq}=(G_cG_s)/(G_c+G_s)$	$W.K^{-1}$
G_p	Probe thermal conductance	$W.K^{-1}$
$G_{p\text{-}w}$	Probe-water thermal conductance	$W.K^{-1}$
$G_{w\text{-}s}$	Water-sample thermal conductance	$W.K^{-1}$
G_Q	Quantum thermal conductance	$W.K^{-1}$
G_{rad}	Thermal conductance of radiation	$W.K^{-1}$
G_s	Thermal conductance of the sample	$W.K^{-1}$
G_{ss}	Thermal conductance of the solid-solid contact	$W.K^{-1}$
G_{total}	The total conductance of the water meniscus	$W.K^{-1}$
G_w	Thermal conductance through the water meniscus	$W.K^{-1}$
h	Heat transfer coefficient	$W.m^{-2}.K^{-1}$
h_g	Global linearized convective and radiative losses	$W.m^{-2}.K^{-1}$
h_k	Meniscus height	m
I	Electrical current	A
K_1	Correction factor	
k_x	X-component of the wave vector	
L	Length	m
L_{wf}	Wiedemann Franz constant	$W.\Omega.K^{-2}$

m	$m=(hp/kS)^{1/2}$	
N	Number of phonon modes	
Nu	Nusselt number	
p	Fin perimeter	m
P	Pressure	bar
P_a	Probe Joule power - Probe free in air	W
P_c	Probe Joule power - Probe in contact with sample	W
P_p	Power dissipated in the probe	W
P_{rms}	Power per unit heater length	$W.m^{-1}$
Pr	Prandtl number	
Q	Heat flux	W
R	Electrical resistance	Ω
Ra	Rayleigh number	
R_a	Tip apex radius	m
R_{ar}	Arithmetic value of roughness	m
R_b	Thermal boundary resistance	$m^2.K.W^{-1}$
R_{bp}	Thermal boundary resistance of the phonon-phonon coupling	$m^2.K.W^{-1}$
R_{be}	Thermal boundary resistance of the phonon-electron coupling	$m^2.K.W^{-1}$
R_g	Gas constant	$J.mol^{-1}.K^{-1}$
R_s	Spreading thermal resistance	$K.W^{-1}$
R_{th}	Interface thermal resistance	$K.W^{-1}$
R_{p-p}	Peak-to-peak roughness	m
R_{sph}	Sphere radius	m
R_{tip}	Tip thermal resistance	$K.W^{-1}$
$R_{interface}$	Thermal resistance at the tip-sample interface	$K.W^{-1}$
R_0	Electrical resistance of the probe at T_a	Ω

RH	Relative humidity	
r_1	Smallest meniscus radius	m
r_{12}	Reflection coefficient at the tip-sample interface	
r_2	Largest meniscus radius	m
S	Section	m^2
r_k	Cavity radius	m
T	Temperature	K
T_a	Ambient Temperature	K
T_m	Probe mean temperature	°C
t_1	Film thickness	m
t_{12}	Phonon transmission coefficient	
V	Voltage	V
V_{air}	Velocity of air molecules	
V_{DC}	Continuous voltage	V
V_m	Molar volume	$m^3.mol^{-1}$
$V_{3\omega}$	Third harmonic voltage	V
w	Width	m
w_d	Dupré Energy of adhesion	N

Greek letters

α	Thermal diffusivity	$m^2.s^{-1}$
β	Temperature coefficient of the electrical resistivity	K^{-1}
γ_w	Water surface tension	$N.m^{-1}$
Δ	Temperature ratio	
$\Delta P/P_c$	Probe Joule power relative difference	

ε	Surface emissivity	
θ	Relative temperature	K
$\bar{\theta}$	Mean Relative temperature	K
θ_{DC}	Continuous relative temperature	K
θ_{2w}	Second harmonic relative temperature	K
γ	C_p/C_v	
λ_{max}	Maximum wavelength of thermal radiation	µm
λ	Thermal conductivity	$W.m^{-1}.K^{-1}$
λ_{pp}	Phonon-phonon thermal conductivity	$W.m^{-1}.K^{-1}$
λ_w	Thermal conductivity of water	$W.m^{-1}.K^{-1}$
λ_{max}	Maximum wavelength of thermal radiation	m
Λ	Phonon mean free path	m
μ	Diffusion length	m
ν	Poisson ratio	
ν_{pa}	Velocity of acoustic phonons	$m.s^{-1}$
ρ	Electrical resistivity	$\Omega.m^{-1}$
χ	Wave vector along z	
Φ	Phase lag	°
Φ_d	Heat flow density	$W.m^{-2}$
Φ_{ref}	Ratio of heat power	
ω	Angular frequency	$Rad.s^{-1}$
Ω	G_{eq}/G_p	

Table of Contents

List of Figures

List of tables

General introduction

The understanding of heat transfer and the improvement of some industrial production processes require the development of sophisticated thermal metrologies. For micro and nanotechnologies in particular, these metrologies should be accurate in terms of measurement of the thermal parameters and spatial resolutions. A perfect example is thermal management in electronics [1]. It is indeed a crucial aspect for the design of integrated circuits due to the integration density achieved nowadays. Everything from the scale of the printed circuit board (a few cm) to that of elementary transistor (a few nm) must be designed to limit power consumption and to facilitate heat dissipation [2, 3]. All micro and nanosystems currently fabricated with microelectronics technology tools such as thin film based devices or micro and nanostructured components also raise similar issues. Moreover, these systems require a precise knowledge of the thermal properties of the constituting materials or of those considered for optimization. Another field is thermoelectric energy conversion, which is one of the ways that might help facing the energy challenge [4]. Searching for a larger thermoelectric figure of merit ZT is of paramount importance. One common feature of recently-discovered thermoelectric materials with ZT>1 is that most of them have very low lattice thermal conductivities [5]. The thermal properties of these new materials need to be characterized. More generally, the development of nanoscale metrologies is required to study of the effects of the nanostructuration process. This type of processes is used to confer revolutionary physical properties to materials. The understanding of the thermal impacts is the key that will allow the predictive modeling of the heat transfer in next-generation systems. It is essential for the design stage and for the improvement in terms of quality and security of systems.

From a fundamental point of view, there has been an urgent need to understand the physics of the heat transfer at the micro and nanoscales. In the case of heat transfer within nanostructures and nanostructured materials or of heat exchange between two systems, the macroscopic thermal models are not valid if the dimensions of the zones of thermal contact and systems become comparable to the mean free path of the heat carriers of the two systems. Several parameters can affect the heat transfer between two systems and they are not fully understood yet. They include the thermal properties of systems, the roughness of material surfaces, the wettability of surfaces, the temperature of materials, etc…

In terms of spatial resolution, the far field optical methods used to characterize the thermal properties of materials are limited by the diffraction limit [6]. In these techniques, the signal detection is performed at distances larger than the wavelength. In order to achieve a better spatial resolution in the determination of thermal properties and studying the heat transfer at submicron scales, Scanning Thermal Microscopy SThM has been developed for more than 25 years [7, 8]. The major part of this manuscript is dedicated to the characterization of the measurement with this technique. Commercialized resistive probes of different spatial resolutions were used to study the thermal system composed by the probe interacting with the sample in SThM (called "probe-sample thermal system" in the manuscript). Such approach would provide a better understanding of the technique and seek its improvement. Another thermal technique, less local because requiring the deposit of resistive wire-probes on the sample surfaces was also developed. It is presented in the last part of the manuscript.

The first chapter introduces the SThM technique. It presents the three resistive probes used in this work. For each of these probes, a state of the art of researches is given in terms of the modeling of the probe-sample thermal system. The chapter presents the experimental and modeling investigations that studied the heat losses to the environment while working under ambient conditions. The heat transfer mechanisms of the heat transfer between the probe and the sample are presented: thermal radiation, thermal conduction at the solid-solid contact, thermal conduction through water meniscus formed at the probe-sample contact and through air. Based on literature researches, each heat transfer mechanism is detailed and analyzed in order to bring out the parameters that affect the mechanism. The tasks to deal with in this manuscript and the experimental conditions are defined.

The second chapter is dedicated to the study of the heat transfer through water meniscus with the Wollaston wire probe (a micrometric probe). Two potential applications related to the results of the study are first presented. The chapter gives then a new methodology to determine the characteristic dimensions of the meniscus, an effective dimensional parameter of the probe apex and the meniscus thermal conductance. The last section of this chapter discusses some preliminary results of experiments performed in an environmental scanning electron microscope (ESEM) in order to observe the water meniscus at the contact between a probe and a sample. This was motivated by the current development of a SThM-ESEM combined system at CETHIL.

Based on the comparison of experimental results obtained with results of simulation for various experimental conditions, a quantitative analysis of the conduction through the solid-solid contact and air is given in the third chapter for the Wollaston probe. The thermal conductance at the solid-solid contact is measured under vacuum conditions on polished samples and the thermal boundary resistance at the tip-sample interface is determined. Later, the thermal conduction through air is determined while taking into account the sample thermal conductivity. The effect of roughness of different samples on the probe-sample thermal interaction is presented. Several criteria are proposed in order to improve the SThM calibration for thermal conductivity measurement.

Chapter 4 mainly focuses on measurement carried out with the KNT probe. Moreover, results obtained with the doped silicon DS probe are presented and discussed. Applying the methodology described in chapter 2 to these probes, the water meniscus conduction is studied on samples of different thermal conductivity. Besides, the results of measurements under vacuum conditions performed on different samples are presented for the KNT probe. The heat conduction at the tip-sample contact is investigated and the determination of the thermal boundary resistance for each sample is addressed. Using various reference samples and while working under ambient conditions, the sensitivity to the sample thermal conductivity is specified for the KNT probe. The last part of this chapter proposes an evaluation of the phonon transmission coefficient at the tip-sample contact.

The last chapter of the manuscript presents the concept of a technique to characterize the thermal properties of anisotropic samples. Based on contact thermal metrologies operating in AC regime, the technique allows studying samples at temperatures above the ambient. The technique is called the “2ω method”. Its principle and first results of experimental work and simulations for the technique validation are presented and discussed. The experimental results on a Si sample are compared with the literature studies. Later, numerical simulation works are presented in order to set a basis to identify the thermal properties of the sample in the in-plane and cross-plane direction of an anisotropic sample with the 2ω method.

Chapter 1

Scanning Thermal Microscopy (SThM): State of the art and exposition of the issues

The Scanning Thermal Microscopy (SThM) with its better spatial resolution than the photothermal methods is used nowadays to characterize the thermophysical properties of materials. However the characterization of materials using SThM probes is still challenging and requires a better understanding and a proper modeling of the probe-sample system. Thus, any interpretation of the measurements must be accompanied with an appropriate modeling of the probe-sample system to identify precisely the properties of the considered materials.

The investigation of the probe-sample system involves studying the heat transfers through three elements: 1) the probe 2) the sample and 3) their surrounding environment.

Therefore, this chapter summarizes, to present, a state of the art of the research studies that involves the SThM to characterize the sample thermal conductivity as well the heat transfer mechanisms between the probe and sample. It gives, in order:

- An introduction of the technique and the description of the resistive probes that are involved in this work.

- The thermal modeling of the probe-sample system currently proposed and used for the interpretation of SThM measurements obtained with these probes.

- The research works performed for studying, describing and identifying the heat losses from the probe to the environment medium.

- The heat mechanisms that exist between the probe and the sample depending on the conditions of experiments.

Based on this commented review, the scientific tasks to deal with in the upcoming chapters are introduced.

1.1 Scanning Thermal Microscopy (SThM)

Scanning Thermal Microscopy (SThM) is a quasi non-destructive technique that allows the characterization of sample materials. The technique is based on Scanning Probe Microscopes (SPM) and allows measurements to be performed with high spatial resolution. SThM was used first in Scanning Tunneling Microscope (STM) [9] and later in Atomic Force Microscopy (AFM) [10] and Scanning Near-field Optical Microscope (SNOM) configurations [11]. However, SThM is mostly used nowadays in an AFM configuration that allows obtaining simultaneous topographical and thermal images. Moreover, the forces that exist between the probe and the sample at the contact can be measured. A schematic of SThM that is based on AFM is presented in Figure 1.1.

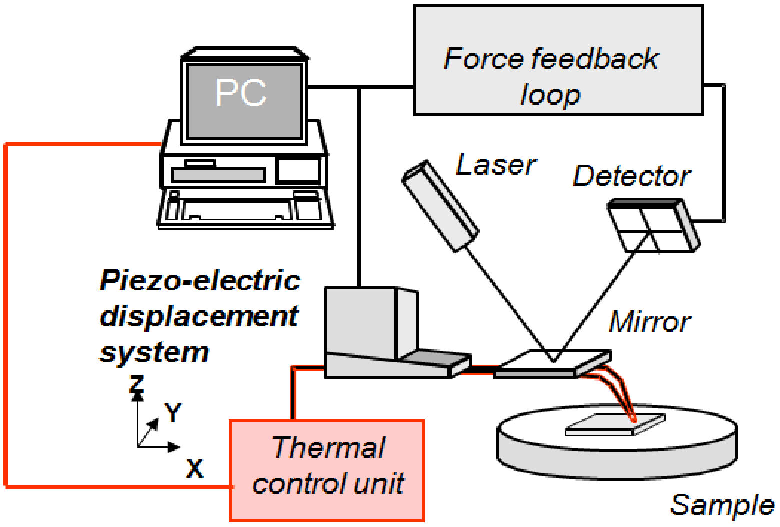

Figure 1.1. Description of the principle of the technique

The probes used in this work operate on an AFM-based SThM technique.

1.2 Operational modes of resistive SThM probes

With the resistive probe, the information about the probe temperature is determined through the measurements of the probe electrical resistivity.

SThM resistive probes can be used in two modes:

a) Passive mode: This mode is mainly used to map the temperature at the surface of active/heating samples to study local heat sources as an example [12]. An electrical current sufficiently small, to avoid a significant additional heating of the probe, flows through the probe while the probe voltage is measured during the sample scanning.

b) Active mode: The probe is simultaneously the heater and the sensor. Either DC or AC (or both) current is injected in the probe.

In both modes, the electrical resistance of the thermosensitive element and thus its temperature is controlled through an electronic unit (Thermal Unit control in Figure 1.1 that can be a Wheastone bridge as an example). However, the probe temperature measured through this unit is the mean temperature of the whole resistive element. As will be seen later, the estimation of the heat transferred to the sample requires the determination of the tip apex temperature. This temperature cannot be deduced directly from the measurements and its determination requires an appropriate description of the probe-sample thermal system.

1.3 Resistive probes description

1.3.1 The Wollaston wire probe

The Wollaston probe has been used widely to characterize solid materials and to study the interaction between the probe and the sample [13, 14]. The resistive element of this probe is a wire of 5 µm in diameter and 200 µm in length. It is made of Pt 90%/ Rh 10% and bent in a V-shape (Figure 1.2). It is obtained by electrochemical etching of the silver shell of the Wollaston wire of 75 µm in diameter [15]. Table 1.1 summarizes the properties of the Wollaston wire probe.

Table 1.1. Properties of the Wollaston wire probe.

Tip	Resistive wire length (µm)	Resistive wire diameter (µm)	Radius of curvature of the apex (µm)	Spring constant ($N.m^{-1}$)	Cut-off frequency (KHz)
Wollaston wire probe	200	5	15	5	240

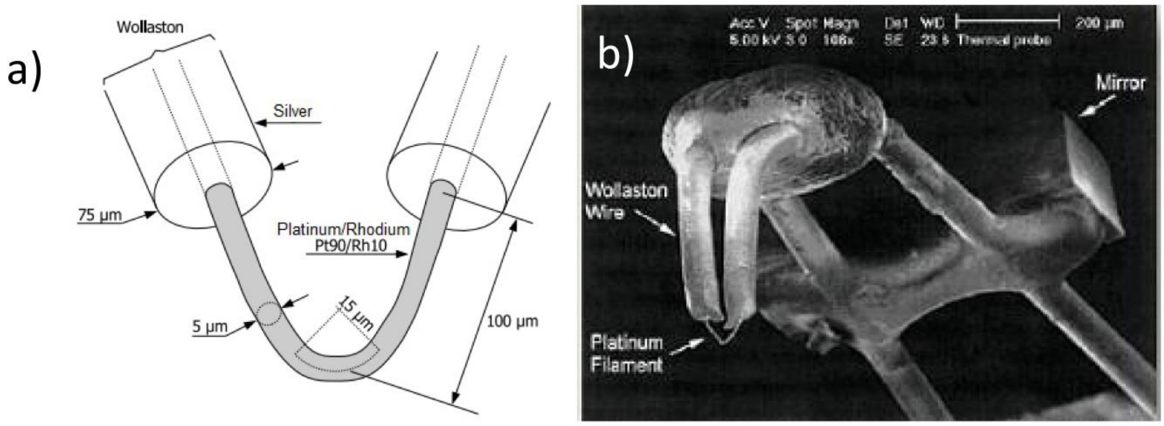

Figure 1.2. a) Description of the Wollaston probe b) SEM (Scanning Electron Microscope) image of the Wollaston probe.

1.3.2 The KNT probe (the palladium or GLA probe)

The KNT probe is basically made for creating hot spots on surfaces and for characterization of polymer layers and thin films [16]. It consists of a thin film Pd as resistor and pads made of Gold deposited on a cantilever as shown in Figure 1.3. The cantilever was first made of Silicon Dioxide (SiO_2) and then changed to Silicon Nitride (Si_3N_4) [17]. The cantilever length, width, thickness are 150 µm, 60 µm and 0.4 µm respectively. The tip height and thickness are respectively 10 µm and 40nm and its width varies between 1.5 and 6 µm. The tip radius is smaller than 100 nm [16, 17] . Figure 1.4 shows SEM images of the considered probe.

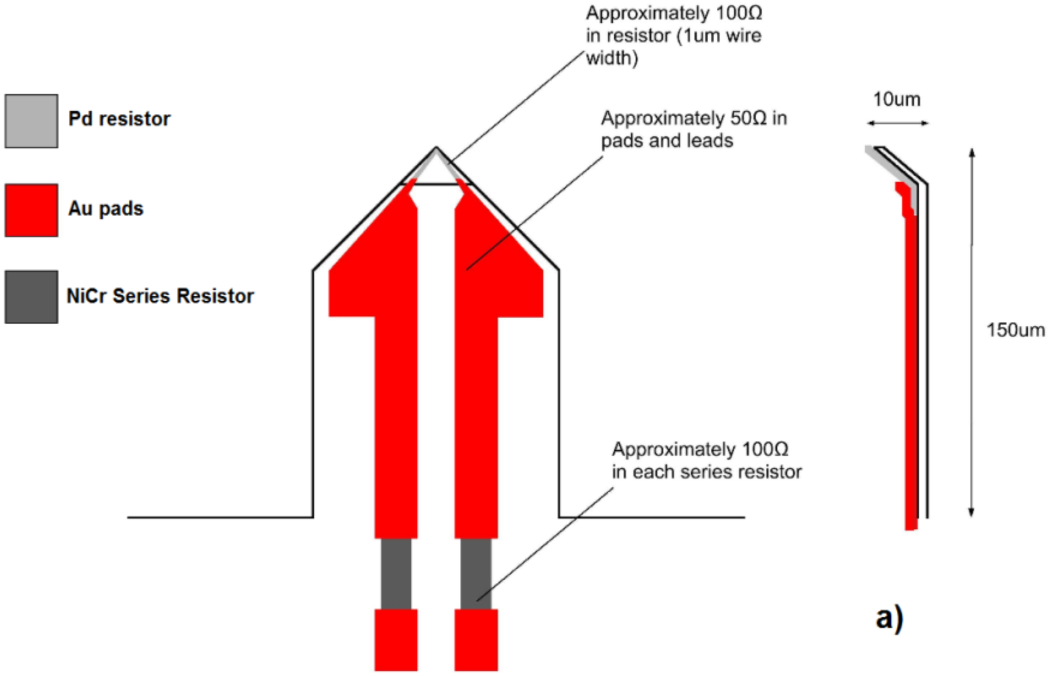

Figure 1.3. Description of the KNT probe (courtesy of Kelvin NanoTechnology).

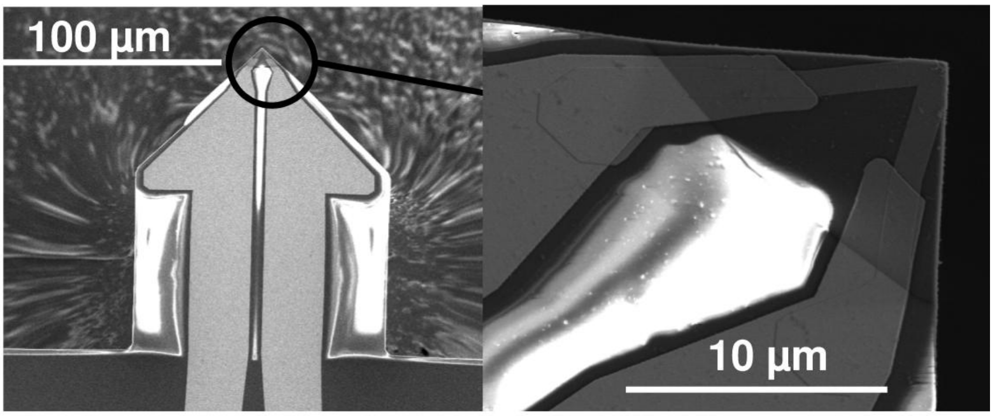

Figure 1.4. SEM images of the palladium probe.

1.3.3 Silicon nanoprobes

The silicon nanoprobes were first developed by IBM for high data-rate storage systems and high-speed nanoscale lithography applications [18, 19]. This type of probe can be also used for other application such as the characterization of polymers [20]. Later, Nelson and King [21] developed similar silicon probes but with pyramidal tips . As seen in Figure 1.5, the cantilever consists of two micrometric legs with high doping level and a low doped resistive element platform. The tip of a nanometric radius curvature has a pyramidal shape (conical in case of IBM probe) is mounted on top of the resistive element. Table 1.2 gives the dimensions of the silicon probes of IBM and the AN-300 commercialized by Anasys Instruments.

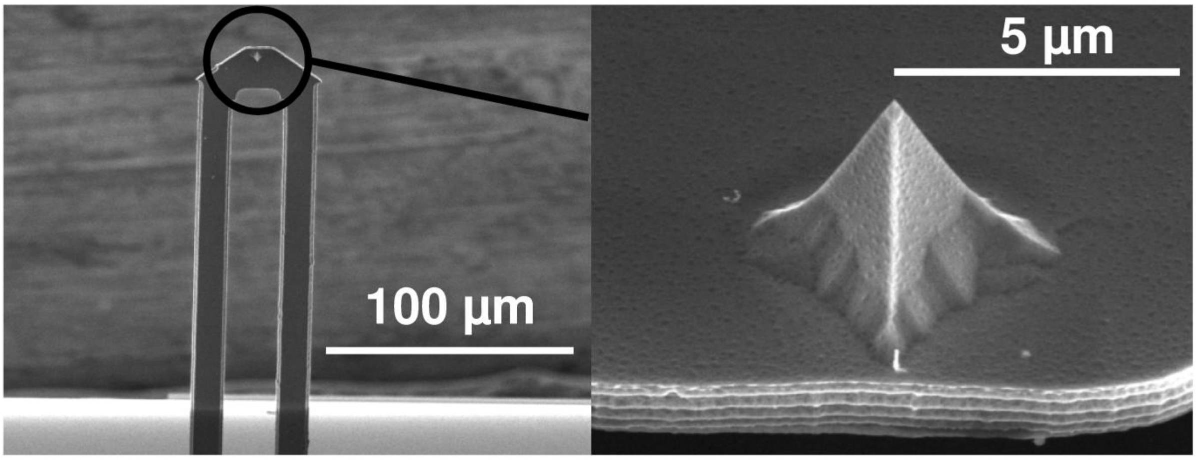

Figure 1.5. SEM images of the Anasys Instruments probes (Anasys instruments).

Table 1.2. Dimensions of different silicon nanoprobes.

Tip	Leg length (µm)	Leg width (µm)	Leg thickness (µm)	Tip height (µm)	Tip radius (nm)	Spring constant ($N.m^{-1}$)	Resonant Frequency (KHz)
AN-300	300	20	2	3-6	< 30	0.5-3	15-30
IBM [18]	50	10	0.5	2	< 20	1	200

Due to the change of the probes configuration and size, each type of probe requires a proper approach of the measurements for a better characterization of the thermal properties of the samples. The models mainly used to describe the probe-sample system are given in the next section.

1.4 Approaches of the measurement

For resistive probes, the analysis and interpretation of measurements requires a specific modeling linking the electrical measurement to the sample thermal properties. The establishment of this modeling requires the estimation of the heat flux transferred from the probe to the sample that is related to the tip apex temperature. The tip apex temperature is often determined by solving the heat equation within the probe.

1.4.1 The Wollaston probe

In his thesis, Lefèvre [22] divided through symmetry the probe-sample system into two parts and each part was modeled as a thermal fin as shown in Figure 1.6.

After writing the heat balance on an element dx of the probe as illustrated in Figure 1.7, the heat equation is:

$$\frac{\partial^2\theta}{\partial x^2} - \frac{hp}{\lambda S}\theta + \frac{\rho I^2}{\lambda S^2}(1+\alpha\theta) = \frac{1}{a}\frac{\partial\theta}{\partial t} \quad (1.1)$$

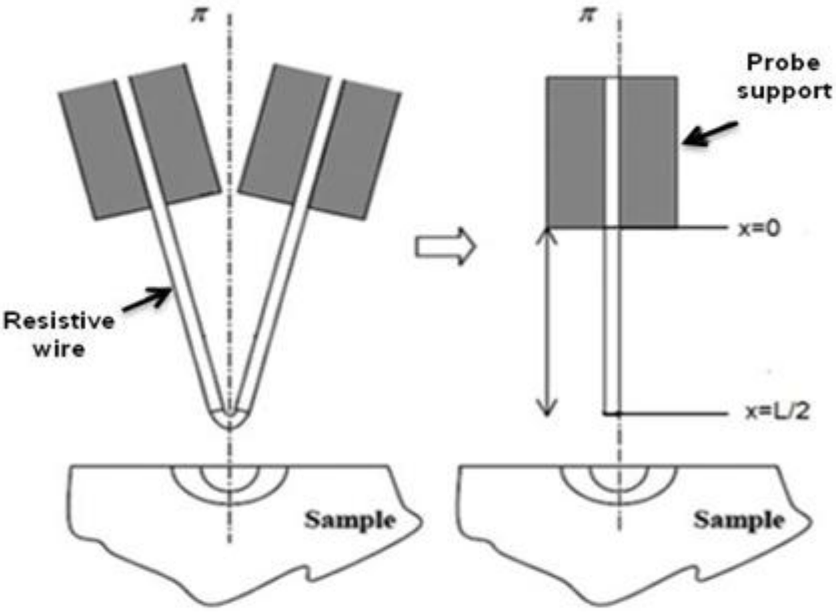

Figure 1.6. Schematic of the description of the Wollaston probe [22].

Here, $\theta = T\text{-}T_a$ is the relative temperature at abscissa x of the fin. p, S, ρ, λ and α are respectively the perimeter, section, electrical resistivity, thermal conductivity and thermal resistivity of the Pt90/Rh10 wire. *h* denotes heat transfer coefficient of the losses to the ambient environment.

Since the section of the Pt90/Rh10 wire is much smaller compared to that of the Wollaston wire, the extremities are assumed to be heat sinks ($T=T_a$ at x=0). Besides, the mean temperature of the probe is usually determined through electronic means (Wheatstone Bridge). Then the term $1+\alpha\theta$ in Equation (1.1) is replaced by $1+\alpha\bar{\theta}$ in first approximation. The probe can be heated through DC or AC current.

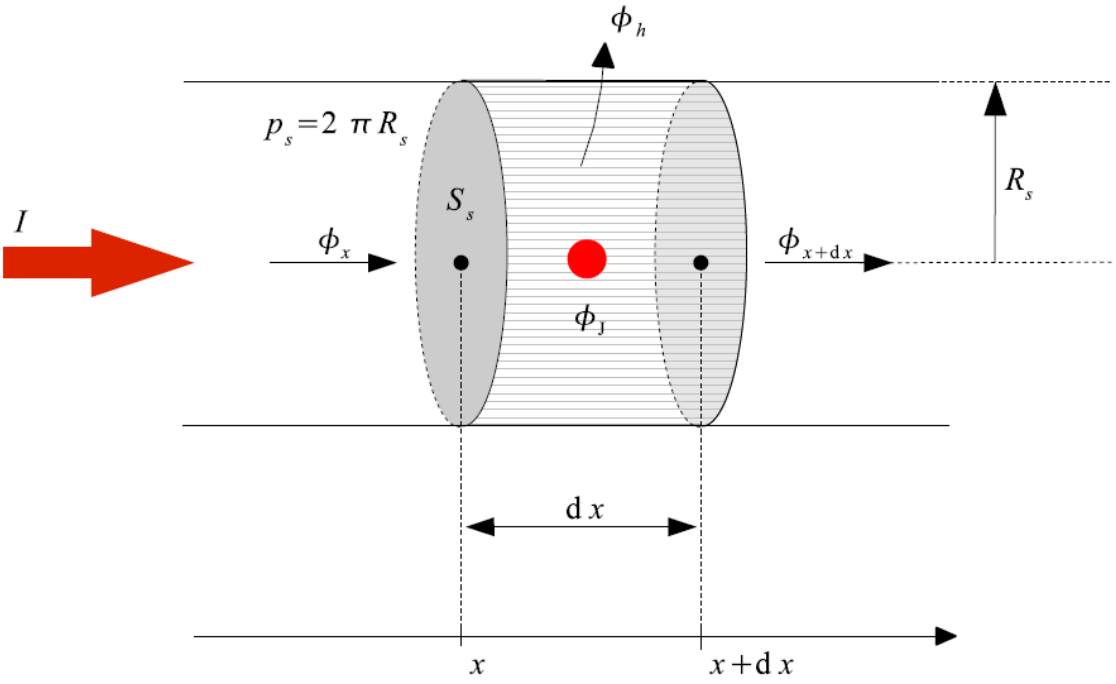

Figure 1.7. The heat balance on a element dx of the Pt90/Rd10 wire [22].

a) DC regime

When the probe is heated through DC current, the time taken by the probe to reach its equilibrium does not exceed 3 ms [22]. Once this time is exceeded, Equation (1.1) is:

$$\frac{\partial^2\theta}{\partial x^2} - \frac{hp}{\lambda S}\theta + \frac{\rho I^2}{\lambda S^2}(1+\alpha\bar{\theta}) = 0 \qquad (1.2)$$

When the probe is far from the contact, the boundary condition at the tip apex is:

$$\frac{\partial\theta}{\partial x}\left(x = \frac{L}{2}\right) = 0 \quad (1.3)$$

When the probe is in contact with the sample,

$$\lambda S \frac{\partial\theta}{\partial x}\left(x = \frac{L}{2}\right) = G_{eq}\theta\left(x = \frac{L}{2}\right) \quad (1.4)$$

where G_{eq} ($\mathrm{W.K^{-1}}$) represents the equivalent thermal conductance between the sample thermal conductance G_s and the probe-sample contact conductance G_c :

$$G_{eq} = \frac{G_s G_c}{G_s + G_c} \quad (1.5)$$

A description of the series of thermal conductances of the probe-sample is presented in Figure 1.8. $R_s = 1/G_s$ is the spreading resistance in the sample where section 1.4 is dedicated to present the modeling of this resistance in its different configurations. The heat mechanisms that operate between the probe and the sample are featured in G_c. Depending on the description of the heat source and on the sample (bulk, layered samples …), different expressions of G_s can be used. We will present more in detail these two thermal conductances later in this chapter.

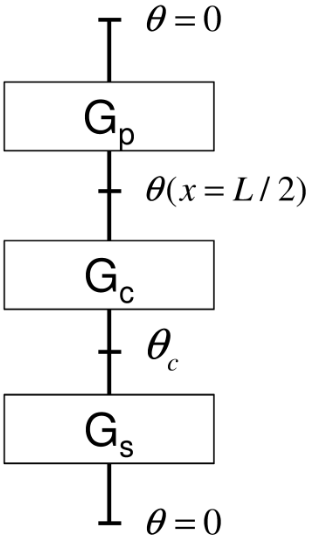

Figure 1.8. Description of the network of the thermal conductances of the probe-sample system.

Let $m^2=hp/\lambda S$ and $\Omega=G_{eq}/G_p$ where $G_p=\lambda S/L$ is the probe thermal conductance. Solving Equation (1.2) with the two conditions (Equations (1.3) and (1.4)), the probe Joule power when in contact is

$$P_c = \frac{\lambda S L^2 m^3 \bar{\theta}[2mLch(\frac{mL}{2}) + \Omega sh(\frac{mL}{2})]}{mL[-4sh(\frac{mL}{2}) + 2mLch(\frac{mL}{2})] + \Omega[4(1-ch(\frac{mL}{2})) + mLsh(\frac{mL}{2})]} \quad (1.6)$$

And when out of contact is

$$P_a = \frac{2kSL^2 m^3 \bar{\theta} ch(\frac{mL}{2})}{2mLch(\frac{mL}{2}) - 4sh(\frac{mL}{2})]} \quad (1.7)$$

The expression $\frac{\Delta P}{P_c} = \frac{P_c - P_a}{P_c}$ was used in the calibration of SThM probes for the measurements of the thermal conductivity of bulk samples [14, 23, 24]. In these works, the heat losses through convection were not taken into account (*h*=0). Under this condition, the resolution of Equation (1.2) leads to:

$$\frac{\Delta P}{P_c} = \frac{3}{4}\frac{G_c G_s}{4(G_p G_s + G_p G_c) + G_c G_s} \quad (1.8)$$

Later in this manuscript, we will show to what extent the coefficient *h* could affect the determination of the thermal conductivity of bulk samples and the thermal interaction parameters between the probe and the sample.

b) Alternating regime

When an AC current (alternating current) $I=I_0 \cos(\omega t)$ heats the probe, the Joule power dissipated in the Pt/Rd wire is:

$$P_p = \frac{RI_0^2}{2}(1+\cos(2\omega \mathrm{t})) \quad (1.9)$$

Then, the temperature in the probe is:

$$\theta(t) = \theta_{DC} + \theta_{2\omega}\cos(2\omega t + \phi) \quad (1.10)$$

The probe voltage can be written as follows:

$$V_p = RI = R_0(1+\alpha\theta_{DC})I_0\cos(\omega \mathrm{t}) + \frac{R_0\beta I_0\theta_{2\omega}}{2}\cos(\omega t + \phi) + \frac{R_0\beta I_0\theta_{2\omega}}{2}\cos(3\omega \mathrm{t} + \phi) \quad (1.11)$$

Under the assumption that the other voltage harmonics are negligible.

Practically, the terms at the first harmonic are deliberately suppressed using a Wheatstone bridge since they are much larger than the terms at the third harmonic $V_{3\omega} = RI = \frac{R_0\beta I_0\theta_{2\omega}}{2}\cos(3\omega \mathrm{t} + \phi)$. Through this expression, the alternating temperature $\theta_{2\omega}$ can be experimentally determined. Through a proper modeling, this temperature can be related to the thermal properties of the sample. This method was first developed by Cahill (well-known 3ω method) [25] and was adapted by Lefèvre [22] to the Wollaston wire probe in the AC regime. For sake of simplification, the complex writing is used ($I = I_0 e^{i\omega t}$) and the temperature in the probe is written as:

$$\theta(t) = \theta_{DC} + \theta_{2\omega} e^{2i\omega t} \quad (1.12)$$

Then the heat equation in the alternating regime becomes [22]:

$$\frac{2i\omega}{a}\theta_{2\omega} = \frac{\rho I_0^2}{2\lambda S^2} - \frac{hp}{\lambda S}\theta_{2\omega} + \frac{\partial^2 \theta_{2\omega}}{\partial x^2} \quad (1.13)$$

The same conditions in Equations (1.3) and (1.4) are used here for the resolution of Equation (1.13):

$$\theta_{2\omega} = \frac{\rho I_0^2}{2Lm^3\lambda S^2} \frac{AG_{eq} + BG_{eq} mL}{[e^{2mL} - 1]G_{eq} + [1 + e^{2mL}]G_{eq} mL} \quad (1.14)$$

where

$$A = -2 - mL + 4e^{mL} - 2e^{2mL} + mLe^{2mL} \quad (1.15)$$

and

$$B = 1 + mL - e^{2mL} + mLe^{2mL} \quad (1.16)$$

Parameters identified with these approaches:

Measuring $\theta_{2\omega}$ through the measurements of $V_{3\omega}$ as a function of the angular frequency ω permits a determination of the equivalent conductance G_{eq} for a specific sample [26]. Thus, with appropriate description of the sample conductance G_s, one can determine the contact conductance G_c for a sample of well-known thermal conductivity. This cannot be done in the DC regime where the determined G_c is equivalent among different samples of well-known thermal conductivity. However, an issue concerning the thermal expansion of the probe while working under the AC regime was reported [27]. In fact, the contact between the probe and the sample is not stable. That could be the reason behind the dispersion of the measurements obtained by Lefèvre [26].Based on these observations, Chapuis [27] suggested that it is better using the DC regime for distances of separation d_s smaller than 50 nm.

1.4.2 The palladium probe

Puyoo [28] used the old palladium probe (with SiO_2 cantilever) in the AC regime to determine the thermal conductivity of silicon nanowires embedded in silicon dioxide sample. In his approach of measurement, he adapted the model of Lefèvre [24] to the palladium probe by describing the probe as two thermal fins composed of two adjacent materials (Pd and SiO_2) as shown in Figure 1.9. The term of diffusion was just taken for the part of SiO_2 since this part has a larger section compared to that of Pd ($S_{SiO2}/S_{Pd} \sim 25$). The same boundary conditions as in Equations (1.3) and (1.4) were taken and the measurements were performed.

Since the dimensions at the tip apex are down to distances compared to the mean free path of material, the thermal conductivity of the probe apex can differ from the one estimated in the diffusive regime [29]. In fact, in the case of Silicon Nitride Si_3N_4 cantilever, the phonon mean free path at room temperature is of the order of 20 nm [30] and the tip radius is about 50 nm. Tovee *et al.* [16] suggested that heat transfer in the probe based on the diffusive regime is a reasonable approximation. They related their approach to the fact that the Knudsen number is smaller in the case of SiO_2 (old cantilever) - $Kn \simeq 0.2$. However, the thermal resistance of the probe R_p determined experimentally in vacuum environment ($R_p = 8 \times 10^4$ K.W^{-1}) is larger than expected with numerical simulations ($R_p = 5.35 \times 10^4$ K.W^{-1} [16]). This could be related to the section decreasing at the probe apex and thus to an additional thermal resistance induced by the boundary scattering within the probe apex to be taken into account [16, 31]. These effect were not taken into account in the numerical simulations as discussed by the authors [16].

An additional issue that faces the description of the probe-sample system is the spreading resistance of the sample R_s. In fact, the radius of the tip-sample mechanical contact might be smaller than the mean free path of heat carriers in the sample and thus an appropriate description of R_{sp} is needed as will be discussed in section 1.4.

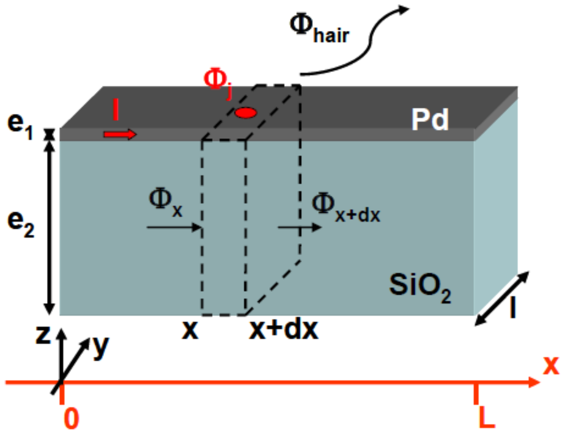

Figure 1.9. The description of the KNT probe [28].

1.4.3 Silicon nanoprobes

The classical description of the heat conduction within the tip of these probes based on the diffusive regime cannot be applied. This is due to the small dimensions and shape of the probe and to the fact that the mean free path of the tip material (Si) is comparable to the tip dimensions. As an example, the mean free path of phonons in Silicon is around 200 nm at room temperature and the radius of the Si tip apex is around 30 nm. Therefore, due to the diffuse scattering of the phonons at the tip boundaries, the thermal resistance of the nanostructures (nano-tip in our case) is increased [32]. While working in an air medium with these probes, most of the heat is transferred from the probe cantilever to the air and thus to the substrate [12].

In their works based on numerical simulations, Nelson and King [33] modeled the overall thermal resistance in the tip is as two parts: a conical resistance R_{cone} (for diffusive part) and a hemispherical resistance R_{sphere} (nanoscaled apex part). The radius of the sphere was assumed the same of the tip apex and the heat transfer in the hemisphere was assumed one-dimensional in Cartesian coordinates [33] and the conduction to the ambient air was neglected. This condition would include less error while working under ultra-vacuum environment where heat conduction through the air is eliminated. The thermal resistance due the phonon scattering at the tip-sample contact is given as a function of an interval of the thermal boundary resistance (Kapitza resistance) R_b ($m^2.K.W^{-1}$) [34] and depends on the sample material [33]. R_b is defined as “the ratio of the temperature discontinuity at the interface to the power per unit area flowing across that interface ($K.m^2.W^{-1}$) [34]”.

Furthermore, Gotsmann *et al.* [12] proposed an analytical model in which the tip-sample system is modeled as a series of thermal resistances as described in Figure 1.10. The temperature at the sample surface can be given through the coefficient Δ:

$$\Delta = \frac{T_s - T_0}{T_{heater} - T_0} = \frac{R_s}{R_{tip} + R_{interface} + R_s} \quad (1.17)$$

Here, R_{sp}, $R_{interface}$, R_{tip} are respectively the thermal resistances of the sample, the interface and the tip. R_{tip} denotes the diffusive part of the tip resistance and the part linked to boundary scattering should be included in $R_{interface}$ [12]. Under UHV conditions (~ 10^{-8} – 10^{-9} mbar), $R_{interface}$ depends on the probe and sample materials and the scattering physics at the interface. The coefficient Δ in Equation (1.17) varies between 0.3 and 0.7 for polymers ($R_s >> R_{interface}$), about 10^{-3}-10^{-4} for metals ($R_s << R_{interface}$) [12]. The described model does not take the losses at the tip apex to the surrounding medium into account and is more accurate for the interpretation of measurements performed under UHV conditions.

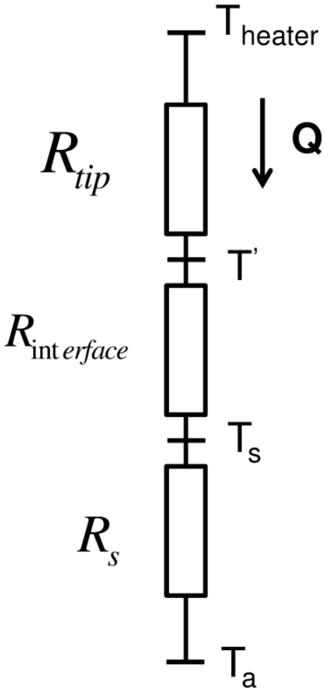

Figure 1.10. Modeling the tip-sample system as given by Gotsmann *et al.* [12].

Moreover, Gotsmann *et al.* [12] modeled $R_{interface}$ through a phonon reflection coefficient r_{12} as shown in Figure 1.11. In this approach, $R_{interface}$ is dependent on the sample material and on the scattering at the interface:

$$R_{interface} = \frac{r_{12}}{1-r_{12}} R_{tip} + \frac{r_{12}}{1-r_{12}} R_s \quad (1.18)$$

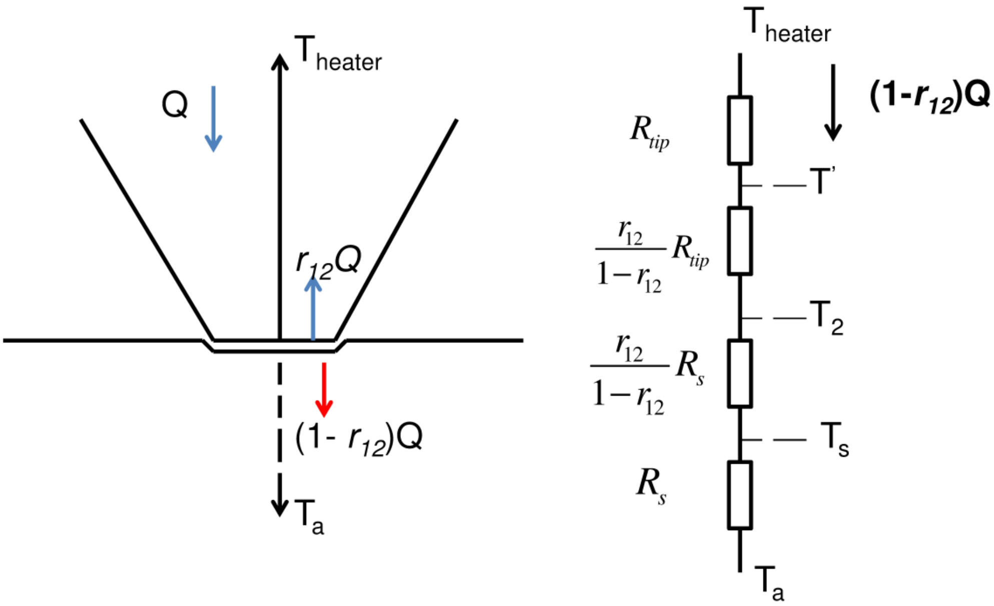

Figure 1.11. Modeling the scattering at the interface through the phonon reflection coefficient r_{12} [12].

As seen in this section, each probe has its own geometrical dimensions and its configuration of the heater. This requires an appropriate model of the probe-sample system for each of these probes described above that takes into account the configuration of the heater and the effect of the decreasing sizes.

The modeling of the probe-sample interaction is related to different parameters in order to quantify the mechanisms of heat transport between the probe and the sample.

1.5 Heat losses through the air

While working under ambient conditions, a fraction of the heat is lost from the probe to the medium environment. When the dimensions go down to the micro-scales, the heat transfer coefficient due to convection becomes smaller as the buoyancy forces decrease [35]. Thus, the heat losses to the air are due to the mechanism of conduction [36]. The equivalent heat transfer coefficient *h* to these losses, which depends on the probe size, is larger than that at macro-scales due to larger surface to volume ratio.

In order to estimate *h* for the Wollaston wire probe, Chapuis [37] measured in AC regime the amplitude of the second harmonic $\theta_{2\omega}$ of the probe temperature at different levels of pressure *P* for a probe away from any contact. The theoretical $\theta_{2\omega} = f(h)$ (see Equation (1.14)) and the measurement $\theta_{2\omega}=f(P)$ permitted to have the graph $h=f(P)$. The graph was fitted with the theory of Lee [38] of the resolution of the Boltzmann equation for the heat transfer through gas molecules between two co-axial cylinders. The obtained value was approximately 3500 W.m^{-2}.K^{-1}. In fact, this value is close to the value given by the correlation given by Taine and Petit [39] for the case of a long vertical cylinder of diameter D and length L:

$$Nu = 0.93(Ra(D)\frac{D}{L})^{0.05} \quad \text{(For Ra(D)D/L < 0.05)} \quad (1.19)$$

Based on this correlation and for the dimensions of the Wollaston wire probe, *h* is around 2800 W.m^{-2}.K^{-1}.

These values are similar too to the values determined by Thierry *et al.* [40] for welded Wollaston wires of different diameters (5 µm, 1.3 and 0.5) by using the two omega method. The identified values for h are 2300, 6500 and 13000 W.m^{-2}.K^{-1} for wire diameter of 5, 1.3 and 0.5 µm respectively.

For the palladium wire, Puyoo [28] identified *h* by comparing the probe signal while working under ambient environment and under vacuum conditions (10^{-5} mbar) where no transfer to the air is assumed. The identified value was about 6600 W.m^{-2}.K^{-1}.

Kim and King [41] used numerical simulations and FE model to determine the heat losses to the air from the silicon cantilever of the silicon probes described in part 1.2.3. The estimated coefficient *h* around the leg was found about 2000 $W.m^{-2}.K^{-1}$ and about 7000 $W.m^{-2}.K^{-1}$ around the heater for a steady state heating.

All the values of *h* in the studies mentioned above show that h is enhanced largely at the small scales comparing to the values at the macro scales. We should mention that these studies identified the values of *h* when the probe is out of contact of the sample. Such values are susceptible to some changes when the probe comes to contact with the sample due to a restricted area of exchange between the probe and the environment medium. This is often neglected in SThM as discussed by Raphael [42]. Moreover, as can be seen, a high dispersion during the evaluation of *h* can be noticed. The dispersion of the values of h is related to the variety of the models of estimating *h* and the boundary conditions at the probe surface. Moreover, the models do not overcome the change in the probe parameters. Lefèvre [22] estimated the error to be less than 3 % while evaluating the heat dissipated within the probe through Joule effect between two cases: h=1000 $W.m^{-2}.K^{-1}$ and h=0.

1.6 Thermal spreading resistance

As seen in the section of the interaction modeling, the exchange between the probe in contact with the sample can be modeled through an equivalent conductance G_{eq} (Equation (1.5)). One of the components of G_{eq} is the thermal spreading resistance R_s in the sample. R_s depends on the description of the thermal boundary condition taken into account at the thermal contact and the sample geometry and dimensions. When the heat is spread into a semi-infinite sample as show in Figure 1.12, the thermal spreading resistance is defined as:

$$R_s = \frac{\overline{T}_{\text{source}} - \overline{T}_{\text{heatsink}}}{Q} \quad (1.20)$$

where Q is the heat transfer rate, $\overline{T}_{\text{source}}$ is the temperature average of the heat source and $\overline{T}_{\text{heat sink}}$ is the temperature of a sink. Describing the area of the thermal contact between the tip and the sample as a circular one of radius *b* one seems the most used. *b* denotes the equivalent radius of the global exchange taking into account all the mechanisms of the heat transfer.

If we consider the source as an isothermal circular area, thus R_s is given by [43]:

$$R_s = \frac{1}{4\lambda_s b} \quad (1.21)$$

where λ_s is the thermal conductivity of the semi-infinite sample.

If the source is considered as an isoflux circular area, then [43]:

$$R_s = \frac{8}{3\pi^2}\frac{1}{\lambda_s b} \quad (1.22)$$

The difference between the Equations (1.21) and (1.22) is around 7%.

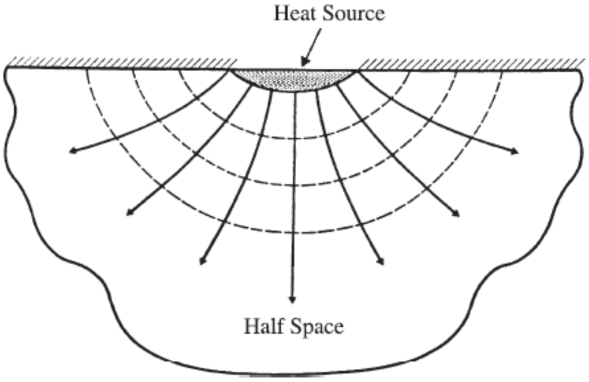

Figure 1.12. Heat flow lines and isotherms during the conduction from a localized heat source [43].

In the modeling of the tip-sample interaction, the ballistic constriction resistance to add here is taken however into account into the resistance of contact $R_{contact}$ (modeling of Nelson and King [21]) and into $R_{interface}$ (Gotsmann *et al.* [12]).

More information about the modeling of the resistance of constriction can be found in ref. [29].

1.7 Heat transfer mechanisms between SThM probes and sample

The thermal conductance at the contact G_c depends on the mechanisms by which the heat is transferred from the probe to the sample. Under ambient conditions and when the probe is out of contact of the sample, the heat transfer is made through radiation and conduction through the air. Two mechanisms are added when the probe gets into contact: the solid-solid contact and the conduction through the water meniscus that is formed between the tip and the sample as shown in Figure 1.13 [13]. In this section, we review the literature works that studied these different modes of the heat transfer or the ones that passed by some measurements that could be an indication to these mechanisms.

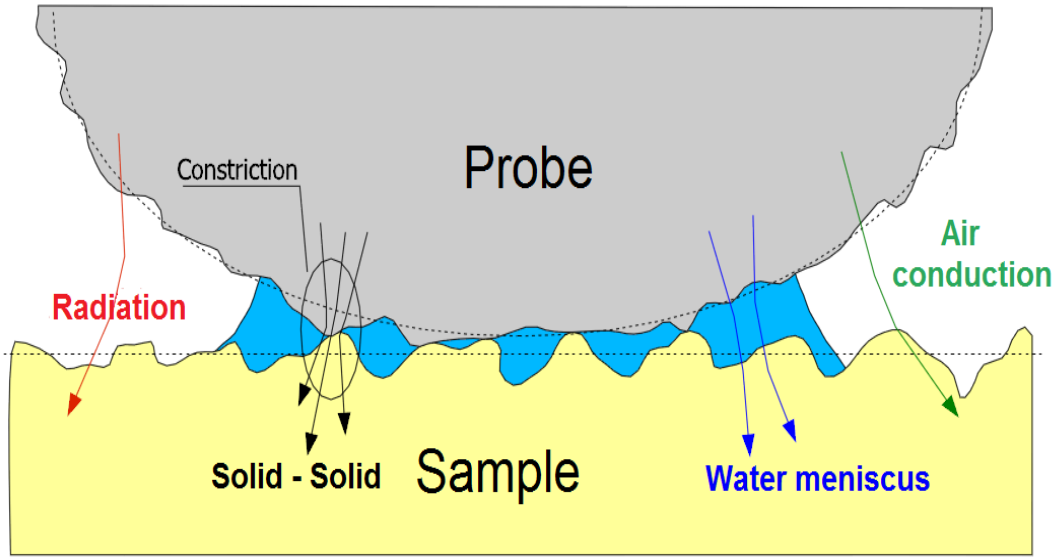

Figure 1.13. Schematic of the different heat mechanism that operate between the probe and the sample [13].

1.7.1 Heat transfer through radiation

Under ambient environment, the thermal conductance due to radiation is much smaller than the ones of other mechanisms [13, 44]. Thus, this heat mechanism is not taken into account while modeling the heat exchange under ambient conditions [13, 14, 44]. To estimate the radiation heat transfer, one must work under special conditions such as ultra-high vacuum (P ~ 10^{-8} – 10^{-9} mbar) environment where conduction through meniscus and through the air might be suppressed.

Under UHV conditions and when the probe is out of contact of the sample, the conduction through air is suppressed and the heat is transferred to the sample only by radiation. When the separation distance between the probe and the sample becomes smaller than the peak wavelength of thermal radiation λ_{max} ($\simeq$ 10 µm at ambient temperature), the heat transfer due to radiation may increase due to evanescent electromagnetic domains close the two surfaces. Still we have to be careful about this hypothesis since any enhancement is dependent on the size of the two bodies [27]. Besides, the heat conductance between the bodies depends on their nature too (dielectrics or metals [27]) as shown by Chapuis [27] through numerical simulations of the heat exchange between sphere of different radius and different materials.

Using the IBM type of silicon probes (part 1.3.3), Hinz *et al.* [45] observed the heater temperature variations while approaching/retracting from a SiO_2 sample under high vacuum conditions (10^{-5} mbar). As shown in Figure 1.14, the heater temperature decreases before the contact (from A to B) and that could be related to the heat transfer through radiation. In fact, the authors suggested this contribution or an electrostatic interaction with the sample [45].

Working under UHV conditions (P ~ 10^{-8} – 10^{-9} mbar), Kittel *et al.* [46] measured the heat exchange power Q between a nanotip of gold at room temperature and a cooled sample (T_{sample} = 100 K) of gold at different distances of separation (from 1 to 100 nm). When the separation is about 1 nm, Q is about 10^{-5} W. If we suppose that the temperature difference is about 200 K, then the radiation conductance G_{rad} is about 5×10^{-8} W.K^{-1}. Narayanaswamy *et al.* [47] determined G_{rad} between a silica sphere of 50 µm in diameter and a substrate of glass for a $\Delta T \simeq 50$ K under high-vacuum conditions (P = 6.7×10^{-5} mbar). At a separation distance of 100 nm, G_{rad} was found around 5×10^{-8} W.K^{-1}. Later, the same group showed how near-field radiation is affected by the nature of the sample [48]. In their work, the heat transfer through radiation between SiO_2 sphere and Au sample did not show any even at a separation distance of 30 nm. That was not the case of SiO_2 sample where the heat transfer showed a significant change above the far-field limit [48].

Therefore, it can be seen that the heat transfer through radiation can be detectable in SThM where accurate measurements might be while working under special conditions (UHV conditions). However, to increase that possibility, the sample (or tips) with their materials and shapes should be appropriately selected [49].

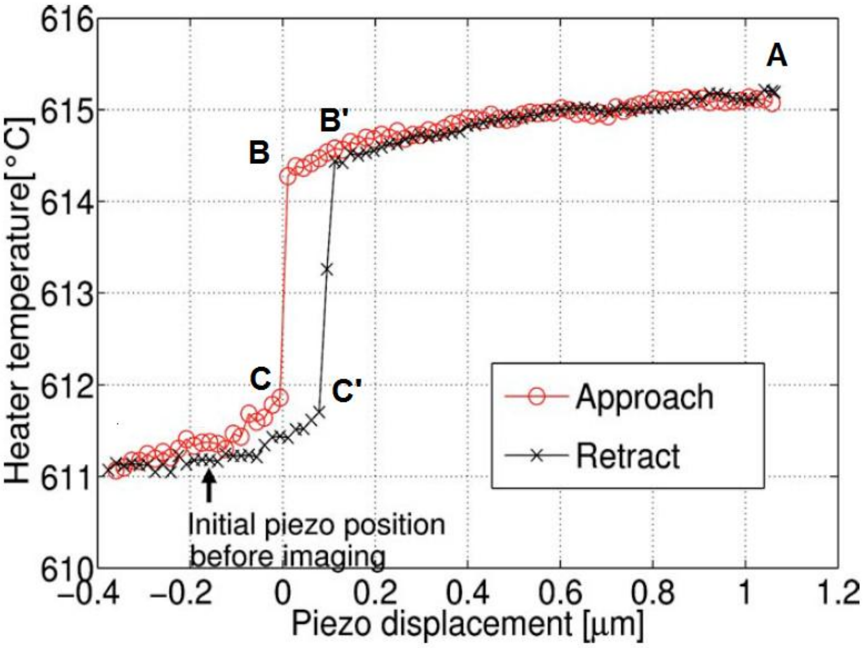

Figure 1.14. Variation the heater temperature of a silicon probe during the approach and retract curves [45] (Frequency of 1 Hz – $P = 10^{-5}$ mbar).

1.7.2 Heat transfer at solid-solid contact

When the tip contacts the sample, a percentage of heat is transferred through the mechanical contact. To quantify this percentage, we need first to determine the radius of contact a_c. Many theories exist already to evaluate a_c and the parameters that affect its value. For an elastic deformation, Hertz firstly estimates a_c between a sphere of radius R_{sph} and a flat surface as follows [50]:

$$a_c = (\frac{F_N R_{sph}}{E^*})^{\frac{1}{3}} \quad (1.23)$$

with F_N the normal load and E^* is the effective Young modulus given as:

$$E^* = \frac{4}{3}(\frac{1-\nu_1^2}{E_1} + \frac{1-\nu_2^2}{E_2})^{-1} \quad (1.24)$$

E_1, E_2 are the Young modules of the sphere and the surface and ν_1 and ν_2 are their Poisson coefficients respectively. This equation does not account for the adhesion between the two bodies. Two models exist and take into account the adhesive forces between a sphere in contact with a plane surface: the JKR (Johnson, Kendall and Roberts) [50, 51] and DMT [50, 52] (Derjaguin, Muller and Toporov) models. These models are adapted to different types of pull-off forces that are defined as the required forces to separate a surface from another surface [53]. The JKR model suggests having non-zero contact area when no normal load is applied. Here, a_c is estimated as [50]:

$$a_c = [\frac{R_{sph}}{E^*}(\sqrt{F_N + F_{ad}} + \sqrt{F_{ad}})]^{\frac{1}{3}} = [\frac{R_{sph}}{E^*}(F_N + 3\pi w_d R_{sph} + \sqrt{6\pi w_d R_{sph} F_N + (3\pi w_d R_{sph})^2})]^{\frac{1}{3}} \quad (1.25)$$

where F_{ad} is the adhesion force and w_d is the Dupré energy of adhesion.

Derjaguin, Muller and Toporov (DMT) assumed that when the sphere and the surface are separated, a_c goes to zero. In the DMT model a_c is determined as [50]:

$$a_c = [\frac{R_{sph}}{E^*}(F_N + F_{ad})]^{\frac{1}{3}} = [\frac{R_{sph}}{E^*}(F_N + 2\pi w R_{sph})]^{\frac{1}{3}} \quad (1.26)$$

The contact when it involves spheres of large radii and of large and short-range pull-off forces is well described with the JKR model [50, 54]. On the other hand, the DMT model explains well the contact of stiff materials and of small and long-range pull-off forces [50, 54]. A transition parameter exist between the two models and known as the Maugis parameter [55].

Generally, in SThM, the mechanical properties of materials used in the different models are the properties at the large scales. More appropriate properties at the micro/nanoscales can be used by taking the estimation of mechanical properties of materials using the nano-indentation techniques. The Hertzian theory is included in the modeling of Majumdar for the solid-solid thermal conductance G_{ss} [44]. Through an effective thermal conductivity of the contact and a conical probe of opening θ, G_{ss} was estimated as:

$$G_{ss} = 2\pi a_c \lambda_{eff} = 2\pi a_c \frac{\lambda_s \lambda_p \tan\theta}{2\lambda_s + \lambda_p \tan\theta} \quad (1.27)$$

where λ_p, λ_s are respectively the thermal conductivity of the probe and the sample. Here, a_c is the radius of the contact area linked to the mechanical contact between the probe and the sample.

Similarly, David *et al.* [14] estimated G_{ss} for the Wollaston wire probe as:

$$G_{ss} = 2\pi a_c \lambda_{eff} = 2\pi a_c \frac{\lambda_s \lambda_p}{\lambda_s + \lambda_p} \quad (1.\ 28)$$

However, this macroscopic formula of the conductance cannot describe accurately a contact in the order of ten of nanometers or less depending on the probe size. If we suppose $a_c = 10$ nm as determined through thermal conductivity calibration by David [56], the values of G_{ss} vary between 7×10^{-8} W.K^{-1} for Silica sample ($\lambda_{SiO2} \simeq 1.2$ W.m^{-1}.K^{-1} at $T=T_a$) and 2×10^{-6} W.K^{-1} for Silicon sample ($\lambda_{Si} \simeq 148$ W.m^{-1}.K^{-1} at $T=T_a$). We have to note that such an approach takes an equivalent a_c among the calibration samples without including the materials mechanical properties (Young modulus E and Poisson ratio v).

Experimentally, the perfect conditions to detect the thermal conduction due to the mechanical contact are to work under vacuum conditions [44]. Under these conditions, there are two modes of heat transfer between the probe and the sample: the radiation and the solid-solid conductances. As mentioned before, the radiation is usually negligible in front of the other mechanisms and thus any change at the contact may be due to the solid-solid conductance. Hinz *et al.* [45] related the heater temperature change observed in Figure 1.14 to the conduction at the mechanical contact. G_{ss} was evaluated around 1.5×10^{-7} W.K^{-1} [45].

However, we can notice a signal shift while approaching and retracting the probe (lines BB' and CC' in Figure 1.14). This shift is similar to the measurements performed by Puyoo with the palladium probe [28]. Puyoo [28] performed simultaneous measurements of the $V_{3\omega}$ probe voltage and the deflection of the cantilever during the approach and retract curves at a pressure of 10^{-5} mbar. As seen in Figure 1.15, a significant change of the $V_{3\omega}$ signal occurred at the contact. But while retracting the probe, the jump-off-contact deflection still exists and the $V_{3\omega}$ signal variation does not take place at the same position while approaching the probe. The jump-off-contact deflection could be related to what remains of the water meniscus + the elastic forces or just the elastic forces. The observed effects might be also related to the nature of the sample (hydrophilic, hydrophobic) and the stiffness of the probe. If this deflection is just due to the elastic forces as the tip snaps into the sample, thus the change of the $V_{3\omega}$ signal is due solely to the solid-solid conduction. One needed parameter here is the probe temperature. We have to note that both of the measurements of Hinz *et al.* [45] and Puyoo [28] are not performed under UHV conditions but at a pressure around 10^{-5} mbar where an eventual meniscus might exist between the probe and the sample.

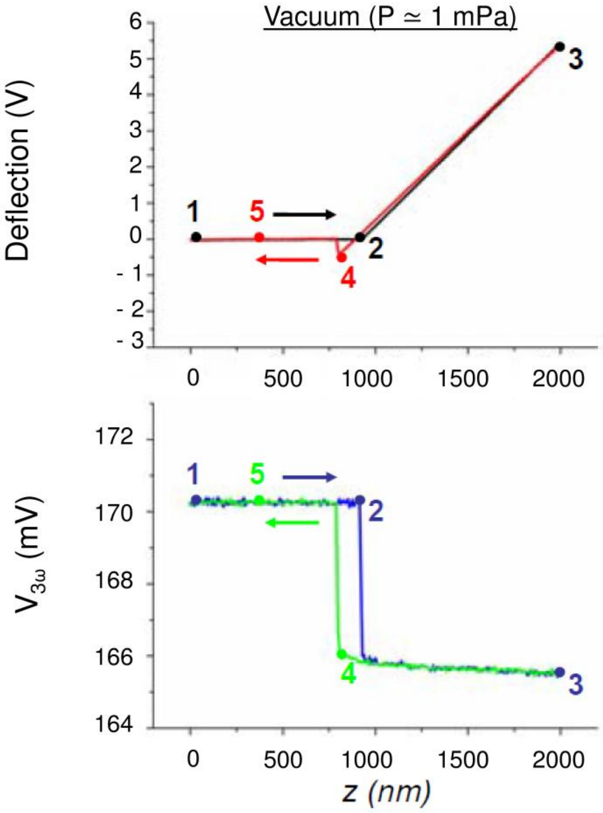

Figure 1.15. The variation of the deflection and $V_{3\omega}$ probe voltage as a function of the probe/sample distance. The probe used here is the palladium probe and the sample is made of Silicon (P=10^{-5} mbar and I_{probe}= 308 µA [28]).

Using the Wollaston wire probe, David [57] measured the thermal signal $\Delta P/P_c$ of the probe in interaction with a silicon sample at different levels of pressure as a function of the probe/sample distance d. As shown in Figure 1.16, $\Delta P/P_c$ stays constant at a pressure of 3 mbar as a function of d until the contact is established. Let us note that these measurements were performed with probe temperatures larger than 100 °C, temperatures at which the water meniscus was assumed vanished. Using his equation of G_{ss} (Equation (1.28)) and the formula of $\Delta P/P_c$ (Equations (1.6) and (1.7)) and including the thermal conductivity of the used silicon sample, we can estimate the value of a_c around 20 nm. Lefèvre [22] performed $\Delta P/P_c$ measurements while varying the force F (given in electrical signal ΔI) on a sample of Hafnium with the same probe. G_{eq} (Equation (1.5)) varied linearly as a function of F as shown in Figure 1.17 and thus he suggested that the G_{ss} varied the same ($G_{ss}=K\times\Delta I$). However, the temperature at which these measurements were performed was not mentioned. If the water meniscus existed between the probe and the sample and the force was varied, the conductance through the water meniscus would have been varied too as a function of F. If the water meniscus was evaporated, then this could significant information of how the applied force by the probe on the sample affects G_{ss}.

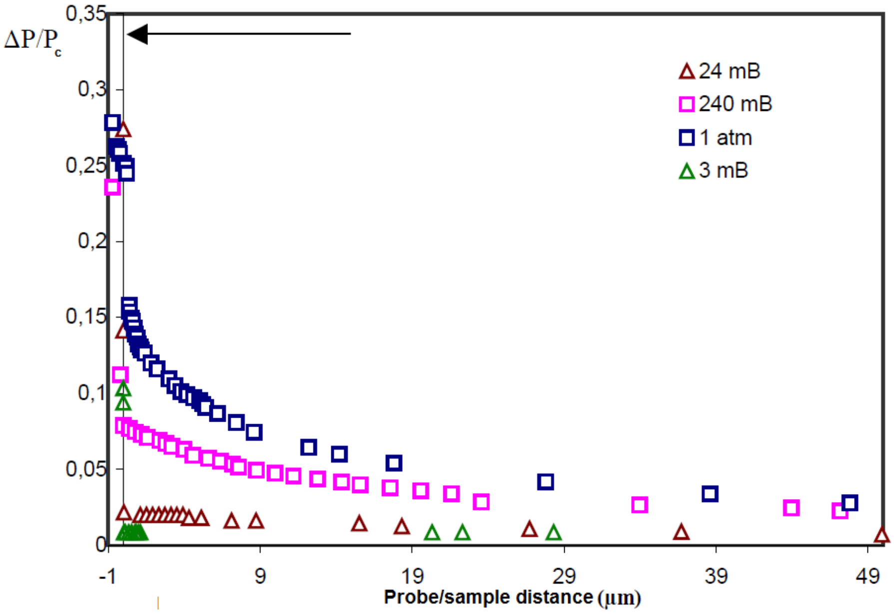

Figure 1.16. Variation of the thermal signal $\Delta P/P_c$ as a function of the probe/sample distance between a Wollaston wire probe and a monocrystalline silicon sample at different levels of pressure[57].

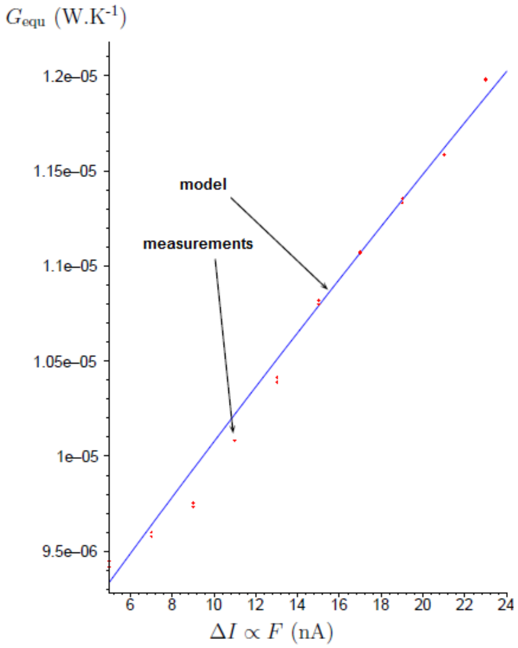

Figure 1.17. Variation of the equivalent conductance G_{eq} as a function of the force signal ΔI for measurements performed on a sample of Hafnium under ambient conditions [22].

As we can notice, the identification of the solid-solid conductance passes too through working under appropriate experimental conditions. Working under high-vacuum conditions assures the suppression of the conduction through air but there is still a doubt whether the meniscus is totally vanished under such conditions. Another needed parameter is the probe temperature while performing the measurements that could leave or suppress the doubt about the existence or the absence of the water meniscus. An estimation of the contribution of the water meniscus to the heat transfer to the sample could help here (see later in Chapter 2).

Besides, in the whole theories and measurements cited above in this section, the contact between the probe and the sample was assumed perfect and no effect of roughness is taken into account. If the measurements are performed under UHV conditions with a rough tip-sample contact, modeling the tip-sample thermal requires a better description of the contact to take into account the additive resistance due to the rough contact.

The information about the effect of the roughness on G_{ss} conduction remains scarce in literature. Recently, Gotsmann and Lantz [58] identified G_{ss} while approaching a flat-punch tip of silicon probe and taC (tetrahedral amorphous carbon) sample surface while performing measurement under high vacuum conditions (P ≃ 6 × 10^{-6} mbar). As can be seen in Figure 1.18, the thermal resistance at the contact is around 2 × 10^{-8} W.K^{-1}. The authors go beyond these measurements to determine the thermal conductance per atom-atom contacts [58]. The applied force between the probe and the sample was estimated and the number of atom-atom contacts is approximated [58]. The conductance per atom-atom contact is given as:

$$G_{atom-atom} = G_Q N t_{12} \quad (1.29)$$

where G_Q is the quantum thermal conductance per phonon mode, N is the number of phonon modes and $t_{12} = 1 - r_{12}$ is the transmission coefficient and r_{12} is the same reflection coefficient already encountered before in Equation (1.18). $G_{atom\text{-}atom}$ was found around 1.2 × 10^{-9} W.K^{-1}.

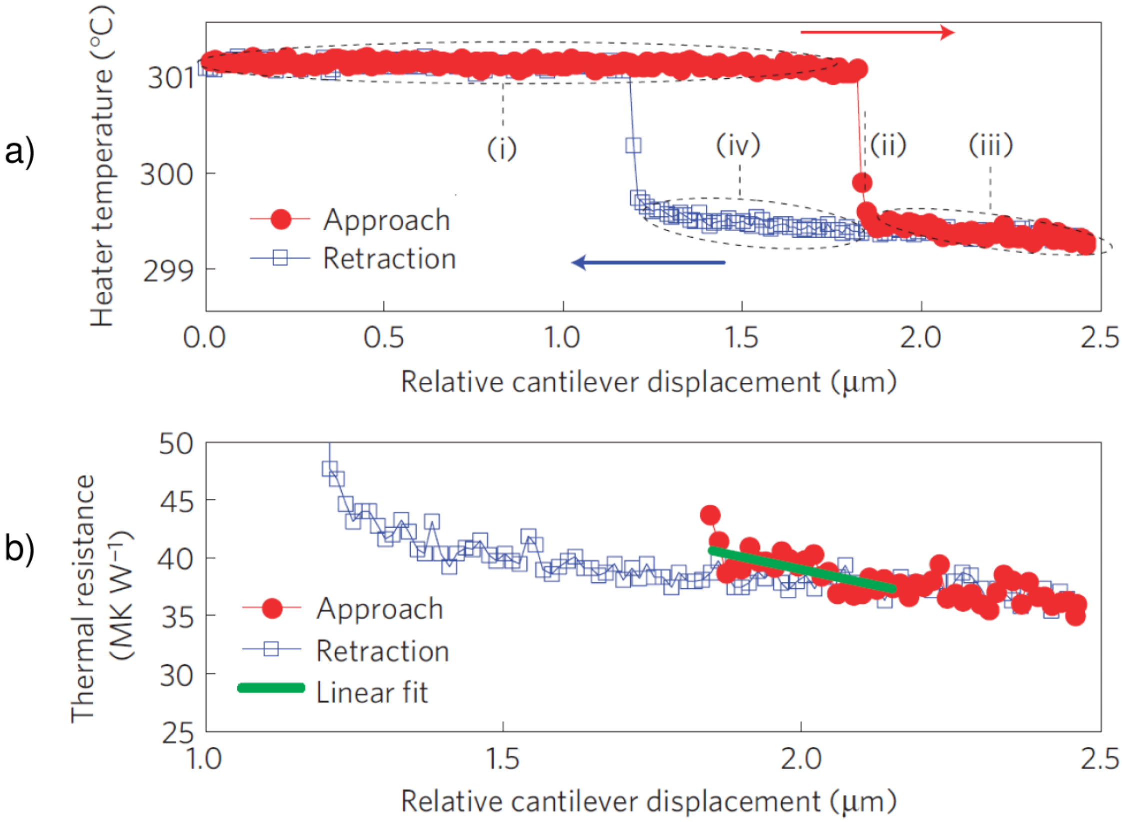

Figure 1.18. Approach and retraction curves between a flat-punch tip and taC sample a) Variation of the heater temperature b) Evaluation of the thermal resistance at the tip-sample contact ($P \simeq 6 \times 10^{-6}$ mbar) [58].

A part of chapter 3 is dedicated to evaluate the solid-solid thermal conductance and to present the effect of roughness on the determination of the thermal conductivity of the samples.

1.7.3 Heat transfer though water meniscus

Under ambient conditions, a film of adsorbed water is formed on the sample due to the capillary condensation of the relative humidity. When the tip gets in contact with the sample, a meniscus takes shapes between the two surfaces. The heat path through water meniscus was not studied in the literature and little information exists about the meniscus thermal conductance. The reason behind is that most the properties of the water at small scales are still unknown and especially the thermal properties. Luo *et al.* [59] suggested that the meniscus conductance G_w is the predominant among the heat mechanisms. G_w was written as:

$$G_w \approx 2\pi\lambda_w R_a[\ln(1+\frac{R_a}{a}(1-\cos\beta))+1-\cos\beta] \quad (1.30)$$

Here, λ_w and a are respectively the thermal conductivity and thickness of the meniscus and R_a is the apex radius. $Sin\,\beta = w/2R_a$ where w=2r_2 is the meniscus width as shown in Figure 1.19.

Their probes were made of thermocouple junctions (Au-Ni or Au-Pt) and the tip radius around 100 nm. By heating the substrate and measuring the voltage of the probes, they found the thermoelectric voltage different to what is expected. It was related to the thermal resistance at the contact between the tip and the substrate. With a modeling of the thermal resistances between the substrate and the tip as illustrated in Figure 1.20, the contact conductance $G_c=1/R_c$ was determined between 4×10^{-6} W.K^{-1} and 2×10^{-5} W.K^{-1} [59]. By modeling all the transfer mechanisms, it was found that the meniscus conductance is around 2×10^{-6} W.K^{-1}. If the heat was transferred mainly by the meniscus, then this value is smaller to what was measured [59]. This difference raises lots of questions about an eventual contribution of the other mechanisms in this heat transfer that limits the characterization of the sample. Few years later, in 2002, the same group questioned their first results based on thermal measurements with the same equipment [60]. The authors estimated that the heat transfer through water would be rather small in front of the thermal conduction due to air, which appeared dominating the thermal interaction between the probe and the sample. They attributed this new result to the fact that the thermal conductances at the probe-water and water-sample interfaces had not been taken into account in the modeling of their previous works [60].

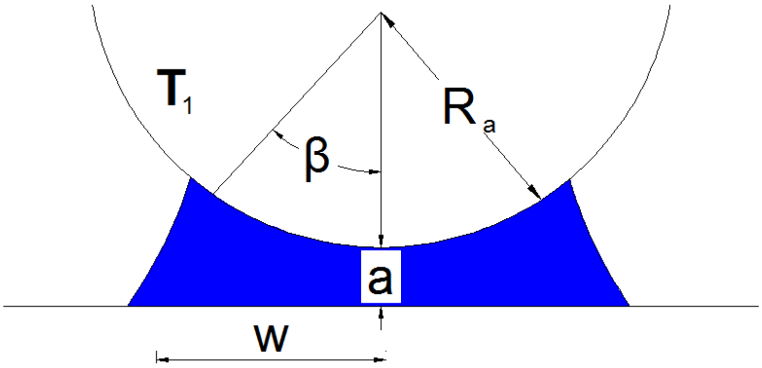

Figure 1.19. Schematic of the meniscus when the probe is in contact with the sample.

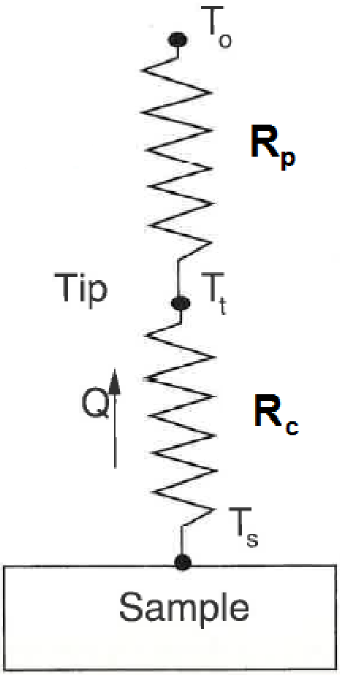

Figure 1.20. A model of the thermal resistances between the substrate and the tip in the experiment of Luo [59].

Using the same configuration (heated substrate and thermocouple probe), Thiery *et al.* [61] determined the ratio of conductances G_p/G_c as a function of the heater temperature T_{heater}. They found that $G_{contact}$ increased up to a limit of temperature around 90 °C and then it decreased slowly (see Figure 1.21). They just suggested that this limit is the liquid-vapor transition. Yet, many questions could be asked about the reasons behind the increasing tendency before the 90 °C and the slight decrease of G_p/G_c after this temperature. We note that the diameter of the thermocouple probe used in their experiment is around 1.3 µm [61]. Gomès *et al.* [62] suggested that the water limit is around 90 °C based on thermal signal measurements of the Wollaston probe operated at three different temperatures. Even though G_w was not determined because these works were among the first ones in SThM, the thermal signal looked different at two probe temperatures 50 °C and 90°C.

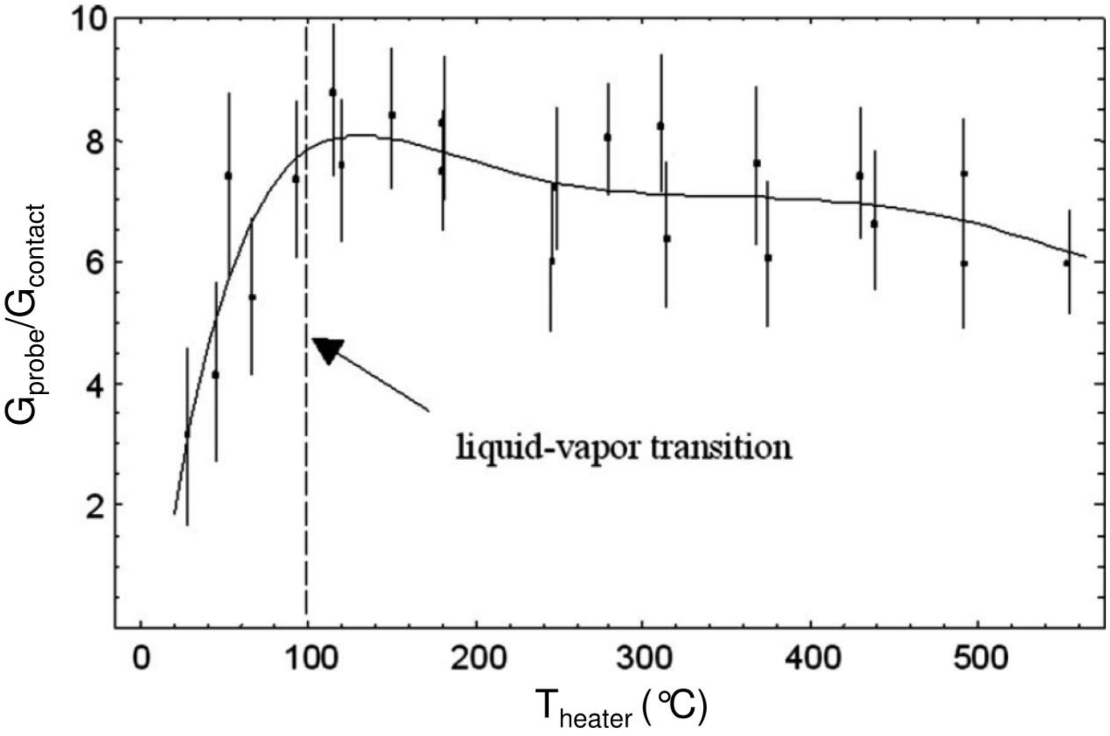

Figure 1.21. Variation of the ratio $G_{probe}/G_{contact}$ as a function of the heater temperature T_{heater} in the experiment of Thiery *et al.* [61].

At a mean probe temperature of 60 °C (temperature in the DC mode T_{DC}), Lefèvre *et al.* [26] used the Wollaston wire probe in the 3ω mode (Equations (1.11) and (1.14)) to estimate the thermal conductance at the contact G_c and the thermal interaction radius b on various samples. They found an equivalent G_c about (4.7–6) × 10^{-6} W.K^{-1} and b about 100-300 nm. As we will see later in the next section, G_c is on the same of the values for the heat transfer through air but b is one order of magnitude smaller. The values of G_c and b are equivalent for a range of frequency between 0 and 10^4 rad.s^{-1}. At low frequencies, $\theta_{2\omega} \simeq \theta_{DC}$ and thus the mean temperature of the probe is about 60 °C. At frequencies larger than the cut-off frequency of the probe, $T_{2\omega}$ becomes much smaller than T_{DC} and thus the probe temperature is around 30 °C. Then, the estimated G_c and b in ref [26] correspond to a probe temperature ranging between 60 and 90 °C. Since the water meniscus might be affected by temperature, the water meniscus conductance as a function of temperature is required here (see Chapter 2).

As the understanding on the heat transfer through water meniscus is not clear yet, this heat path is usually avoided in the measurements. In fact, the probe is heated up to temperatures higher than 100 °C [13, 14] or the measurements are performed under vacuum conditions [45, 58] and in the two cases the water meniscus is supposed to have vanished. We should be aware that the first assumption is a point of view based on the thermodynamic laws at large scales. For the second, a doubt appears whether a high-vacuum level is sufficient to evaporate totally the water meniscus or the measurements must be performed under ultra-vacuum conditions with appropriate cleaning methods.

In order to answer the questions about the heat transfer through water meniscus and for a better understanding for the transfer at the contact, Chapter 2 displays in details the meniscus “issue”. This study passes around the terms that affect principally the meniscus heat path: probe shape and size, sample nature (hydrophilic and hydrophobic), capillary forces, sample roughness, probe temperature and relative humidity.

1.7.4 Heat transfer through air

The air conductance to the sample is dependent on the separation distance d_s between the probe and the sample. When d_s is much larger than air phonon mean free path Λ_{air} ($d_s >> \Lambda_{air}$), thus the conduction regime is diffusive and dependent directly on d and the Fourier law is applicable. When $d_s << \Lambda_{air}$, thus the air gap conductance cannot be estimated from the continuum theory and the conductance is estimated from local conductances [44]. Moreover, since the conduction between the tip and the sample cannot be assumed as an interaction between two plane surfaces, there is always a geometry factor δ in the conductance expressions.

In the diffusive regime, the air conductance coefficient was given by Shi *et al.* [60] as follows:

$$h_{diffusive} = \frac{\delta k_a}{(y + d_s)} \quad (1.31)$$

and in the ballistic regime as follows:

$$h_{ballistic} = \frac{\delta C V_{air}}{3(1 + 2f)} \quad (1.32)$$

where λ_a, C and V_{air} are the thermal conductivity, heat capacity and velocity of air molecules respectively. f is given as follows:

$$f = \frac{2(2 - A)\gamma}{A(\gamma + 1)\,\mathrm{Pr}} \quad (1.33)$$

where A is the accommodation factor (0.9 for air), Pr is the Prandtl number and γ is the ratio between the heat capacities at constant pressure and at constant volume.

Between the two regimes, Shi *et al.* [60] introduced the slip regime for $\Lambda < (y+d_s) < 100\Lambda$ where h_{slip} is given as:

$$h_{slip} = \frac{\delta \lambda_a}{(y+d_s)+2f\Lambda} \quad (1.34)$$

d_s is taken here as the separation between the end of the tip apex and the sample and $(y+d_s)$ is the distance between a point on the tip surface and the sample.

The conductance through air G_{air} is then given as:

$$G_{air} = \iint h_{\text{(diffusive, ballistic or slip)}} dxdy \quad (1.35)$$

Lefèvre [22] determined the equivalent conductance G_{eq} (Equation (1.5)) after measuring the thermal signal as a function of the distance between the Wollaston probe and the sample. As shown in Figure 1.22, G_{eq} shows 1/z dependence as a function of the distance down to distances around 300 nm. In spite of an unclear curve at the small distances because of the large steps of the used motor, the deviation from 300 nm to the contact could be a sign of the ballistic regime. Measurements with small steps of motion would let us better understand this regime.

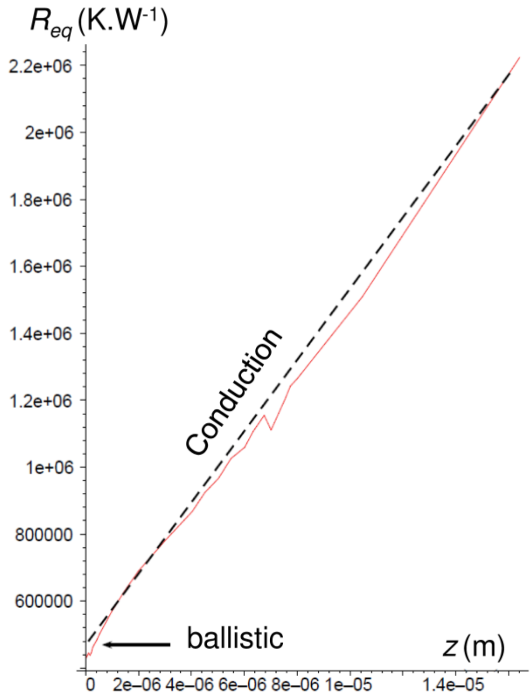

Figure 1.22. Variation of the equivalent resistance $R_{eq}=1/G_{eq}$ as a function of the distance between the Wollaston probe and a Silver sample [22].

Chapuis [27] used a global expression for the conductance through air that account for the ballistic and diffusive regime at the same time:

$$G_{air} = \int \frac{\lambda_{air}}{d_s + z(x,y) + \Lambda} dxdy \quad (1.36)$$

The numerical results were compared with experimental results obtained with the Wollaston probe (Figure 1.23). The numerical simulations do not fit the experimental results since the probe is assumed to a perfect torus and the roughness is neglected in the model. However, the two curves have the same tendencies with a decreasing slope at the "large distances" that is due to the diffusive regime and a limit that is due to the ballistic limit.

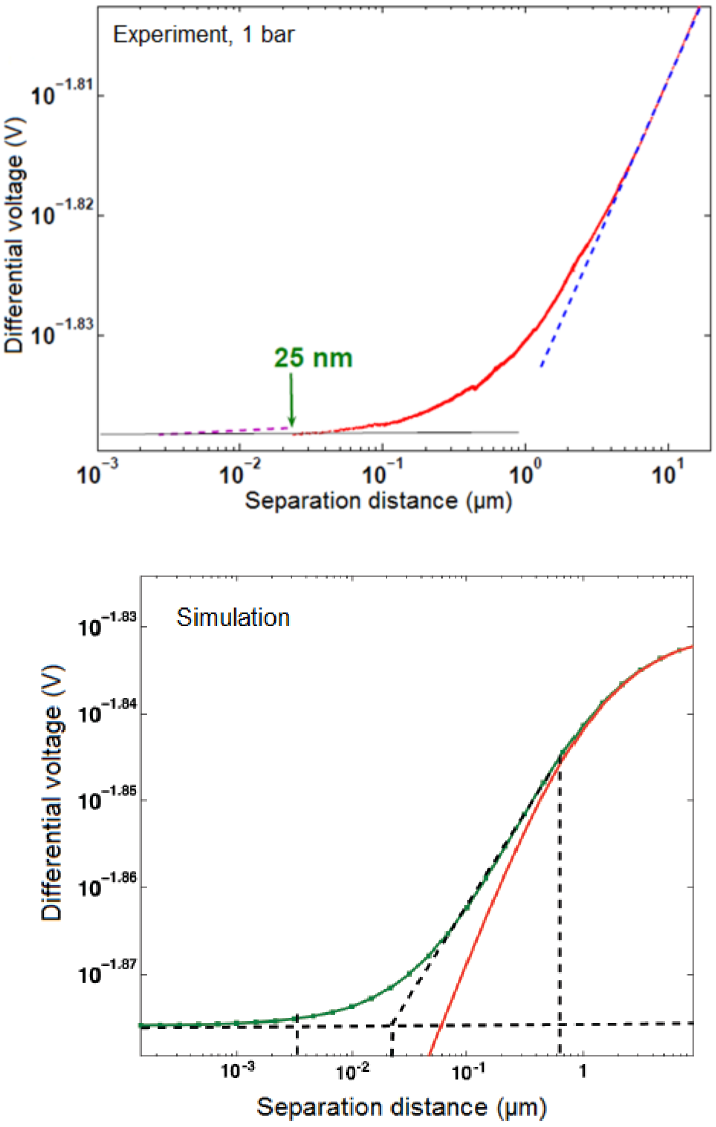

Figure 1.23. Differential tension (V) as a function of the separation distance between the probe and the sample. The red line and the green line represent respectively the diffusive model and the complete regime [27].

Moreover, Chapuis [27] identified the effect of the pressure on the heat transfer through air. The heat transfer to the sample before the contact decreases due to the rarefaction of the heat carriers as shown in Figure 1.24.

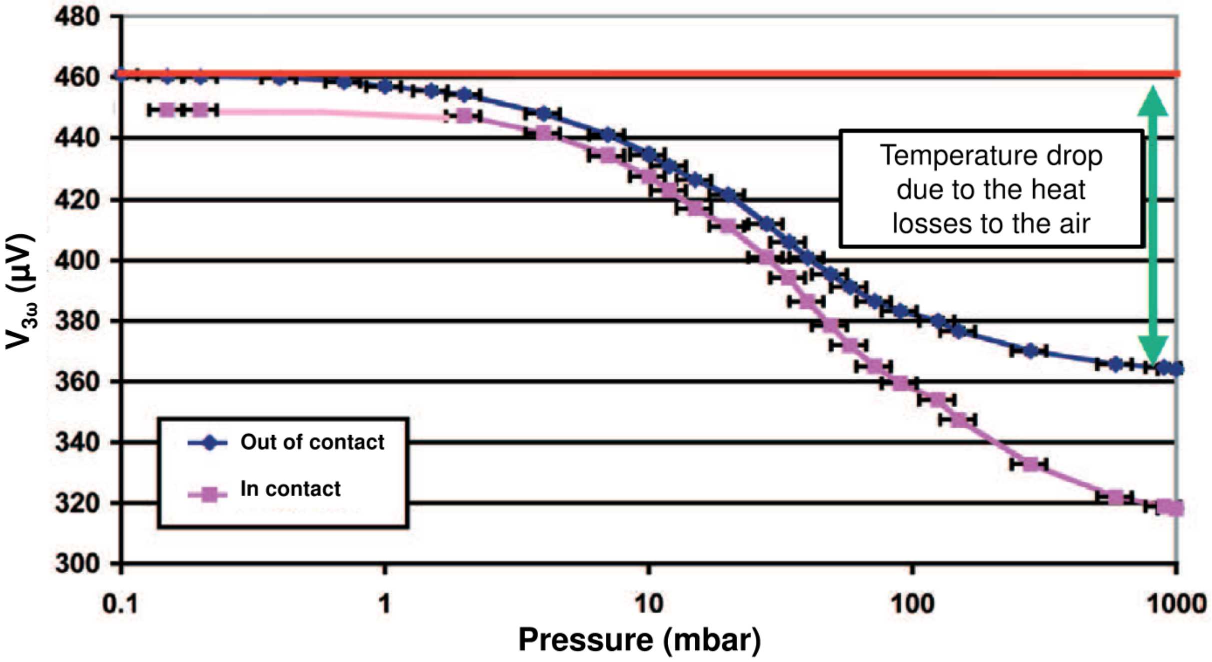

Figure 1.24. Variation of the probe 3ω voltage $V_{3\omega}$ as a function of the pressure when the probe in contact and out of contact with a Yttrium oxide sample [27].

In order to compare the different conductances of the various heat mechanisms, Chapuis [27] measured the variation of the voltage signal measured as a function of the probe/sample distance. Figure 1.25 shows that the signal jump at the mechanical contact (from C to D) is much smaller than the drop due the heat transfer through air before the contact (from A to B). These results show that in this case the conduction through air is the predominant mechanism in the tip-sample thermal interaction.

Supposing that the meniscus disappears at probe temperatures larger than 100 °C, Lefèvre [24] and David [14] estimated an equivalent G_{air} and b_{air} ($G_c \simeq G_{air}$ and $b \simeq b_{air}$) using DC calibration with the Wollaston probe (Equation (1.8)). The calibration includes various samples of well-known thermal conductivity. The obtained values of G_{air} and b_{air} are respectively around 5×10^{-6} W.K^{-1} and 1 µm [14, 24]. These values are used to determine the unknown thermal conductivity of solid materials. Even though it is a fast calibration, the used procedure can generate a significant error. This due to the fact that the determined G_{air} and b_{air}

cannot be taken constant among all the used samples. While increasing the sample thermal conductivity λ_s, G_{air} increases and b_{air} decreases. In other terms, the heat flux lines go perpendicularly to the sample surface when λ_s is large and along the surface when it is low [22].

Chapter 3 deals with this problematic and shows a new methodology to improve the DC calibration with the Wollaston wire probe. This methodology helps decreasing the error while estimating the thermal conductivity of materials and especially materials with low thermal conductivity (between 0.1 and 3 W.m^{-1}.K^{-1}).

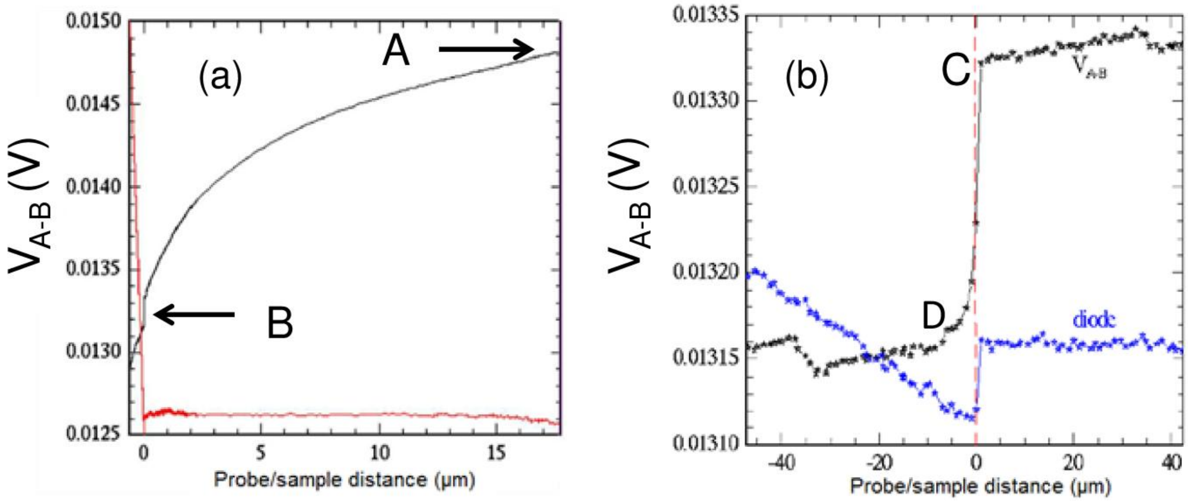

Figure 1.25. (a) Differential tension as a function of the probe/sample distance for a sample of Niobium (λ= 59 W.m^{-1}.K^{-1}). A zoom at the contact zone is shown in Figure (b) [27].

We have to note that while working with the silicon probes, a huge difficulty is to determine experimentally the heat conduction through air between the tip and the sample. In fact , the heat transferred through the air gap from the cantilever is greater than the one transferred from the tip though air to the substrate while working under ambient conditions [63]. The conductance of the heat path is on the order of 10^{-5} W.K^{-1} [12]. This value is much larger than the value of the thermal conductance through the tip and at the tip-sample interface (~10^{-8} – 10^{-9} W.K^{-1}). Thus, estimating the tip-air-substrate conductance needs a high sensitivity and appropriate modeling to separate this conductance from the cantilever-air-substrate thermal conductance. Analytically, Chapuis *et al.* [64] studied that quasi-ballistic heat transfer through between a nano-tip and a substrate. The studied nano-tip has almost the same geometry of the silicon probes. The given approach can be used to compare future experimental results where the heat through air is exclusively transferred from the tip.

Through finite elements analysis FEA model, Tovee *et al.* [16] studied the sensitivity of the palladium probe in air conditions. As a first approach, the model assumed a temperature continuity across the tip-sample interface [16]. The apex temperature and the heater temperature change when the probe is in contact were calculated [16]. The simulations showed that the probe sensitivity is limited to few W.m^{-1}.K^{-1} as shown in Figure 1.26. Later, using the same probe Bosse *et al.* [65] identified the thermal conductivity of amorphous and crystalline phases in GeTe and $Ge_2Sb_2Te_5$ films while working under ambient conditions. The thermal conductivity of the samples varied between 0.2 and 1.95 W.m^{-1}.K^{-1} [65]. This interval lies in the range of sensitivity determined by Tovee *et al.* [16].

Juszczyk *et al.* [66] performed numerical simulations in air conditions for the case of the palladium probe. The same geometry of the probe was taken into account but the probe material was varied for three different thermal conductivities [66]. A continuity of temperature was assumed at the interface between the probe and the sample. The sensitivity when the thermal conductivity of the probe substrate is about 30 W.m^{-1}.K^{-1} (close to the case of silicon nitride) was up to few tens of the sample thermal conductivity as shown in Figure 1.27.

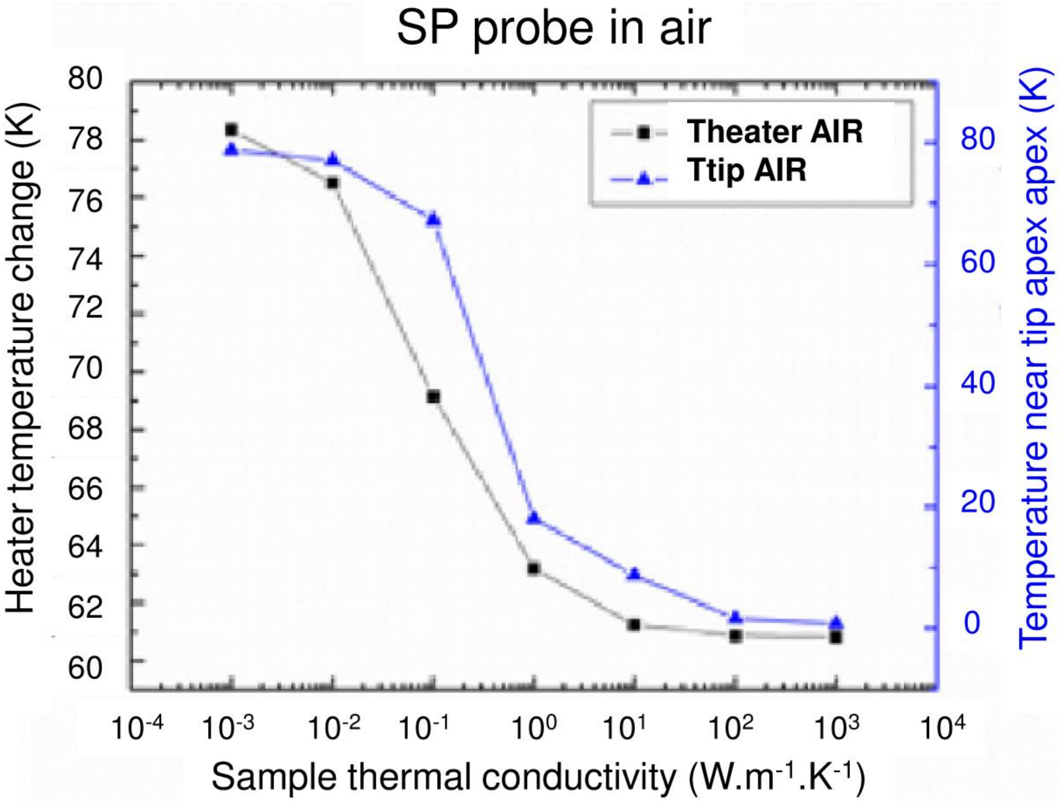

Figure 1.26. Sensitivity of the palladium probe for materials of various thermal conductivities of samples [16].

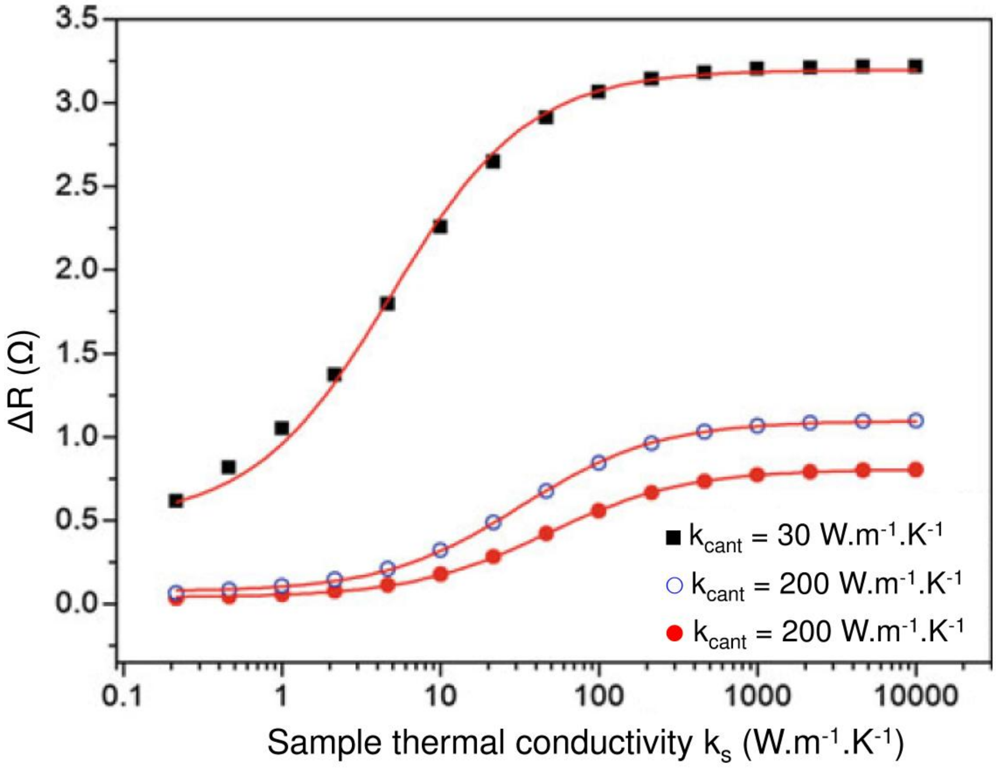

Figure 1.27. Variation of the probe electrical resistance when the tip contacts the sample as a function of the sample thermal conductivities. The simulations accounts for three conductivities of the probe materials [66].

1.8 Conclusions

In this chapter, we have seen that the heat transfer between SThM probes and samples depends on various factors. These factors involve the shape and size of the probes, probe temperature, the sample nature, the applied load, the surfaces and the environmental conditions. An accurate thermal characterization requires a convenient modeling of the tip-sample system. The modeling is accomplished first by modeling the heat transfer through the tip, the thermal interaction between the probe-sample and through the sample. Modeling the heat transfer through the tip becomes difficult when the tip dimensions decreases and become comparable to the mean free path of the heat carriers. The thermal interaction between the probe and the sample is dependent on the configuration of the probe (in contact or out of the contact with the sample), the environment (vacuum or under ambient air), the relative humidity, the sample nature (insulators or conductors) and the applied force. We add to these elements, the interaction of the probe with the environment while working under air environment.

The upcoming chapters deal with some of the questions mentioned in this chapter. They especially aim to provide answers to the following questions.

- The study and the quantification of the heat transfer through water meniscus has been, to date, carried out simultaneously to the one of the other heat transfer mechanisms of the probe-sample thermal interaction: *Can we propose a new methodology to specify this heat transfer mechanism and have a more accurate quantitative estimation of the thermal conductance* $G_{total,meniscus}$ *independently of the other mechanisms? What is the dependence of this heat transfer mechanism on the probe temperature? Does its contribution to the probe-sample thermal interaction depend on the size of the probe and sample properties? Can we avoid it to simplify the analysis of the other heat transfer mechanisms?*
- The study of the thermal conduction at the mechanical contact between probe and sample requires working under vacuum conditions to strongly reduce the heat transfer through air: *Under these conditions and assuming the radiative heat transfer negligible and the water meniscus vanished between the probe and samples, how do the characteristic parameters of the probe-sample mechanical contact influence the SThM measurement? What is the contribution of this heat mechanism to the probe-sample heat transfer? Is it dependent on the probe and on the sample? How and why? Can we identify parameters used to describe the heat transfer at solid-solid interfaces from measurements carried out under vacuum conditions?*
- SThM calibration and measurements are often carried out under ambient conditions within the framework of the identification of the thermal conductivity of materials. *What is the rate of heat losses from the probe to its surrounding environment through thermal convection and conduction through air? In the frame of the description of the probe-sample system with a thermal conductance network, what is the dependence on the sample thermal conductivity* λ_s *of the various thermal conductances involved? Once this dependence clarified, what is the sensitivity to* λ_s *of current SThM probes?*

A detailed approach of all these questions is given for the Wollaston probe through the chapters 2 and 3 of this thesis. Chapter 4 addresses some of them for the KNT and doped Si DS probes.

Chapter 2

Analysis of heat transfer in the water meniscus at the tip-sample contact in SThM

As seen in the first chapter, information about the heat path through the water meniscus remains scarce. Reaching a better understanding of the interaction between the sample and the probe requires an investigation of this heat transfer mechanism. Therefore, this chapter deals with the heat transfer through water meniscus that is formed at the probe-sample contact under ambient conditions in scanning probe microscopy (SPM). First, we present two selected applications where the water meniscus (or water film) is the center of interests and how they lie within our proper interests. Later, we investigate the heat conduction through the water based on the analysis of the pull-off forces on a hydrophilic sample using the Wollaston wire probe at different probe temperatures. Through these measurements, the dimensions of the water meniscus are determined based on literature models of the meniscus. The thermal conduction of the water meniscus is quantified as a function of the probe temperature. The effect of roughness on the pull-off forces is shown on the same sample. Moreover, measurements of pull-off forces on hydrophobic sample of graphite are presented.

At the end of this chapter, results of first experiments performed in an ESEM chamber are presented and analyzed.

2.1 Motivations

2.1.1 Potential applications related to the water meniscus for heated AFM probes

Under ambient conditions, a water film is formed on the surfaces due to capillary condensation of the relative humidity. Because of several related applications or issues (some examples are given below), much interest has been shown in studies around the phenomena of capillary condensation.

Since the size of the MEMS/NEMS is being reduced, some tribological issues are reported. The term “stiction” (static friction) has been used too to describe the motion between two surfaces [67]. While working under ambient environment, stiction happens because of the condensed water layer between the surfaces [67, 68]. The corresponding capillary forces of the water film could produce damage in the performance of MEMS/NEMS and might stop their functioning [67, 69]. Since these systems are mostly fabricated from silicon, Bhushan *et al.* [70] studied the adhesive forces between a ball of hydrophilic Si(100) against a specimen wafer of Si(100) as a function of the relative humidity and the temperature of a heated stage. To compare his experimental results, Bhushan [70] identified also the adhesive forces between three hydrophobic films of DLC, Z-DOL, and HDT in contact with a ball of Si(100). He found that the adhesive forces on Si(100) sample are larger than those of DLC, Z-DOL, and HDT, linking this observation to the hydrophilic or hydrophobic character of the sample surfaces [70].

Stiction forces can be reduced by changing the surface properties [71-73] or by reducing the contact area [68], but the solutions to reduce the contact surface remain scarce and challenging. Based on AFM, dynamic force modulation shows a reduction in the stiction at low [74] and high [75] frequencies. Thermally-controlled devices may be another alternative not yet explored.

In contrast to MEMS/NEMS, Dip-pen nanolithography (DPN) takes advantage of the existing water nano-layers.DPN is a scanning probe lithography technique where an AFM tip, coated with a chemical compound or mixture acting as an "ink”, is used to create patterns (on scales of under 100 nanometers)directly on a substrate.

The DPN technique, introduced by Piner in 1999 [76], consists of transporting molecules to substrate using an AFM tip. The molecules are transported through the water meniscus formed between the tip and the substrate as shown in Figure 2.1 [76]. Therefore, the writing rate depends on the water meniscus volume and the relative humidity [76].

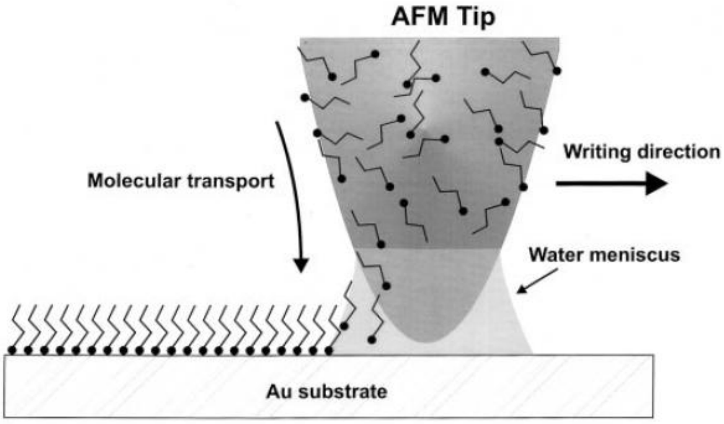

Figure 2.1. Schematic of the principle of Dip-pen nanolithography (DPN) [76].

Weeks *et al.* [77] studied the effect of humidity on the size of dots fabricated by DPN, by placing the AFM in an environmental chamber. They found high dependence of the dots diameter on the relative humidity [77]. The DPN technique has proved to have high potential for many applications. It has been widely used to set Biomolecular Micro- and Nanoarrays on surfaces [78]. Such microarrays are nowadays used widely in oncology to assess the Deoxyribonucleic Acid (DNA) in patient tumors [79]. DPN is used also to identify the cells adhesion mechanism and to study the interaction between some biomolecules for biorecognition processes [78, 80]. Moreover, DPN is used in electrochemical mode to deposit nanofeatures of metals on substrates [81]. Li *et al.* [81] were the first to use the electrochemical dip-pen lithography to deposit small amounts of Pt on Si wafers [81]. In this configuration, the condensed water meniscus between the tip and the substrate serves as an electrochemical cell where the metal is dissolved [81]. Depending on the application of the DPN method, the use of a thermally-controlled AFM tip could here be a way to improve or optimize patterning.

As can be seen for both the applications cited above, the water meniscus that forms due to the capillary condensation may have a crucial role in the operating principle of systems and process. This has motivated a deep scientific research the last fifteen years for characterizing the properties of water at micro and nanoscales and investigating the parameters that affect those properties.

2.1.2 Characteristic dimensions and properties of the water small layers adsorbed on a surface

The characterization of the water film adsorbed on surfaces is usually performed through AFM (Atomic force microscopy) or AFM-based technique like scanning Kelvin probe force microscopy [82] or STM (Scanning Tunneling Microscopy**)** [83]. These techniques provide a better spatial resolution than optical techniques that are limited by the diffraction limit. In order to calculate the adhesive forces, the film thickness or the film physical properties [84-86], characterization of the water film is mostly carried out with tips with small radii of curvature, due to their better force resolution [53]. The thickness of the water film on the surface of a sample does not exceed few nanometers as shown in Figure 2.2 [87]. The factors that play the major role in determining the film thickness: the surface character (hydrophilic or hydrophobic) [82, 88] and the relative humidity [87]. An additive error could be added while determining of the water thickness due to the water condensation around the tip especially while working with hydrophilic tips [89]. In fact, Mate *et al.* [90] found a difference comparing the results of the local film thickness determined with AFM and with ellipsometry. That was linked to the water condensation around the tip [53]. Santos *et al.* [89] presented an interesting model, validating with some experiments on a BaF_2 substrate, to calculate the true height of water layers on both hydrophilic and hydrophobic surfaces. A crucial parameter is added to these parameters is the sample roughness parameter of either the tip or the sample while studying the interaction forces between the tip and the sample [91-94]. The dimensions of the meniscus at the tip-sample contact are estimated by using the Young-Laplace and Kelvin Equations.

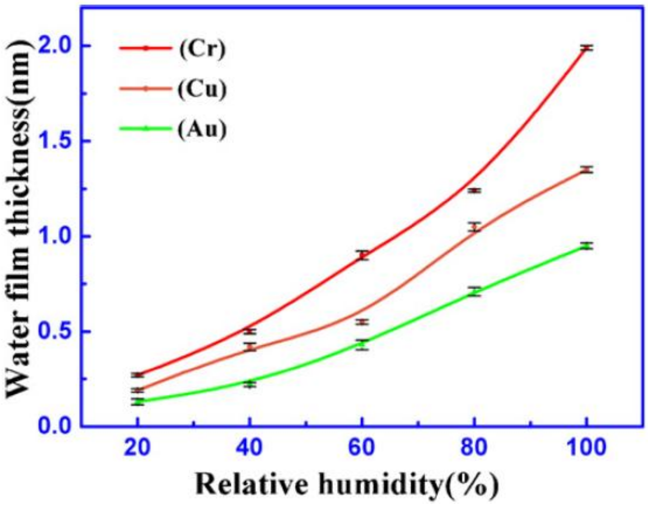

Figure 2.2. Evolution of the water film thickness as a function of the relative humidity for three types of materials: chromium Cr, copper Cu and gold Au. The measurement were performed using a scanning Kelvin probe force microscope (SKPFM) [87].

2.1.3 Young-Laplace and Kelvin Equations

Let us consider the case of a capillary of large width in a longitudinal tube as illustrated in Figure 2.3.

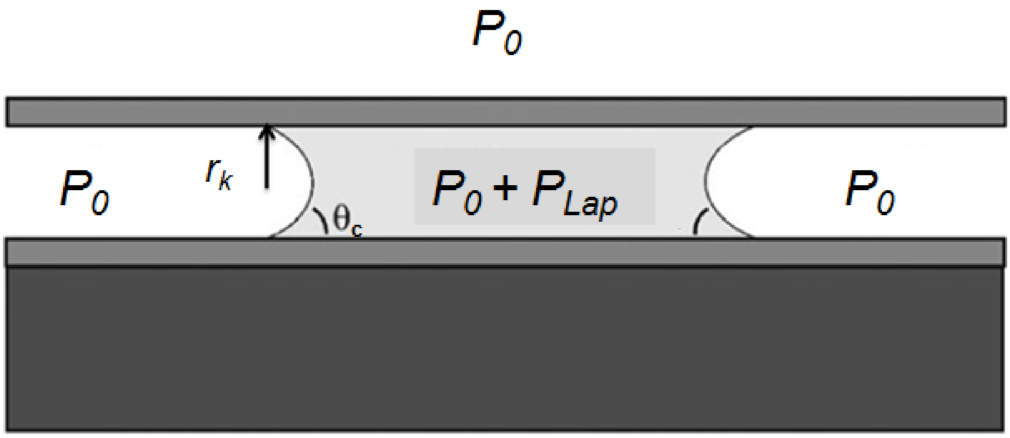

Figure 2.3. Schematic of a capillary confined in a longitudinal tube [95].

Due to the strong curvature of the cavity of radius r_k, the pressure in the liquid is negative [95]. The pressure in the liquid is the sum of a negative Laplace pressure P_{Lap} and the atmospheric pressure P_0 and given by [96]:

$$P_{liquid} = P_0 - \gamma_w \cos\theta_c / r_k \quad (2.1)$$

where γ_w is the surface tension of the liquid and θ is the contact angle (see Figure 2.3). As a simplification, the angle θ_c is usually taken equal to 0 while talking about hydrophilic surfaces. Equation (2.1) represents the well-know Laplace equation. At a stable state of the capillary, the liquid and vapor have the same chemical potential $\mu_{vap}(P_{vap}) = \mu_{liq}(P_{liq})$. Assuming the vapor as an ideal gas, we can write then [95]:

$$\mu_{vap}(\mathrm{p}_{vap}) = \mu_{vap}(P_{sat}) + RT\ln(\mathrm{RH}) \quad (2.2)$$

$$= \mu_{vap}(P_{sat}) + V_m(P_{liq} - P_{sat}) \quad (2.3)$$

and

$$P_{liq} - P_{sat} = \frac{R_g T \ln(RH)}{V_m} \quad (2.4)$$

where R_g is the gas constant, $RH = p_{vap}/p_{sat}$ is the relative humidity and V_m is the molar volume. Due to the large magnitude of p_{liq}, $p_{liq}-p_{sat}$ is almost equal to $p_{liq}-p_0$. Therefore, using Equation (2.1), Equation (2.4) can be written [97]:

$$r_k = \frac{\gamma_w V_m}{R_g T \ln(RH)} \quad (2.5)$$

Equation (2.5) is the well-known Kelvin equation.

Little information exists yet in the literature on the temperature-dependence of the meniscus. Since our SThM is an AFM-based technique with a heated probe, our study goes in the direction of fulfilling more information in that field.

2.2 Methodology developed and used to investigate the temperature-dependence of the meniscus

2.2.1 Experimental approach

The SThM probe to be used has to provide high sensitivity to the interaction between the probe and the sample where the heat transfer to the water meniscus could be detected. Majumdar *et al.* [44] suggested that increasing the tip radius can result basically in increasing the meniscus diameter and its thermal conductance (see Chapter 1, section 1.6.3). So, we start our study here by using the Wollaston probe of larger radii even if thermal probes with nanoscale curvature radius are nowadays available [15]. The geometrical dimensions and material of this probe are given in the first section of chapter 1. Since the AC mode can induce a problem at the contact in terms of extension of the probe and thus a consequence on the stability of the water meniscus (see chapter 1), heating the probe through DC electrical current was preferred.

While working under ambient conditions, the capillary forces are the dominant forces among the pull-off forces as suggested by Cappella *et al.* [53]. Since the water meniscus might be affected by temperature, measurements of the pull-off forces at different levels of T_m would reveal a possible eventual change in the interaction forces between the probe and sample. We used a sample of hydrophilic germanium Ge. Figure 2.4 shows the contact between a water droplet deposited on the surface of the Ge sample. The sample surface is hydrophilic as the contact angle between the droplet and the sample surface is around 27 ± 3.

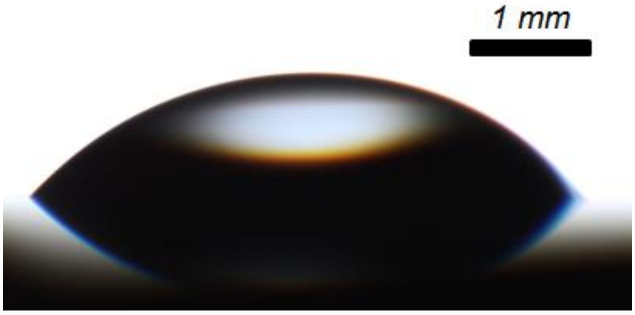

Figure 2.4. Image of the contact between the water droplet and the sample of Ge.

Our AFM is an NTEGRA Probe Nanolaboratory of NT-MDT. More technical information can be found in Appendix A. Using a balanced Wheatstone bridge with a feedback circuit, the mean probe temperature T_m is maintained constant while approaching the sample. The experiments were performed under ambient conditions (T_a=30 °C and RH=40 %) and force-distance (approach-withdrawal) curves were plotted for various T_m. Figures 2.5.a, 2.5.b and 2.5.c show an example of different force-distance curves performed at different levels of T_m for the sample of germanium Ge. We noticed first that the cantilever elastic constant, which is defined by the slope of the curves after contact, remains constant while varying T_m. Since no hysteresis is found between the approach and withdrawal curves in contact, we can say that the deformation under the tip due to the indentation, is totally elastic [53, 98]. The gap δ between the withdrawal curve (in blue) and the axis of the initial cantilever deflection DFL represents the adhesive forces (see Figure 2.5.a). The pull-off forces can be determined by multiplying the distance φ_c times the spring constant of the probe. The spring constant of the probe is estimated to 5 N.m^{-1} with an uncertainty around 20 % [99].

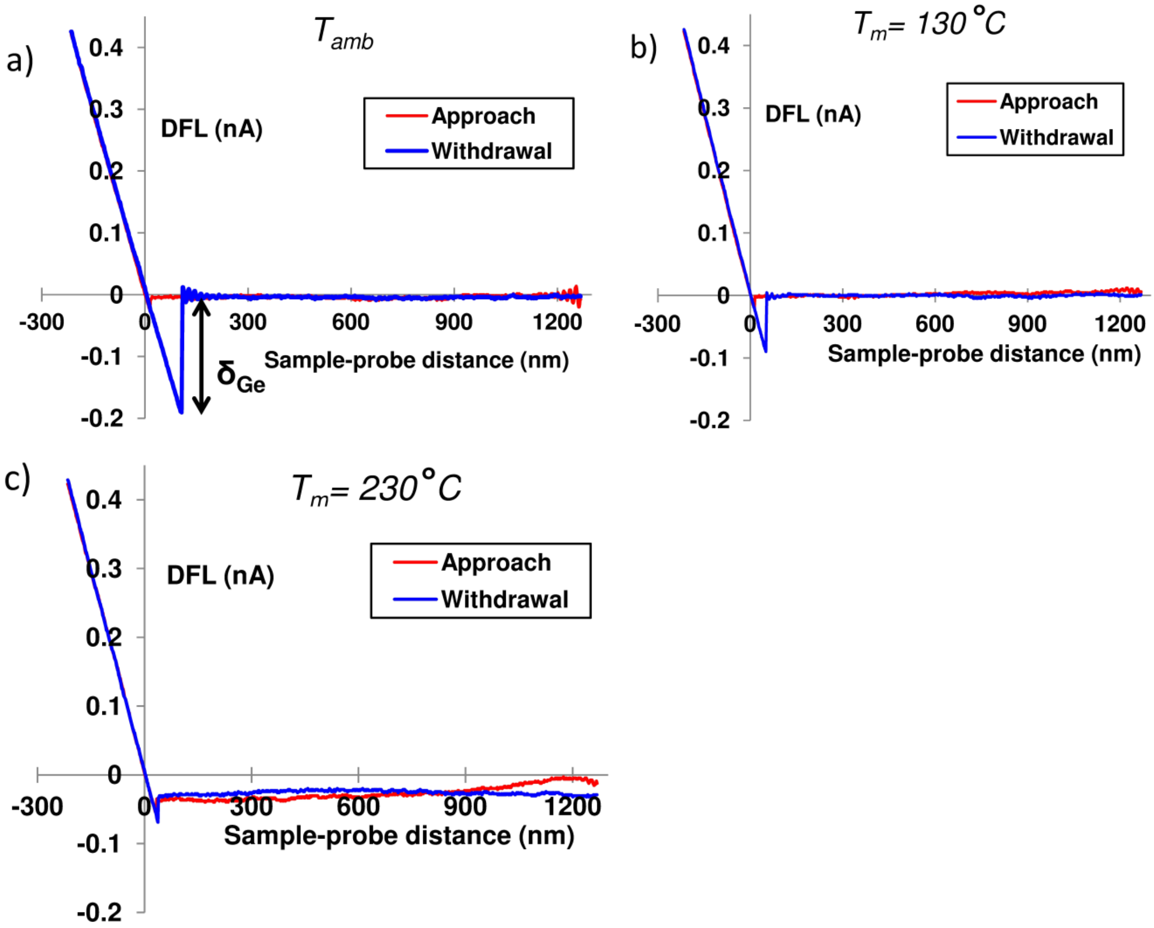

Figure 2.5. Spectroscopy curves performed on Germanium (Ge) for different probe mean temperature: (a) Ambient temperature, (b) T_m= 130 °C and (c) T_m= 230 °C.

We have to note that the force-distance curves can be performed within different durations up to 60 seconds. This duration is the maximum time permitted by our AFM. We observed that while modifying the duration of the curves, the pull-off forces are almost constant for tip-sample contact time τ_{ts} larger than one second. That is in accordance with the measurements of the pull-off forces performed by Sirghi [100] between a classic hydrophilic silicon AFM tip (tip radius of 30 nm) in contact with a hydrophilic glass sample. Figure 2.6 presents the variation of the pull-off curves as a function of the contact time obtained by Sirghi [100]. Starting from a time contact of 40 ms, the pull-off forces remain constant and the meniscus reaches its thermodynamic equilibrium. In the case of our measurements, it can be said therefore that the meniscus is at its thermodynamic equilibrium.

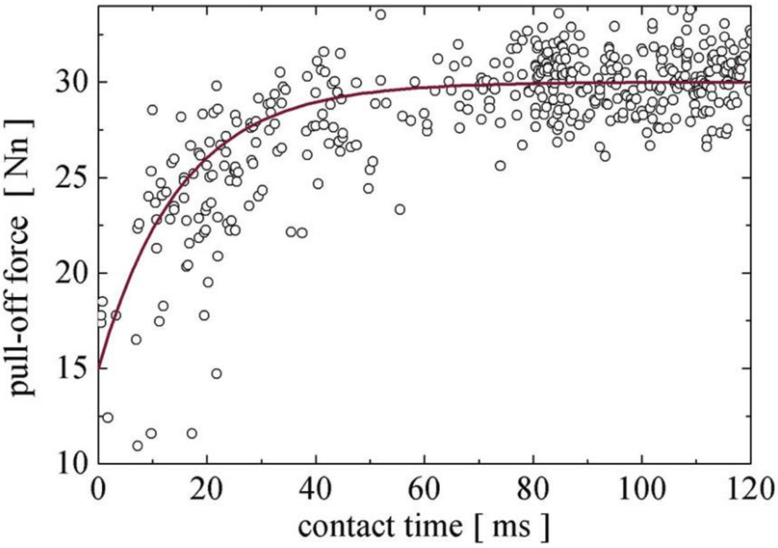

Figure 2.6. Dependence of the meniscus pull-off force on the tip−sample contact time [100].

Figure 2.7 shows the variation of the pull-off forces measured as a function of T_m. As can be seen, the value F_{po} of the pull-off forces decreases when increasing the temperature until a certain limit of T_m between 120 ºC and 150 ºC beyond which F_{po} becomes almost constant. At this range of T_m, it can be said that the meniscus largely evaporated. Moreover, we observe a hysteresis in the measurements while increasing T_m and decreasing T_m. We do not have a full understanding for this hysteresis at the moment, but among the causes which could be related one should consider the hysteresis during the evaporation and the capillary condensation at the probe-sample contact. At this time, this phenomenon is not fully understood, although the reported hysteresis during evaporation and the capillary condensation at the probe-sample contact as observed by Crassous *et al.* [101] is expected to be at least partly responsible.

Note that no significant changes were observed for the force magnitude and tendencies when changing the probes, even though the Wollaston wire probes that were used for the experiments are manually fabricated and then poorly reproducible.

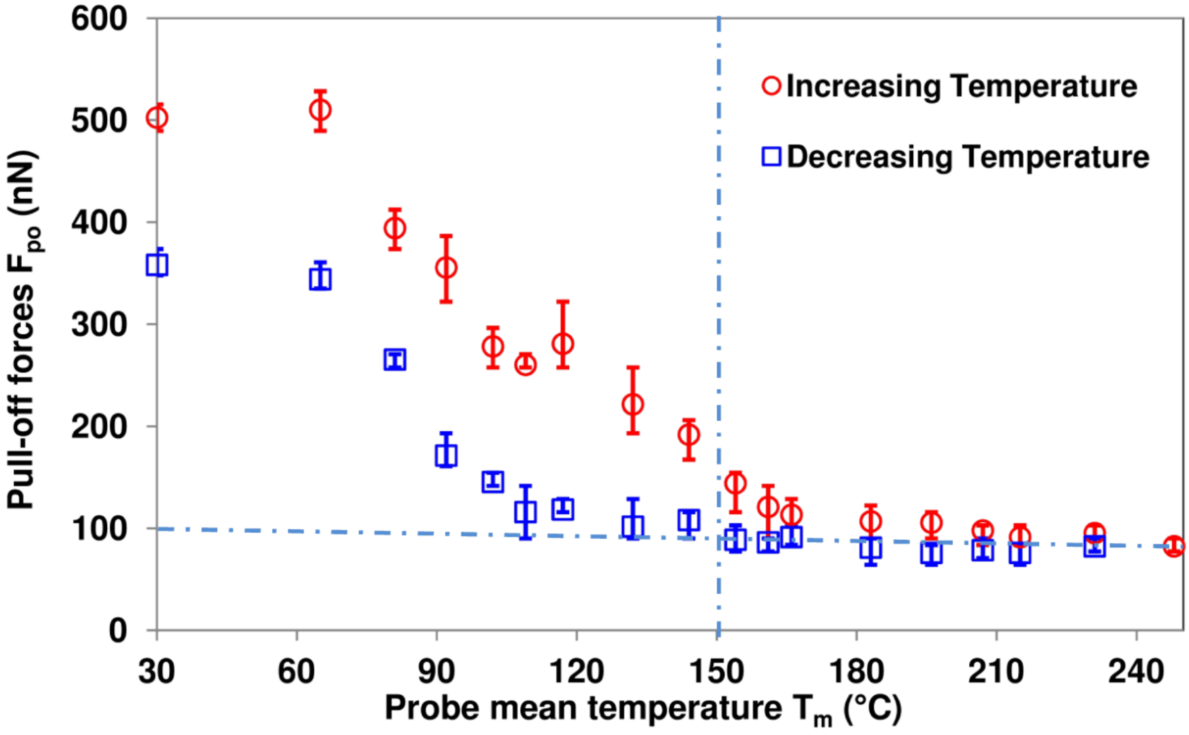

Figure 2.7. Variation of the pull-off forces F_{po} as a function of the probe mean temperature T_m for the sample of polished germanium.

2.2.2 Derived parameters: Meniscus parameters and thermal conductance of probe-sample heat transfer through water

The total thermal conductance to be considered to describe the probe-sample heat transfer through water G_{total} is the inverse of the sum of the inverses of three conductances: the conductance at the probe-water interface $G_{p\text{-}w}$; the conductance at the water-sample interface $G_{w\text{-}s}$; and the conductance due to the conduction through the meniscus G_{water}. The latter may be calculated from Equation (1.30). However, the measurements of pull-forces correspond to measurements of forces when the probe contacts the sample (a=0) [97]. Consequently, $R_{water}=1/G_{water}$ becomes negligible, so that G_{total} is only governed by $G_{p\text{-}w}$ and $G_{w\text{-}s}$.

The thermal conductance per surface area at the interface between hydrophilic solids and water was investigated by Ge *et al.* [102]. The determined values lie between 100 and 180 MW. m^{-2} K^{-1} [102]. We consider an average value $H = h_{p\text{-}w} = h_{w\text{-}s}$= 140 MW.$m^{-2}$.$K^{-1}$ in this study. To estimate the conductances $G_{p\text{-}w}$ and $G_{w\text{-}s}$, the value of the largest radius associated to the meniscus r_2 is needed as shown in Figure 2.8. r_2 can be estimated as a function of T_m while taking into account the Kelvin Equation (see Equation 2.5) and the geometrical dimensions of the meniscus between the probe apex and the sample.

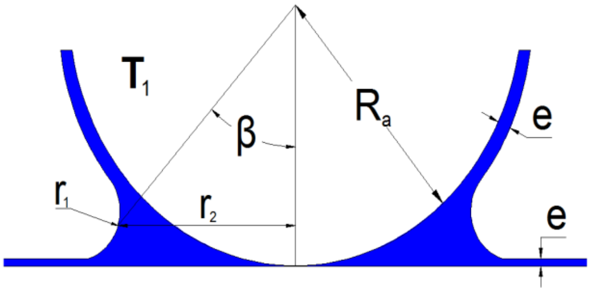

Figure 2.8. Schematic of the meniscus when the probe is in contact with the sample.

Using the Kelvin equation (Equation (2.5)), the equilibrium radius of the meniscus $r_k \approx r_1$ (see Figure 2.8) can be calculated. As said before, since for the case in study both the probe and the sample are hydrophilic, the water film thickness on the probe and the sample surface area must be taken into account. Crassous and Charlaix [103] developed the expression of the capillary forces F_{cap} for such a configuration (see Figure 2.8):

$$F_{cap} = 4\pi\gamma_w R_a \left(\frac{2r_1 + 3e}{2r_1}\right) \quad (2.6)$$

The magnitudes of the pull-off forces F_{po} at relatively high temperatures are assumed to primarily due to the elastic forces (Figure 2.7). Measurement of pull-off forces under vacuum conditions in the future could reveal more information about this assumption. To obtain the variation of the capillary forces F_{cap} as a function of the probe mean temperature T_m, the minimum value of the measured forces is then subtracted: $F_{cap}(T_m)= F_{po}(T_m)- F_{po}(T_{m,max})$. We have considered the case of perfect wetting on the probe surface and on the sample surface, which corresponds to a single monolayer $e \simeq 0.15$ nm [104]. From the values of F_{cap} at room temperature, we deduce an estimation of $R_a \simeq 0.35$ µm. From the values of F_{cap} at room temperature, an estimate of $R_a \simeq 0.35$ µm was deduced. In fact, the micro-fabrication process of the Pt/Rd wire consists in drawing out the wire that leads to the appearance of many grooves at the probe surface as shown in Figure 2.9. As a consequence, this configuration is closer to a cylinder in contact with the sample surface. Thus, the radius R_a in Equations (1.30) and (2.6) is almost twice that of the groove as explained on Figure 2.10 (in our case $R_2 \simeq 15$ µm and $R_2 >> R_1$). This value is in good agreement with the dimensions of the asperities at the Wollaston probe apex observed by David *et al.* [14].

From the geometrical considerations of Sirghi et *al.* [100], F_{cap} can be expressed as follows:

$$. \qquad F_{cap} \simeq \frac{\gamma_w}{r_1} \pi r_2^2 \qquad (2.7)$$

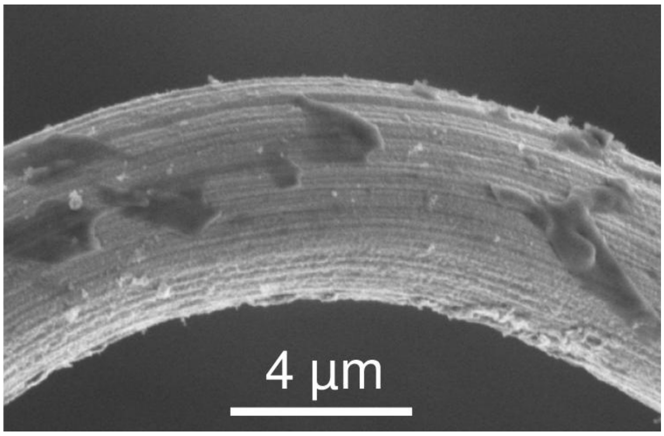

Figure 2.9. Scanning Electron Microscopy SEM image of a Wollaston wire probe apex.

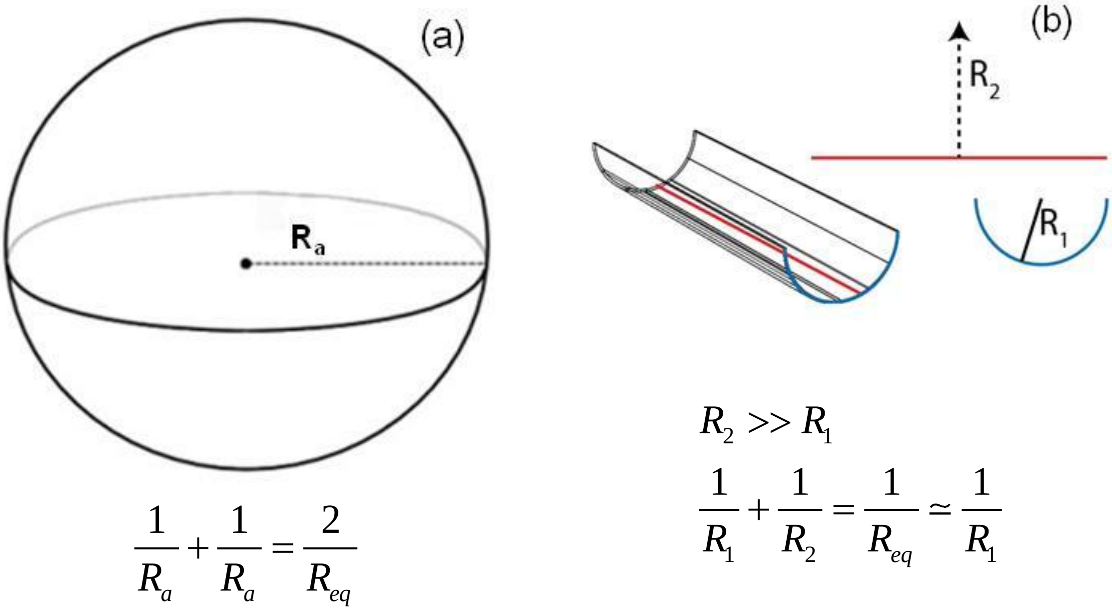

$$\frac{1}{R_a} + \frac{1}{R_a} = \frac{2}{R_{eq}}$$

$$R_2 >> R_1$$

$$\frac{1}{R_1} + \frac{1}{R_2} = \frac{1}{R_{eq}} \simeq \frac{1}{R_1}$$

Figure 2.10. Schematic of a sphere and a cylinder with their radii of curvature

To calculate r_2, we make the assumption that the water meniscus confined between the probe and the sample is at the temperature $T=(T_m+T_a)/2$. It should be noted that this approximation is valid for samples of high thermal conductivity (case of germanium) where the temperature of the sample surface under the tip apex is almost at T_a [105, 106] and as will be shown in Chapter 3. In the case of samples with low thermal conductivity, the sample surface has almost the same temperature of the probe apex. In this case, it is more appropriate to use the apex temperature as the temperature of the water layer. For each value of T_m, a corresponding value of r_2 is then deduced from Equation (2.7) using our measurements of F_{cap}.

2.2.3 Results

The variations of r_2 as a function of T_m deduced from Equation (2.7) are shown in Figure 2.11.

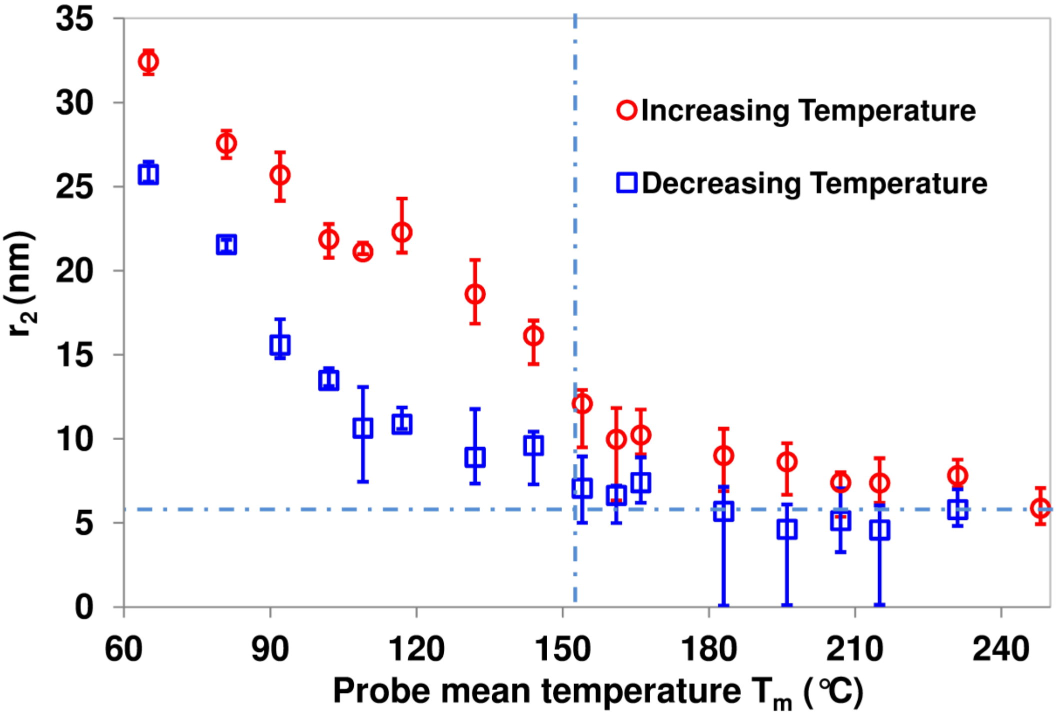

Figure 2.11. Radius of the curvature of the meniscus r_2 as a function of the Wollaston probe mean temperature T_m for the Ge sample (T_a= 30 °C, *RH*= 40 %).

Once r_2 is determined, the values of $G_{p\text{-}w}$ and $G_{w\text{-}s}$ can be estimated by multiplying the areas $S_{p\text{-}w}$ and $S_{w\text{-}s}$ by H and therefore G_{total} can be calculated. Figure 2.12 shows the variation of G_{total} as function of T_m.

When the meniscus is large, the values of G_{total} are one order of magnitude lower than the values of the thermal conductance due to the heat transfer through air ($G_{air} \simeq 4.5$ µW.K^{-1}[14] and $G_{air} \simeq 2.5$ µW.K^{-1}[13]). As a consequence, the thermal conductance through the water meniscus cannot be predominant in the thermal interaction between the probe and the sample [107]. It is striking that our findings are in accordance with the observations made with a nanoprobe [60], even though the tackled sizes are very different. Note that the values of H=100 or 180 MW.m^{-2}.K^{-1} induce a maximum shift of 25 % of the values of G_{total} (see Figure 15). A variation of the probe temperature T neither modifies this conclusion. We underline that our analysis justifies SThM calibration methods that have been developed previously with the same kind of microprobes at temperatures T_m larger than 100 °C [14, 24]. As the meniscus is almost evaporated at these relatively high temperatures, it has a smaller impact on the heat transfer to the sample and simplifies the analysis [107].

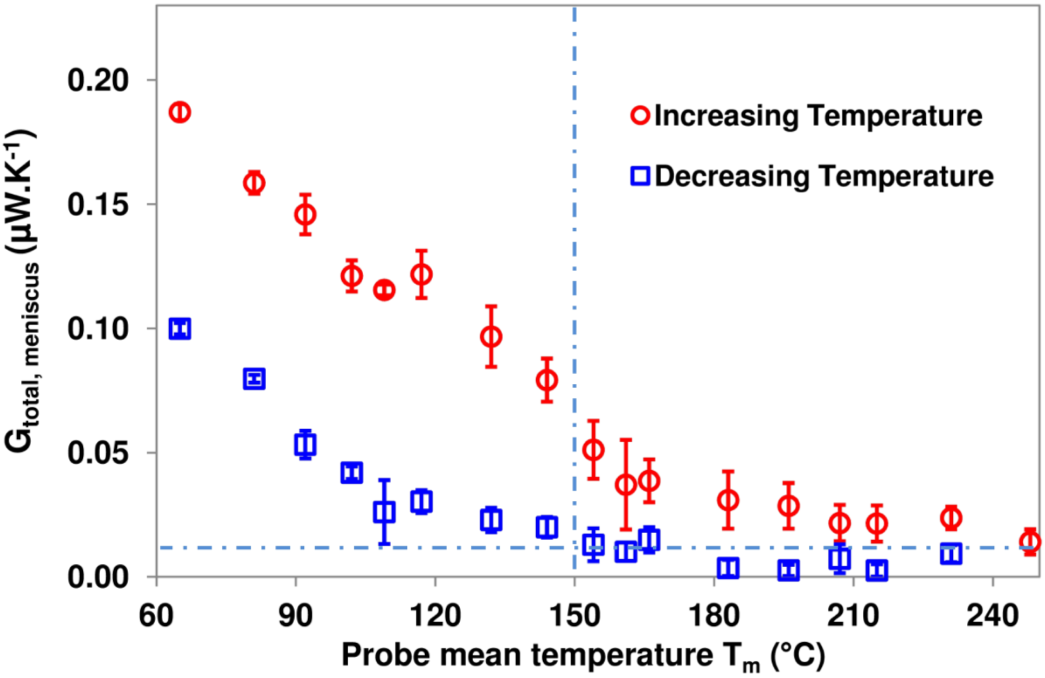

Figure 2.12. Total thermal conductance of the meniscus G_{total} as a function of the Wollaston probe mean temperature T_m for the Ge sample (T_a= 30 °C, RH= 40 %).

As seen in this section, the conduction through the water meniscus is not the predominant mechanism in the thermal interaction between the probe and the sample. The water meniscus conduction is at one order of magnitude smaller than the heat conduction through air [13, 14] (see later in chapter 3). The methodology applied here can help quantifying the heat transfer through the meniscus by measuring the pull-off forces between a probe and the sample. As observed, the meniscus that is responsible of the stiction can largely disappear at large probe temperature and thus that might be an alternative solution for the stiction reduction in the case of NEMS/MEMS devices. Moreover, the variation of the meniscus dimensions at different probe temperatures can open an avenue for different applications such as the thermally-controlled dip-pen nanolithography.

An important factor helped accomplishing this study is the small value of roughness of the Ge sample (arithmetic value of roughness R_{ar}= 0.54 nm and maximum peak-to-peak roughness $R_{p\text{-}p}$=5 nm measured by AFM). The next section investigates the impact of the sample roughness factor using the Wollaston probe and compares the measurements with the ones presented before on the polished germanium sample and with the results of the scientific literature for SPM studies of the roughness effect. Moreover, to conclude this part of the study, measurements of pull-off forces on a hydrophobic sample (graphite) were performed and compared with literature studies.

2.2.4 Effect of roughness on the pull-off forces on hydrophilic surfaces

In order to focus our study on the effect of roughness on the pull-off forces, we perform our measurements on a rough sample of germanium Ge. Its roughness parameters are R_{ar}= 27 nm and $R_{p\text{-}p}$= 277 nm measured by AFM. Figure 2.13 presents the variations of the pull-off forces F_{po} as a function of T_m on the sample of rough germanium. The measurements were performed also at different points at the sample surface for each probe temperature. As in the curves of the polished Ge sample (see Figure 2.7), the curves of F_{po} here show a decreasing tendency up to a temperature around 120 ^{o}C where the F_{po} stays almost constant. We noticed that this value is smaller than the value observed in the case of the polished Ge. That might be related to an additional thermal resistance due to the sample roughness effect. In fact, an additional resistance at the contact induces a larger apex temperature (see chapter 1). Therefore, the temperature of the water meniscus between the tip apex and the sample might be larger in the case of the rough Ge than that of the polished Ge.

The mean values of F_{po} are smaller than those obtained in the case of polished germanium (see Figures 2.7 and 2.13). The surface roughness reduces basically the real contact area between the probe and the sample. This has a significant impact on the capillary forces as studied by Rabionvich *et al.* [94]. At relative low humidity level as in our case (RH≈ 40 %), we can expect a decrease in the mean values of the capillary forces [94].

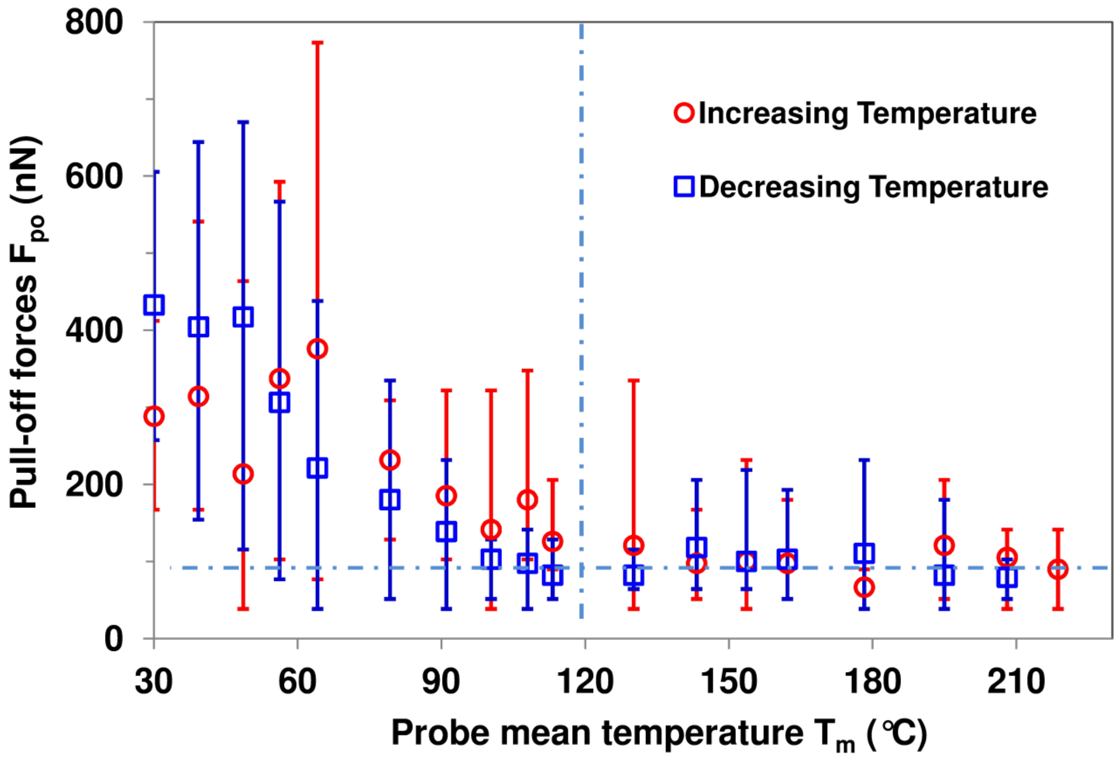

Figure 2.13. Variation of the pull-off forces F_{po} as a function of the probe mean temperature T_m for the sample of rough germanium.

An illustration between the contact between the probe and a surface asperity is given in Figure 2.14. In fact, there is only a thin mono-molecular film that exists at the contact and the meniscus, if it is formed, is very small and the capillary adhesion is then reduced [94]. Ata *et al.* [108] studied the variation of the adhesion forces as a function of the roughness parameter R_{ar} at the contact between a glass sphere of 10 µm in radius and a Si wafer. They found a decreasing tendency until a limit where the asperity height becomes larger than the double of the equivalent radius of curvature [108]. That is related to our case where R_{ar} is much larger than $2\times r_{eq}$ and can explain the lower values of the pull-off forces measured at various positions at the sample surface. This regime is known as the "asperity regime" as defined by Halsey [109] where a single asperity is in contact with the probe. We also noticed that error bars are much larger in Figure 2.13 and the hysteresis is hardly observed in this case.

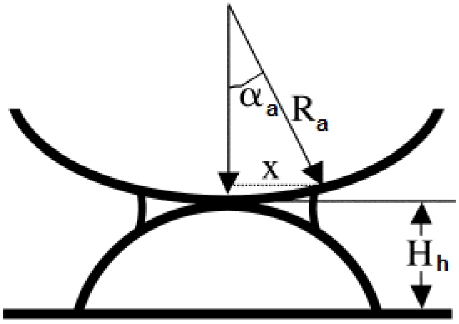

Figure 2.14. Schematic illustration of the meniscus of a contact between the probe and a surface asperity [94].

2.2.5 Measurement of the pull-off forces on hydrophobic surface

Due to its hydrophobic character, a graphite sample is considered in this part. Figure 2.15 presents the variation of pull-off forces F_{po} as a function of the probe mean temperature T_m.

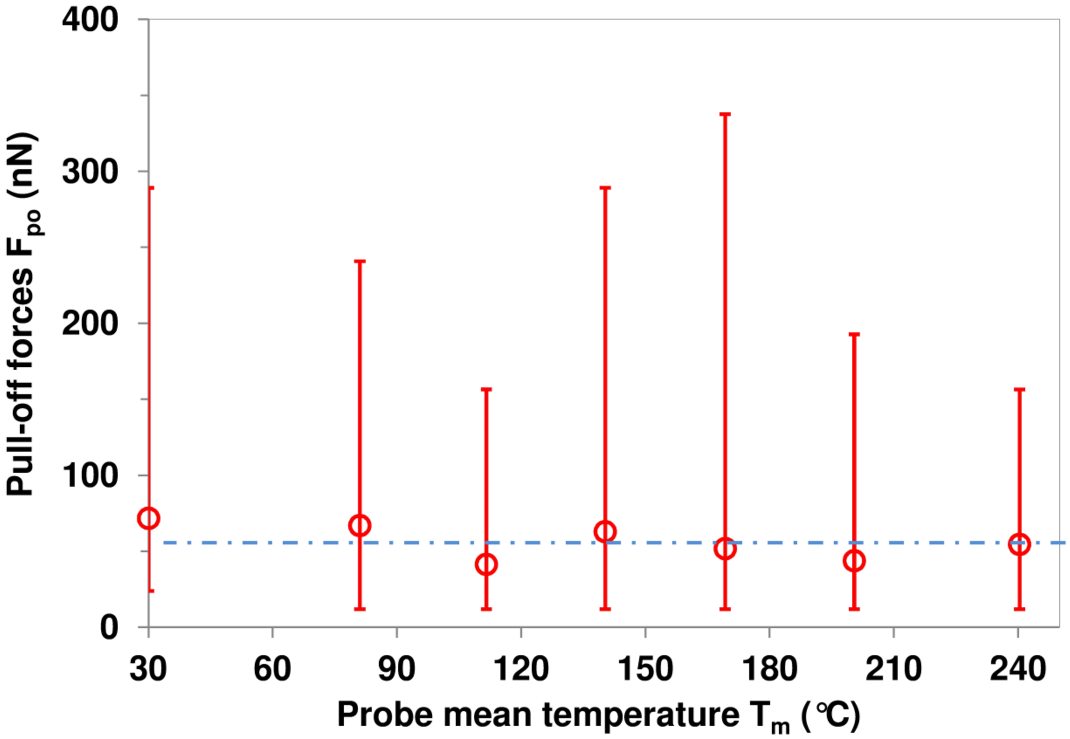

Figure 2.15. Variation of the pull-off forces F_{po} as a function of the probe mean temperature T_m for the sample of graphite.

At each T_m, the measurements were performed at minimum of 15 points at the sample surface. The error bars in Figure 2.15 denotes the maximum and the minimum of F_{po} among the population of points. We can notice that the mean values F_{po} is almost constant as a function of T_m. In fact, it could be related to the non-formation of a meniscus between the tip apex and the graphite sample. Our measurements curve are similar to that obtained by He et *al.* [110] given in figure 2.16. The pull-off forces F_{po} were measured as a function of the relative humidity between hydrophobic tip (apex radius ≃ 10 – 20 nm) and a hydrophilic silicon sample [110]. No variation of F_{po} was observed as a function of RH (see Figure 19) and that was related to the meniscus that was not formed between the tip and the sample [110]. That is probably our case as the mean values F_{po} in Figure 18 is close to the values of F_{po} at large values of T_m in the case of the polished Ge (see Figure 2.7) where the meniscus largely disappeared.

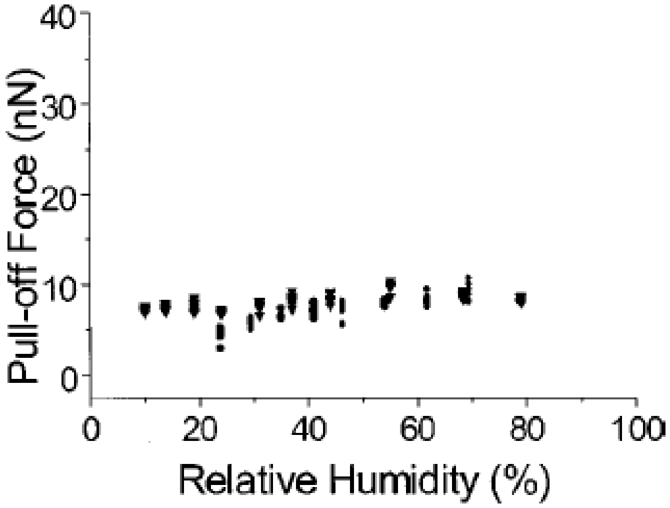

Figure 2.16. Pull-off force as a function of RH measured between a hydrophobic tip and a flat silicon sample [110].

We observed in addition that at each T_m, one or two points among the population have much larger values of pull-off forces than all the other points (see Figure 2.15). The experiment was repeated many times and the same behaviour was always observed. In fact, that might be related to the study of Luna *et al.* [111] where nanodroplets of water were observed on the graphite surface using Scanning Force Microscopy (SFM). Thus, the large values of F_{po} observed during the measurements might be the results of the contact between the probe and adsorbed nanodroplets on the graphite sample.

As seen for the case of hydrophobic sample, the meniscus is not formed at the tip-sample contact and thus no heat conduction through meniscus exists for this type of samples. Interestingly, a small group of measurements shows high value of pull-off forces. That might be related to nanodroplets of water that exist on the sample surface as suggested in the scientific literature.

2.3 Preliminary experiments performed in the frame of the development of a SThM-ESEM combined system

CETHIL is currently developing a SThM-ESEM combined system. This part reports the results of preliminary experiments carried out in an Environmental Scanning Electron Microscope (ESEM) with the Wollaston probe in order to evaluate the possibility to observe the meniscus under such conditions. The probe was not heated in these first experiments.

The ESEM offers a direct imaging of the meniscus in a variable-pressure environment. By decreasing the temperature of the meniscus, the curvature radius of the meniscus r_k is expected to increase (see Equation (2.5)). The probe is usually brought into contact with a cooled substrate [112, 113]. Figure 2.17 shows an ESEM image of the water meniscus at the contact between the Wollaston wire and a substrate of germanium Ge. The temperature of the substrate was about 2 °C and the relative humidity is around 90 %. As can be seen, the curvature radius of the meniscus r_k increases while decreasing the temperature and its imagining is easier to perform.

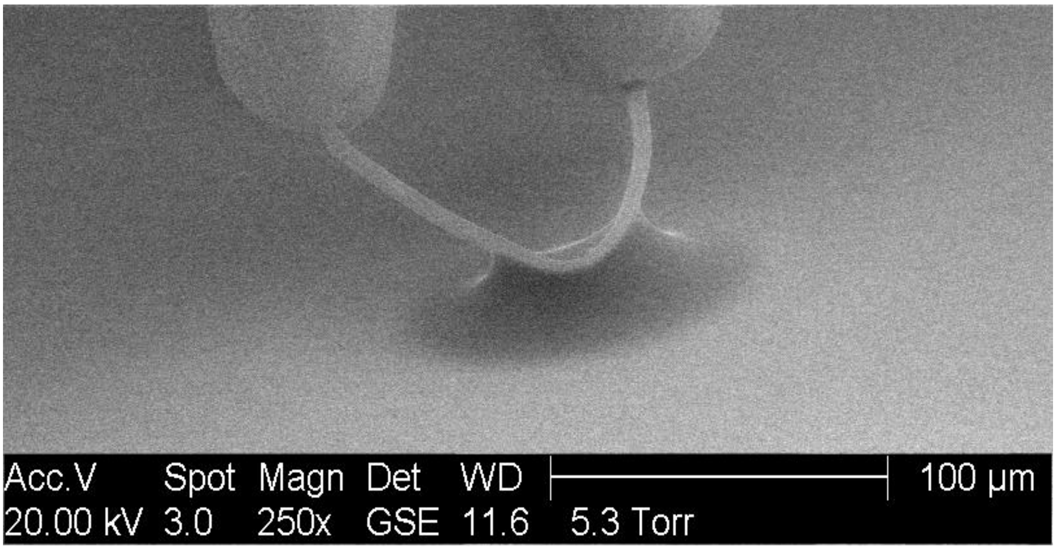

Figure 2.17. ESEM image of the water meniscus formed at the contact between Wollaston wire and germanium sample ($T_{substrate}$≃ 2 °C, *RH* ≃ 90 %).

Weeks and Vaughn [112] were the first to image the meniscus between the probe and the sample in an ESEM. Figure 2.18 shows the values obtained of the meniscus height h_k=2r_k [112]. These values are much larger than the values expected with the Kelvin Equation [112].

Similar experiments were performed by Van Honschoten *et al.* [95] and Greiner *et al.* [113] and the same difference was also observed. As an example of such a difference, the radius of curvature r_1 observed at RH= 98 % in ESEM was about 200 nm where as in the Kelvin Equation the value is expected to be around 27 nm [95]. Van Honschoten *et al.* [95] related this difference to either an additional pressure induced by the electron beam that is focused on the meniscus and/or the meniscus contact with the microscopic liquid film on the substrate. In the case of perfect wetting, the liquid film of thickness e is governed by the disjoining pressure. This pressure is the difference between the pressure of the vapor around the liquid film and the pressure of liquid [104].

In order to investigate these effects, a substrate of Germanium was placed in an ESEM chamber. The substrate was cooled through a Peltier cooler. The relative humidity was between 95 % and 100 %. The electron beam was focused on a specific zone on the substrate up to a time limit where no change is observed on the liquid film on the substrate. Immediately after, the beam was zoomed-off and an image was collected of the liquid film that could show two zones: one where the electron beam was focused and another where the e-beam was not focused on. Figure 2.19 shows an example of different images collected at different places on the substrate sample at $T_{substrate} \simeq 2$ °C. The electron beam was focused around 30 minutes on the zone that appears on the left. The liquid film appears obviously to be larger in the zone where the electron beam was not focused. It can be said in this case that the electron beam factor is important and its effect on observing the dimensions of the liquid film or the meniscus is significant. In our experiment, the electron beam charges and reduces the water film observed on the substrate surface. We illustrate the contact between the probe and sample in an ESEM chamber as shown in Figure 2.20. Figure 2.20.a corresponds to the case where there is no effect of the electron beam and the small radius of the meniscus and the water film thickness are respectively r_1 and e. On the other hand, Figure 2.20.b corresponds to the one where the electron beam is focused on the probe-sample contact and reduces the water layers as shown before. In this case, r'_1 and e' correspond respectively to the radius of the meniscus and the water film thickness. Since e' is smaller than e as shown before, we can imagine than $r'_1$is larger than r_1. That might be the reason between the difference observed while predicting the equivalent radius $r_k \simeq r_1$ through the Kelvin Equation and observing that radius in an ESEM chamber as seen in refs [95, 112, 113]. The future experiments in the

SThM-ESEM combined system should take the effect of the e-beam while analyzing the experiments in ESEM.

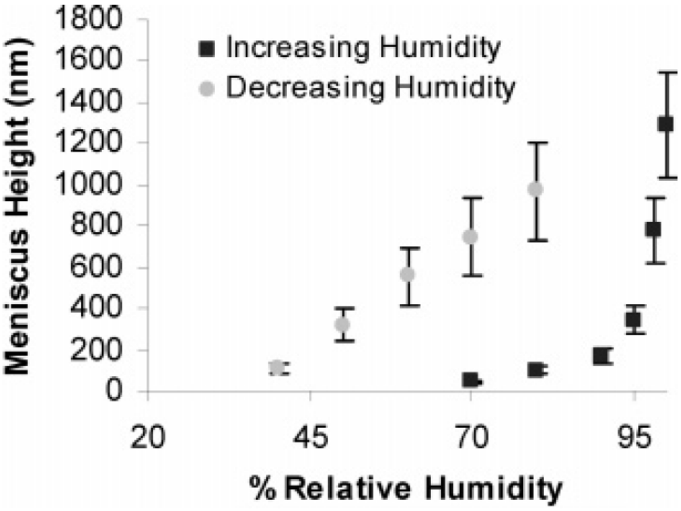

Figure 2.18. Meniscus height (nm) as a function of the relative humidity for a SiN cantilever tip in contact with a silicon substrate at a temperature of 5 °C .

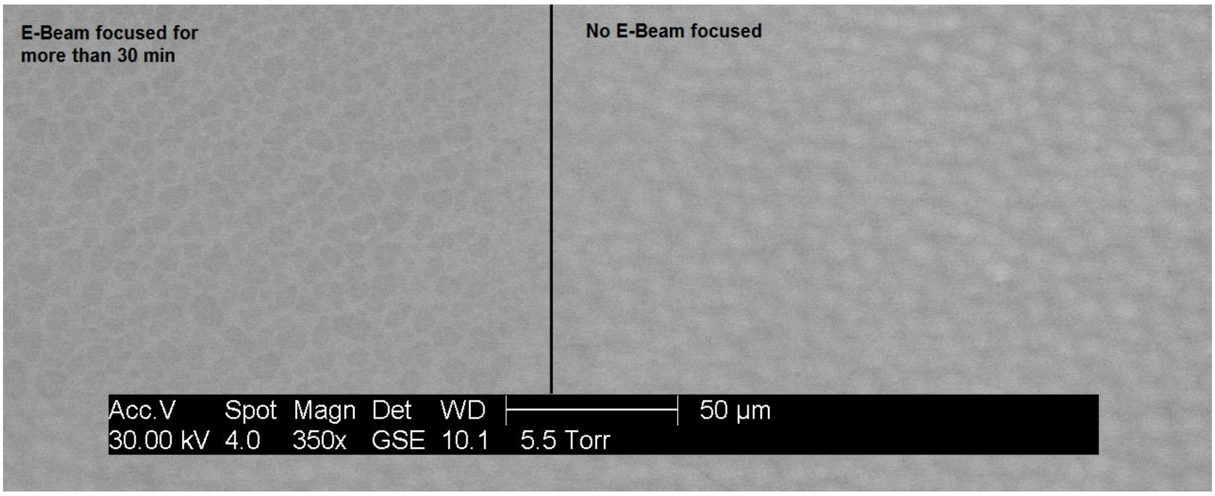

Figure 2.19. ESEM image of a liquid film on a Ge substrate showing two different zones of the liquid film ($T_{substrate}$≃ 2 °C, RH between 95 and 100 %).

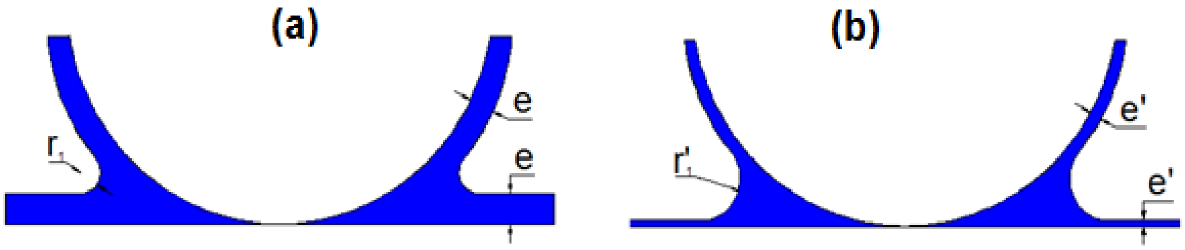

Figure 2.20. Schematic diagram of the cases (a) where the electron beam is not focused (b) and when it is focused in an ESEM chamber on the probe-sample contact.

2.4 Conclusion

In summary, this chapter dealt with the heat transfer through water meniscus between the Wollaston probe and samples. First, we have investigated the thermal conduction through the water meniscus at the contact between the probe and a hydrophilic sample of germanium Ge. The values of the pull-off forces were measured whilst increasing and decreasing the probe mean temperature. The measurements show a progressive evaporation of the meniscus until a certain limit beyond which the pull-off forces remain constant. The experimental measurements were linked to the pull-off forces at elevated probe temperatures to allow the water meniscus contribution to the tip-sample heat transfer to be quantified. The largest radius of the meniscus was estimated using published models. The total thermal conductance of the meniscus was then calculated while accounting for the thermal conductance at the probe-meniscus and meniscus-sample interfaces. The results show that the meniscus thermal conductance is at most one order of magnitude lower than the conductance through air for the same probe. In addition, the effect of roughness on the pull-off forces was shown on hydrophilic surfaces. The obtained results were discussed with what was observed through literature models and measurements. Moreover, the pull-off forces were measured on a hydrophobic sample of graphite as function of the probe temperature. Our results suggest the non-formation of a meniscus between the probe and the sample except for one or two points among large population of points where the meniscus is linked to a nano-droplet as suggested in the scientific literature. The same methodology is used in the case of smaller probes (KNT and DS probes) as it will be seen in Chapter 4.

In the aim of developing a SThM-ESEM combined system, the last part of this chapter reported the results of first experiments performed in an ESEM. Our results outline a first effect showing that the effect of the electron beam on SThM measurement has to be studied and to be taken into account while analyzing measurements with the SThM-ESEM system in future works.

Chapter 3

Probe-sample thermal system in DC Scanning Thermal Microscopy investigated with the Wollaston probe

As seen in Chapter 2, the thermal conduction through water meniscus does not play a dominant role in the thermal interaction between the SThM probe and a sample in the case of the Wollaston probe. In order to achieve a quantitative analysis of the probe-sample thermal interaction with this type of probe, the chapter is dedicated to study the probe-sample heat transfer by two other mechanisms: thermal conduction through solid-solid contact and thermal conduction through air. Studying these mechanisms requires knowledge of the probe thermal properties once it is heated to temperatures above the ambient. Once the probe thermal conductance is identified, measurements under vacuum conditions will be first used to determine the thermal conductance through the mechanical contact. Thermal boundary resistances at the tip-sample contact will be determined for different materials.

The analysis of measurements performed under ambient conditions will be then used to specify the heat losses to the environment and reach a better understanding of the probe interaction with the surrounding medium. Later, the parameters of the probe-sample thermal interaction through air (effective thermal conductance G_{air} and thermal radius b_{air}) will be studied as a function of the sample thermal conductivity. The effect of roughness of samples on the measurement will be shown through a discussion of experimental results obtained with different materials. These results helped us to establish a procedure of experiments to reduce the error during the determination of the thermal conductivity of bulk samples. Based on this procedure, the thermal conductivity of samples for thermoelectric applications is determined in the last part of the chapter.

3.1 Influence of the probe temperature T_m on the thermal signal $\Delta P/P_c$ and on G_p

Studying the heat transfer between the probe and the sample through the meniscus as a function of the probe mean temperature T_m raised the question about an eventual effect of the variation of T_m on the heat transfer between the probe and the sample. Since the Wollaston probe is used in this chapter, our experiments were dedicated to the measurements of the probe Joule power relative difference of the probe $\Delta P/P_c$ (Equations (1.6) and (1.7) in Chapter 1). A sample of germanium Ge and a Wheatstone bridge to control T_m were used. Figure 3.1 shows the variation of $\Delta P/P_c$ as a function of T_m. While increasing T_m, $\Delta P/P_c$ decreases but the slope of the curve $\Delta P/P_c=f(T_m)$ decreases as a function of T_m.

If we adapt the modeling of the probe-sample thermal system as three thermal conductances in series (probe, thermal contact and sample), the variation $\Delta P/P_c=f(T_m)$ can be linked to:

(1) The variation of the thermal conductance at the contact G_c where the conductances of the different heat mechanisms are included

or/and

(2) The variation of thermal conductance of the probe G_p.

We start by identifying the variation of $G_p=f(T_m)$, as studying the thermal conduction through solid-solid contact and the thermal conduction through air requires the value of G_p as it will be seen later.

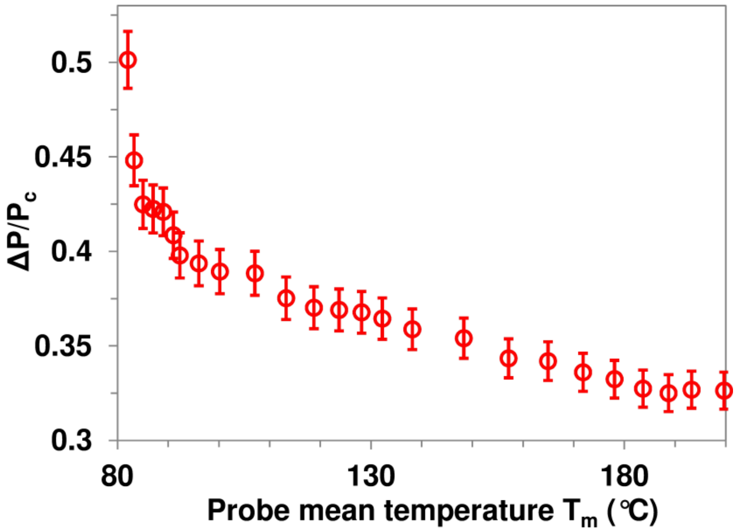

Figure 3.1. Variations of the probe Joule power relative difference as a function of the probe mean temperature when the probe contacts a sample of germanium Ge (T_a = 30 °C and RH= 40 %).

3.2 Influence of the probe mean temperature T_m on G_p

The thermal conductance of the probe G_p was used to describe the heat flux between the probe supports (in Wollaston wire) and the probe apex [14, 22, 57] in the thermal conductivity calibrations and the studies of the probe-sample thermal interaction that used the Wollaston probe [22, 57]. In these calibrations, the boundaries between the Pt/Rh wire and the probe supports were supposed at ambient temperature ($T_{support}=T_a$) [14, 22, 57]. The thermal conductance of the probe G_p has been given as [14, 22, 57]:

$$G_p = \frac{\lambda_p S_p}{L_p} \quad (3.1)$$

where λ_p, S_p and L_p are respectively thermal conductivity, section and length of the resistive Pt/Rh wire. The thermal conductivity of the probe λ_p was taken constant whatever the probe temperature (λ_p = 38 W.m^{-1}.K^{-1} at T_a) and thus $G_p=G_{p1}$ = 3.73 × 10^{-6} W.K^{-1} [14, 22, 57].

However, the probe is heated to temperatures larger than the ambient temperature raising questions about the variations of λ_p or the validity of Equation (3.1) based on the assumption taken in the thermal conductivity calibrations ($T_{support}=T_a$ [14, 22, 57]). Any variation of G_p should be taken into account in order to quantify accurately the heat mechanisms between the probe and the sample. Moreover, the effect of the variation of the probe temperature on the thermal interaction between the probe and the sample has not been shown yet.

In order to estimate the temperature dependence of G_p, thermal measurements were carried out under vacuum conditions (P= 5 × 10^{-5} mbar) where the probe is away from any contact. Under these circumstances, probe losses to the surrounding gas may be neglected (h=0 W.m^{-2}.K^{-1}). Supposing that the probe supports are at ambient temperature, the apex relative temperature θ_{apex} ($\theta_{apex}=T_{apex} - T_a$) is equal to 1.5 times the probe relative mean temperature θ_m ($\theta_m=T_m - T_a$) [22]. G_p can be calculated as [22]:

$$G_p = \frac{P_p}{(T_{apex} - T_a)} = \frac{P_p}{\theta_{apex}} = \frac{2P_p}{3\theta_m} \quad (3.2)$$

where P_p is the power dissipated in the probe.

In practice, a Wheatstone bridge was used to control T_m and the variation of P_p was monitored. The red circles in Figure 3.2 give the variation of G_p estimated from measurements with Equation (3.2) as a function of T_m. The values of G_p increase with the increase of T_m.

Two suggestions can be given to explain this variation:

1) The hypothesis of a probe support at ambient temperature in (1) is too simplifying,

and/or

2) The thermal conductivity of platinum $\lambda_{Pt/Rh}$ changes with the variation of T_m. The Wiedemann–Franz law gives the empirical relationship between the thermal conductivity of a metal λ (Pt/Rh in our case) and the electrical resistivity ρ at a temperature T as follows:

$$\lambda = \frac{L_{wf} T}{\rho} \quad (3.3)$$

where $L_{wf} = 2.44 \times 10^{-8}$ W.Ω.K^{-2}.

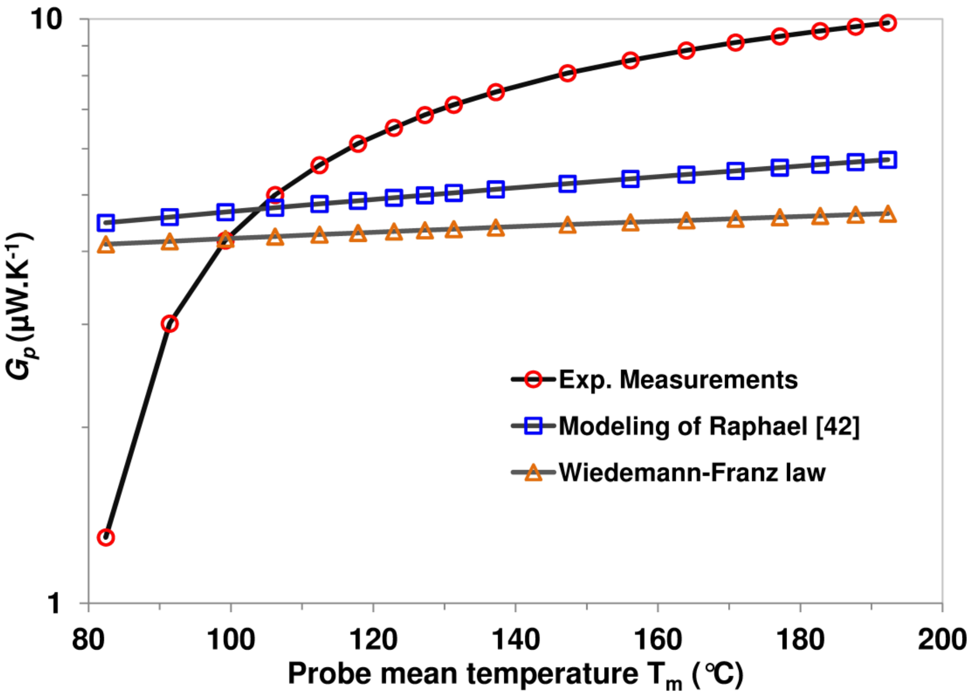

Figure 3.2. Variations of the probe conductance G_p as a function of the probe mean temperature T_m.

If we take T=T_m in Equation (3.3), we can have an estimation of the variation of $\lambda_{Pt/Rh} = f(T_m)$ and therefore G_p=$f(T_m)$ following Equation (3.1). The triangle marks in Figure 3.2 give the variation of G_p following the Wiedemann–Franz law. As can be seen, this variation does not follow the curves of the values determined through the measurements. Besides, Raphael [42] estimated $\lambda_{Pt/Rd}$ at three levels of probe mean temperature through AC measurements and multi-frequency modeling as shown in Figure 3.3. The square marks on Figure 3.2 show the variation of G_p if we adopt the same variation of $\lambda_{Pt/Rh}$ [42] over our range of probe mean temperature. The variation of $\lambda_{Pt/Rh}$ in this case does not also explain the variation of G_p=$f(T_m)$.

It can then be said that the difference between the two curves obtained in Figure 3.2 are related to the boundary conditions of heat sink taken at the probe support in the modeling of the approaches of Lefèvre [22], David *et al.* [14] and Raphael [42].

In the following, we have considered: (1) the probe supports as heat sinks and (2) the values of $G_p=f(T_m)$, determined from Equation (3.2) and experimental data as shown in Figure 3.2, to estimate the thermal conductances through the solid-solid contact G_{ss} and through air G_{air}.

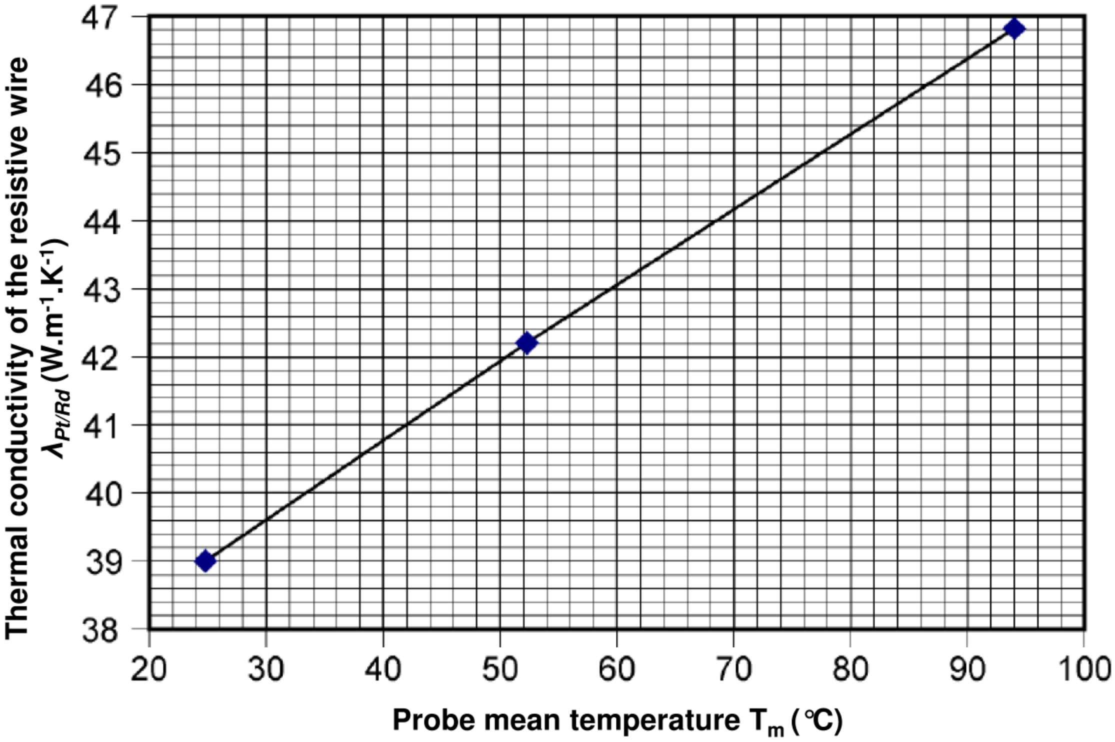

Figure 3.3. Variation of $\lambda_{Pt/Rd}$ as a function of T_m as determined by Raphael [42].

3.3 Thermal conductance at the solid-solid contact G_{ss}

The expressions of the thermal conductance for the heat transfer through solid-solid contact G_{ss} proposed by Majumdar [44] and then by David [57] implies an increase of G_{ss} when the thermal conductivity of the sample λ_s increases (Equations (1.27) and (1.28) – Chapter 1). For samples with high thermal conductivity like silicon ($\lambda_{Si} \simeq 148$ W.m^{-1}.K^{-1}), the value of G_{ss} calculated with these expressions has the same order of magnitude of the thermal conductance through air G_{air} (for Si, $G_{ss} \simeq 2 \times 10^{-6}$ W.K^{-1} and $G_{air} \simeq 2.5 \times 10^{-6}$ W.K^{-1} [14, 24]) if we assume mechanical contact radius a_c of 10 nm. While performing DC calibration of the Wollaston wire probe under ambient conditions (see chapter 1, section 1.3.1), $G_{ss} = f(\lambda_s)$ while assuming a_c= 10 nm. Compared to the calibration curves that does not include G_{ss} [22], the calibration of David [57] induced a better fit of the measurements of the Joule power relative difference $\Delta P/P_c$ as a function of λ_s as shown in Figure 3.4.

However, G_{ss} and G_{air} are correlated in these measurements since they are performed under ambient conditions and the estimation of G_{ss} is based on macroscopic analytical expressions.

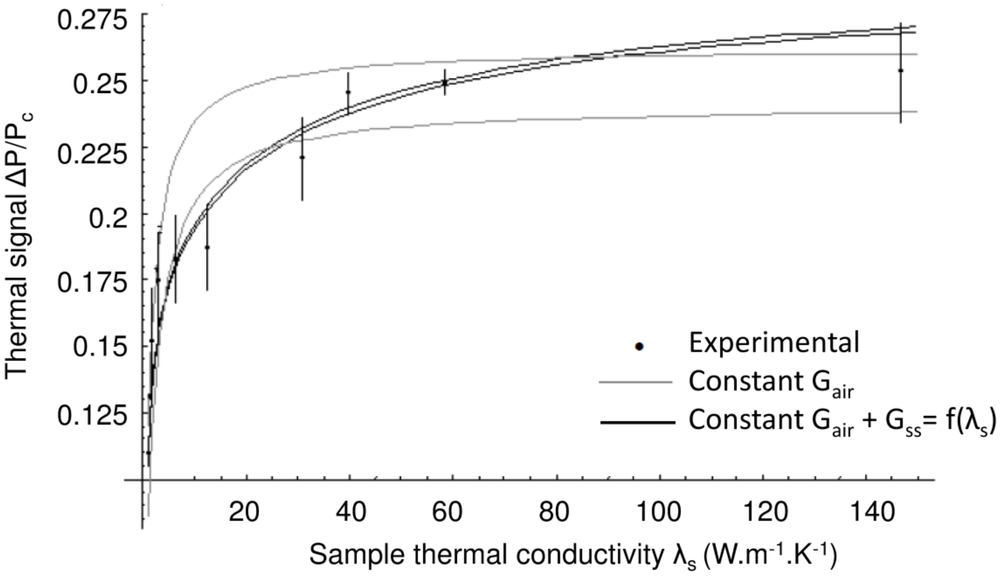

Figure 3.4. ***$\Delta P/P_c$*** **Calibration curves obtained by David [56] under ambient conditions (*a_c* = 7.5 nm, *G_{air}* =4.5 × 10^{-6} W.K^{-1}).**

In order to distinguish between G_{ss} and G_{air} and to have a better estimation of G_{ss} between the Wollaston probe and the sample in the present works, thermal measurements measured under vacuum conditions were performed. The probe and sample were mounted in a Scanning Electron Microscope (SEM) chamber. The pressure in the chamber was about 5 × 10^{-5} mbar. Under these conditions, the conduction through air and the heat losses to the environment are eliminated ($h \simeq 0$) [44, 45]. The probe was heated up to 140 ^{0}C to eliminate the rest of the meniscus that might exist between the probe and the sample as seen in Chapter 2. As explained in Chapter 1, the thermal conduction through radiation G_{rad} may be assumed negligible in comparison to the other mechanisms. It can be supposed that under such circumstances the signal change at the contact is mainly due to the conduction at the mechanical contact. The measurements were performed on three samples of low roughness parameters (measured with AFM) and different thermal conductivities as listed in Table 3.1. The choice of low roughness is to reduce the errors while estimating a_c.

Under these circumstances, $\Delta P/P_c$ can be written as:

$$\frac{\Delta P}{P_c}=\frac{3}{4}\frac{G_{ss}G_s}{4(G_pG_s+G_pG_{ss})+G_{ss}G_s} \quad (3.4)$$

G_s is the thermal conductance of the sample given as [29]:

$$G_s = 4K_1\lambda_s a_c \quad (3.5)$$

where K_1 is a correction factor for the diffusive thermal conductance and is about 0.694 [114, 115].

Table 3.1. ***ΔP/P_c*** **results for the samples of Mica, Germanium and Silicon under vacuum conditions (values of λ_s were given by the suppliers, Goodfellow and Neyco).**

Sample (λ_s)	MICA (5 $W.m^{-1}.K^{-1}$)	germanium (58.6 $W.m^{1}.K^{-1}$)	silicon (148 $W.m^{1}.K^{-1}$)
a_c (nm) values determined with Hertz's model	≃12.5 ± 0.9	≃13.7 ± 1	≃ 12.8 ± 1
Arithmetic value of roughness R_{ar}	0.28	0.7	0.25
Maximum peak-to-peak roughness R_{p-p}	2.68	4.75	1.85
Mean free path of phonons Λ	??	~ 200 [116]	~ 260 [116]

Figure 3.5 shows the variation of the thermal signal measured for the different samples. The measurements were performed with two probes and repeated at an atmospheric pressure P=0.28 mbar. No significant difference was observed between the measurements at $P=5 \times 10^{-5}$ mbar and P=0.28 mbar. It can be said that the heat losses to the environment and conduction through air are almost negligible at these pressures in agreement with the experiments of Chapuis [27]. The applied force between the probe and the samples was around 500 ± 100 nN. Since we supposed the elimination of the water meniscus, a_c was estimated for the three considered sample materials using the Hertzian model as shown in Table 3.1 (Equation (1.23) – Chapter 1). In this estimation, the radius of the sphere in contact with the sample was estimated around 0.35 µm as seen in Chapter 2 (Equivalent radius of a cylindrical groove). Based on these values and Equations (3.4) and (3.5), G_{ss} can be evaluated. Figure 3.6 shows the evaluated values of G_{ss} for the different samples. We can notice that the values of G_{ss} increase as function of λ_s. However, these values are at least one order of magnitude smaller than the values of the thermal conductance due to the heat transfer through air ($G_{air} \simeq 7$ $\mu W.K^{-1}$) as it will be seen in the following parts of this chapter.

Therefore, the variation of $G_{ss}=f(\lambda_s)$ (Equation (1.28)) overestimates G_{ss} and does not explain the better fit of $\Delta P/P_c=f(\lambda_s)$ obtained by David *et al.* [56] (see Figure 3.3).

From the determined values of G_{ss}, we can access to the value of an effective thermal boundary resistance R_b (K.m^2.W^{-1}) at the probe-sample interface. G_{ss} can be expressed as [12, 33, 117]:

$$G_{ss} = \frac{\pi a_c^2}{R_b} \quad (3.6)$$

Here, $G_{ss}=1/R_{ss}$ where R_{ss} denotes the ballistic resistance at the tip-sample constriction for the case of Ge and Si samples. For these samples, the mean free path Λ of the samples is much larger than the contact radius a_c as can be noticed in Table 3.1 (MICA is expected to be extremely anisotropic).

Figure 3.7 shows the values of R_b identified through our experiments. We can notice that the values of R_b are in the range of 10^{-9} m^2.K.W^{-1}, in agreement with the order of magnitude of the values mentioned in the literature [12, 33]. The values identified for R_b by Stoner *et al.* through picosecond optical technique were about 5 × 10^{-9} m^2.K.W^{-1} for Al/Al_2O_3 interfaces [118]. The values of R_b identified by Stevens *et al.* [119] by the transient thermoreflectance technique between Pt/Si are in the range of 7 × 10^{-9} m^2.K.W^{-1}. Using the same technique, Komarov *et al.* [120] identified values for R_b for Au/Si (metal-semiconductor) interfaces ranging from 5.5 to 7 × 10^{-9} m^2.K.W^{-1}. These values are in agreement with Molecular Dynamics (MD) simulations performed for the case of Au/Si interfaces by da Cruz *et al.* (R_b= 6.3 × 10^{-9} m^2.K.W^{-1} [121]). These values are of the same order of magnitude of our results for the case of the MICA sample (PtRd/MICA interface) but larger than the identified values for the cases of PtRh/Si and PtRh/Ge interfaces as shown in Figure 3.7.

Recently, Yang et *al.* [122] determined the values of R_b for the case of metal-semiconductor (Al/Si) interfaces through non-equilibrium molecular dynamics (NEMD) method. The electron-phonon coupling was taken into account to evaluate R_b [122]. The identified values of R_b were between 2.1 and 2.7 × 10^{-9} m^2.K.W^{-1}). These values are closer to our cases of PtRh/Si and PtRh/Ge interfaces where R_b varies between 1.14 and 1.4 × 10^{-9} m^2.K.W^{-1} for PtRh/Si interfaces and between 2.8 and 3.35 × 10^{-9} m^2.K.W^{-1} for PtRh/Ge interfaces.

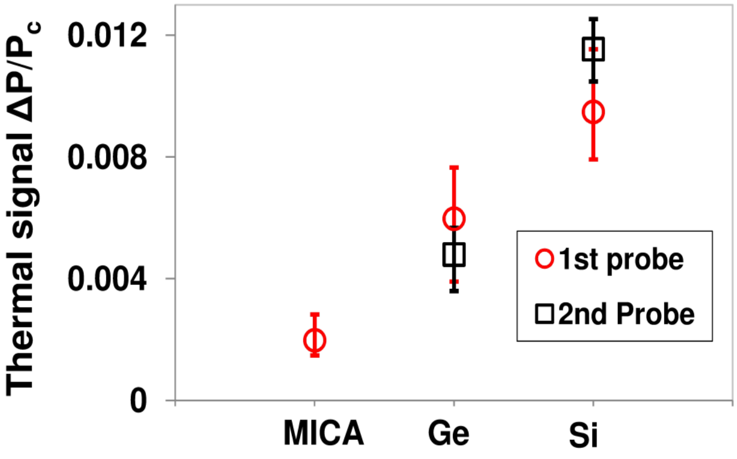

Figure 3.5. Variation of the thermal signal for the three materials (MICA, Ge and Si) under vacuum conditions (T_m= 140°C, RH=40 %, T_a=30 °C).

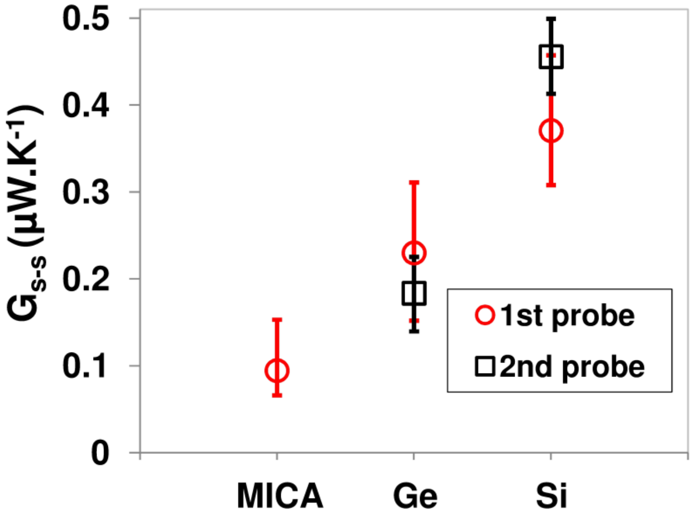

Figure 3.6. Estimation of the thermal conductance at the solid-solid contact G_{ss} for the three materials (MICA, Ge and Si).

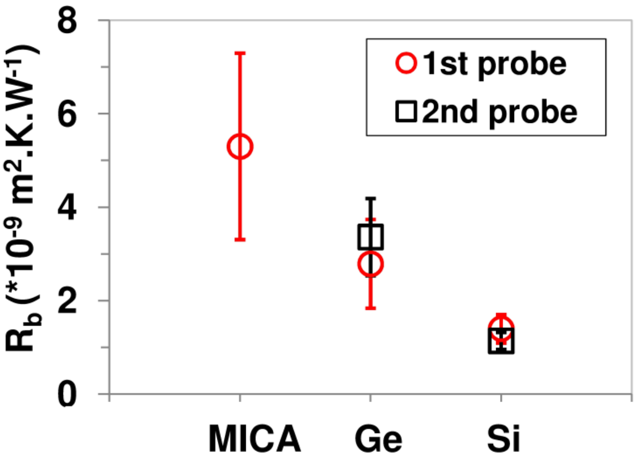

Figure 3.7. Thermal boundary resistance R_b ($m^2.K.W^{-1}$) identified for the three materials (MICA, Ge and Si).

As seen in this part, working under vacuum conditions does not increase the sensitivity in the calibration with the Wollaston probe for materials with high thermal conductivity like silicon and germanium. In fact, the sample thermal conductance G_s is on the order 5×10^{-6} W.K^{-1} while the tip-sample contact conductance G_{ss} is on the order the 10^{-7} W.K^{-1}. This makes it difficult to determine experimentally the thermal properties of the sample materials while working under vacuum conditions. However, experimental measurements under these conditions are of high interest for the study of the heat transport at interfaces.

The next section investigates the heat transfer to the sample through the air. The involved heat transfer mechanism appears be dominant in the tip-sample thermal interaction. We aim in this section to understand better the heat transfer to the sample and to reduce the error during the characterization of the thermal conductivity of the sample material.

3.4 Measurements under ambient conditions

3.4.1 Determination of the coefficient *h* of the heat losses to the environment

While working under ambient conditions, the thermal signal $\Delta P/P_c$ is related to the coefficient h that defines the heat losses to the medium environment (see Equations (1.6) and (1.7)). To be able to determine the parameters of the tip-sample interaction through air, the coefficient h should be first estimated.

The evaluation of h by Chapuis ($h \approx 3000$ W.m^{-2}.K^{-1} [27]) was based on supposing that the probe interaction with the environment is based on the mechanism of conduction instead of convection. Since the natural convection phenomenon is driven by the buoyancy forces, an orientation of the Wollaston probe might provide a clue to estimation the participation of the phenomenon of convection. The probe was oriented up to 70 ° from its initial position as illustrated in Figure 3.8. We observed no significant change of the signal measured (see Appendix A) while performing the measurements under air conditions and at P=2 mbar as shown in Figure 3.9. This result is in accordance with what expected by the Grashof number Gr that gives the ratio of the buoyancy forces to the viscous forces [123]. In our case, for a difference of temperature of around 100 °C between the probe and the environment, Gr is smaller than 1 and thus the convection effects are negligible in front of those of the heat conduction [124]. Therefore, the heat losses to the environment are mainly due to the heat conduction and the assumption taken by Chapuis is valid in this case.

The value of h = 3000 W.m^{-2}.K^{-1} is taken into account in our study in the following parts.

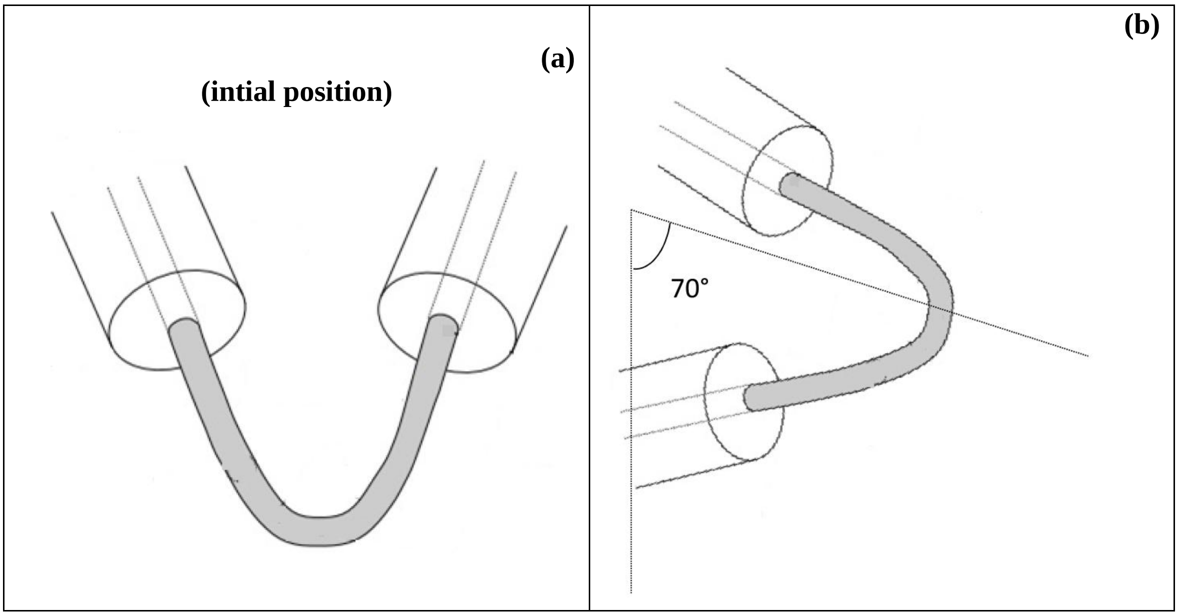

Figure 3.8. Schematic of the probe in two different positions.

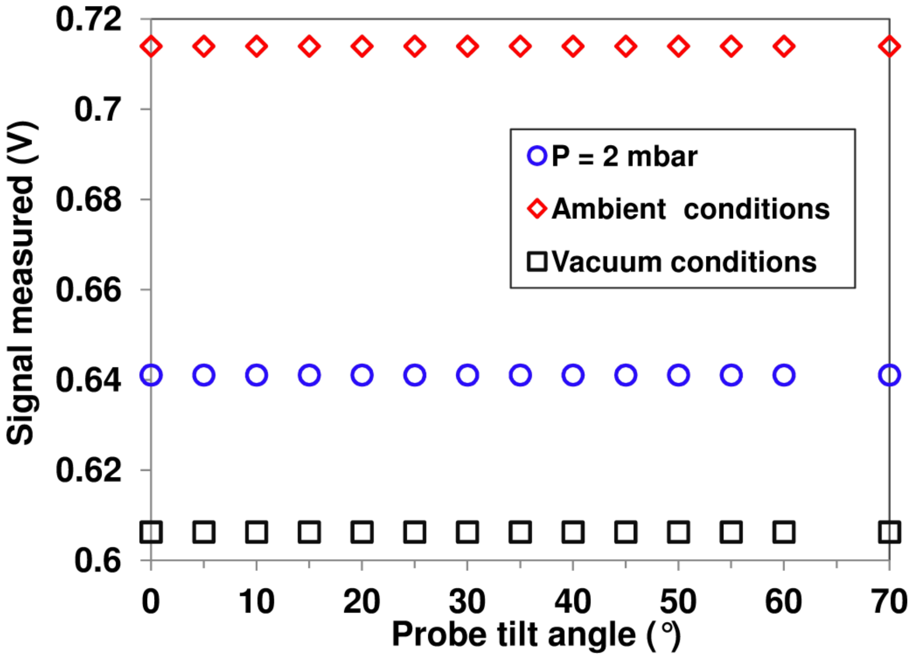

Figure 3.9. Voltage of the probe in different conditions for different tilts of the probe.

3.4.2 Heat conduction through air to the sample

A. Experimental study

We try in this part to study the heat transfer between the probe and the sample through air in order to quantify the air conduction parameters (b_{air},G_{air}) and to provide more accurate determination of thermal conductivity of bulk samples. For materials with low thermal conductivity λ_s, the probe provides a high level of sensitivity to λ_s as seen in Figure 3.4. The sensitivity decreases with the increase of λ_s. The thermal conductivity limit for the calibration with the Wollaston wire is between 20 and 30 $W.m^{-1}.K^{-1}$ [26, 57]. When λ_s exceeds that limit, the thermal signal $\Delta P/P_c$ is almost constant (see Figure 3.4). Therefore, we chose to perform our measurements with samples of thermal conductivity that is smaller than 15 $W.m^{-1}.K^{-1}$. The samples used in this calibration are listed in Table 3.2. λ_s is between 0.1 and 13 $W.m^{-1}.K^{-1}$.

Table 3.2. List of the calibration samples used in the measurements with their roughness parameters measured with AFM (values of λ_s were given by the suppliers, Goodfellow and Neyco).

Sample material	Thermal conductivity ($W.m^{-1}.K^{-1}$)	Arithmetic roughness R_{ar}(nm)	Peak-to-Peak roughness $R_{p\text{-}p}$ (nm)
Polyimide PI	0.17	5	57
Silicon dioxide SiO2	1.2	3.25	54.2
Zirconium dioxide ZrO2	2.5	0.8	5
Cadium Selenide CdSe	3.49	0.86	13.5
Cadmium telluride CdTe	6.28	3.7	44.9
Zinc Telluride ZnTe	12.36	5.08	51.2

The measurements for our thermal conductivity calibration were performed under ambient conditions (T_a= 25 ^{0}C, RH= 40 %) at a mean probe temperature T_m of 140 ^{0}C. The water meniscus has almost vanished at this temperature (see Chapter 2) and the solid-solid thermal conductance G_{ss} is at least one order of magnitude smaller than the conductance through air G_{air} (see section 2 of this chapter). The $\Delta P/P_c$ model is described in Chapter 1 (see Equations (1.6) and (1.7)). The thermal conductivity calibration with the measurements of $\Delta P/P_c$ consists in evaluating two mean values that denote the heat transfer to the sample through air: the thermal interaction radius $b=b_{air}$ and the thermal conductance at the contact $G_c = G_{air}$. Figure 3.10 shows the variations of $\Delta P/P_c$ as a function of λ_s. The experimental curve $\Delta P/P_c$=f(λ_s) is similar to those curve observed in Figure 3.4. Table 3.3 shows the mean values identified for G_{air} and b_{air} while taking into account the heat losses to the environment

h = 3000 W.m^{-2}.K^{-1}. Even though the values of G_{air} (G_{air} = 6.64 µW.K^{-1}) are in the same of order of magnitude of the values identified in other studies using the same probe ($G_{air} \simeq$ 4.5 µW.K^{-1}[14, 57] and $G_{air} \simeq$ 2.5 µW.K^{-1}[13, 22, 24]), we can notice that the values of b_{air} are one order of magnitude larger than expected (b_{air} ~ µm [13, 14, 22, 24, 57]). Unlike our experiments, we observe that the literature studies do not always account for samples of thermal conductivity smaller than 1 W.m^{-1}.K^{-1} [22, 57]. In our measurements, this range of thermal conductivity is represented by the sample of polyimide Po (λ_{Po} = 0.17 W.m^{-1}.K^{-1}). If we identify G_{air} and b_{air} while exempting the sample of Po from the calibration, we observe that the determined values of b_{air} (b_{air}= 4 µm) are in the same order of those estimated elsewhere [22, 57]. In fact, when λ_s decreases the heat flux lines tend to spread since the heat is not attracted efficiently by the sample anymore and then the thermal exchange radius b_{air} increases as illustrated in Figure 3.11. Therefore, it can be said that the choice of calibration samples has a significant effect on the identification of the thermal interaction parameters between the probe and the sample. Moreover, the difference between the two cases (h= 0 and h = 3000 W.m^{-2}.K^{-1}) in the determination of the interactions parameters is at least about 20 % as can be noticed in Table 3.3.

Table 3.3. Identified parameters of the probe-sample thermal interaction for the two cases: *h*=0 and *h*=3000 W.m^{-2}.K^{-1}.

Heat losses coefficient	b_{air} (µm)	G_{air} (µW.K^{-1})
h = 3000 W.m^{-2}.K^{-1}	14.7± 1.6	6.64 ± 0.16
h = 3000 W.m^{-2}.K^{-1} (Polyimide exempted)	4 ± 0.05	7.38 ± 0.27
h = 0 W.m^{-2}.K^{-1}	11.5 ± 1.2	5.09 ± 0.13
h = 0 W.m^{-2}.K^{-1} (Polyimide exempted)	3.12 ± 0.04	5.64 ± 0.2

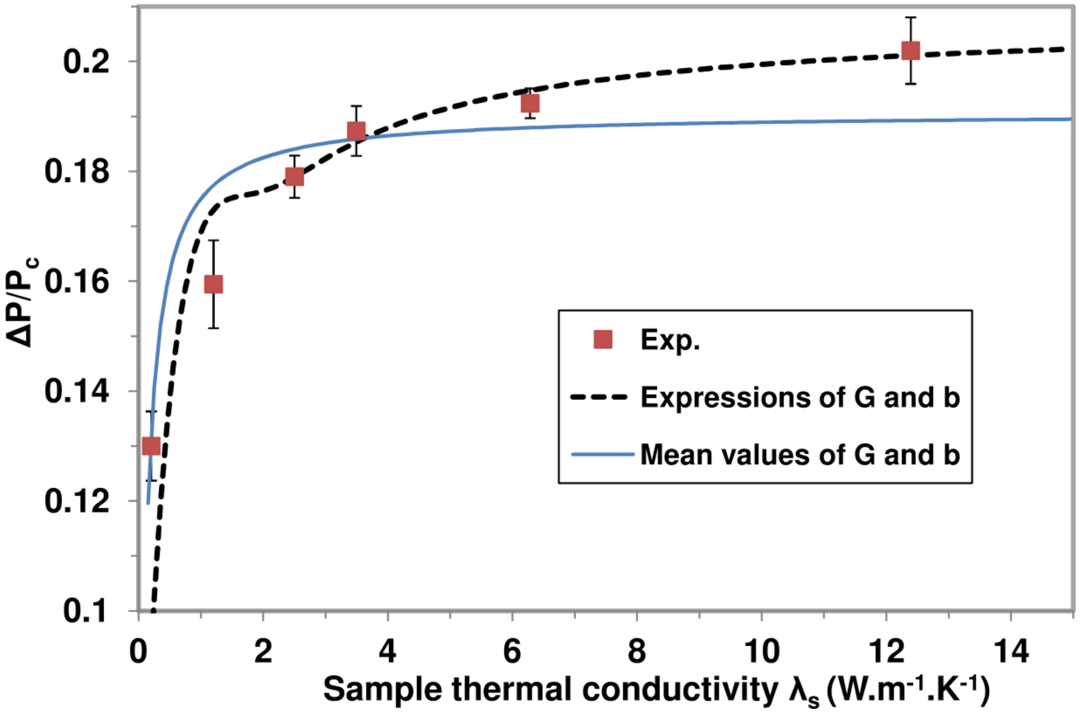

Figure 3.10. ***$\Delta P/P_c$*** **variation as a function of the thermal conductivity** ***λ_s*** **(*T_a*=30°C, *RH*=40%).**

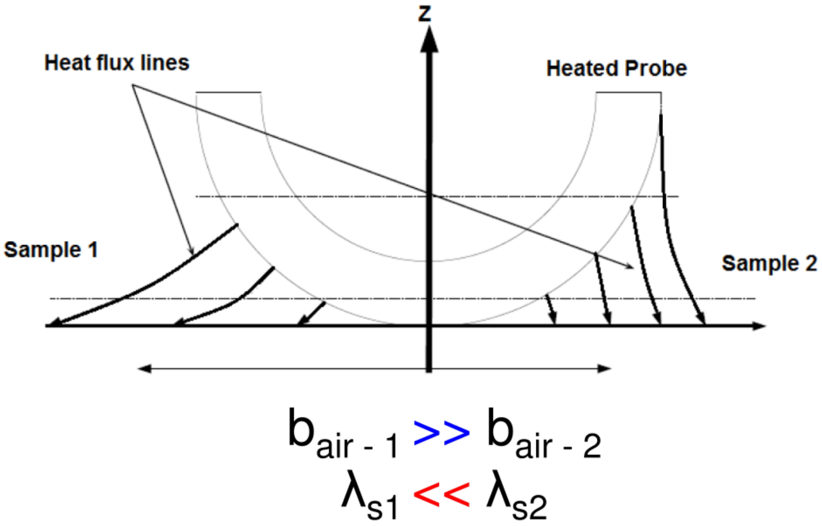

Figure 3.11. Schematic of the heat flux lines for two samples of different thermal conductivity ***λ_s*.**

The calibration curve $\Delta P/P_c = f(\lambda_s)$:

As said before in this section, the thermal interaction parameters vary when the thermal conductivity of the sample changes. Searching for a solution to apply these variations to the calibration curve $\Delta P/P_c=f(\lambda_s)$, we consider the mean values of G_{air} and b_{air} between two consecutives calibration samples. The values of G_{air} and b_{air} are indicated in Table 3.4. The variation of G_{air} and b_{air} as a function of λ_s are shown in Figure 3.12. Here, the thermal conductivity of an interval is represented by the mean value of the two interval bounds. As can be seen, the variations of G_{air} and b_{air} are not negligible especially for the samples of low thermal conductivity λ_s.

Table 3.4. Mean values of G_{air} and b_{air} for different intervals of the thermal conductivity λ_s.

Interval of λ_s	b_{air} (µm)	G_{air} (µW.K^{-1})
[0.17;1.2]	24.5 ± 4.5	5.5 ± 0.1
[1.2;2.5]	4.35 ± 0.07	7.19 ± 0.25
[2.5;3.49]	3.14 ± 0.12	7.72 ± 0.36
[3.49;6.28]	2.87 ± 0.4	7.73 ± 0.42
[6.28;12.36]	2.35 ± 0.77	7.77 ± 0.54

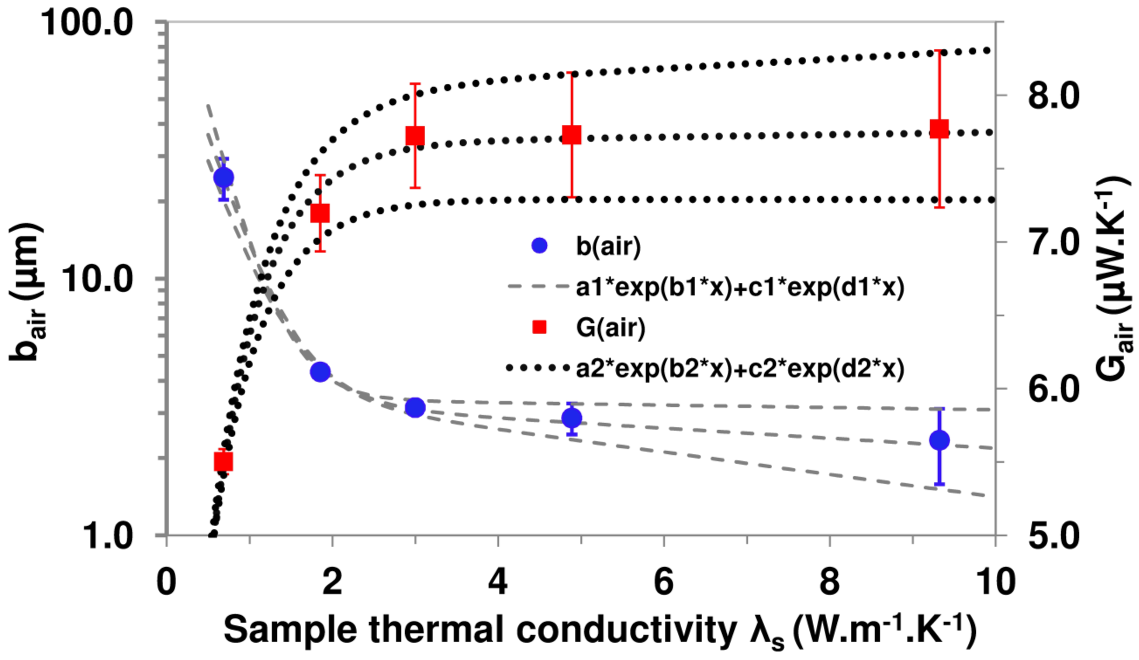

Figure 3.12. Variation of b_{air} and G_{air} as a function of λ_s and their corresponding fitting curves (a_1= 1.05E-04, b_1=-2.32, c_1=3.42E-06, d_1=-0.04492; a_2=7.77E-06, b_2=-5.18E-04 , c_2=-5.47E-06, d_2=-1.197).

We could adapt through empirical expressions the best fits for the variations of b_{air} and G_{air} as a function of λ_s (see Figure 3.12). In order to apply the variations of the parameters of the conduction through air to the experimental calibration, these expressions are inserted in the formula of $\Delta P/P_c$. The corresponding curve of $\Delta P/P_c$ is shown in Figure 3.10 in dotted line. Apparently, taking into account the variations of G_{air} and b_{air} as a function of λ_s assures a better curve rather than having constant values among all the range of the thermal conductivity (see Figure 3.10). The difference between these curves is the variation of the parameters that are linked to the conduction through air.

In the next section, we investigate the heat transfer through air to the sample with the Wollaston probe through numerical simulations in order to confirm our experimental investigation and to monitor the variations of the interactions parameters between the probe and the sample. The aim of these simulations is to shed light on the interaction between the probe and materials of low thermal conductivity and to have a precise idea of the limitation of the thermal conductivity calibration using the Wollaston wire probe.

B. Numerical study of the heat transfer through air

Numerical simulations were done using COMSOL Multiphysics. The geometry of the model is shown in Figure 3.13. Because of its symmetry, half of the probe is modeled (half-toroid) and the symmetry plane is insulated. The solid that represents the semi-infinite sample is of 500 µm in thickness, 500 µm in width and 1 mm in length. The air surrounding the probe is represented through a solid 2 where the thermal conductivity of the air is inserted. The probe supports are represented through a cylinder of silver of 75 µm in diameter and 100 µm in length. The mesh consists of 8000 elements. The probe is at a distance of 70 nm from the sample surface. The mesh was 8 times refined at a cubic volume of 4×10^6 µm^3 near the probe apex. The air and the sample surfaces are at initial temperature of 300 K. A condition of continuity is assumed at the boundary condition between the probe and its support. The boundaries of the solids 1 and 2 are maintained at 300 K. The heat flux is calculated the sample surface as shown while varying the thermal conductivity of the sample λ_s.

We define Φ_{ref} as the heat power calculated with respect to a sample of large thermal conductivity. Figure 3.14 presents the variations Φ_{ref} transferred to the sample as a function of λ_s. Increasing the geometrical dimensions of solid 1 and solid 2 by a factor of 2 induces a maximum deviation of Φ_{ref} by 4%. The heat power is calculated with respect to a sample of infinite thermal conductivity and for two initial temperatures of the toroidal tip: 400 K and 500 K. The variations of Φ_{ref} are not affected by the temperature. This shows that the heat transfer through air does not vary with the variation of the probe temperature (Figure 3.14). The curves reach a limit for λ_s between 20 and 50 W.m^{-1}.K^{-1} where Φ_{ref} does not vary anymore. That limit is close to the limit of the experimental curves of $\Delta P/P_c$ where $\Delta P/P_c$ reaches a limit at a thermal conductivity between 20 and 30 W.m^{-1}.K^{-1} [26, 57]. Moreover, the slope of the variations of $\Phi_{ref}(\lambda_s)$ is at its max at the zone where λ_s is smaller than 2 W.m$^-$

^{1}.K^{-1}. That is identical to the behaviour of the interaction parameters of the conduction through air G_{air} and b_{air} determined in the last section (see Figure 3.12).

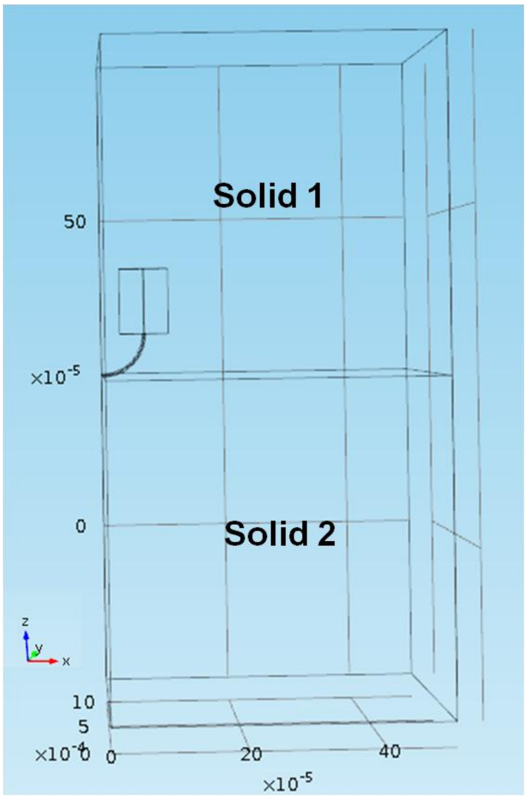

Figure 3.13. The model of the probe being at proximity of the sample.

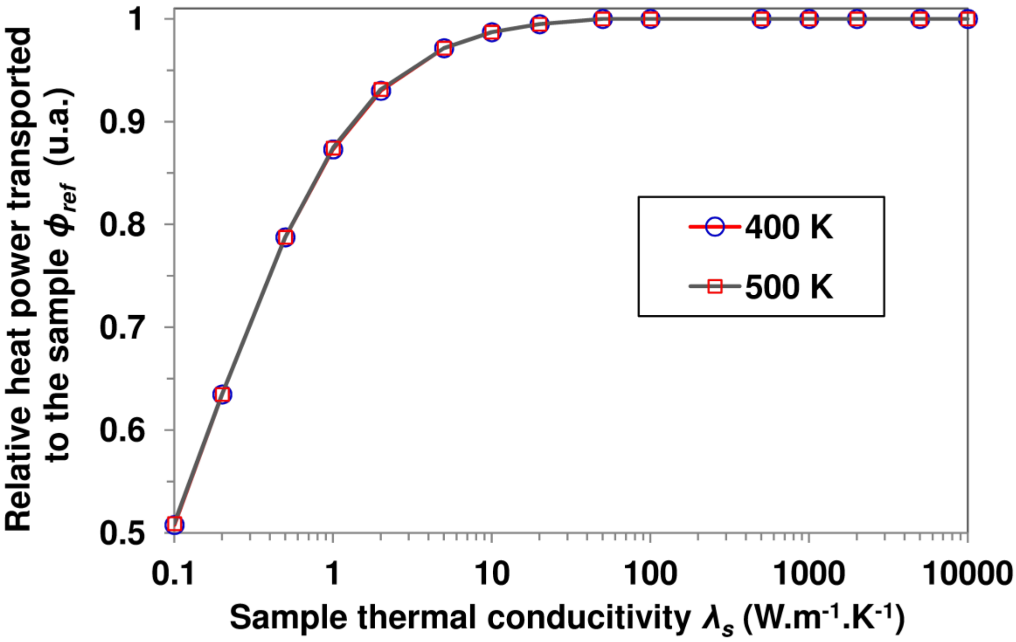

Figure 3.14. Calculated relative heat power transferred to the sample as a function of its thermal conductivity λ_s.

Based on the variations of Φ_{ref}, it was important to determine a criterion that allows us to evaluate the variation $b_{air}=f(\lambda_s)$ in these numerical simulations. Let us remind that b_{air} by its definition is the radius of an equivalent discoidal area on the sample surface. That area is at a uniform sample temperature called T_s. The Wollaston probe is not symmetric in the two axes X and Y and the shape of the related equivalent area is an ellipse on the sample surface [22]. In this case, b_{air} can be taken as the equivalent radius among the radii of the ellipse:

$$b'_{air} = \sqrt{\frac{b_x^2}{2} + \frac{b_y^2}{2}} \quad (3.6)$$

Figures 3.15 and 3.16 show respectively the variations of the temperature at the sample surface in the two directions X (major axis) and Y (minor axis) for different values of the thermal conductivity of the sample λ_s. As expected, when λ_s decreases and thus the heat flux lines go further along the surface, the temperature is larger at a given position in the two axes directions.

Let us assume that the distances X and Y equal to the thermal interaction radii b_x and b_y, the temperature is $(T_A-T_{amb})/ 2$. The point A is shown on the abscissa axis in Figures 3.15 and 3.16 where the temperature is at its max on the sample surface. Based on Equation (3.6) and our criterion, b_x and b_y can be evaluated. The variations of b_x, b_y and b_{air} as a function of λ_s are presented in Figure 3.17. The curves vary largely when λ_s is smaller than 2 $W.m^{-1}.K^{-1}$. This is in accordance with the curves of determination of $b_{air}=f(\lambda_s)$ (see Figure 3.12). The values of b_{air} in Figure 3.17 are larger than those shown in Figure 3.12 but have the same order of magnitude. The results are striking here since the model does not reflect properly the probe interaction with the surrounding medium. These simulations emphasize our suggested arguments presented in the experimental part. They show that the conduction through the air depends strongly on the thermal properties of the sample.

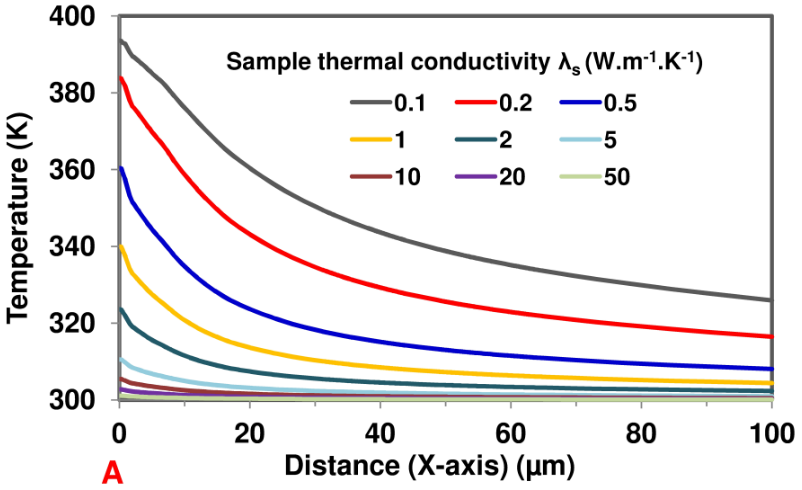

Figure 3.15. Variation of the temperature on the sample surface in the direction of the major axis X.

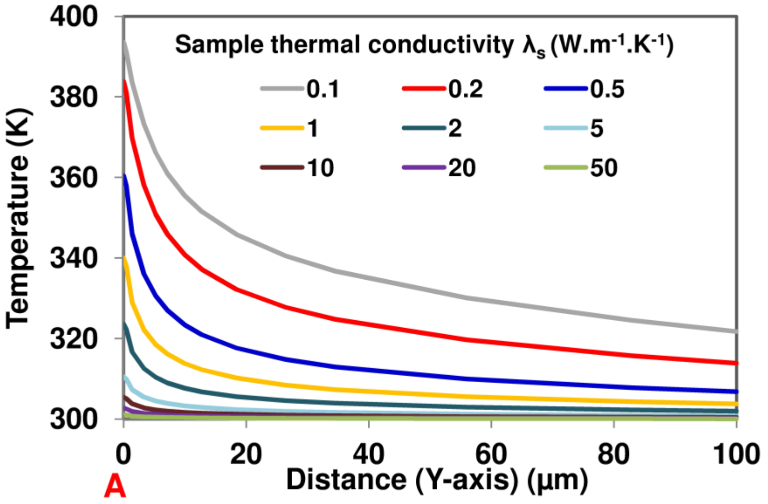

Figure 3.16. Variation of the temperature on the sample surface in the direction of the minor axis Y.

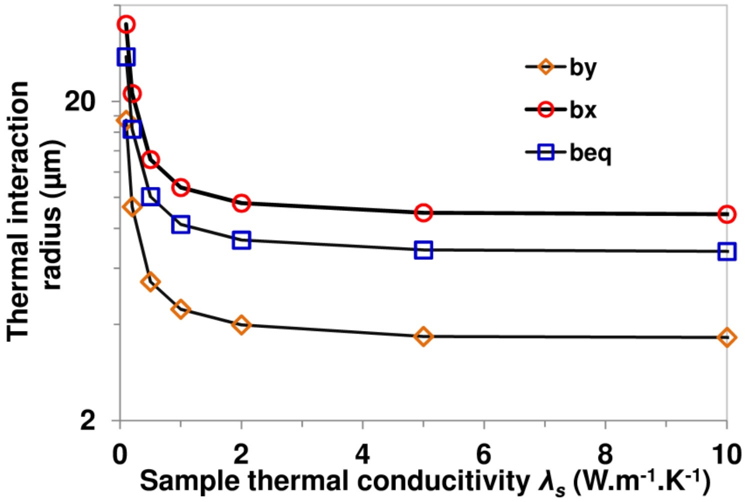

Figure 3.17. Variation of the thermal interaction radii b_x, b_y and b_{eq} as a function of the thermal conductivity λ_s.

In summary, the parameters of the thermal exchange through air G_{air} and b_{air} are dependent on the thermal properties of the sample. In the previous models for the Wollaston probe, these values were taken constant for a set of calibration samples. In the frame of calibration for thermal conductivity measurement, we have shown that the determination of these parameters is affected by the thermal conductivity of the calibration samples. The experimental identification of G_{air} and b_{air} was confirmed through numerical simulations of the probe-sample interaction. These simulations reveal a variation of the heat received at the sample surface when λ_s varies. Moreover, b_{air} was estimated by adopting a random criterion and its variation as a function of λ_s is similar to what expected through the identification based on the experimental measurements.

During the measurements and the numerical simulations, the contact between the probe and the sample was supposed perfect. The arithmetic roughness R_{ar} of our calibration samples does not exceed 6 nm as already listed in Table 3.2. In the following section, we identify the effect of roughness of samples on the heat transfer through air using sample of different levels of roughness.

3.4.3 Effect of roughness of the samples on the heat transfer to the sample

We considered two samples of silicon dioxide SiO_2 and Germanium Ge. The values of the roughness parameter R_a of these samples are listed in Table 3.5.

The thermal signal $\Delta P/P_c$ was measured for the different samples under ambient conditions and is shown in Figure 3.18. The index (i) denotes the samples SiO_2 or Ge with the smoothest surfaces. The roughness parameters of these two samples (SiO_2(i) and Ge(i)) can be found in tables 3.1 and 3.2. $\Delta P/P_c$ is almost the same for the SiO_2 samples (see Figure 3.18). However, $\Delta P/P_c$ decreases significantly while increasing the roughness parameters of the sample of germanium. These variations are due to the increase of the resistance at the contact due to the roughness parameters. As the roughness parameters are in the same order of the radius of the groove at the probe apex ($R_a \simeq 350$ µm as seen in Chapter 2), the additive resistance at the contact might be due to the air regions between the asperities.

The difference observed for the two materials is linked to the difference between the thermal conductances G_s of the two samples. Under ambient conditions, G_s is about 2×10^{-5} W.K^{-1} for the sample SiO_2 whereas it is about 5×10^{-4} W.K^{-1} for the sample of Ge (see Equation (1.21)). Based on a modeling of two conductances in series (G_s and $G_{contact}$), the signal $\Delta P/P_c$ for the

Ge samples is more sensitive to the variation of G_c and thus to the sample roughness than the one measured for the SiO_2 samples.

These measurements can give an idea of the effect of the roughness in reducing the conduction at the tip-sample thermal contact, especially in the case of highly conducting samples. Therefore, it is highly recommended that both the calibration samples and the sample to be characterized have polished surfaces.

Table 3.5. Samples with the values of their roughness parameters (R_{ar} and R_{p-p}) and corresponding identified thermal conductivity λ_s.

Samples	Arithmetic roughness R_{ar} (nm)	Peak-to-Peak Roughness R_{p-p} (nm)
SiO_2(1)	20 ± 2	500 ± 80
SiO_2(2)	58 ± 6	800 ± 100
Ge(1)	27 ± 5	270 ± 50
Ge(2)	67 ± 8	900 ± 100

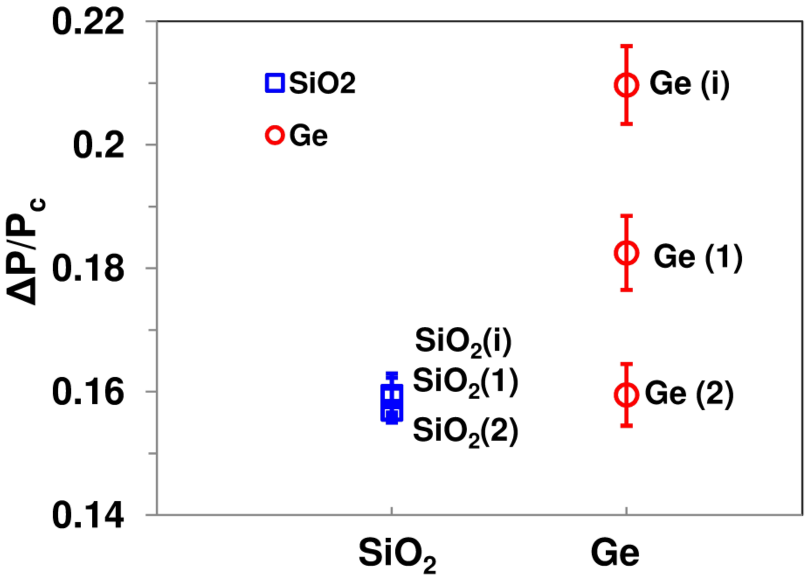

Figure 3.18. Variation of the thermal signal $\Delta P/P_c$ for the different samples of different roughness parameters (T_a= 25 ^{0}C, RH= 40 %).

3.5 Variations of $\Delta P/P_c$ as a function of T_m

In Chapter 2, we determined the thermal conductance of the water meniscus as a function of the probe mean temperature T_m. In this chapter, we determined an effective thermal conductance of the probe and the thermal conductances through the mechanical contact and air. Based on these results with the Wollaston probe, we are able to model the variation of

$\Delta P/P_c$ as a function the probe mean temperature T_m and compare it to the measured $\Delta P/P_c=f(T_m)$ on the sample of Ge (see Figure 3.1). In fact, our modeling takes into account the variation of (1) the thermal conductance of the meniscus $G_{total,meniscus}$ as a function of T_m (see Chapter 2), (2) the variation of the probe conductance $G_p=f(T_m)$ (section 3.1), (3) the thermal conductance at solid-solid contact G_{ss} (section 3.3) and the thermal interaction parameters G_{air} and b_{air} (section 3.4). We suppose that the temperature of the air around the probe stays the same. In fact, a significant increase of the air temperature and thus of G_{air} would introduce an increasing curve $\Delta P/P_c=f(T_m)$, in contradiction with the one obtained in Figure 3.1. Therefore, G_{air} was assumed constant as a function of T_m. Figure 3.19 shows the variations of the modeled $\Delta P/P_c$ as a function of T_m for the sample of Ge. Even though the values here are different from those determined experimentally in Figure 3.1, the same tendency is found here. The difference between Figures 3.1 and 3.19 can be related to 1) the variation of G_{air} and b_{air} since the probe used here is not the same one used in section 3 and/or 2) the values of G_p in contact with the sample are different from the one when it is free from any contact. At the contact, the temperature field along the probe changes due to the heat flux transferred from the probe to the sample and therefore G_p cannot be evaluated from Equation (3.2).

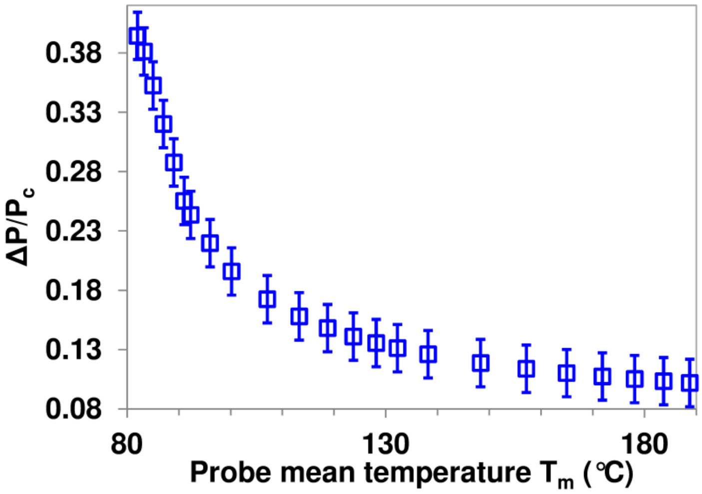

Figure 3.19. Variation of the modeled $\Delta P/P_c$ as function of the probe mean temperature T_m for the sample of germanium Ge.

3.6 Approach for a more accurate thermal conductivity calibration

The determination of the thermal conductivity of materials requires the estimation of the parameters of probe-sample interaction through air in the calibration methodology that we propose here.

As seen in the previous sections, several significant errors can be introduced and have to be avoided to determine accurately the parameters of interaction G_{air} and b_{air}, therefore the calibration procedure should include:

- The accurate estimation of the probe conductance G_p at the considered probe mean temperature at which the measurements are performed.
- The coefficient h of the heat losses to the environment.
- Polished samples where the experiments are performed.
- The variation of G_{air} and b_{air} as a function of λ_s through empirical expressions of $G_{air}=f(\lambda_s)$ and $b_{air}=f(\lambda_s)$ similarly to the one obtained in Figure 3.12.

Zhang *et al.* [125] determined the thermal conductivity of thick films of Bi_2Te_3 and Bi_2Se_3 with SThM using the Wollaston probe (λ_{Bi2Te3}=0.36 W.m^{-1}.K^{-1} and λ_{Bi2Se3}=0.52 W.m^{-1}.K^{-1}). The film thermal conductivities were identified using two calibration samples of thermal conductivities λ_s=1 W.m^{-1}.K^{-1} and λ_s=1.5 W.m^{-1}.K^{-1}. In their calibration, they assumed that the interaction parameters (G_{air} and b_{air}) are constant for the thermal conductivity of samples that lies between 0.1 and 2 W.m^{-1}.K^{-1} [125]. This assumption could involve a significant error while characterizing their samples. In order to calculate the error that depends on the choice of the calibration samples, we take into a similar calibration two samples made of: polyimide (λ_{Po} = 0.17 W.m^{-1}.K^{-1}) and silicon dioxide SiO_2 (λ_{SiO2} = 1.2 W.m^{-1}.K^{-1}). The thermal interaction parameters G_{air} and b_{air} were determined before in this chapter (G_{air}= 5.5 W.K^{-1} and b_{air}= 24.5 µm). If we suppose that the thermal conductivities of the samples of Bi_2Te_3 and Bi_2Se_3 are the same of what was determined [125], then we can calculate their approximate Joule power relative difference : $\Delta P/P_c$(Bi_2Te_3)= 0.147 and $\Delta P/P_c$(Bi_2Se_3)= 0.152. On the other hand, we take the SiO_2 and ZrO_2 samples into the calibration as reference samples. We already identified mean values of G_{air} and b_{air} between these samples (G_{air}= 7.19 W.K^{-1} and b_{air}=4.35 µm). The thermal conductivity of these two calibration samples has almost the same range of those samples taken by Zhang *et al.* [125]. Therefore, based on the $\Delta P/P_c$(Bi_2Te_3) and $\Delta P/P_c$(Bi_2Se_3) values that were determined in the last step, we can estimate the "new" thermal conductivity of the Bi_2Te_3 and Bi_2Se_3 samples. In this parallel calibration, the thermal conductivities of these samples: λ_{Bi2Te3} = 0.854 and λ_{Bi2Se3} = 0.97 W.m^{-1}.K^{-1}. These two values are very different from the values obtained in the mentioned study [125]. It can be said then that the determination of the thermal conductivity of the materials λ_s depends on the thermal conductivity of the calibration samples. Therefore, it is better that the range of the thermal conductivity of the calibration samples covers the thermal conductivity of the material to be characterized.

As a conclusion, it can be said that an attention should be paid to the evaluation of the interaction parameters of the conduction through air. In the zone of sample thermal conductivity where the probe is highly sensitive, these parameters vary largely. Assuming these parameters constant induces a significant error on the experimental characterization of the samples while working with the Wollaston probe.

3.7 Determination of the thermal conductivity of Ba_8Si_{46} clathrates

This part is dedicated to characterize the thermal conductivity of samples of barium silicon Ba_8Si_{46} clathrates [126]. They are used in thermoelectric applications and are expected to have low thermal conductivity λ_s [126]. That is convenient for our measurements as the more λ_s decreases the more the technique is sensitive. We followed the procedure mentioned in section 3.6 for an accurate thermal conductivity calibration. The calibration samples are the same used before and listed in Table 3.3. The obtained thermal conductivity of the of Ba_8Si_{46} clathrates is about 1.7 ± 0.17 $W.m^{-1}.K^{-1}$ [126]. That is in agreement with the expected thermal conductivity through modeling with this material.

3.8 Conclusion

In this chapter, our study of the thermal interaction between the probe and the sample included the quantification of the heat transferred to the sample through the solid-solid contact and through air. In order to estimate accurately the contribution of these two heat mechanisms, the effective probe conductance was first determined as a function of the probe mean temperature. The probe conductance was shown to depend on the probe temperature. This is related to the boundary conditions taken through the modeling. A more realistic model should be developed with more appropriate boundary conditions in order to estimate accurately the probe conductance.

The heat conduction through the mechanical contact was estimated while performing measurements under high vacuum conditions. The measurements were performed using three polished samples of different thermal conductivity. The contribution of this heat mechanism appears to be much smaller than that of the heat conduction through air. Through these measurements, the thermal boundary resistance was determined for the interfaces PtRh/Si ($1.14\text{-}1.4 \times 10^{-9}$ $m^2.K.W^{-1}$) and PtRh/Ge ($2.8\text{-}3.35 \times 10^{-9}$ $m^2.K.W^{-1}$). The obtained results appeared to be in good agreement with the values of thermal boundary resistance announced in the scientific literature for contact between a metal and a semiconductor material.

For measurements under ambient conditions, the probe voltage was measured while rotating the Wollaston probe in order to identify a variation of the convective heat transfer coefficient. The conduction appears to be the dominant mechanism in the heat losses of the probe to its surrounding environment. Later, the variation of the interaction parameters of the conduction through air was monitored as a function of the thermal conductivity of the sample by performing measurements under ambient conditions with reference samples. The variation of these parameters appears to be significant especially in the range of samples of low thermal conductivity. As shown in this chapter, neglecting this variation might introduce a large error during the thermal characterization of the samples of interest. Based on our experimental results in chapter 2 and this chapter, the thermal signal variations for the sample of Ge as a function of the probe temperature were sketched. The variations follow the same trend of the experimental curve despite a difference between the simulated values and the ones determined experimentally. A procedure was drawn in order to perform more accurate thermal conductivity calibrations. We followed this procedure to characterize the thermal conductivity of Ba_8Si_{46} clathrates for thermoelectric applications.

Chapter 4

DC Scanning Thermal Microscopy with probes of nanoscale radius of curvature

In this chapter, we investigate the probe-sample thermal system for probes with tip of nanoscale curvature radius. This chapter consists mainly of two parts that are dedicated to measurements performed with (1) KNT probes (Pd/Si_3N_4) and (2) doped silicon Si probes respectively.

The first part concerns the investigation of the different heat mechanisms that operates between the KNT probe and the sample. We study the effect of reducing the apex radius on the probe-sample thermal interaction. Similar methodologies used with the Wollaston probe are used to quantify the heat conduction through water meniscus (pull-off measurements), at the solid-solid contact (vacuum conditions) and through air (measurements using reference samples). We also analyze the possibilities of the calibration with this probe for thermal conductivity measurement.

In the second part, we studied the thermal conduction through water meniscus with the doped silicon probe. We explain the methodology and approach used in the calibration of the apex temperature. The heat conductance through meniscus is determined as a function of the apex temperature.

The last part of this chapter is dedicated to explain the idea of identifying the phonon transmission coefficient at the tip-sample interface while working with SThM probes. Based on our measurements of the boundary thermal resistance on different samples, we explain the methodology used to determine this coefficient and give some perspectives for its estimation using the different probes considered in this work.

4.1 Study of the probe-sample thermal with the KNT probe

4.1.1 Thermal conduction through the water meniscus

The measurements of the pull-off forces with the Wollaston probe on a hydrophilic sample, already described in Chapter 2, showed the variation of the dimensions and the thermal conductance of water meniscus as a function of the probe temperature. The pull-off forces varied between 100 and 500 nN and the variation of the largest radius r_2 was estimated between 5 and 35 nm (see Chapter 2). The heat conduction through the meniscus appeared to be at least one order of magnitude lower than the heat conduction through air.

Searching for a better resolution of the pull-off forces and meniscus and in order to monitor the effect of nano-tip on the heat conduction through water meniscus, the KNT probe is used here. The expected radius of curvature of the tip apex is expected to be around 50 nm [16]. The temperature coefficient β of the electrical resistivity of the probe was measured using a specific oven at different levels of temperature. The obtained value is about $8 \pm 0.1 \times 10^{-4}$ K^{-1}. This value is close to the value obtained by Puyoo ($\beta = 6.9 \times 10^{-4}$ [28]). It is used in the following to determine the probe mean temperature T_m..We have to note that this value includes the information about the temperature coefficients of the resistive Pd wire β_{Pd} at the tip extremity and the two NiCr resistors β_{NiCr} deposited on the cantilever. To estimate the values of β_{Pd} and β_{NiCr}, the probe was shortcut at the resistors using an adhesion layer of silver. β_{NiCr} was then estimated around $1.65 \pm 0.05 \times 10^{-4}$, which is also close to the value obtained by Puyoo ($\beta_{NiCr} = 2.4 \times 10^{-4}$ [28]). Assuming the probe resistive elements cited above at a same temperature T_m when the probe is in the oven, the value β_{Pd} can be estimated using the following equation:

$$R_{eq}\beta = R_{NiCr}\beta_{NiCr} + R_{Pd}\beta_{Pd} \quad (4.1)$$

The estimated value is around $\beta_{Pd} = 1.37 \pm 0.02 \times 10^{-3}$. This value is similar to the one determined by Puyoo [28] ($\beta_{Pd} = 1.2 \times 10^{-3}$). However, little information exists yet about the real temperature field within the cantilever when a current heats the probe. Its determination constitutes a perspective of this work.

In this work, the probe mean temperature T_m was controlled using a Wheatstone bridge with a feedback circuit. We used two hydrophilic samples of two different thermal conductivities: polyimide Po (λ_s=0.17 W.m^{-1}.K^{-1}) and germanium Ge (λ_s=58.6 W.m^{-1}.K^{-1}). Under ambient conditions (T_a=30, RH=40 %), force-distance curves were performed at different levels of probe mean temperature for the two samples and the pull-off forces F_{po} were determined. The spring constant of the probe is around 0.35 N.m^{-1} [16]. The measurements were performed up to a maximum T_m around 140 °C. The maximum working temperature of this probe is around 150 °C [16]. A thermal control unit was designed and used to control the probe temperature. More details can found in appendix A. Figure 4.1 shows the variations of F_{po} as function of T_m for the two samples of Po and Ge. For the case of Po sample, F_{po} decreases progressively up to a certain limit of T_m around 110 °C beyond which they are almost constant. Unlike the sample of *Po,* the curves obtained for the *Ge* sample shows that the evaporation of the meniscus is not the same where large amount of meniscus remains even at high T_m. The difference between the variations of $F_{po}=f(T_m)$ for both samples can be related to the difference of thermal conductivity λ_s between samples and thus to the difference between their spreading resistances. Figure 4.2 shows a description of the probe-sample thermal system using a network of thermal resistances in series. R_{probe} describes the thermal diffusive resistance of the probe. The ballistic part of this last one is included in the contact thermal resistance $R_{contact}$ following a similar description of the one proposed by Gotsmann *et al.* [12]. As a reminder, Δ gives the temperature at the sample surface:

$$\Delta = \frac{T_{\text{sample surface}} - T_{amb}}{T_{apex} - T_{amb}} = \frac{R_s}{R_s + R_{contact}} \quad (4.2)$$

Figure 4.3 presents a schematic description of the variation of R_{sample} and Δ as a function of λ_s. The spreading thermal resistance R_s is inversely proportional to λ_s (see Chapter 1). For low values of λ_s, R_s dominates $R_{contact}$ whereas $R_{contact}$ is larger than R_s in the case of large values of λ_s. Therefore, the temperature at the sample surface is larger in the case of the polymeric sample. The numerical simulations through finite element analysis FEA performed by Tovee *et al.* [16] confirm our analysis. While working under ambient conditions, the temperature near the apex is almost the same of the heater in the case of samples of λ_s in the range of our sample of polyimide [16]. In the case of samples of λ_s in the range of the germanium sample , the temperature near the tip is closer to the ambient temperature [16].

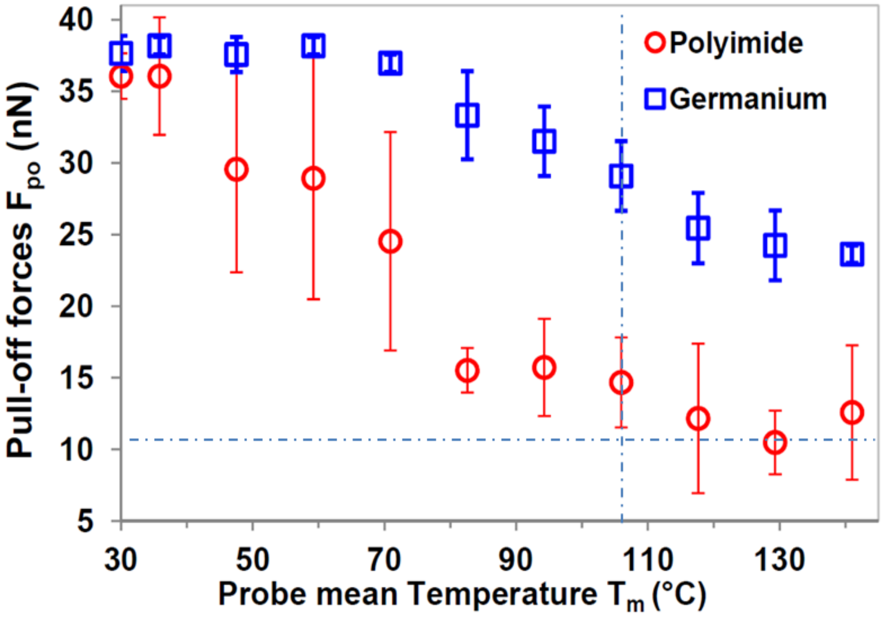

Figure 4.1. Variation of the pull-off forces as a function of the probe mean temperature for the contact between KNT probe and samples of Po (red circles) and Ge (blue squares).

Through the variation of the pull-off forces (see Figure 4.1), we can notice that the measurement dispersion in the case of sample of Po is larger than those obtained in the case of the sample of Ge. That might be related to the difference of roughness of the two samples. The roughness parameters of the Po and Ge samples are respectively: R_{ar}= 5 nm; R_{p-p}=57 nm and R_{ar}= 0.7 nm; R_{p-p}=4.75 nm. A similar effect was found in the measurements with the Wollaston wire (see chapter 2).

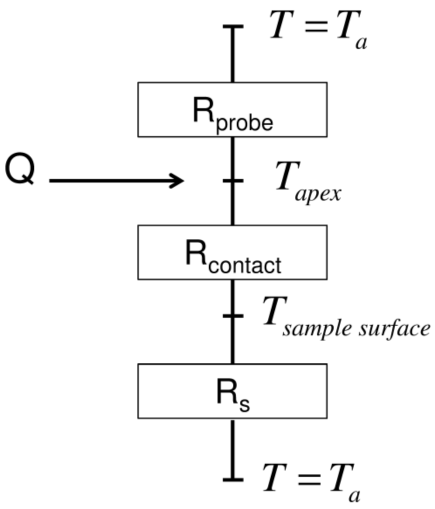

Figure 4.2. Network of thermal resistance in series as a description of the probe-sample thermal system.

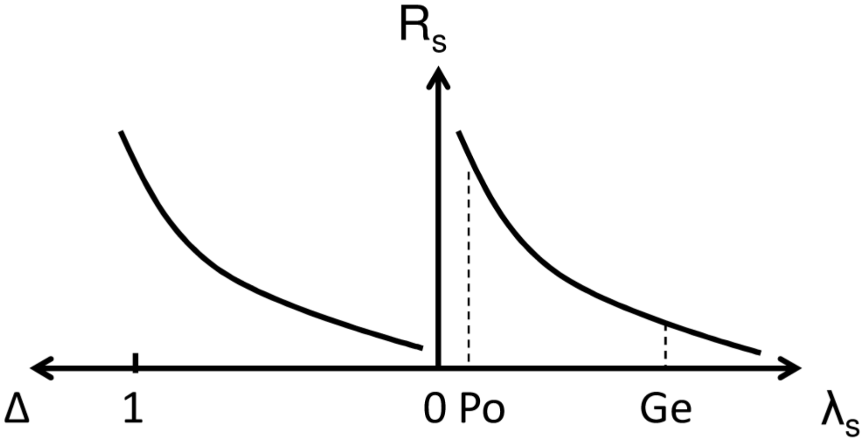

Figure 4.3. Schematic description of the variation of R_{sample} and Δ as a function of λ_s.

The methodology used in chapter 2 to estimate the thermal conduction through water meniscus is used again here. As a reminder, the total thermal conductance of the water meniscus can be expressed as:

$$\frac{1}{G_{total}}=\frac{1}{G_{probe-meniscus}}+\frac{1}{G_{meniscus}}+\frac{1}{G_{meniscus-sample}} \quad (4.3)$$

The thermal conductance through meniscus tends to a large value as the probe contacts the sample (see Equation (1.30)). The determination of $G_{probe\text{-}meniscus}$ and $G_{meniscus\text{-}sample}$ requires the determination of the meniscus dimensions. The small radius of curvature r_1 is determined through the Kelvin Equation (see Equation (2.5)). Based on what was stated above (see Equation 4.2), the temperature of the meniscus is supposed equal to T_m in the case of Po and to $(T_m + T_a)/2$ in the case of Ge in this Equation. The apex radius and the meniscus largest radius $r_2=f(T_m)$ are respectively deduced from the equations of the capillary forces F_{cap}: Equations (2.6) and (2.7). We suppose that the pull-off forces at high T_m in the case of Po $F_{po}(T_{m,max}, \mathrm{Po})$ are mainly due to the elastic forces. Therefore, $F_{cap}=f(T_m)$ for both samples are deduced as follows:

$$F_{cap}(T_m)=F_{po}(T_m)-F_{po}(T_{m,max},\mathrm{Po}) \quad (4.4)$$

The radius of apex R_a estimated is around 25 nm (Equation 2.6). This is close to the values estimated for this probe (~ 50 nm [16]). We note that different force-distance curves were performed using different probes at ambient temperature on a sample of Ge. The capillary forces at T_a varied between 30 and 90 nN. Based on our estimation methodology using Equation (2.6), the tip apex radius R_a can vary from 20 nm to 70 nm for these probes. These data are close to the estimated values (~ 50 nm [16]).

Figure 4.4 shows the variations of the meniscus radius r_2 as a function T_m for the two samples of Po and Ge. It can be said that the possible resolution achieved for these variations with the KNT probe is on the nm range.

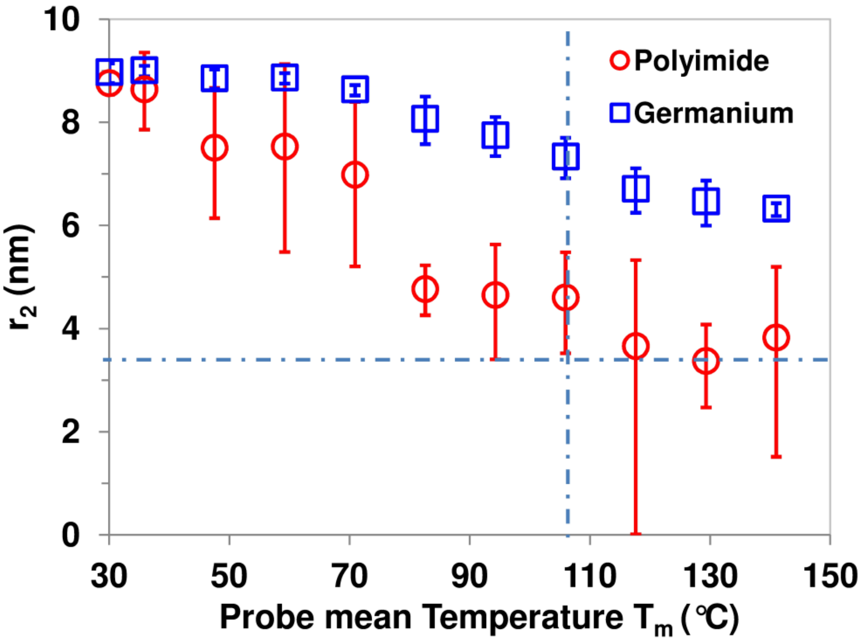

Figure 4.4. Variation of the larger radius r_2 of the meniscus as function of the probe mean temperature T_m for the contact between KNT probe and samples of Po (red circles) and Ge (blue squares).

Figure 4.5 shows the total thermal conductance of the water meniscus $G_{total,\ meniscus}$ as a function of T_m for the two samples of Po and Ge. As it will be seen later in this chapter, these values are much smaller than the values of the heat conduction through air. Moreover, our study validates the approach of Shi and Majumdar [60] in quantifying the thermal conduction to the sample through the water meniscus. In their study, the tip radius was around 45 nm and $G_{total,\ meniscus}$ was estimated around 6.7 nW.K^{-1} [60]. This is in the range of our estimated values (see Figure 4.4). However, the temperature of the heated sample in the study of Shi and Majumdar is missing and should have been specified [60].

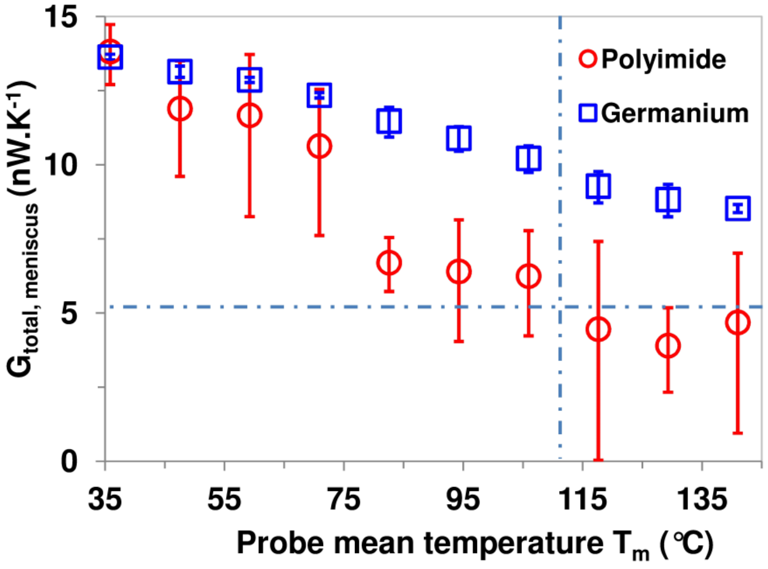

Figure 4.5. Variation of the total thermal conductance of water meniscus G_{total} as function of the probe mean temperature T_m for the contact between KNT probe and samples of Po (red circles) and Ge (blue squares).

4.1.2 Thermal conduction through the solid-solid contact:

Working under ambient conditions makes it difficult to distinguish between the thermal conduction through air and through the mechanical contact. In order to quantify the thermal conduction through the solid-solid contact and to study the heat transport at the tip-sample interface, it is preferable to work under vacuum conditions [44]. Under these conditions, we assumed that the heat transfer through radiation to the sample is basically small compared to the conduction at the mechanical contact [44, 114]. In order to quantify the thermal conductance at the solid-solid contact G_{ss} between the KNT probe and the sample, measurements at P=0.28 mbar were performed. At this pressure, we supposed that the heat conduction through air to the sample and environment are negligible based on SThM measurements of Chapuis [27].

Since the temperature field within the probe is yet unknown, we have supposed in a first approach that only the extremity of the probe is heated. The supports of the resistive part are assumed to be heat sinks and the Pd/Si_3N_4 part of the probe to be thermal fins [28]. The total electrical resistance of the probe at T_a is 365 Ω. Based on discussions with the fabrication group of this probe, the electrical resistance of the Pd wire at the probe extremity is around 150 Ω. The remaining electrical resistances are linked basically to the Ni/Cr resistors and Au pads.

At first, the probe thermal conductance G_p is required to quantify G_{ss} based on experimental measurements. Through the Wheatstone bridge with its feedback and the signal measured (see Appendix A), G_p can be calculated using Equation (3.2). The temperature coefficient of the electrical resistivity of the Pd wire is $\beta_{Pd} = 1.37 \times 10^{-3}$ as discussed in the section 4.1. Figure 4.6 shows the variation of G_p as a function of the probe mean temperature T_m (°C). These variations are similar to those obtained with the Wollaston probe and related to the heat sink boundary conditions taken at the supports of the Pd wire as discussed in Chapter 3.

Two samples of germanium Ge and silicon Si were used in the measurements of G_{ss} (R_{ar}= 0.28 nm; $R_{p\text{-}p}$=1.85 nm for Si and R_{ar}= 0.7 nm; $R_{p\text{-}p}$=4.75 nm). The measurements were performed at $T_m \simeq$ 67 °C (G_p = 2.07 µW.K^{-1} as shown in Figure 4.6) and at P=0.28 mbar. Figure 4.7 shows the measurements of the thermal signal $\Delta P/P_c$ for the two samples. The model of $\Delta P/P_c$ is given in chapter 3 as a function of the three conductances: G_p, G_{ss} and the sample conductance G_s given as:

$$G_s = 4K_1\lambda_s a_c \quad (4.5)$$

where K_1 = 0.694 [114].

The radius of the contact a_c can be determined through the DMT (Derjaguin, Muller and Toporov) model (see Chapter 1). Through force-distance curves, the estimated applied force F_N is around 20 ± 5 nN and the adhesive force component for this probe on both samples is around 75 ± 5 nN. The estimated radius a_c is around 3 nm. However, this value does not explain the measurements of $\Delta P/P_c$ (see Equation 3.4). A similar issue was noticed by Pettes and Shi [114] where the SThM measured signal could not be explained by a contact radius of few nm estimated through the DMT model. In their study, the contact was between a silicon tip ($R_a \simeq$ 60 nm) and a silicon substrate [114]. The issue is linked to the critical information about the contact [114]. The contact appeared to be made in a zone where the contact radius is similar to the radius of the tip apex [114]. In our case, the contact is made between the Si_3N_4 substrate of the probe with the sample surface based on discussion with fabrication group. Through the measurement of the capillary forces for this probe, the apex radius of our probe is around 50 nm. This value is close to the value of the Si tip of Pettes and Shi [114]. If we assumed our a_c to be around 50 nm, therefore the estimated values of G_{ss} for Ge and Si samples are respectively 0.67 ± 0.04 µW.K^{-1} and 0.44 ± 0.06 µW.K^{-1}. These values are in the same order of magnitude of those obtained by Pettes and Shi (G_{ss} = 0.66-2 µW.K^{-1} [114]). The values of G_{ss} are smaller than those linked to the conduction through air. The thermal boundary resistance R_b can be estimated through the Equation (3.6) where the interface is assumed as a site for phonon scattering [33, 114]. The obtained values of R_b for the tip-sample contact for Ge and Si samples are respectively $1.15 \pm 0.1 \times 10^{-8}$ $m^2.K.W^{-1}$ and $1.75 \pm 0.25 \times 10^{-8}$ $m^2.K.W^{-1}$. These values lie in the range of values reported in the scientific literature for R_b ($2 \times 10^{-9} - 5 \times 10^{-8}$ $m^2.K.W^{-1}$) [12, 33, 118, 121, 122]. In the section 4.3 of this chapter, we discuss a way allowing the identification of the transmission coefficient at the tip-sample interface from our values of R_b.

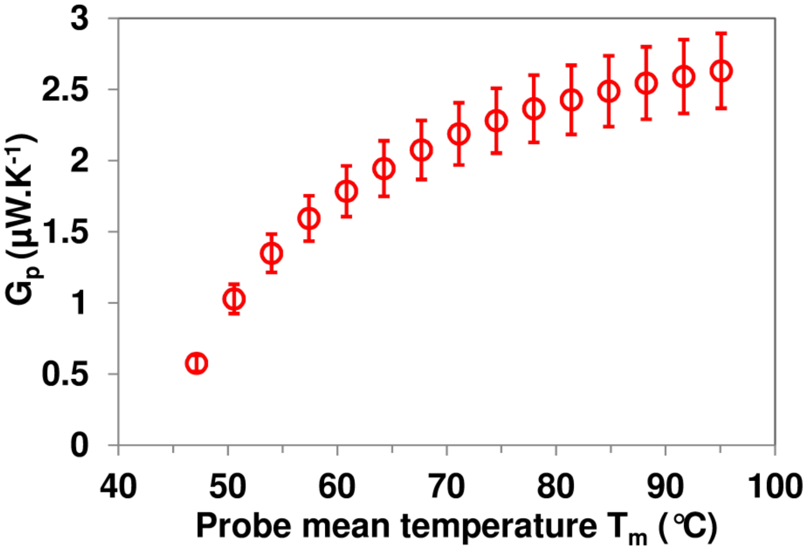

Figure 4.6. Thermal conductance of the probe as a function of the probe mean temperature T_m (P=0.28 mbar, T_a=30 °C).

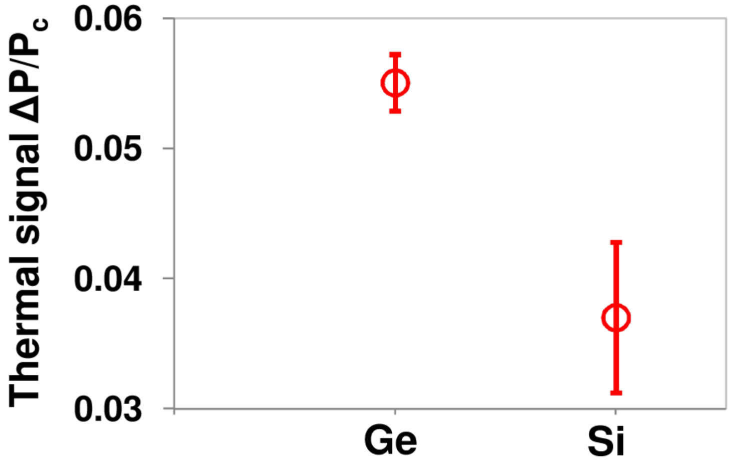

Figure 4.7. Thermal signal $\Delta P/P_c$ for the two samples of Ge and Si (P = 0.28 mbar, T_a = 30 °C).

4.1.3 Thermal conduction through air

In order to quantify the parameters of the thermal conduction through air G_{air} and b_{air}, measurements of the thermal signal $\Delta P/P_c$ as a function of the sample thermal conductivity λ_s were performed under ambient conditions (T_a=30 °C, RH= 40 %).

Since the thermal conductance of the probe G_p changes as a function of T_m (see Figure 4.6), the thermal signal $\Delta P/P_c$ was measured as a function of T_m for a sample of germanium. Figure 4.7 shows the variation of $\Delta P/P_c$ as a function of T_m. The tendency shown by the curve $\Delta P/P_c=f(T_m)$ is similar to the one obtained with the Wollaston wire as discussed before and seen in chapter 3.

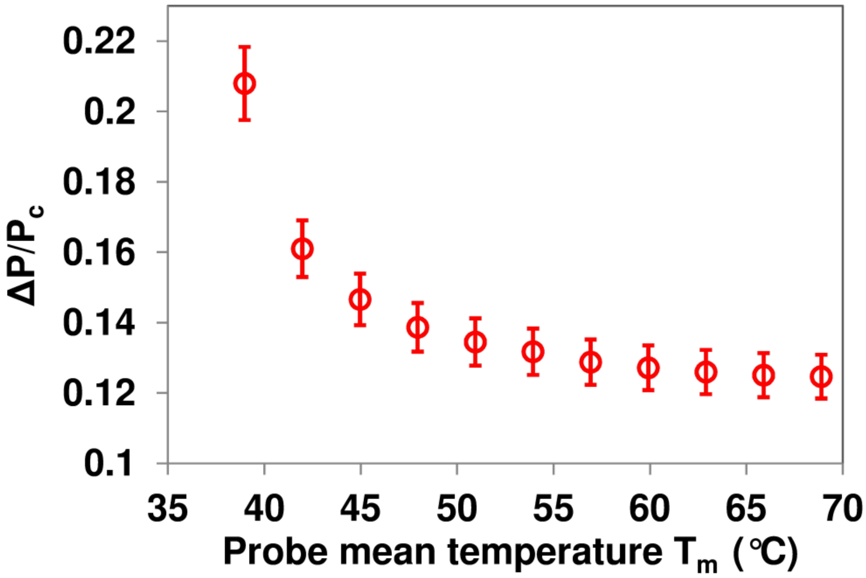

Figure 4.8. Thermal signal $\Delta P/P_c$ as function of the sample thermal conductivity λ_s (T_a=30 °C, *RH*= 40 %).

Two kinds of measurements of $\Delta P/P_c=f(\lambda_s)$ at two different temperatures T_m were performed.. The reference samples used in these measurements are the same already used in this chapter and Chapter 3. Figure 4.9 gives the curves $\Delta P/P_c=f(\lambda_s)$ for T_m= 40 °C and T_m=65 °C. It shows that the sensitivity of the KNT probe to the sample thermal conductivity is limited to a maximum limit around a few W.m^{-1}.K^{-1} for the used experimental conditions.

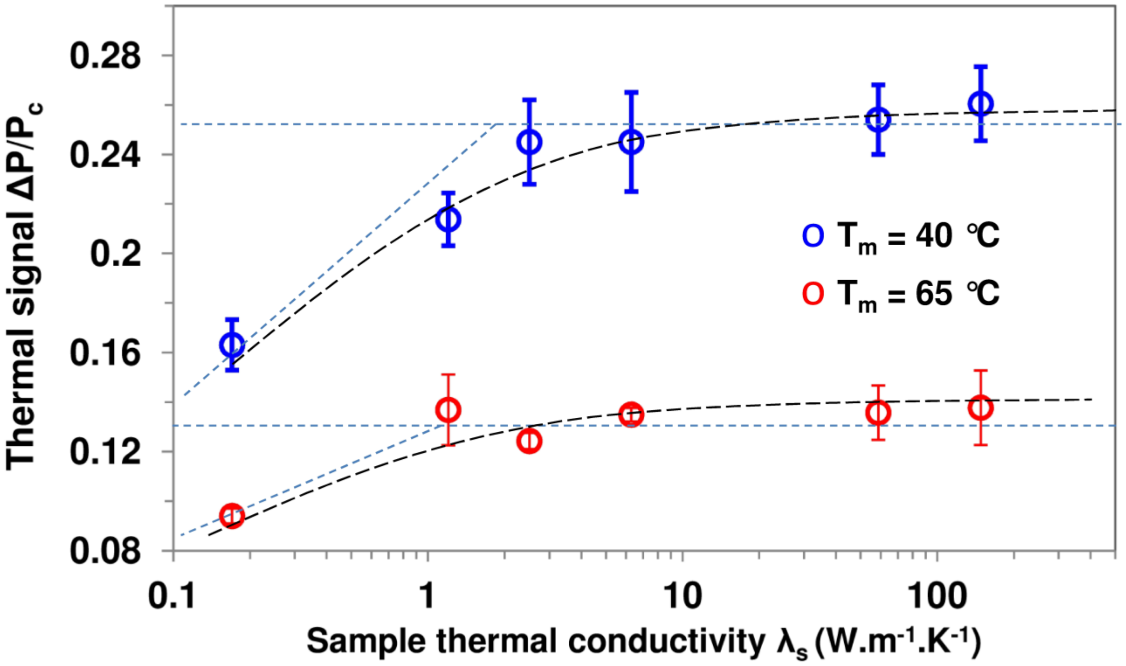

Figure 4.9. Thermal signal $\Delta P/P_c$ as function of the sample thermal conductivity λ_s for T_m= 40 °C (blue circles) and T_m= 65 °C (red circles) (T_a=30 °C, RH= 40 %).

The model $\Delta P/P_c$ described in chapter 1 (part 1.2.1) was used here to determine the effective values of G_{air} and b_{air}. The values of G_p and $G_{total,meniscus}$ are the ones determined in Figures 4.5 and 4.6. Based on our measurement of the solid-solid thermal conduction (see last section), the mean value of 0.5 µW.K^{-1} was taken for G_{ss}. The values of the heat losses through conduction to the environment h are taken equal to 7000 W.m^{-2}.K^{-1} as identified by Puyoo for this probe [28]. The mean values of G_{air} and b_{air} were extracted from $\Delta P/P_c$ measurements for the samples of polyimide Po (0.17 W.m^{-1}.K^{-1}) and silicon dioxide (1.2 W.m^{-1}.K^{-1}). Table 4.1 presents the values determined of G_{air} and b_{air}. At T_m= 40 °C, the mean values of b_{air} and G_{air} are respectively 2.72 µm and 0.57 µW.K^{-1} whereas at T_m=65 °C, b_{air} and G_{air} are respectively 4 µm and 1.45 µW.K^{-1}. As we can notice, the values determined for b_{air} and G_{air} at two probe mean temperatures are respectively micrometric and around 1 µW.K^{-1}.

Table 4.1. Thermal interaction parameters G_{air} and b_{air} determined for two different temperatures.

T_m	b_{air} (µm)	G_{air} (µW.K^{-1})
40 °C	2.72 ± 0.5	0.57 ± 0.4
65 °C	4 ± 0.3	1.45 ± 0.3

As expected for this small tip, the values of the effective parameters G_{air} and b_{air} are smaller than the values determined for the Wollaston wire probe shown in chapter 3 for the same range of λ_s (b_{air}= 25 µm and G_{air}= 5.5 µW.K^{-1}). For the KNT probe, the values of the total conductance water meniscus $G_{total,meniscus}$ is also much smaller than G_{air} (see Figure 4.5). However, the value of the solid-solid conductance G_{ss}, which are close to those of the conduction through air, cannot be neglected while describing the heat transfer between this probe and the sample.

A 3D model is needed to map the temperature field within the probe to determine more accurately the probe-sample interaction through the different heat transfer mechanisms.

4.2 Study of the probe-sample thermal system with doped silicon (DS) probes:

4.2.1 Thermal conduction through the water meniscus

The details about the geometry of the DS probes are discussed in chapter 1. The DS probe here used is the AN-300 type. For this probe, the difficulty in estimating the temperature of the tip apex is due to the positioning of the heater. In fact, the heater is not positioned at the tip extremity but above the tip. Therefore, the determination of the tip temperature includes the determination or measurement of the heater temperature and afterwards the modeling of the heat transfer through the tip (diffusive and ballistic – see chapter 1) in order to determine the apex temperature.

In this part, the conduction through the water meniscus between the DS probe and sample is studied on polymeric samples. In order to determine the apex temperature, we used three references samples of polymers of well-known melting temperatures as listed in Table 4.2 (Anasys Instruments). The calibration of the apex temperature is obtained from measurements of the cantilever deflection performed on these polymers as shown in Figure 4.9. This technique is called the Local Thermal Analysis (LTA). It consists on monitoring the cantilever deflection during a controlled fast heating while the tip remains in contact with the surface. The drop of the deflection signal is a sign of the melting of the polymer (see Figure 4.10). The corresponding heating voltage at the deflection drop corresponds then to the melting temperature of the polymer. The heating is made by the NanoThermal Analyzer (NanoTA2) system of Anasys Instruments. More information can be found in appendix A. The uncertainty linked to the calibration of the tip apex with such polymers remains very small. This is due to the fact that the spreading resistance for polymers R_{sample} is much larger than the thermal resistance of contact $R_{contact}$ [12]. Following Equation (4.2), the temperature at the tip apex is almost the same at the polymer surface. Figure 4.11 shows the heating voltage as a function of the apex temperature. For an accurate calibration, the apex temperature is calibrated between two consecutive melting temperatures.

Table 4.2. List of the reference polymers with their corresponding melting temperatures. (reference Anasys instruments).

Reference polymer	Melting temperature (°C)
Polycaprolactone PCL	55 °C
Polyethylene PE	116 °C
Polyethylene terephthalate PET	235 °C

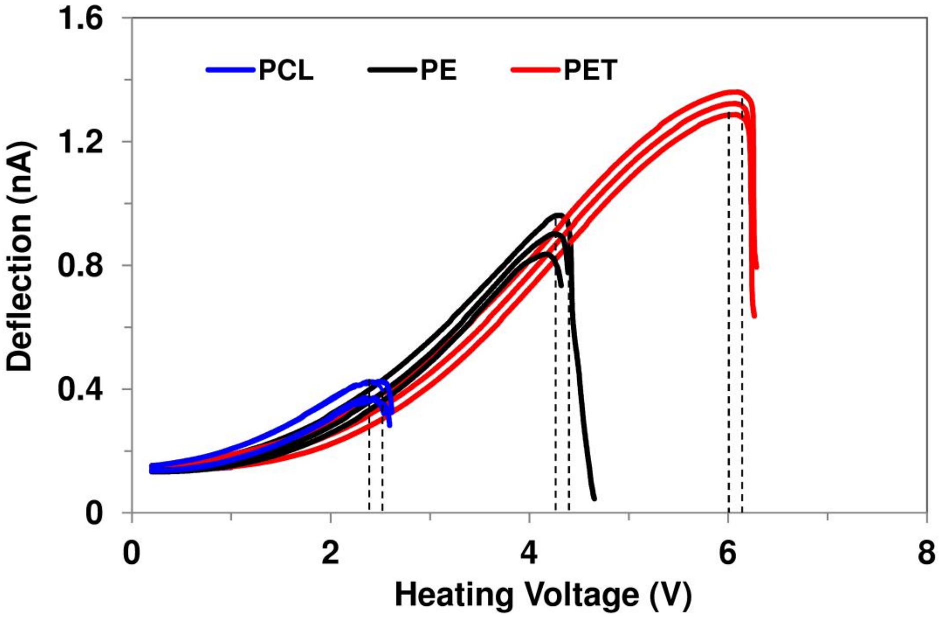

Figure 4.10. Monitoring the probe cantilever deflection as a function of the probe heating voltage of the three reference polymers.

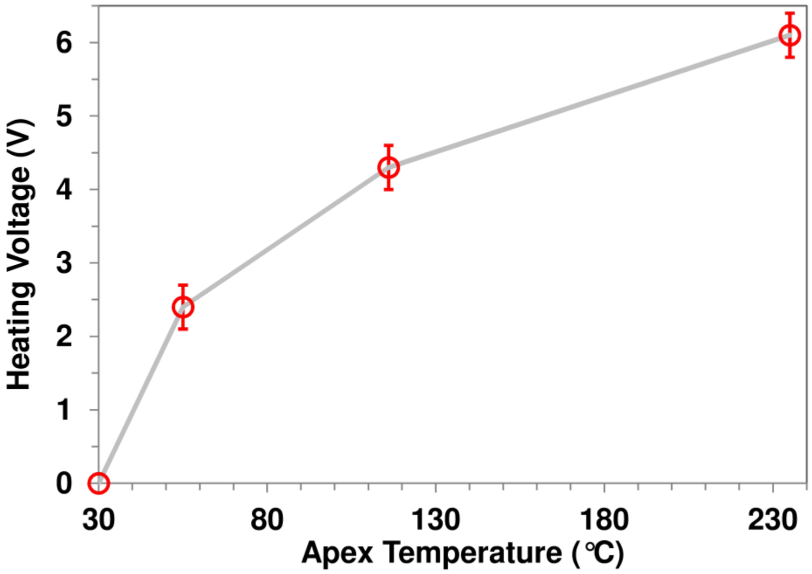

Figure 4.11. Heating Voltage (V) as a function of the apex temperature (°C).

Based on our calibration, a polymeric sample of hydrophilic polyimide Po (R_{ar}= 5 nm; R_{p-p}=57 nm) was used to study the conduction through water meniscus between the DS probe and the sample. We followed the same procedure used to study this heat mechanism for the Wollaston probe (see chapter 2) and the KNT probe (section 4.1 in this chapter). The spring constant of the AN-300 probe is around 0.35 N.m^{-1} [16]. Figure 4.13 shows the variation of the pull-off forces F_{po} as a function of the apex temperature. The pull-off forces decreases progressively until an apex temperature limit beyond which they become almost constant. The large error bars (specifying the dispersion of measurements) are due to the roughness of the sample as noticed before in the case of the Wollaston probe and the KNT probe. Greiner *et al.* [113] performed measurements of F_{po} under ambient conditions as a function of the heater temperature for a contact between the same kind of probe and a SiO_2 sample as seen in Figure 4.13. The limit reached by these measurements is close to our limit as shown in Figure 4.13 (≃ 25 nN). The radius of the apex R_a for the used DS probe was estimated around 45 nm. This is in good agreement with the reported values of R_a of these probes (≃ 50 nm) [16]. Figure 4.14 presents the variations of the largest radius of meniscus r_2 as a function of the apex temperature T_{ap}. These values are in the range of the determined values for the KNT probe (see Figure 4.4). Figure 4.15 shows the variation of the total conductance of the water meniscus G_{total} as a function of T_{ap}. These values of are at least one order of magnitude smaller than the values of the solid-solid conductance G_{ss} reported for this type of probes (G_{ss} ≃ 0.5 µW.K^{-1} [12, 45]).

As a conclusion, whatever the probe is, the water meniscus does not play a dominant role in the probe-sample thermal interaction.

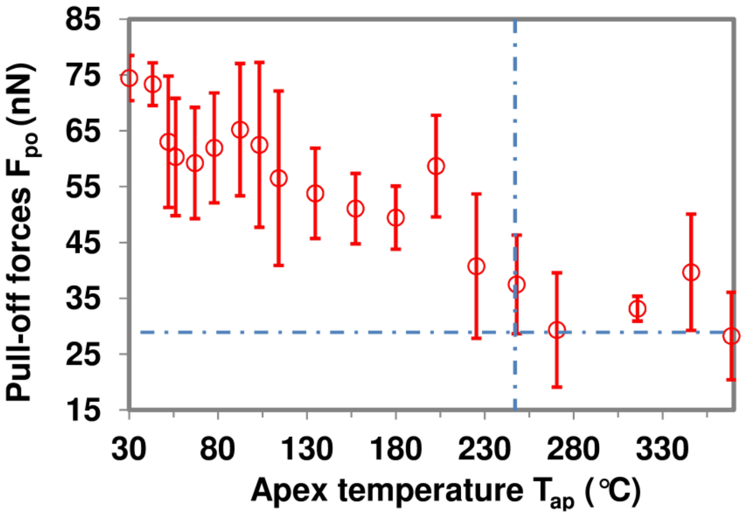

Figure 4.12. Pull-off forces F_{po} as a function of the apex temperature T_{ap} for a contact between the DS probe (AN-300) and Po sample (T_a=30 °C, RH= 40 %).

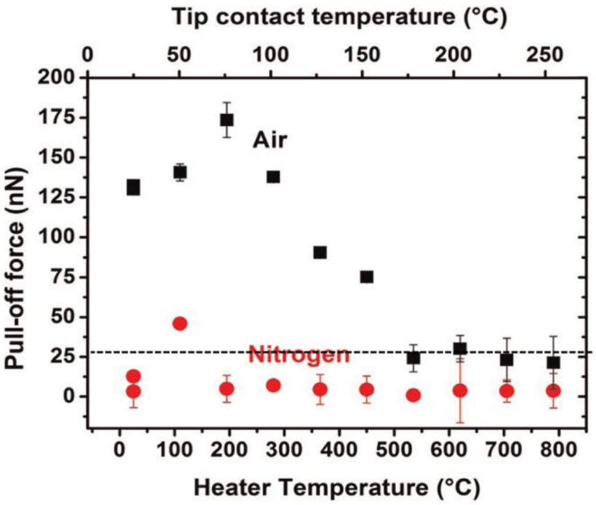

Figure 4.13. Pull-off forces F_{po} as a function of the heater temperature for a contact between the DS probe (AN-300) and silicon dioxide SiO_2 sample [113].

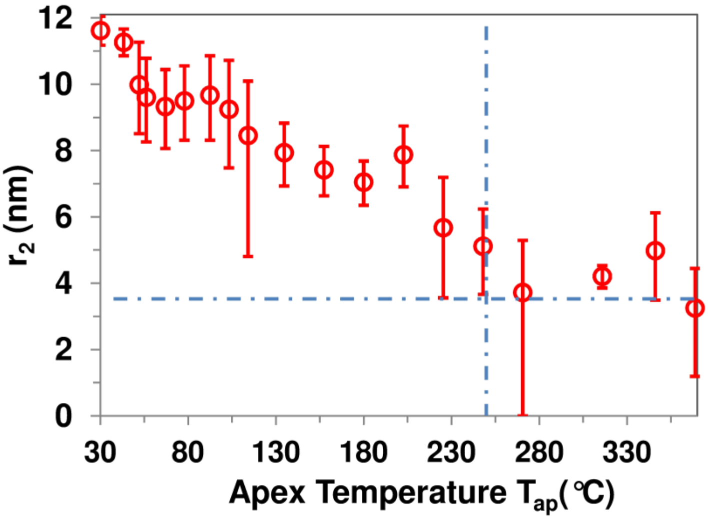

Figure 4.14. Variation of the larger radius r_2 of the meniscus as function of the apex temperature $T_{ap}$for the contact between DS probe and sample of Po (T_a=30 °C, RH= 40 %).

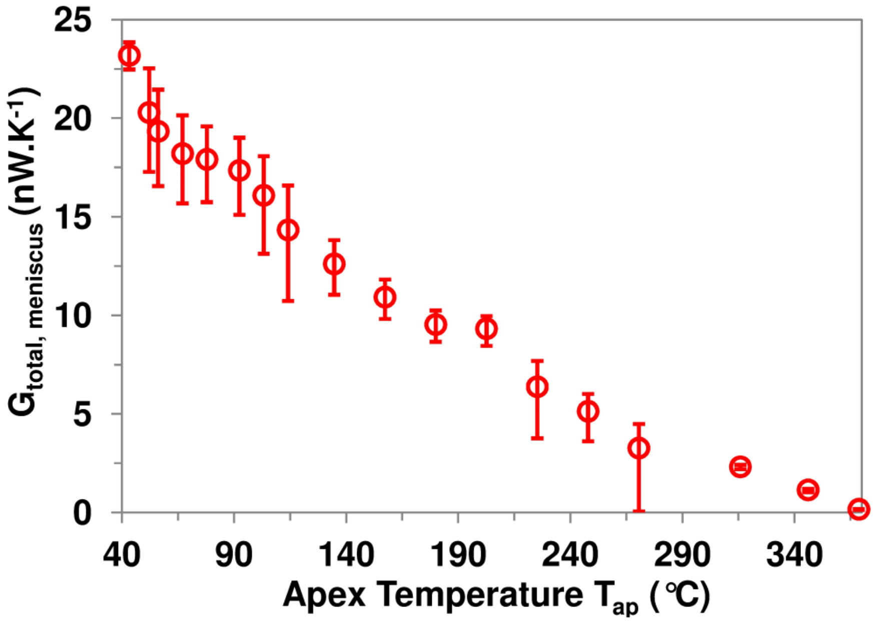

Figure 4.15. Variation of the total thermal conductance of water meniscus $G_{total,\ meniscus}$ as function of the apex temperature T_{ap} for the contact between DS probe and sample of Po (T_a=30 °C, RH= 40 %).

4.3 Determination of the transmission coefficient at interfaces from SThM measurements

SThM has been recently an experimental tool used to determine the phonon transmissivity t_{ij} at interfaces [58, 114]. The evaluation of the transmissivity requires the determination of the thermal contact resistance at the tip-sample interface [58, 114]. As seen in this chapter and in Chapter 3, it is preferable that the experiments are performed under vacuum conditions where the conduction through air is eliminated.

When the two sides are insulators or semi-conductors, the thermal boundary resistance R_b is linked to the phonon interaction and R_b is noted as R_{bp} [117]. This is the case of our contact between the KNT probe (Si_3N_4) and samples of germanium and silicon. If at least one side is a metal, the electrons-phonons interaction should be then taken into account in R_b. In this case, the phonons in the metal transmit their energy to the electrons [127] and R_b can be assumed to be the sum of the phonon-electron interaction in the metal and phonon-phonon interaction between the two materials [117, 122]: $R_b = R_{bp} + R_{be}$. R_{be} is the thermal boundary resistance linked to the phonon-electron coupling. This is the case between our Wollaston probe and samples of MICA, germanium and silicon (see Chapter 3).

There are two models that have been used widely to evaluate t_{ij}: the acoustic mismatch model (AMM) and the diffuse mismatch model (DMM) [116, 117]. The AMM model assumes that scattering at interfaces is totally elastic. It means that the transmission and reflection of phonons occur at the same frequency as the incident phonon. In the DMM model, the reflection coefficient r_{ji} in a material is equal to the transmission t_{ij} from the other material [116]. Based on the energy conservation principle, $t_{ij}= 1 - t_{ji}$ [116]. The AMM model appears to be more appropriate to be used at low temperatures while the DMM model is more used at temperatures higher than the ambient [116, 117]. Therefore, we used the DMM as a model to estimate t_{ij} from our experimental results.

Following the phonon dispersion of both materials in contact, the transmission coefficient from material (1) to material (2) t_{12} is expressed in the DMM model as [116]:

$$t_{12} = \frac{C_{pa,2} v_{pa,2}}{C_{pa,1} v_{pa,1} + C_{pa,2} v_{pa,2}} \quad (4.7)$$

where C_{pa} and v_{pa} are respectively the heat capacity and group velocity of acoustic phonons.

The thermal boundary resistance linked to phonons R_{bp} is expressed as [116]:

$$R_{bp} = \frac{4}{t_{12} C_{pa,1} v_{pa,1}} = \frac{4}{t_{21} C_{pa,2} v_{pa,2}} \quad (4.8)$$

In the case of contact between the KNT probe and nonmetallic samples ($R_b = R_{bp}$), t_{12} can be calculated directly from our measurements. C_{pa} and v_{pa} can be calculated using the phonon dispersion relation for Ge and Si found respectively in Refs. [128] and [129]. The coefficient t_{12} was found to be of 0.62 ± 0.03 for KNT/Ge contact and 0.9 ± 0.015 for KNT/Si contact.

To evaluate t_{12} in the case of the contact between the Wollaston and samples, we need to distinguish first between R_{bp} and R_{be}. R_{be} can be expressed as follows [127]:

$$R_{be} = \sqrt{\frac{1}{G_{ep} \lambda_{pp}}} \quad (4.9)$$

where G_{ep} ($W.m^{-3}.K^{-1}$) and λ_{pp} are respectively the volumetric phonon-electron coupling constant and the phonon thermal conductivity in the Pt/Rh wire. The information about λ_{pp} is in general difficult to find for metals where the heat conduction is dominated by electrons [117]. In our case, the evaluation of t_{12} requires also the phonon dispersion of Pt/Rh.

The procedure followed in this study can be applied especially for the DS and KNT probes where the phonon dispersions of the probes materials are available. The experiments can be performed on different materials of acquired phonon dispersion in order to evaluate the phonon transmission at the tip-sample interface.

4.4 Conclusion

In this chapter, the probe-sample heat transfer was studied using two different probes with tips of nanoscale curvature radius.

As for the Wollaston probe, the meniscus conductance was determined as a function of the probe temperature for the KNT probe. The thermal conduction through water meniscus appears to be negligible in front of the heat conduction through air for this probe. Our results are in good agreement with the ones of previous approaches. They consolidate and validate them.

Experimental measurements were performed under vacuum conditions on two samples of germanium and silicon. Based on these measurements, the heat conductance through the solid-solid contact and the thermal boundary resistance was determined for both the samples ($1.15 \pm 0.1 \times 10^{-8}$ m^2.K.W^{-1} for KNT/Ge and $1.75 \pm 0.25 \times 10^{-8}$ m^2.K.W^{-1} for KNT/Si). The results are in agreement with the values reported in scientific literature.

Under ambient conditions, tendencies of the thermal signal as a function of the probe mean temperature similar to those seen with the Wollaston probe were observed. The curves of the thermal conductivity calibration show that the sensitivity of the KNT probe is limited to a maximum value of λ_s around a few W.m^{-1}.K^{-1}. From this curve, the thermal interaction parameters of the conduction through air were evaluated. It appears that the conduction through air is the dominant heat mechanism in the heat transfer between the probe and the sample but the solid-solid heat conduction is not negligible in the heat transfer contrary to the case of the Wollaston probe. Using the doped silicon probe, the heat conduction through water meniscus to a sample of polyimide was determined. The apex temperature was calibrated using different polymers of known melting temperatures. The heat conduction through the meniscus is also negligible in front of the values of the heat conductance through solid-solid contact reported in the literature.

The last part of the chapter was dedicated to the investigation of the phonon transmission at interfaces based on the evaluation of the boundary resistance through SThM measurements. The DMM model can be used to determine the transmission coefficient at the tip-sample interface. The transmission coefficient was determined in the case of the contact between KNT probe and our nonmetallic samples. In the case of the Wollaston wire, the electron-phonon should be taken into account as a part of the thermal boundary resistance to evaluate the phonon transmission coefficient. Another parameter that should be taken in the evaluation is the roughness of both the probe and the sample.

Chapter 5

Development of a technique for investigation of thermal properties of solid materials at temperatures above the ambient

This chapter describes the development of a technique that should allow in short terms the measurement of the thermal properties of anisotropic thin solid films at different levels of temperature above the ambient. The technique uses a set of deposited resistive wires. Before exposing the originality of the proposed technique by giving its principle, a review of the methods that involve deposited wires on the thin film to be characterized is given. Then the work of modeling carried out to design the setup for a simple reference sample in the frame of a first step of validation of the proposed method is described. The setup, the measurements and results obtained for this reference sample are discussed. To finish the chapter, some results of numerical simulations are used to estimate the potentiality of the method to determine the in-plane and cross- plane components of the thermal conductivity of anisotropic samples.

5.1 Main thermal techniques using deposited resistive heater and probe

The AC methods are the most used nowadays among the deposited wires techniques. The reason is that DC techniques give measurements with large equilibrium time and are more dependent on the thermal resistances at the substrate boundaries [130, 131]. The first technique of this type for measuring the thermal properties of bulk materials was developed by Cahill [25] and called the “3ω method”. In practice, a long metallic wire of finite width $2b_w$ and length l is deposited on the substrate surface as illustrated in Figure 5.1. The wire is heated with an alternating current I of magnitude I_{ac} at angular frequency ω=2πf. The principle of the electrical measurement has already been described in Chapter 1.

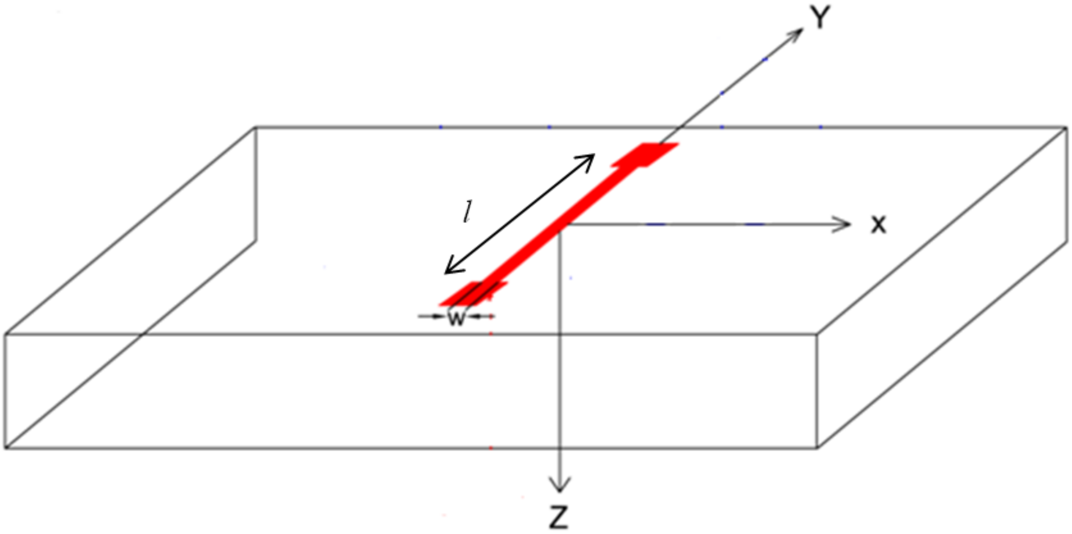

Figure 5.1. Schematic of 3ω method where a metallic wire (heating wire) is deposited on the sample to be characterized.

In the material, the conductive diffusion of the AC heating produces a continuous temperature variation called θ_{DC} and alternating temperature oscillations at angular frequency 2ω called $\theta_{2\omega}$.

As reminder, the third harmonic voltage of the wire $V_{3\omega}$ can be linked to the properties of the material through the expression of the harmonic temperature $\theta_{2\omega}$, as:

$$V_{3\omega} = \frac{R_0 \beta I_{ac} \theta_{2\omega}}{2} \cos(3\omega t + \phi) \quad (5.1)$$

where R_0 is the electrical resistance of the wire at ambient temperature and β is the temperature coefficient of the electrical resistivity of the wire.

α and μ are respectively the thermal diffusivity of the sample and the thermal diffusion length in the sample material and given as:

$$\alpha = \frac{\lambda_s}{d_0.C} \quad (5.2)$$

and

$$\mu = \sqrt{\frac{\alpha}{2\pi f}} \quad (5.3)$$

where λ_s, d_0, and C are the sample thermal conductivity, density, and heat capacity respectively.

In the case of a homogeneous and isotropic bulk material that can be described as a semi-infinite substrate and for $\mu >> b_w$, the alternating temperature $\theta_{2\omega}$ at the heater can be expressed as:

$$\Delta T_{2\omega,s} = -\frac{P_{rms}}{2\pi\lambda_s}(\ln(2\omega) + \ln(\frac{b_w}{\alpha}) - 2c) - i\frac{P_{rms}}{4\lambda_s} \quad (5.4)$$

where c is a constant equal to 0.9228 [132] and $P_{rms} = \frac{RI_{ac}^2}{2l}$ is the power per unit heater length [25]. In order to perform measurements at different levels of temperatures and to eliminate the effects of radiation, the samples were placed in specific cryostats and the measurements performed from 30 to 750 K [25].

Later, Cahill *et al.* [133] extended the measured 3ω method to measure the cross-plane thermal conductivity $\lambda_{\perp f}$ of thin films with a thickness of a few tens of nanometers. The heater width $w=2b_w$ is much larger than the film thickness d_f and the film is deposited on a substrate of high thermal conductivity. Then, the film can be described as a 1D thermal resistance. It can be shown that this thermal resistance, $d_f/\lambda_{\perp f}$, adds an additional second harmonic temperature to expression (5):

$$\Delta T_{2\omega,f} = \frac{P_{rms}}{\lambda_{\perp f}}\frac{d_f}{2b_w} \quad (5.5)$$

Here, the thermal conductivity of the substrate is obtained from the slope of the curve $\Delta T_{2\omega} = f(\omega)$ and the film thermal conductivity is calculated from the temperature drop through the film (Equation (5.5)). Let us note that the obtained thermal conductivity of the film is an average along the frequency interval. In this approach, the series of resistances must be known between the heater and the substrate. Kim *et al.* [134] noticed a variation of the estimated value of the substrate thermal conductivity that was linked to the thermal resistance between the heater and the film.

In this method, controlling the current frequency and thus the penetration depth allows us to eliminate the thermal resistance at the lower boundary of the substrate. The method was known later as the “slope method”.

Later, Borca–Tasciuc *et al.* [135] developed the differential method to determine the thermal conductivity components of anisotropic substrates and very thin films.

In the case of anisotropic semi-infinite substrate:

$$\Delta T_{2\omega} = \frac{-P_{rms}}{2\pi l\lambda_{s,y}}[\ln(2\omega)+\ln(\frac{b_w^2}{\alpha_{s,y}\lambda_{s,xy}})-2\,\mathrm{c}]-\mathrm{i}(\frac{P_{rms}}{4lk_{s,y}\sqrt{\lambda_{s,xy}}}) \quad (5.6)$$

where $\lambda_{xy}=\lambda_x/\lambda_y$, x and y refer to the in-plane and cross-plane directions respectively.

The case of an anisotropic film deposited on a substrate was also developed to study an eventual lateral spreading in the film. The measurement is performed in two steps:

- First, with the heater directly deposited on the substrate (S)

- Second, with the heater deposited on the film-substrate (f+S) system.

The thermal conductivity of the film can be calculated from the temperature rise [135]:

$$\Delta T_{2\omega,f} = \Delta T_{2\omega,f+S} - \Delta T_{2\omega,S} = \frac{P_{rms}d_f}{2b_w l\lambda_{f,y}} C_1 C_2 \quad (5.7)$$

where

$$C_1 = 1-\frac{\lambda_{f,x}\lambda_{f,y}}{\lambda_s^2} \quad (5.8)$$

and

$$S = \frac{2}{\pi}\int_0^{\infty}\frac{\sin^2\Sigma}{\Sigma}\frac{\tan(\Sigma C_3)}{[1+(\sqrt{\lambda_{f,y}\lambda_{f,x}}/\lambda_S)\tanh(\Sigma \mathrm{C}_3)]C_3}\,d\Sigma \quad (5.9)$$

and

$$C_3 = \sqrt{\lambda_{f,xy}}(\lambda_f / \mathrm{b}_w) \quad (5.10)$$

For the measurements of the in-plane thermal conductivity of thin films, Zhang and Grigoropoulos [136] were the first to develop the phase-shift method for the deposited wires. The method, which had been widely used before but with optical heating, consists of a heater deposited on the suspended thin film of interest as shown in Figure 5.2. In such configuration, the effects of the interface between the thin film and the substrate are avoided [136]. The suspended film is settled on two substrates that act as two thermal sinks. An alternating current is passed through the heater and a sensor at distance X from the heater is used to detect the attenuation of the thermal waves. Assuming 1D lateral heat conduction, $\Delta T_{2\omega}$ at a distance X from the sensor is [136]:

$$\Delta T_{2\omega}(X) = A_1\sqrt{\frac{\alpha_f}{2\omega}}e^{-\frac{X}{\mu}}e^{-i\frac{X}{\mu}-i\frac{\pi}{4}} \quad (5.11)$$

and

$$A_1 = \frac{P_{rms}}{4d\lambda_f} \quad (5.12)$$

where d is the thickness of the film. The variation of the frequency ω allows us to determine the thermal properties of the thin film ($\alpha_{//f}$, $\lambda_{//f}$). In this technique, one must pay attention to the radiation and convection losses that can affect the thermal measurements.

When the suspended film of interest is electrically conducting, it can be used as a heater and sensor too as studied Lu *et al.* [137] in the alternating regime. The thermal properties of the film are obtained solving the 1D heat conduction equation [137]. Bourgeois *et al.* [138] used the method of Lu *et al.* [137] to measure thermal conductance of silicon nanowires at low temperatures (less than 2 K). The same group studied the effect of the roughness of the nanowires surfaces on the thermal conductance of silicon wires at low temperatures [139].

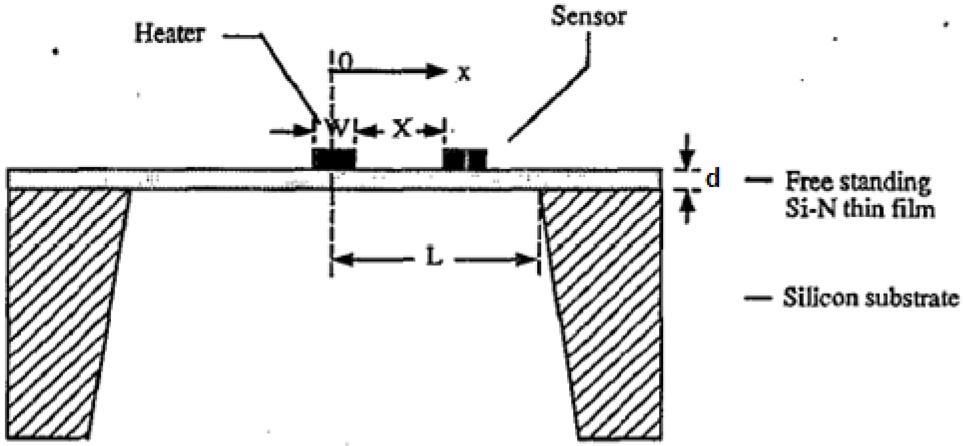

Figure 5.2. Schematic of the phase-shift method used by Zhang and Grigoropoulos [136].

Using a similar technique, Lui and Asheghi [140] performed measurements for the case of an insulating silicon film of interest in the temperature range of 300–450 K in the steady state regime. A metallic layer was deposited on the silicon film as the measurements were less consistent with heavily doped silicon substrates as mentioned by the authors [140]. The measurements were performed in two steps to ensure no current leakage through the silicon and to avoid the uncertainties of the metallic layers [140]:

- In the first step, with the suspended metallic heaters alone,

- In the second step, with the suspended metallic heaters covered with the film of interest.

We have to note that the configuration of suspended structures require a high level of precision during the micro-fabrication and for some types of films it is inconvenient or impossible [141].

Another method to determine the in-plane thermal conductivity of thin films is to use different heaters of different widths and each heater is subjected to harmonic heating. Ju *et al.* [142] used this technique to determine the thermal conductivity of anisotropic films of polyimide. Here, the alignment of molecular chains to the in-plane direction is the main source of anisotropy in polyimide films [142]. The cross-plane thermal conductivity can be determined in the case of a heater width that is much larger than the film thickness. The in-plane component can be determined in the case of a narrow heater as seen in the 3ω differential technique. Using this approach, Lui *et al.* [143] determined the thermal conductivity of anisotropic strained Si/Ge superlattices.

The same sample type was used by Jang *et al.* [144] to determine the in-plane thermal conductivity of encased graphene and ultrathin graphite. However, the configuration here consists of different sensors, of same length, deposited on the sample surface at different distances from the heater as shown Figure 5.3. For related applications (encased graphene layers devices), two insulating layers (ox in figure 5.3) surround the graphene of interest that have a high in-plane thermal conductivity [144]. In this case, the heat is spread laterally in the film of interest and down to the substrate [144].

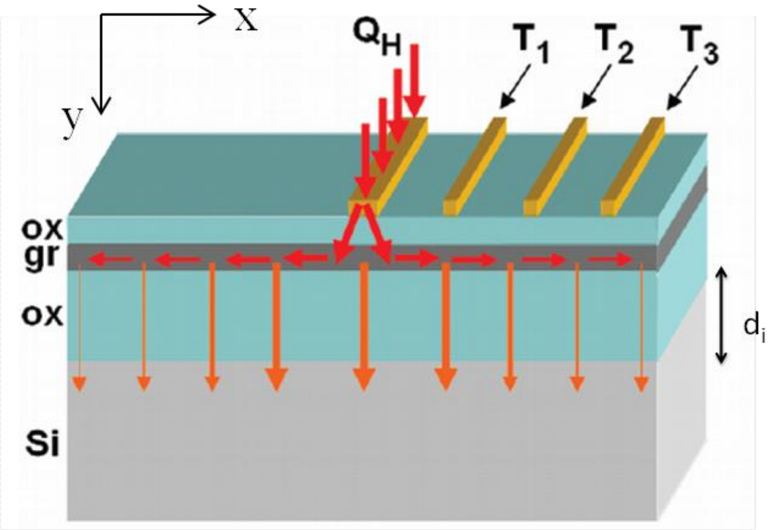

Figure 5.3. The configuration of the sample used by Jang *et al.* [144].

The in-plane thermal conductivity $\lambda_{f,x}$ is determined by measuring the attenuation of the temperature amplitude along the sample:

$$T_h - T_0 = \frac{Q_H}{2l}\sqrt{\frac{d_i}{\lambda_{i,y}\lambda_{f,x}d_f}}e^{-\frac{x}{\mu_1}} \quad (5.13)$$

where *i* denotes the lower insulating film and μ_1 is given as:

$$\mu_1 = \sqrt{\frac{\lambda_{f,x}d_f d_i}{\lambda_{i,y}}} \quad (5.14)$$

The measurements were performed at temperatures up to 300 K in a specific cryostat. As can be seen from the techniques listed above, we are able nowadays to determine the anisotropic thermal properties of thin films. One limiting factor while observing all the techniques is the heavy conditioning needed to perform measurements at different temperature levels. Moreover, the number of measurement at temperatures above the ambient is much smaller in comparison to measurements at low temperatures. All of the studies need a specific cryostat either to eliminate effect of air convection (or conduction) or to go down in temperatures or oven to go up in temperatures. Moreover, measurements in the alternating regime require a small current to avoid an additional heating of the substrate.

In this chapter, we describe a method and a technique inspired from the studies above to determine the anisotropic thermal properties thin films above ambient temperature. This technique allows us to avoid the need for a special conditioning for our sample of interest. We start by a 1D model that allows us to determine the in-plane properties of the film. Later, we give an analytical model that allows us to determine also the cross-plane properties of the same film. The factors that affect our studies in terms of loss through convection and radiation and thermal contact resistance(s) are also investigated.

5.2 Proposed method

5.2.1 General principle

Our sample consists of a deposited film on a substrate as shown in Figure 5.4. An array of parallel and long resistive wires is deposited on the front surface and back surface of the sample. One of the resistive wires (in red in Figure 5.4) is heated with an alternating current I of magnitude I_{ac} at angular frequency $\omega=2\pi f$. This wire is the thermal source for the sample. The heating produces a continuous temperature ΔT_{DC} and alternating temperature oscillations $\Delta T_{2\omega}$. The other wires are the probing wires. The information about the thermal properties of the samples requires the determination of $\Delta T_{2\omega}$.

By measuring the electrical resistance change of the probing wires $\Delta R_{2\omega}(x)$, the surface temperature $\Delta T_{2\omega}(x)$ is detected:

$$\Delta R_{2\omega}(x) = R_0(x).\beta.\Delta T_{2\omega} \quad (5.15)$$

Here, $|x|$ is the distance from the heating wire, $R_0(x)$ is the electrical resistance of the probing wire at ambient temperature T_a and β is the temperature coefficient of the electrical resistivity. A direct current i_0 of small magnitude is generated through the probing wires for the $\Delta R_{2\omega}(x)$ measurements. Using a lock-in amplifier, the second harmonic voltage at the probing wires can be measured:

$$\Delta V_{2\omega}(x) = \Delta R_{2\omega}(x)\, i_0 = R_0(x).\beta.\Delta T_{2\omega}(x).i_0 \quad (5.16)$$

We have to note that in these measurements careful attention must be paid to the nature of the substrate. If the substrate is electrically conductive, then an insulating layer should be deposited between the metallic heater and the substrate in order to avoid an eventual current leakage through the substrate.

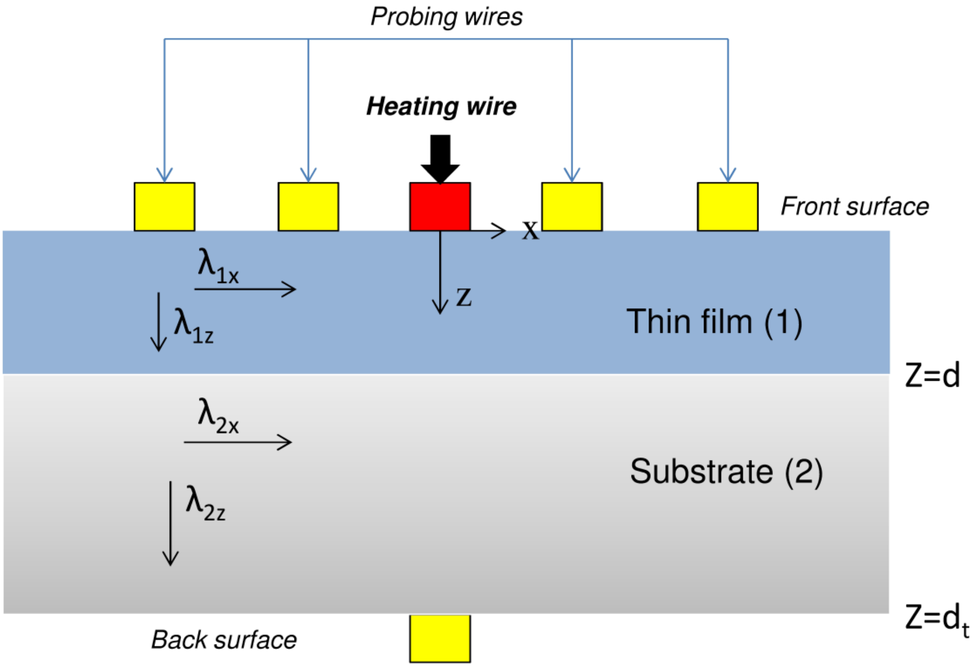

Figure 5.4. Schematic of method principle.

5.2.2 Associated thermal modeling in the alternating regime

Assuming a heater of width *w* in the X direction and infinite length in the Y direction, a two-dimensional thermal waves propagation regime may be considered in the sample.

The sample is heated on its surface by a heat flow density Φ_d modulated at the angular pulsation 2ω and homogeneous on the width *w* of the heating wire. The indexes 1 and 2 denote the film and the substrate respectively.

The axes *x,z* denote respectively the in-plane and cross-plane directions.

The heat flow density received by the sample across the surface (z=0) is:

$$f(x,\mathrm{z}) = \phi\,\mathrm{rect}_w(x)\delta(z) + h_g T(x,z)\delta(z) \qquad (5.17)$$

where $rect_w$ denotes the rectangle function, h_g is the global linearized convective and radiative sample-surrounding exchange coefficient. In the Fourier space, Equation (5.17) is as follows:

$$\tilde{f}(k_x,\mathrm{z}) = \frac{\phi_d}{\sqrt{2\pi}}\frac{w}{2}\sin c(k_x\frac{w}{2}) + h_g\,\tilde{T}(k_x,z=0)\,(5.18)$$

where k_x is the x-component of the wave vector.

Due to the finite thickness of the sample, the temperature field in the sample may be expanded in the following plane waves spectrum:

$$T_{2\omega}\left(x,z\right) = \frac{1}{\sqrt{2\pi}}\int_{-\infty}^{+\infty}\tilde{T}\left(k_x,z\right)e^{ik_x x}dk_x \; (5.19)$$

The temperature field in the film can be expressed as:

$$T_{2\omega}\left(x,z\right) = \frac{1}{\sqrt{2\pi}}\int_{-\infty}^{+\infty}\tilde{T}_1\left(k_x,z\right)e^{ik_x x}dk_x = \frac{1}{\sqrt{2\pi}}\int_{-\infty}^{+\infty}(\tilde{T}_1^{+}\,e^{i\chi z} + \tilde{T}_1^{-}\,e^{-i\chi z})e^{ik_x x}dk_x \qquad (5.20)$$

where $\chi = \sqrt{i\frac{2\omega}{\alpha_{1z}} - \frac{\alpha_{1x}}{\alpha_{1z}}k_x^2}$ is the wave vector along Z (condition that Im(χ)≥0)), $\tilde{T}_1^{+} = \tilde{T}_1^{+}(k_x,z=0)$ is the incident mode, $\tilde{T}_1^{-} = \tilde{T}_1^{-}(k_x,z=0)$ is the reflected mode and α_1 is the film thermal diffusivity.

The boundary condition at the sample surface is given as:

$$\tilde{f}\left(k_x,z=0\right) = -\lambda_{1z}\frac{\partial T_1\left(k_x,z\right)}{\partial z} \qquad (5.21)$$

Following Equations (5.18) and (5.21):

$$\tilde{T}_1^{+} = A - B\tilde{T}_1^{-} \qquad (5.22)$$

where

$$A = \frac{-\phi_d w sinc\left(k_x \frac{w}{2}\right)}{\sqrt{2\pi}\left(h_g + i\chi_1\lambda_{1z}\right)} \quad (5.23)$$

and

$$B = \frac{\left(h_g - i\chi_1\lambda_{1z}\right)}{\left(h_g + i\chi_1\lambda_{1z}\right)} \qquad (5.24)$$

The boundary condition at *Z=d* (see Figure 5.4) is given as (conservation of heat flux):

$$-\lambda_{1z}\frac{\partial T_1\left(k_x, z\right)}{\partial z} = -\lambda_{2z}\frac{\partial T_2\left(k_x, z\right)}{\partial z} \quad (5.25)$$

and therefore:

$$-i\chi_1\lambda_{1z}\tilde{T}_1^+ e^{i\chi_1 d} + i\chi_1\lambda_{1z}\tilde{T}_1^- e^{-i\chi_1 d} = -i\chi_2\lambda_{2z}\tilde{T}_2^+ e^{i\chi_1 d} + i\chi_2\lambda_{2z}\tilde{T}_2^- e^{-i\chi_2 d} \quad (5.26)$$

Based on Equation (5.22):

$$\tilde{T}_1^- = \frac{-\chi_2\lambda_{2z}\tilde{T}_2^+ e^{i\chi_1 d} + \chi_2\lambda_{2z}\tilde{T}_2^- e^{-i\chi_2 d} + \chi_1\lambda_{1z}A_1 e^{i\chi_1 d}}{\chi_1\lambda_{1z}C} \quad (5.27)$$

and

$$\tilde{T}_2^+ = \frac{-\chi_1\lambda_{1z}A_1 e^{i\chi_1 d} + i\chi_1\lambda_{1z}\tilde{T}_1^- C - i\chi_2\lambda_{2z}\tilde{T}_2^- e^{-i\chi_2 d}}{-i\chi_2\lambda_{2z}e^{i\chi_2 d}} \quad (5.28)$$

The discontinuity of the temperature between the film and the substrate at *Z=d* implies that:

$$-R_{th}\lambda_{2z}\frac{\partial \tilde{T}_2\left(k_x, z\right)}{\partial z} = \tilde{T}_1(k_x, \mathrm{Z} = d) - \tilde{T}_2(k_x, Z = d) = \tilde{T}_1^+ e^{i\chi d} + \tilde{T}_1^- e^{-i\chi d} - \tilde{T}_2^+ e^{i\chi d} + \tilde{T}_2^- e^{-i\chi d} \quad (5.29)$$

with R_{th} (K.W^{-1}) is the thermal resistance at the contact between the film and the substrate.

Taking into account Equations (5.22) and (5.28), $\tilde{T}_2^-$ can be expressed as a function of $\tilde{T}_1^-$:

$$\tilde{T}_2^- = D + E\tilde{T}_1^- \quad (5.30)$$

where

$$D = \frac{Ae^{i\chi_1 d}}{2e^{-i\chi_2 d}}\left(1 - \frac{\chi_1\lambda_{1z}}{\chi_2\lambda_{2z}} + iR_{th}\chi_1\lambda_{1z}\right) \quad (5.31)$$

and

$$E=\frac{Ae^{i\chi_1 d}+e^{-i\chi_1 d}+\frac{\chi_1\lambda_{1z}}{\chi_2\lambda_{2z}}-iR_{th}\chi_1\lambda_{1z}C}{2e^{-i\chi_2 d}} \quad (5.32)$$

At the back surface (*Z=d$_t$*):

$$-\lambda_{2z}\frac{\partial\tilde{T}_2\left(k_x,z\right)}{\partial z}=h_g\,\tilde{T}_2(k_x,Z=e_t) \quad (5.33)$$

and therefore:

$$-i\chi_2\lambda_{2z}\tilde{T}_2^{+}e^{i\chi_2 d_t}+i\chi_2\lambda_{2z}\tilde{T}_2^{-}e^{-i\chi_2 d_t}=h\tilde{T}_2^{+}e^{i\chi_2 d_t}+h\tilde{T}_2^{-}e^{i\chi_2 d_t} \quad (5.34)$$

Using Equations (5.28) and (5.30), $\tilde{T}_1^{-}$ can be expressed as:

$$\tilde{T}_1^{-}=\frac{F}{G} \quad (5.35)$$

where

$$F=Ae^{i\chi_1 d}e^{i\chi_2(d_t-d)}(-\chi_1\lambda_{1z}-\frac{h_g\chi_1\lambda_{1z}}{\chi_2\lambda_{2z}})+i\chi_2\lambda_{2z}D(e^{i\chi_2(d_t-d)}+e^{-i\chi_2 d_t})-h_gD(e^{i\chi_2(d_t-d)}+e^{-i\chi_2 d_t})(5.36)$$

and

$$G=Ce^{i\chi_2(d_t-d)}(-\chi_1\lambda_{1z}-\frac{h\chi_1\lambda_{1z}}{\chi_2\lambda_{2z}})+h_gE(e^{i\chi_2(d_t-d)}+e^{-i\chi_2 d_t})+i\chi_2\lambda_{2z}(e^{i\chi_2(d_t-d)}+e^{-i\chi_2 d_t}) \quad (5.37)$$

At the front surface of the sample, the average of the temperature on the width of the probing wires *w* for a distance *x* from the source (heating wire) can therefore be calculated:

$$\Delta T_{2\omega}\left(x_i,z=0\right)=\frac{1}{w}\int_{x_i-w/2}^{x_i+w/2}T_{2\omega}\left(x_i,z=0\right)dx=\frac{1}{w}\int_{x_i-w/2}^{x_i+w/2}\frac{1}{\sqrt{2\pi}}\int_{-\infty}^{+\infty}(\tilde{T}_1^{+}+\tilde{T}_1^{-})e^{ik_x x}dk_x \quad (5.38)$$

and the temperature at the back-surface is:

$$\Delta T_{2\omega}\left(x=0,z=d_t\right)=\frac{1}{w}\int_{x_i-w/2}^{x_i+w/2}T_{2\omega}\left(x=0,z=d_t\right)dx=\frac{1}{w}\int_{x_i-w/2}^{x_i+w/2}\frac{1}{\sqrt{2\pi}}\int_{-\infty}^{+\infty}(\tilde{T}_2^{+}e^{i\chi_2 d_t}+\tilde{T}_2^{-}e^{-i\chi_2 d_t})e^{ik_x x}dk_x$$

(5.39)

The sample temperature at any instant in the stationary regime is the sum of the two components T_{DC} and $\Delta T_{2\omega}$.When an alternating current passes across the heater, this latter is expected to act as a low-pass filter. The technique consists of adjusting the frequency of the current in order to get a condition where $T_{DC} >> \Delta T_{2\omega}$. Satisfying this condition allows us to determine the thermal properties of the considered materials through the variation of $\Delta T_{2\omega}$ at the temperature T_{DC}.

The temperature T_{DC} is controlled by the amplitude of the alternating current generated within the heater, and the thermal properties of the sample at this temperature level is characterized through the model already discussed above.

In the next part, we adjust the analytical model for a simple reference material in order to determine the thermal properties of the sample at different levels of T_{DC}.

5.3 Establishment of the method for a simple reference material

5.3.1 The reference material

Because of its well-known thermal properties versus the temperature, we used a sample of isotropic pure silicon as reference material. Table 5.1 gives the values of the thermal properties of silicon determined in literature at different levels of temperature. The value of d_0 was determined equal to 2329 kg.m^{-3} for highly pure silicon at a temperature of 298 K [145]. As the thermal expansion coefficient does not exceed 1 % at temperature below 600 K [146], we considered it constant as a function of temperature in our work.

Table 5.1. Thermal properties of pure silicon at different temperature levels.

Temperature (K)	C (J.Kg^{-1}.K)[116]	λ (W.m^{-1}.K^{-1})[147]	α_{ref} ($\times 10^{-5}$ m^2.s^{-1})[a]	α_{exp} ($\times 10^{-5}$ m^2/s)[148]
300	703	148	9.03	8.8
400	760	105	5.93	5.33
500	800	80	4.29	3.8

[a] Data calculated with Equation (5.2) and values of k and C from Table 5.1.

For the test and the method demonstration, a specific sample made of silicon was prepared. Its thickness, width and length were 200 μm, 7 mm and 10 mm respectively.

5.3.2 Design of the resistive wire array

Using COMSOL Multiphysics, numerical simulations of the thermal behavior of the Si sample were performed to determine the wires length for which the analytical 2D model is applicable and to design the electrical chip. The design includes the determination of the distances between the heating wire and the probing wires.

A) Determination of the probing wires length

3D COMSOL model was first made. As the heating wire is located at the middle on the sample surface, quarter of the system was modeled. A volumetric term of the power P_v is inserted in the section of the heating wire. For the coefficient of heat losses to the environment, we assumed h= 5 W.m^{-2}.K^{-1}, the emissivity ϵ equal to 1 at the sample and wires surfaces and a negligible thermal contact resistance between the wires and the sample. Let us remember that $\Delta T_{2\omega}$ has no effect on the global sample temperature as our current frequency is much larger than the cut-off frequency of the hot wire. Figure 5.5 shows the top view of the isotherm distributions at the sample surface when a electrical current amplitude I_{ac}=60 mA heats the sample. First, it can be said that the sample is approximately isothermal as the temperature gradient between the heater and the sample extremity does not exceed 3 K in this case. This gradient usually lies in the range of uncertainty of the thermal properties determination (see Table 5.1). Moreover, Figure 5.6 shows the variation of $\Delta T_{2\omega}$ for different lengths as a function of the distance from the heating wire. We can notice that there is no difference for the different representative curves. That confirms that the probing wires temperatures are uniform along their length (y direction) and justifies the large length of the heater as in this configuration the heat flows perpendicularly to the probe wires. Based on these simulations, the wire array design was fabricated as will be seen in the following part.

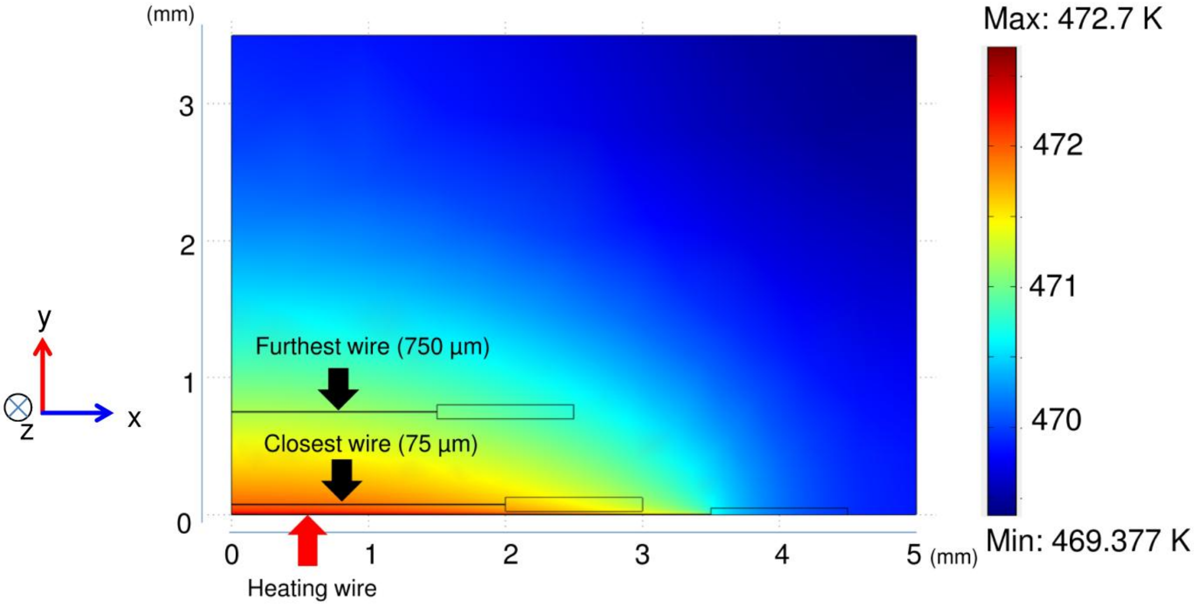

Figure 5.5. Top view of the model showing the distribution colored with isotherms while generating current amplitude I_{ac} of 60 mA.

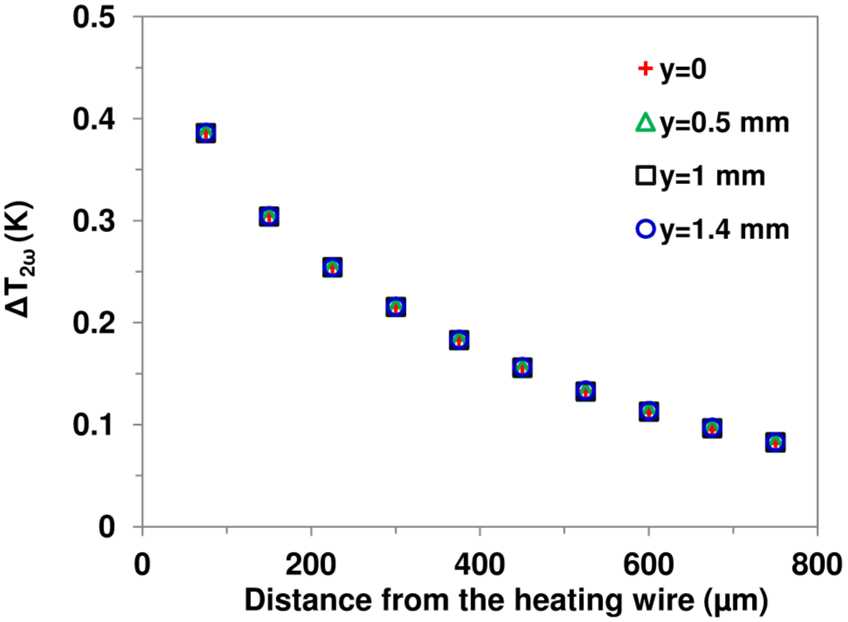

Figure 5.6. Variation of $\Delta T_{2\omega}$ for different lengths as a function of the distance from the heating wire.

B) Wire array material

As illustrated in Figure 5.7, the heating wire (in red) is located in the middle of the sample surface. The probing wires (in blue) are located on both sides of the heating wire. The main process chosen for fabricating this wires array is photolithography and lift-off. The schematic diagram of the fabrication process flow is shown in Figure 5.8 [149].

After substrate cleaning, a 2 µm–thick nLOF negative photoresist is spun on the silicon wafer. The resist is baked on a hotplate at 110°C for 1 min. A UV exposure is then carried out (Figure 5.8.a). A post bake is performed at 110°C on a hotplate for 1 min. This bake is immediately followed by the resist development in a AZ-351B solution for 60 s, leaving an array of line openings into the resist layer on top of the sample [149]. After the photolithography step, a chromium/ gold bilayer, respectively of 50 nm-thick (Cr) and 450 nm thick (Au), is deposited on top of the sample by sputtering (Figure 5.8.b). The chromium is used as an adhesion layer to stick the gold on silicon. Finally the lift-off step is performed in an acetone bath under ultrasonic excitation (Figure 5.8.c) [149].

Table 5.2 gives the value of the wires section S, electrical resistivity ρ and the coefficient β. Using Atomic Force Microscopy (AFM) in tapping mode, S was measured. Figure 5.9 shows an example of the section measurements. As noticed, the wire real section obtained after the process fabrication is uniform but not square as expected. The wires length L is of several millimeters and was measured with optical microscopy. The length of the heating wire is seven mm and varies between 3 and 4 for mm for the probing wires. The justification of the wires length is given in the next section. By measuring the wire electrical resistance R by 4-point probes method (4-probe sensing) at ambient temperature, ρ was determined. The chip (sample + wires) was placed in a specific oven and heated to different temperature levels. Then, β was determined from the wire resistance measurements: $R = R_0(1+\beta(T-T_a))$.

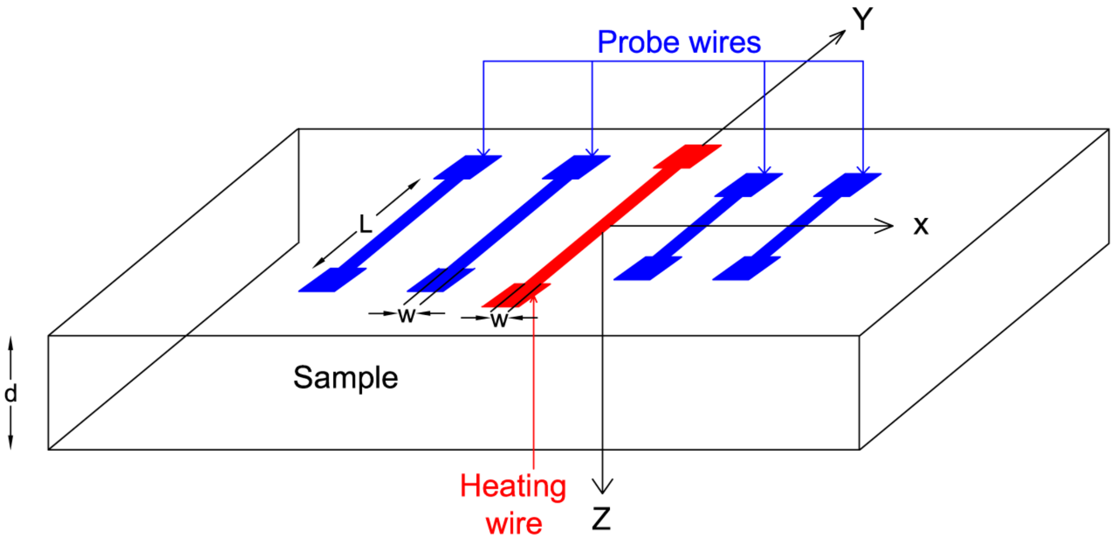

Figure 5.7. Schematic of the implemented sample.

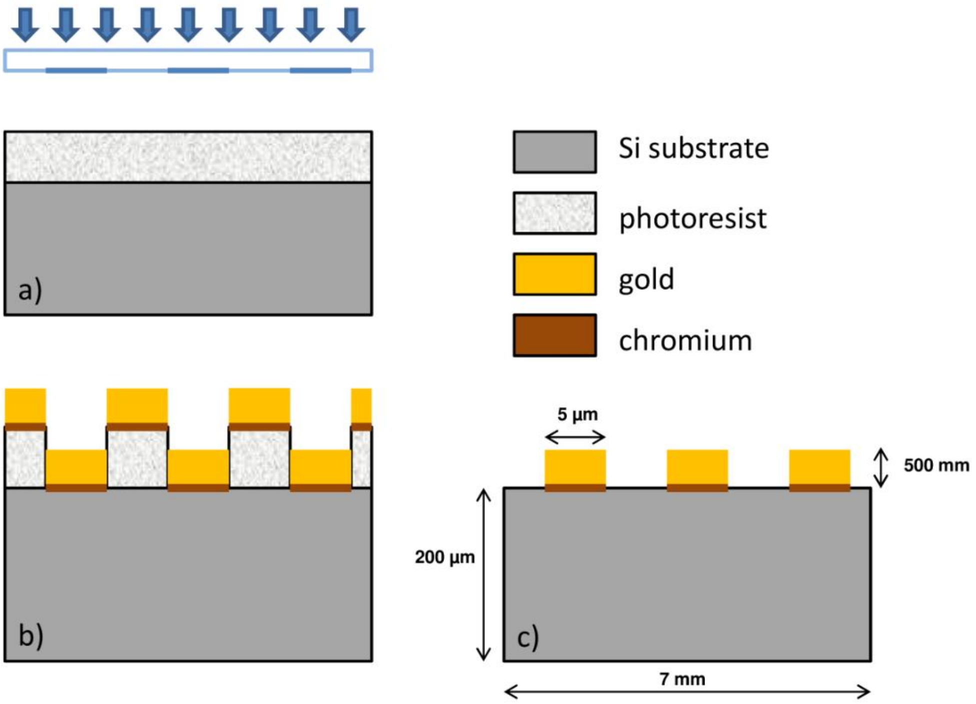

Figure 5.8. Process flow for the deposition of the metallic wires array. (a) Photolithography, (b) Metal deposition, (c) Lift-off process.

Table 5.2. Measured properties of the wires.

Section S (m²)	Electrical resistivity ρ (Ω.m) at T_a	Coefficient of temperature β (K^{-1})
$1.66 \pm 0.15 \times 10^{-12}$	$4.15 \pm 0.1 \times 10^{-8}$	$8.8 \pm 0.05 \times 10^{-4}$

The mask design is shown in Figure 5.10. Actually, the probe wires (in yellow) are connected to the pads through connection wires of large section. Due to this large section, these connection wires have negligible electrical resistance compared it to that of the probe wires and have no effect on the measurements.

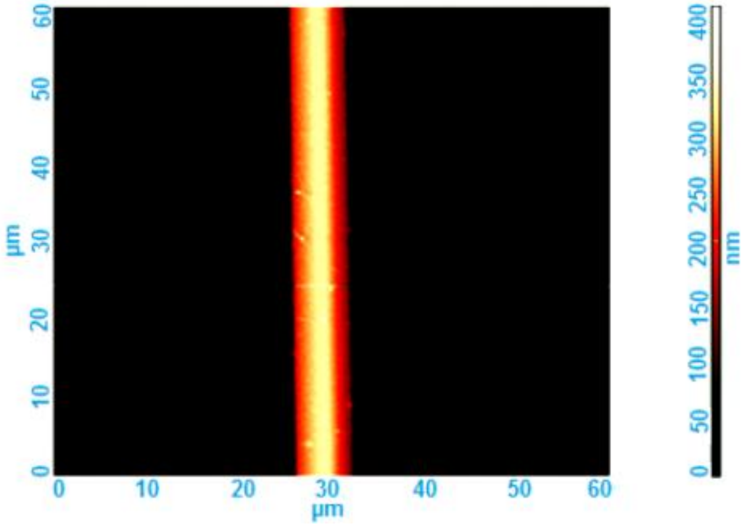

Figure 5.9. AFM 2D image of a gold wire.

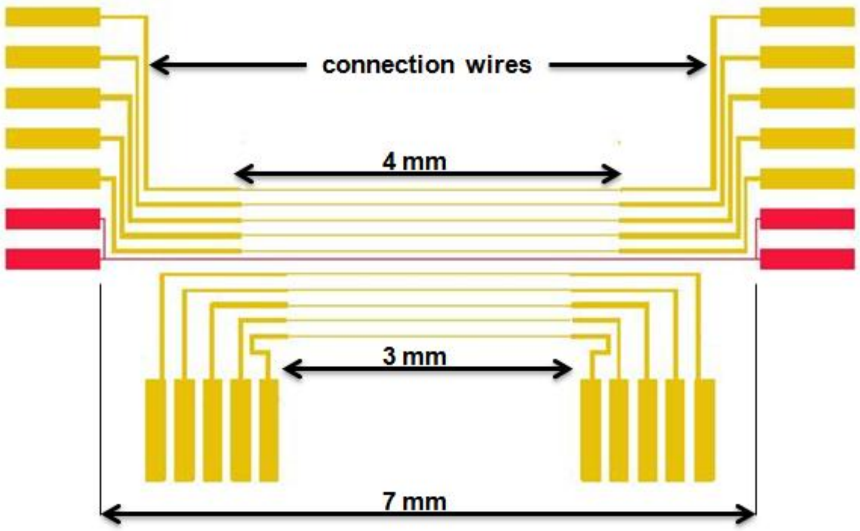

Figure 5.10. The mask design showing the probe wires (in yellow) and the heater (in red).

C) Comparison between 2D and 3D COMSOL models

Before getting to the 2D analytical model already described in section 3, 2D COMSOL model was built to compare the difference in terms of the $\Delta T_{2\omega}$ and T_{DC} with respect to the 3D model as illustrated in Figure 5.11. Because of its symmetry, half of the system was established. In order to be able to compare between the 2D and 3D simulations, the same boundaries conditions were maintained. Figure 5.12 presents a comparison between the variations of $\Delta T_{2\omega}$ for the 2D and 3D models as a function of the distance from the heating wire for the same boundary conditions and I_{ac}=60 mA. We found that whatever the boundaries conditions and the current amplitude are $\frac{\Delta T_{2\omega}(x,3\mathrm{D})}{\Delta T_{2\omega}(x,2\mathrm{D})} \simeq \frac{1+\beta\Delta T_{DC}(3\mathrm{D})}{1+\beta\Delta T_{DC}(2\mathrm{D})}$. In fact, the difference between ΔT_{DC}(3D) and ΔT_{DC}(2D) is related to the fact that in the 2D model, the length of the wires is assumed the same of the sample.

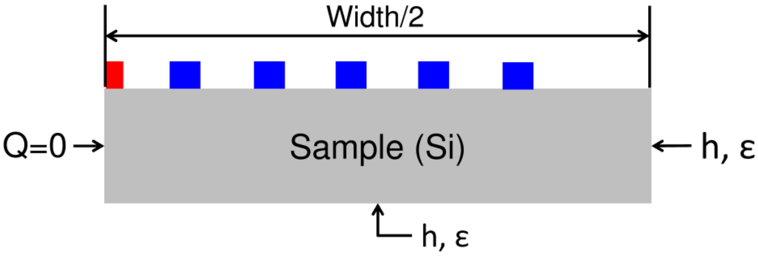

Figure 5.11. Schematic of the 2D COMSOL model.

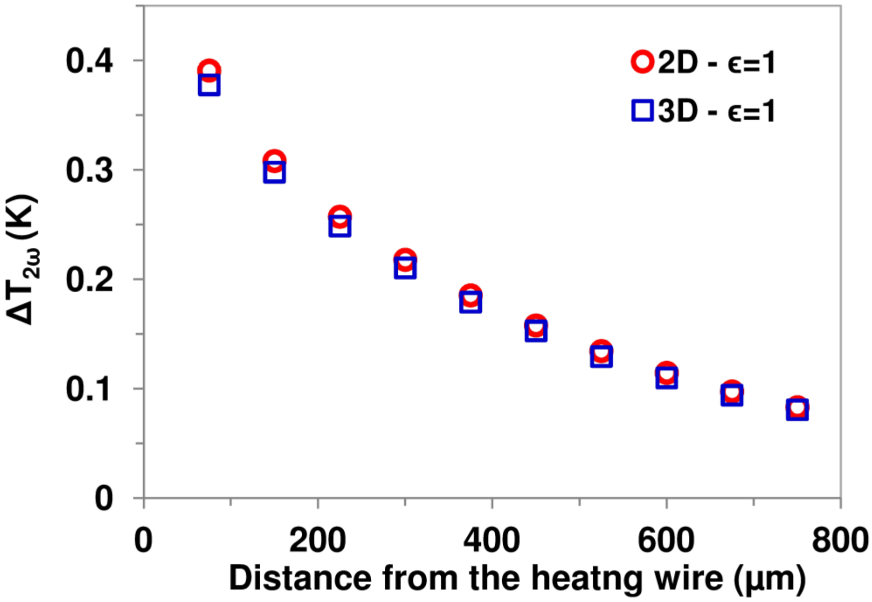

Figure 5.12. Variation of $\Delta T_{2\omega}$ in the two COMSOL configurations (2D and 3D) as a function of the distance from the heating wire for Si sample (f= 40 Hz, ϵ=1, h= 5 W.m^{-2}.K^{-1} and I_{ac}=60 mA).

5.4 Analysis of the influence parameters

5.4.1 Effect of the heat losses on T_{DC} and $\Delta T_{2\omega}$

Figure 5.13 shows the variation of the sample temperature T_{DC} ($T_{sample}=T_{DC}+\Delta T_{2\omega}$ and $T_{DC} >> \Delta T_{2\omega}$) for different values of sample emissivity ϵ and convective heat losses coefficient h. As can be seen, the heat losses through radiation and convection play a crucial role in the determination of T_{DC}. Besides, the heat losses have an effect on the determination of $\Delta T_{2\omega}$. Figure 5.14 presents the variations of $\Delta T_{2\omega}$ and ϵ as a function of h and ϵ for different values of h and ϵ. As can be seen, the heat losses are not negligible and affect the temperatures T_{DC} and $\Delta T_{2\omega}$.

In our technique, the temperature T_{DC}, at which the sample thermal properties are determined through measured $\Delta T_{2\omega}(x)$, is measured experimentally through the probing wires:

$$T_{DCexp}=(1/N)\Sigma_{i=1} (R(x_i)-R_0(x_i))/(R_0(x_i).\beta)+T_a \quad (5.40)$$

where N is the number of the probing wires and i is an index for a considered probing wire.

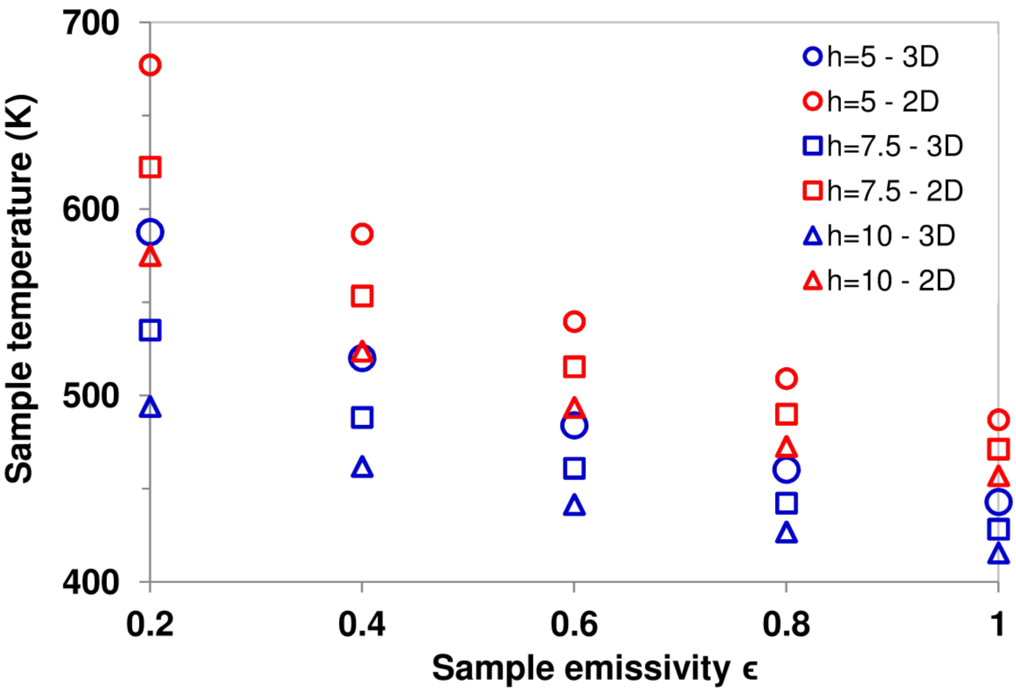

Figure 5.13. Effect of the heat losses on the temperature of the sample T_{DC} in 2D and 3D COMSOL configurations (I_{ac}=60 mA).

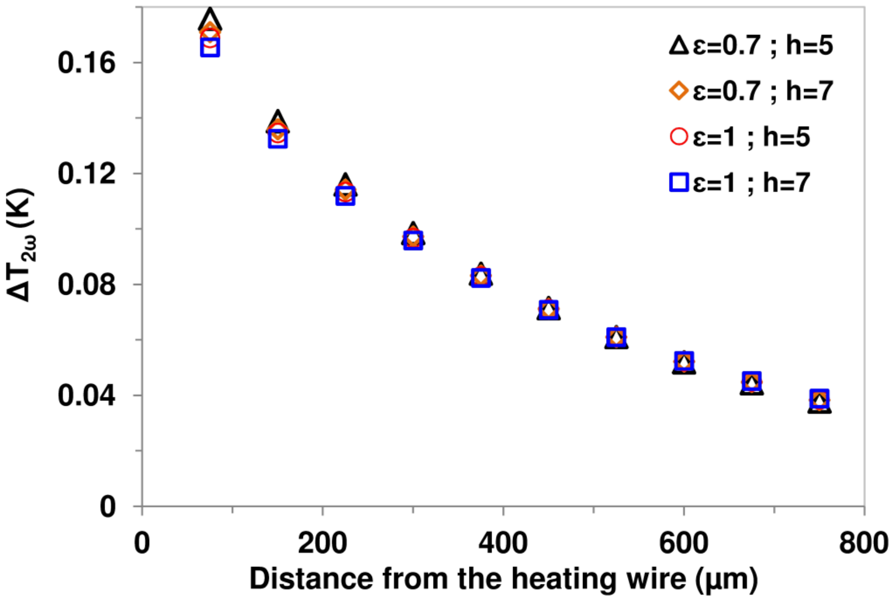

Figure 5.14. Variations of $\Delta T_{2\omega}$ as a function of the distance from heating wire for different values of h and ϵ (I_{ac}=40 mA, f=40 Hz).

5.4.2 Effect of the resistance of contact between the heater and the wire

The interface thermal resistance R_{th} between the wires and the substrate is given by:

$$R_{th} = R_{Au/Cr} + R_{Cr} + R_{Cr/Si} \quad (5.41)$$

where $R_{Au/Cr}$, R_{Cr} and $R_{Cr/Si}$ are the thermal resistances at Au/Cr interface, within the Cr layer and at Cr/Si interface respectively. R_{Cr} is equivalent to d_{Cr}/λ_{Cr}, where d_{Cr} is the thickness of the chromium layer and λ_{Cr} is the chromium thermal conductivity. This resistance is about 10^{-10} m^2.K.W^{-1}. $R_{Au/Cr}$ and $R_{Cr/Si}$ are dependent on the interface geometry, the materials properties, the process of deposition of the wires on the substrate, etc… However, the values of the thermal resistances found in the scientific literature for metal/semiconductor lie in the range of 10^{-8} m^2.K.W^{-1}. They include the determination of R_{th} at Au/Si interface with transient thermo-reflectance [120, 150], with picosecond optical technique [118], and with simulations of molecular dynamics at Si/Au [151] and Si/Pb [152] interfaces. Besides, Gundrum [153] measured R_{th} at Al/Cu interface equal to 0.25×10^{-9} m^2.K.W^{-1} using thermo-reflectance.

Using frequency-dependent photothermal radiometry (PTR), the thermal resistance between the wires pads (supports) and the sample was measured [154]. The identified value of R_{th} is about $3 \pm 0.5 \times 10^{-7}$ m^2.K.W^{-1}. We assumed that R_{th} is the same value for the contact between the heating wire and the sample. R_{th} was inserted in the numerical simulations in order to investigate the difference in the variation of T_{DC} and $\Delta T_{2\omega}$. The variation of T_{DC} does not exceed 2 K and is less than the uncertainty of identifying the thermal properties of the sample (see Table 5.1). Figure 5.15 presents the variation of $\Delta T_{2\omega}$ for two cases: R_{th}= 3 × 10^{-7} $m^2.K.W^{-1}$ and for a perfect contact (R_{th}=0). As can be observed, the difference between the values $\Delta T_{2\omega}$ is small (less than 1%).

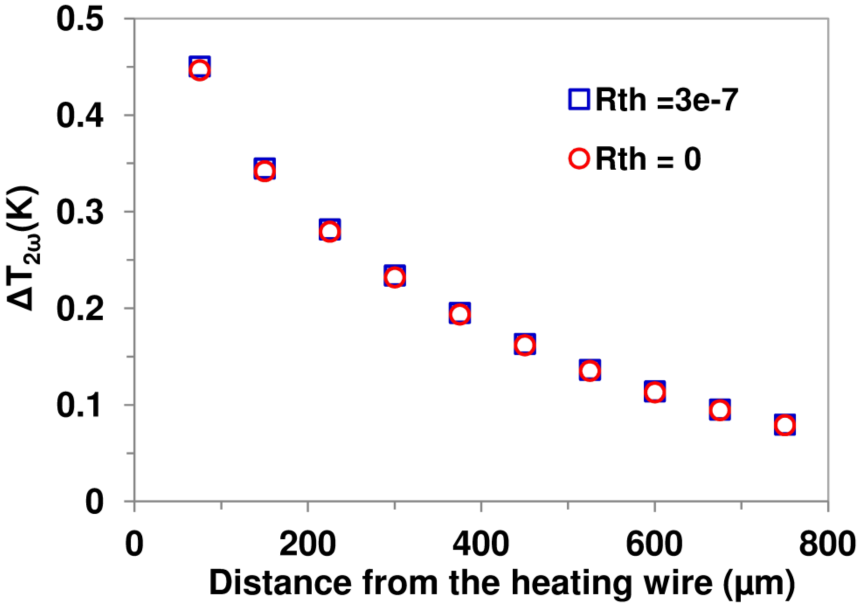

Figure 5.15. Variation of $\Delta T_{2\omega}$(K) (calculated in 2D COMSOL configuration) as a function of the distance of the heating wire (µm) for a perfect contact (R_{th}=0) and for R_{th}= 3 × 10^{-7} $m^2.K.W^{-1}$.

5.5 Way for the simplification of the thermal model: 1D approach

After pointing out the difference between the 2D and 3D COMSOL configurations, we make here a comparison between the 2D numerical simulations, the analytical model and the simplified 1D approach model (Equation 5.11). We determine the range of frequencies of the heating current and the distances between the wires where the 1D approach is valid.

For our silicon Si isotropic sample, several simplifications are applied to the analytical model already described in the section 5.2: (1) R_{th}=0, (2) d=0, $\tilde{T}_1 = \tilde{T}_2$ and $\lambda_x = \lambda_z$ ($\alpha_x = \alpha_z$).

As a reminder, the 1D approach model is given as:

$$\Delta T_{2\omega}(X) = A_1\sqrt{\frac{\alpha_s}{2\omega}}\, e^{-\frac{X}{\mu}} e^{-i\frac{X}{\mu}-i\frac{\pi}{4}} = \frac{P_{rms}}{4d\lambda_s}\sqrt{\frac{\alpha_s}{2\omega}}\, e^{-\frac{X}{\mu}} e^{-i\frac{X}{\mu}-i\frac{\pi}{4}} \quad (5.42)$$

where d is the thickness of the sample, λ_s and α_s are the thermal conductivity and diffusivity of the Si sample and $\mu = \sqrt{\frac{\alpha}{\omega}} = \sqrt{\frac{\alpha}{2\pi f}}$ is the diffusion length in the sample.

Figures 5.16 and 5.17 show respectively the variations of $\Delta T_{2\omega}$ and the phase lag Φ_1 (°) as a function of the distance from the heating wire. As can be seen, the analytical model fits well the 2D numerical simulations in the two curves. On the other hand, the 1D approach curves follows the same trend of the other curves after exceeding a distance larger than 225 µm from the heating wire as indicated in Figures 5.16 and 5.17. For distances less than the sample thickness d, the Z part of the heat flux cannot be neglected and as a result the one-dimensional conduction model is not valid anymore, in analogy with the scale analysis shown by Bejan [123].

In the case of the 1D approach, the in-plane thermal diffusivity of the sample α can be determined from the exponential tendency of the amplitude $\Delta T_{2\omega}$ and the linear tendency of the phase lag ϕ (°). Moreover, the in-plane thermal conductivity λ_s is determined through the term A_1 (see Equation 5.11). For $|x_{min}|$ = 225 µm, the 1D approach is valid and the uncertainty of the thermal properties determination of is less than 4 %. Considering the identified frequency range, the sample thickness d tends to be smaller than μ when f decreases. A critical frequency f_{cr1} that should not be exceeded to maintain $\mu>d$ $(f<f_{cr1})$. Working with frequencies larger than f_{cr1} induces a non-uniform sample temperature along Z and so the 1D model cannot be applicable. Another condition of the frequency is the limitation of the half-width of the sample so that $5\mu<L/2$ $(f>f_{cr2})$. For example, for a sample temperature of 500 K, 15 Hz $<f<$ 160 Hz. At this range of frequencies, the current frequency is much larger than the low cut-off frequency of the system that is estimated about 5 mHz. Let us note that the simulations presented in this part of this section concern the case of perfect contact between the wires and the substrate (R_{th}=0 $m^2.K.W^{-1}$). The thermal properties of silicon (k, d and C) and their dependence on temperature were used for the calculations.

Based on the determined criterion, the 1D approach was used to determine the thermal properties of the silicon sample. We have to note that when changing the substrate material, some adjustments have to be applied in terms of the sample dimensions, range of frequency of the heating current and distances between the probing wires so that the 1D approach can be valid.

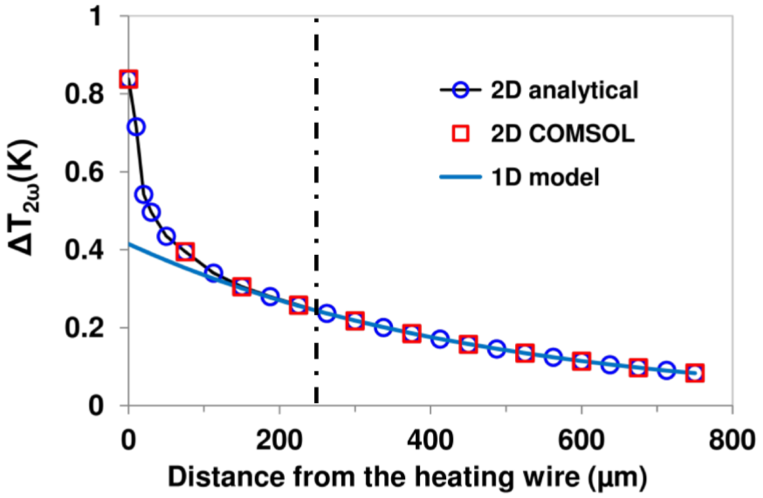

Figure 5.16. Comparison of $\Delta T_{2\omega}$ between the analytical model, 2D numerical simulations and 1D approach (I_{ac}=60 mA, ϵ=1 and h=5 W.m^{-2}.K^{-1}).

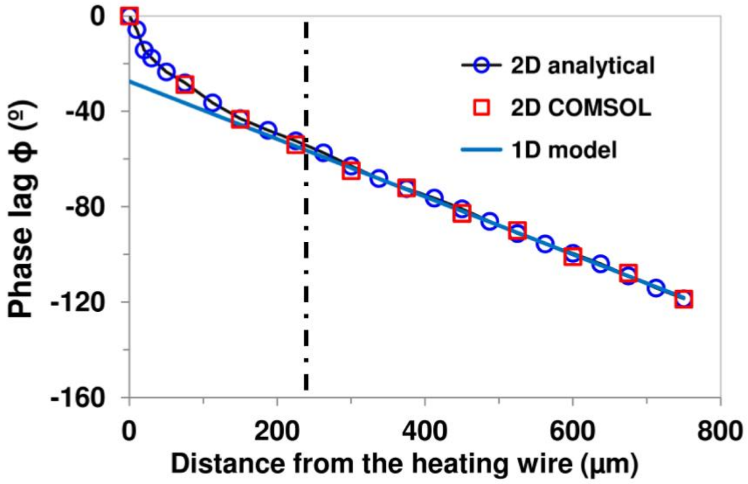

Figure 5.17. Comparison of the phase lag (º) between the analytical model, 2D numerical simulations and 1D approach (I_{ac}=60 mA, ϵ=1 and h=5 W.m^{-2}.K^{-1}).

5.6 Experimental Set-up

The experimental set-up is illustrated in Figure 5.18. In this set-up, the AC generator (1) is connected to the current amplifier (2) to generate an alternating current I_{ac} through the heating wire. This wire in red is deposited on the mask (3) and mounted in series with a resistance of 1 KΩ to measure the heating current (4). The resistance is linked to an ampere-meter (5) for an accurate measurement of I_{ac}. A DC current generator (6) produces i_0 of small magnitude through the probing wires in yellow. Synchronized with the AC generator, the lock-in amplifier (7) detects the signal $V_{2\omega}$ and the phase lag Φ at the probing wires.

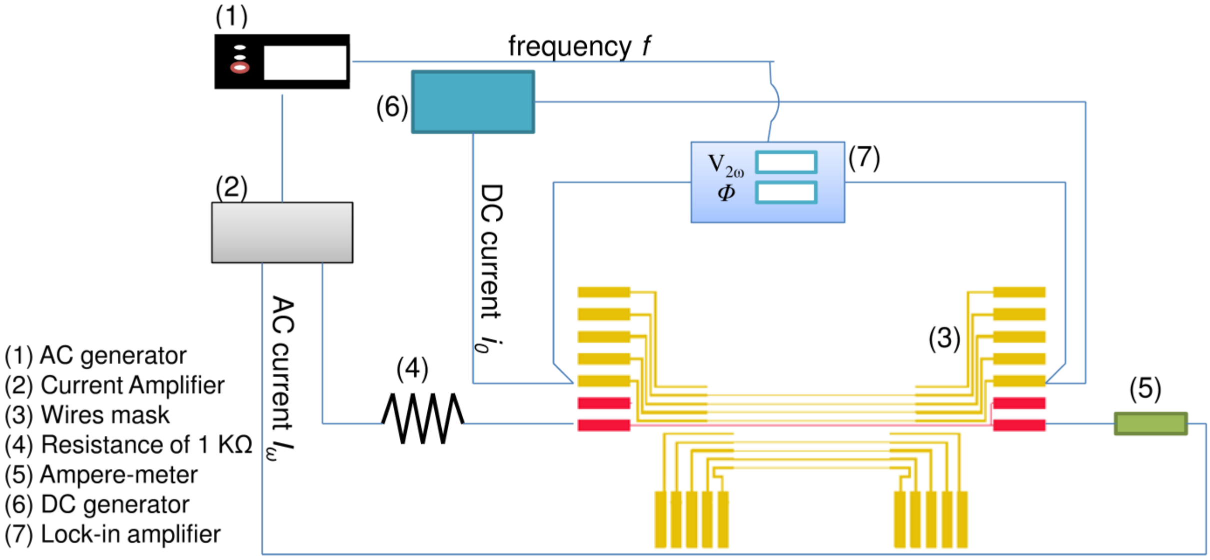

Figure 5.18. Schematic of the experimental set-up.

As seen in Figure 5.19, two Printed Circuit Boards PCB 1 and PCB 2 are used to integrate the chip into the electrical circuit. Electrical connections link the chip to the BNC plugs at the PCB 1. Each deposited wire on the silicon sample has a number at the PCB 1 plugs. PCB 1 is attached to the PCB 2 by small pins. Bonding wires made of gold of few millimeters in length and 25 µm in diameter connect the pads with PCB 2. As reported by Ji *et al.* [155], the electrical resistances of the bonding wires and the bond interfaces do not exceed hundred mΩ. In this work, these resistances are supposed negligible comparing them to those of the wires. Moreover, using a multimeter, it was verified that the electrical resistances of the connection between the PCB 1 and the pins of the PCB 2 are of few mΩ. Taking all of this into account, it can be said that the electrical resistances measured at the PCB 1 plugs correspond to the wires of the electrical chip.

5.7 Experimental results

The measurements were performed under ambient conditions (T_a=30°C, RH≃40%).

Experiments were performed for frequencies between 20 Hz and 80 Hz to meet the requirements of the 1D model. Two different magnitudes I_{ac}, 40 and 60 mA, were used to heat the sample. Figures 5.20 and 5.21 give an example of the measurements for I_{ac} of 60 mA for three different frequencies: 40, 55, and 80 Hz. For both I_{ac}, the exponential tendency of $\Delta T_{2\omega}$ and the linear tendency of Φ are found as a function of $|x|$.

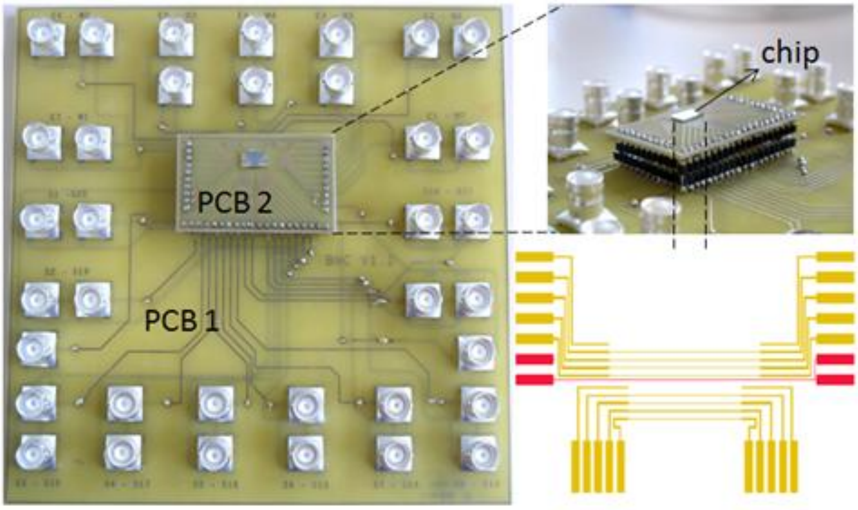

Figure 5.19. Electrical connections of the measurements.

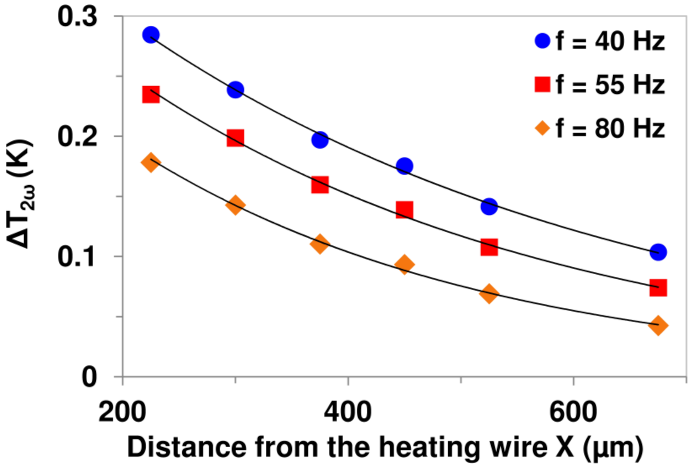

Figure 5.20. Experimental variations $\Delta T_{2\omega}$ as a function of the distance from the heating wire for I_{ac}=60 mA and for different frequencies.

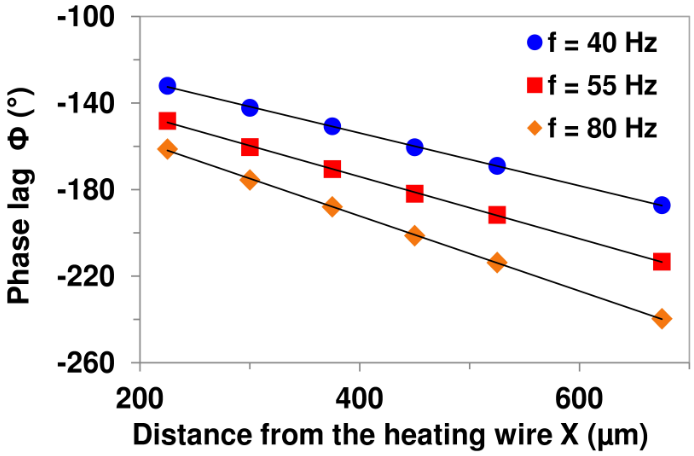

Figure 5.21. Experimental variations of the phase lag ϕ as a function of the distance from the heating wire for I_{ac}=60 mA and for different frequencies.

Let α_{am} and α_{Φ} the values of thermal diffusivity respectively extracted through the amplitude $\Delta T_{2\omega}$ and the phase lag Φ. Through the parameter A_1 of the exponential tendency of $\Delta T_{2\omega}$ (see Equation (5.42)), λ can be determined directly. Table 5.3 gives the values of the estimated thermal properties of the sample and their corresponding temperatures. Using Equation (5.40), the sample temperature T_{DCexp} is determined experimentally. The experimental results obtained are in good agreement with the literature values already listed in the table 5.1 [156].

Table 5.3. Si thermal properties experimentally determined.

I_{ac} (mA)	α_{am} ($\times 10^{-5}$ m².s^{-1})	α_{Φ} ($\times 10^{-5}$ m².s^{-1})	λ (W.m^{-1}.K^{-1})	T_{DCexp} (K)[a]
40	6.5±0.5	6.8±0.5	127±8	365±5
60	5±0.1	5.5±0.1	86.5±5	465±5

[a] Temperature experimentally determined using Equation (5.40) at the probing wires.

5.8 Case of anisotropic samples

The next part includes numerical and analytical simulations in order to determine the thermal properties of anisotropic materials.

Once the experiments are performed and the experimental results are obtained, a numerical optimization technique is needed to determine the thermal properties of the thin solid films when using the 2D analytical model. One of the techniques that can be used and that is developed in CETHIL is the Particle Swarm Optimizers (PSO). The approach has been used in various scientific communities: combustion, pure applied mathematics….

5.8.1 In plane thermal conductivity

Until this part, the study was made to determine of thermal properties of isotropic samples. We extend our study in this section to include bulk samples of anisotropic thermal properties.

Here, we consider two extreme cases: a) when the thermal conductivity in the x-direction λ_x is much larger than the one in the z-direction λ_z ($\lambda_x >> \lambda_z$) and b) when $\lambda_x << \lambda_z$. These two cases are not realistic and therefore determination of thermal properties of anisotropic materials will lie within these two cases.

The dimensions of the sample are taken the same of the isotropic Si substrate used in the experiments before.

a. $\lambda_x >> \lambda_z$

The low thermal conductivity of the sample $\boldsymbol{\lambda_z}$ taken here is equal to 2 W.m^{-1}.K^{-1}. In the *x*-direction, the thermal properties are the same of Silicon Si. Numerical simulations were performed using COMSOL Multiphysics and the 2D analytical model presented in section 3. The variation of the temperature T_{DC} is around 5 K from 10 µm to 750 µm as distances from the heating wire as shown in Figure 5.22. As said before, such variations are small and within the uncertainties of the determination of thermal properties of solid materials at temperatures larger than the ambient temperature. Figures 5.23 and 5.24 show the variations of the phase lag Φ and the amplitude $\Delta T_{2\omega}$ as a function of the distance from the heating wire where I_{ac}=60 mA for the analytical model (section 3) and the numerical simulations. As can be seen, the analytical model can describe well the variations of Φ and $\Delta T_{2\omega}$ in order to determine the in-plane thermal properties of the considered sample. The 1D model was tested in this case and the in-plane thermal properties were found again.

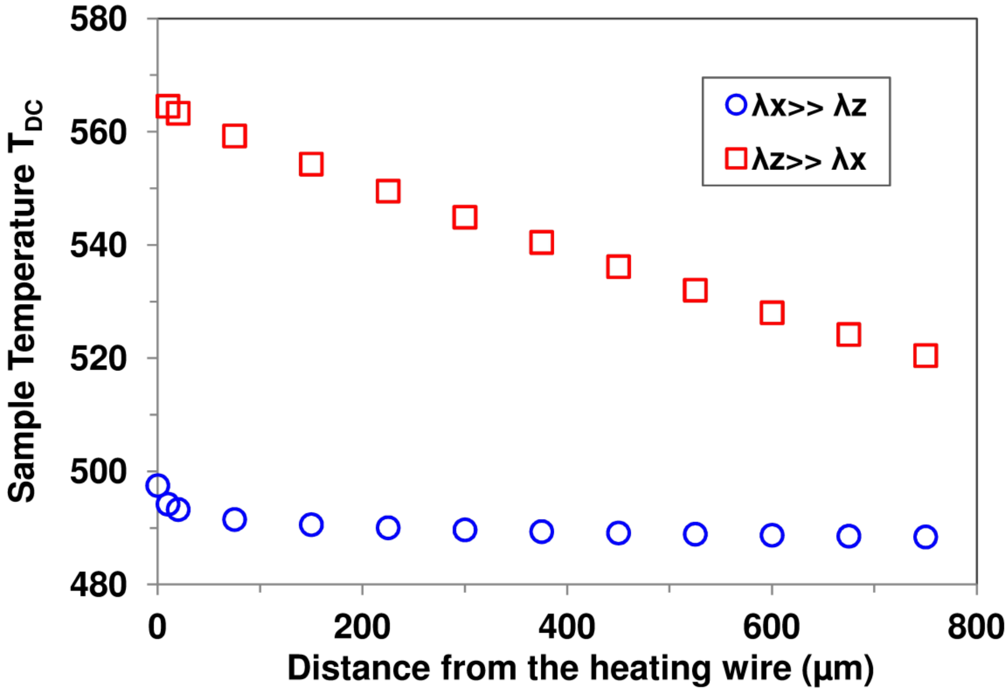

Figure 5.22. Simulated Variation of the sample temperature T_{DC} as a function of the distance from the heating wire for the two cases: $\lambda_x >> \lambda_z$ and $\lambda_x << \lambda_z$ (I_{ac}=60 mA, ϵ=1, h=5 W.m^{-2}.K^{-1}).

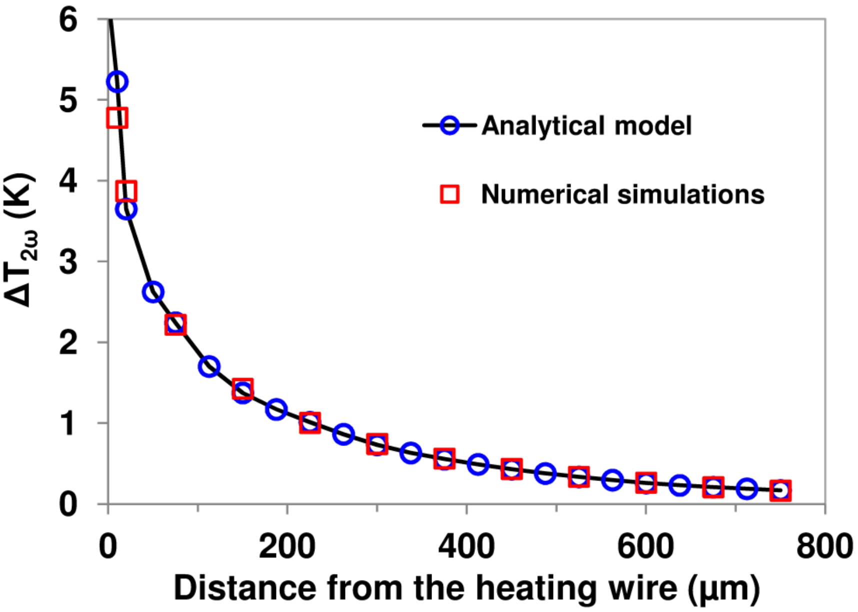

Figure 5.23. Simulated Variation of $\Delta T_{2\omega}$ as a function of the distance from the heating wire for the numerical simulations and the 2D analytical in the case of anisotropic sample ($\lambda_x >> \lambda_z$, I_{ac}=60 mA, f=40 Hz and ϵ=1, h=5 W.m^{-2}.K^{-1}).

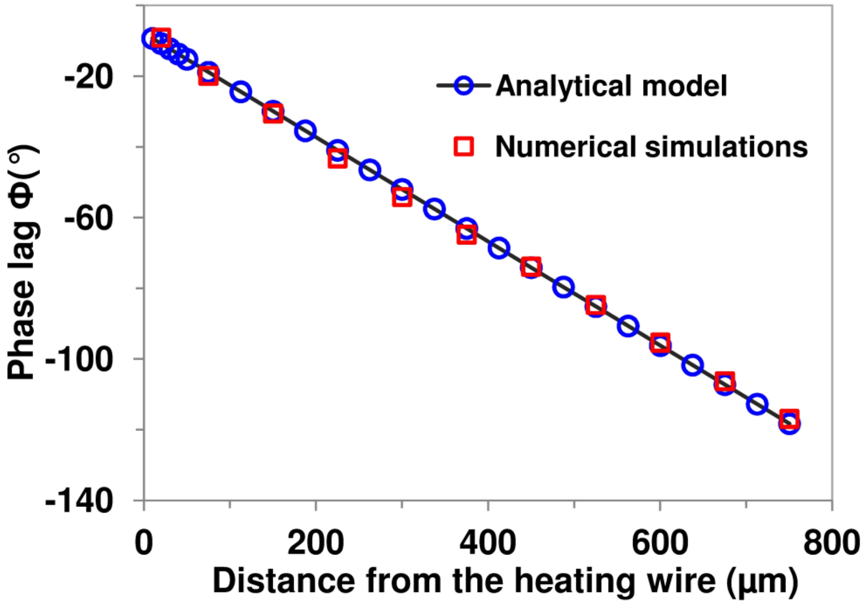

Figure 5.24. Simulated Variation of the phase lag ϕ as a function of the distance from the heating wire for the numerical simulations and the 2D analytical in the case of anisotropic sample ($\lambda_x >> \lambda_z$, I_{ac}=60 mA, f=40 Hz and ϵ=1, h=5 W.m^{-2}.K^{-1}).

b. $\lambda_z >> \lambda_x$

In this case, λ_x is taken equal to 2 W.m^{-1}.K^{-1} and the thermal properties are the same as the silicon in the z-direction. As shown in Figure 5.22, the sample is not isothermal. Figure 5.25 and 5.26 present the variations of the phase lag Φ and the amplitude $\Delta T_{2\omega}$ as a function of the distance from the heating wire. The analytical model fits almost the numerical model despite some uncertainties where the curves do not follow the variation of the numerical simulations. That might be related to the significant variation of the sample temperature T_{DC} in this case as shown in Figure 5.22. In fact, the thermal properties inserted in the analytical model correspond to the mean temperature of the variations of T_{DC} whereas in the numerical simulations the thermal properties are as a function of the temperature.

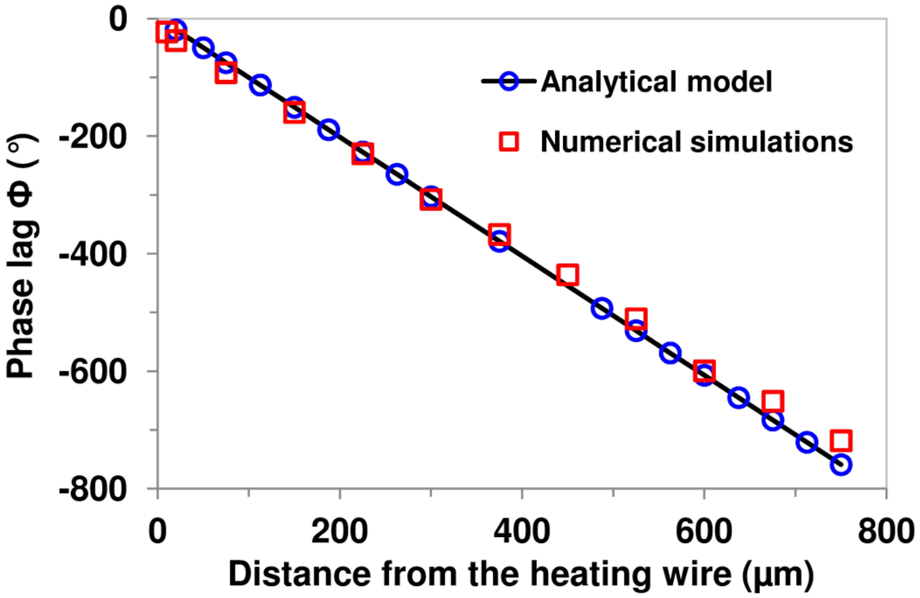

Figure 5.25. Simulated variation of the (a) phase lag (b) $\Delta T_{2\omega}$ as a function of the distance from the heating wire for the numerical simulations and the analytical model in the case of anisotropic sample ($\lambda_x << \lambda_z$, I_{ac}=60 mA, f=40 Hz and ϵ=1, h=5 W.m^{-2}.K^{-1}).

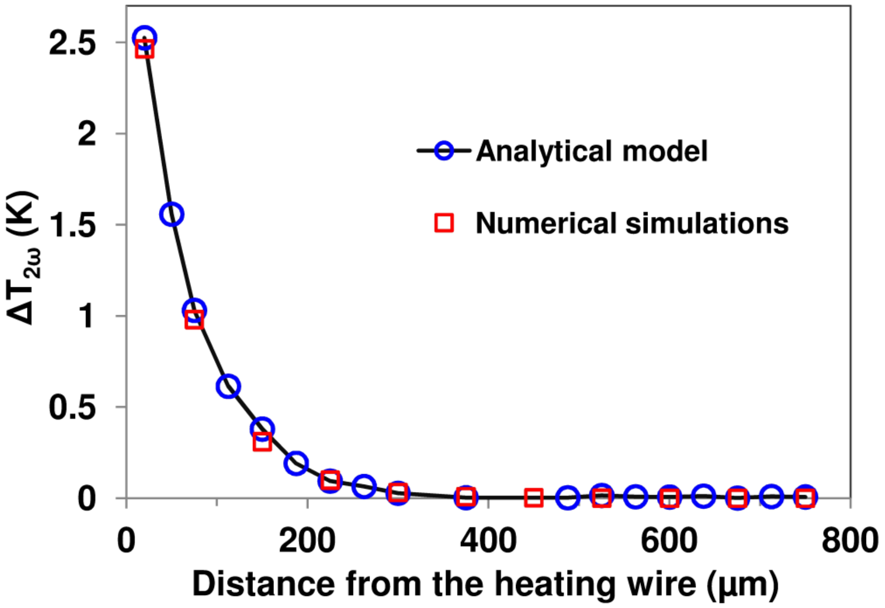

Figure 5.26. Simulated variation of the (a) phase lag (b) $\Delta T_{2\omega}$ as a function of the distance from the heating wire for the numerical simulations and the analytical model in the case of anisotropic sample ($\lambda_x << \lambda_z$, I_{ac}=60 mA, f=40 Hz and ϵ=1, h=5 W.m^{-2}.K^{-1}).

5.8.2 Cross-plane thermal properties

The principle of the measurement of the thermal properties in the cross-plane direction is illustrated in Figure 5.4.

A probing wire might be inserted at the back surface of the substrate. The variation of $\Delta T_{2\omega}$ can be detected as a function of the current frequency in order to determine the thermal properties of the substrate at the temperature T_{DC}, which depends on the value of I_{ac}.

Figures 5.27 and 5.28 show respectively the variations of the Φ and $\Delta T_{2\omega}$ as a function of the current frequency for the numerical simulations and the analytical model. Here, the thermal properties and dimensions of the sample are the same of isotropic Si used before in our experiments. As can be observed, the analytical model fits perfectly the numerical simulations in terms of the amplitude $\Delta T_{2\omega}$ the phase lag Φ curves.

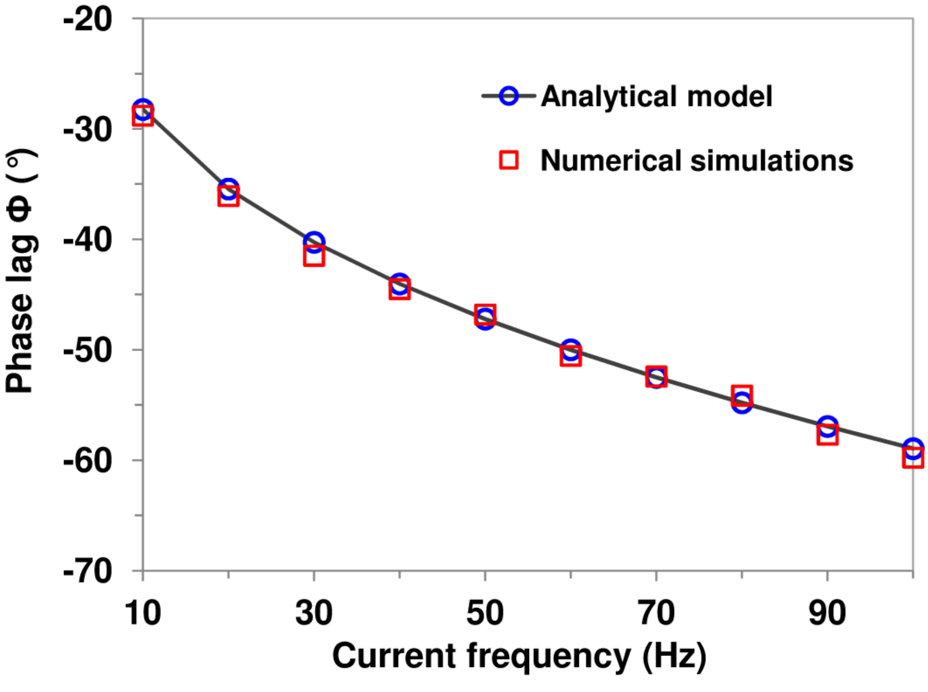

Figure 5.27. Variation of the phase lag ϕ as a function of the current frequency for the numerical simulations and the analytical model for the back surface probing wire ($\lambda_x << \lambda_z$, I_{ac} = 60 mA, f = 40 Hz and ϵ=1).

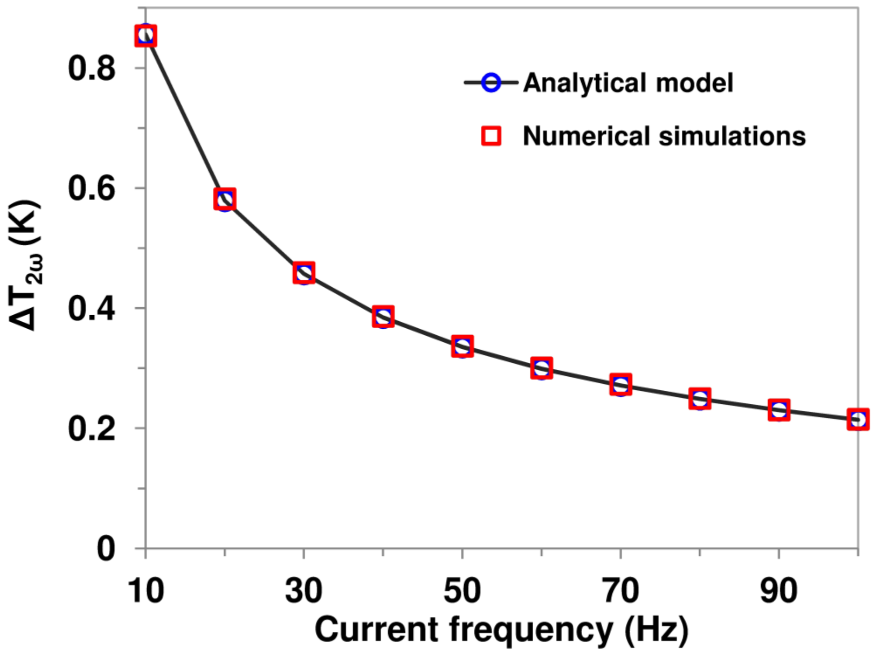

Figure 5.28. Variation of $\Delta T_{2\omega}$ as a function of the current frequency for the numerical simulations and the analytical model for the back surface probing wire (λ_x<< λ_z, I_{ac}=60 mA, f=40 Hz and ϵ=1).

5.9 Conclusions and Perspectives

This chapter reports the first steps of the development of a technique of characterization of the thermal properties of anisotropic solid thin films at temperatures larger than the ambient temperature.

The technique principle is based on the adaptation of the membrane method principle used in modulated regime. The modulated heating induces two temperatures in the sample: constant and alternating temperatures. The frequency of the current that should be used is larger enough than the cut-off frequency so that the alternating temperature is much smaller than the constant temperature. An array of resistive wires of different lengths has to be deposited on the front and back surfaces of the sample of interest. The longest wire heats the sample with an alternating current while the other wires detect the variation of the alternating temperature. The measured alternating temperature helps identifying the thermal properties of the sample at a temperature controlled by the magnitude of the heating current. The technique does not need the determination of the heat losses to the environment since the sample temperature is measured through the probing wires. The length of the wires is justified through 3D simulations. The difference between 3D and 2D numerical configurations is noticed and explained. 2D analytical model is introduced to determine the film thermal properties in the two directions. The analytical model fits well the numerical simulations in the case of isotropic samples. The range of frequency and the distance of the probing wires are determined to ensure the validity of the 1D approach model. First set of measurement were performed on an isotropic Silicon sample. The thermal properties determined at different temperatures from ambient to 500 K are in good agreement with the values of the scientific literature.

The identification, of the in-plane component of the thermal conductivity for an anisotropic sample is discussed. The 2D analytical model fits exactly the numerical simulations when the parameter λ_{xz} is much larger than 1 and some uncertainties are observed when λ_{xz} is much smaller than 1.

Moreover, the analytical model is able to describe the variation of the alternating temperature in the z-direction in order to identify the cross-plane thermal properties of the sample where the curve of 2D numerical simulations fit the curve of the analytical model.

Seeking the thermal characterization of complex materials such as multilayered materials deposited on a silicon substrate, the perspectives of this work are based on its technical adaptation for such applications. The future works include the depositing of resistive wire on both surfaces of thin films in order to experimentally determine their anisotropic thermal properties.

General conclusions

This manuscript was dedicated to the description and specification of the measurement with two thermal metrologies for the characterization of thermal conductivity of materials: the Scanning Thermal Microscopy (SThM) and the 2ω method.

Based on a global state of the art of SThM in chapter 1, we raised the questions regarding the probe-sample thermal system in order to better understanding the SThM measurement and to achieve more accurate thermal characterization of materials. The heat losses to the environment and the different heat transfer mechanisms that exist between the probe and the sample were detailed. The resistive probes used in the experiments mentioned in this manuscript were described and the tasks to be dealt with in our study were defined.

A methodology of work was initiated to study the heat transfer through water meniscus in SThM in chapter 2. This methodology was used with the Wollaston wire probe (chapter 2) and with the KNT and doped silicon (DS) probes (chapter 4). The capillary forces were determined based on measurements of pull-off forces on hydrophilic samples as a function of the probe temperature. The dimensions of the meniscus were derived from these forces values by using literature modeling. For the three probes, the total thermal conductance of the meniscus was determined. The results have shown that this heat transfer mechanism is not predominant in the thermal interaction between the probe and the sample in SThM. Furthermore, this contribution depends strongly on the probe temperature where the meniscus stability has been observed. This lies in the interest of different applications such as controlled dip-pen nanolithography. The meniscus almost disappears at high probe temperatures showing that thermally-controlled system can be an alternative solution to reduce stiction at the nanoscale. On the other hand, the first results of the investigation of SThM probe-sample thermal interaction through water meniscus in an environmental scanning electron microscope (ESEM) were presented and discussed. The differences observed between the literature ESEM experimental studies and the theory (Kelvin Equation) of the meniscus dimensions were clarified. The effect of the electron beam should be taken into account while working in ESEM.

The quantification of the thermal conduction at the solid-solid contact and through air requires the comparison between SThM measurements and modeling results. The thermal conductance of the probe was shown to be a crucial modeling parameter to be determined for a more efficient approach of the measurements. In fact, the effective probe thermal conductance changes as a function of the probe temperature and cannot be assumed constant depending on the boundary conditions taken at the heater supports.

Working under vacuum conditions, the thermal conduction at the solid-solid contact was studied for the Wollaston and KNT probes. In the case of the Wollaston, the experimental results have shown that this heat transfer mechanism was previously overestimated in the probe-sample thermal interaction. The thermal conduction at the mechanical contact is small compared to heat conduction through air. However, for the case of the KNT probe, the results have shown that the conductance through solid-solid contact should be taken into account while modeling the probe-sample thermal interaction. For both these probes, the boundary resistance was determined for different polished samples and the obtained values are in good agreement with literature values. For the Wollaston probe, the thermal resistance of the phonon-electron coupling in the Pt/Rh wire is needed to estimate the transmission coefficient at the tip-sample interfaces. This coefficient can be determined directly in the case of the KNT probe (0.62 ± 0.02 for KNT/Ge and 0.9 ± 0.015 for KNT/Si).

Under ambient conditions and using different reference samples, the probe thermal signal was measured as a function of the sample thermal conductivity for the Wollaston and KNT probes. SThM with the Wollaston probe then appears sensitive exclusively to the sample thermal conductivity λ_s on a range limited to low λ_s up to around 10 $W.m^{-1}.K^{-1}$. With the KNT probe, the sensitivity is lost for λ_s larger than few $W.m^{-1}.K^{-1}$. The modeling parameters of the thermal conduction through air were determined using reference samples in the ranges of sensitivity of these probes. The results have pointed out that these parameters depend on the sample thermal conductivity. In the case of the Wollaston probe, numerical simulations were performed and have confirmed our analysis. Measurements on different rough samples have shown that the roughness of the sample surface increases the thermal resistance at the probe-sample contact. It is a crucial factor and should be taken into account during the SThM probe calibration and the thermal characterization of materials. A methodology of work was set and applied to identify the thermal conductivity of Ba_8Si_{46} clathrates with the Wollaston probe. 3D modeling should be developed in order to provide a better description of the probe-sample system and more specifically of the thermal interaction through air while taking into account the real shape of the probe.

The summary of the thermal parameters of interaction of the different heat transfer mechanisms obtained using the Wollaston and KNT probe is given in the table below. We consider for each mechanism its thermal conductance *G* and thermal contact radius *b*.

Summary of the thermal parameters of the different heat transfer mechanisms based measurements with the Wollaston and KNT probes.

Heat transfer mechanism		Wollaston probe	KNT probe
Water meniscus (large meniscus)	$G_{total,\ meniscus}$ (µW.K^{-1})	0.2	0.013
	$b_w \approx r_2$ (nm)	35	9
Solid-solid	G_{ss} (µW.K^{-1})	~ 0.3	~ 0.5
	$b_{ss} \approx a_c$ (nm)	~ 10 nm	~ 50 nm
air	G_{air} (µW.K^{-1})	~ 6	~ (1-2)
	b_{air} (µm)	(2 – 24)	~ 5 for low λ_s

The first steps of the development of a thermal metrology for thermal characterization of anisotropic thin films were also presented. The method, which we have called the "2ω method", should allow the identification of the thermal diffusivity and conductivity of materials at temperatures higher than the ambient. It consists of a network of resistive wires deposited on the surface of the sample to be characterized. One of the wires serves for heating the sample in the alternating regime while the others are used as temperature sensors. A 2D model that describes the thermal behavior of the implemented sample was developed. This model was based on the resolution of the heat equation in the Fourier space. Simulations with this model developed in this chapter have shown the possibility to determine the thermal properties of materials in the in-plane and cross-plane directions. The modeling was also used to derive from experimental measurements the thermal conductivity and diffusivity of a reference sample of isotropic silicon. The obtained results at different temperatures ranging from ambient to 500 K were in good agreement with literature values. They validate the method proposed by CETHIL. The further steps include the electrical implementation and the study of thin film samples with deposited wires on their both surfaces.

Appendices

Appendix A: NTEGRA Probe Nanolaboratory, thermal control unit and the NanoTA2

A.1) NTEGRA Probe Nanolaboratory

The Atomic Force Microscope (AFM) used in our measurement is a part of the NTEGRA Probe Nanolaboratory that is commercialized by NT-MDT. Figure A.1 presents an image and an illustration of this AFM with its principal parts. The scanner is located at the sample stage. The head can be changed depending of the application.

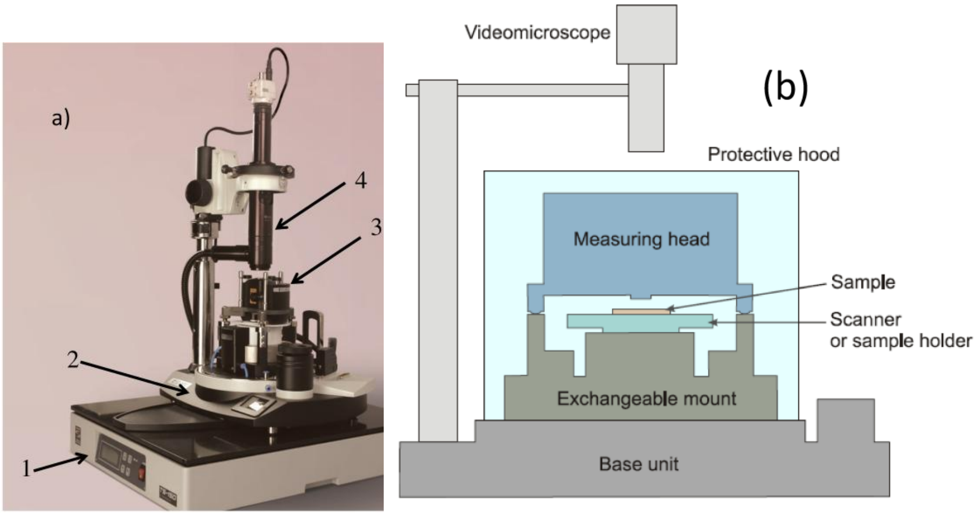

Figure A.1. (a) Image of the probe NTEGRA Probe Nanolaboratory: 1- Vibration isolation system 2- base unit 3- measuring head 4- optical viewing system. (b) Illustration of the basic part of the NTEGRA Probe Nanolaboratory (NTMDT/ User's manual).

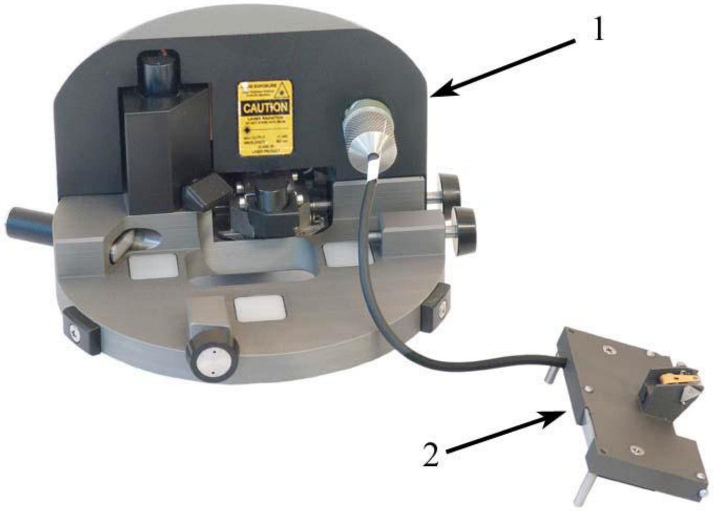

Figure A.2. Image of the 1- AFM head (universal head) and 2- probe adjustment unit (NTMDT/ User's manual).

Image A.3 shows an image of the adjustment unit that consists of a probe holder and a connector that links the unit to the measuring head. In the case of SThM probes, the blue wire links the probe to its thermal control unit (Wheatstone bridge or NanoTA2).

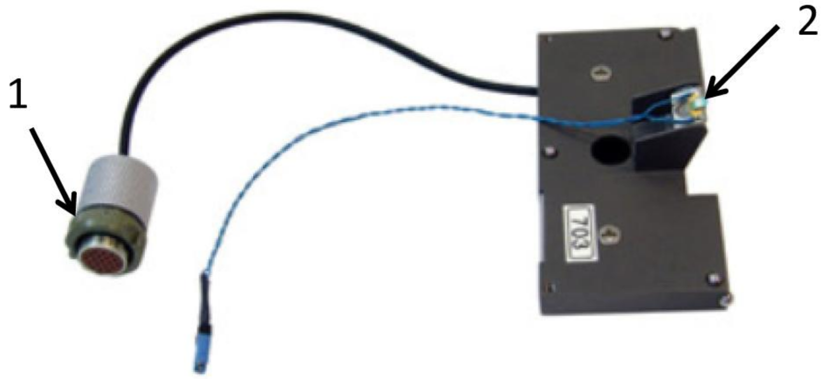

Figure A.3. Image of the adjustment unit: 1) Probe holder and 2) connector to the measuring head (NTMDT/ User's manual).

To perform measurements under vacuum conditions (low vacuum operation (10^{-3} torr)), a protective hood is mounted on the base unit with the help of a metallic frame as shown in Figure A.4.

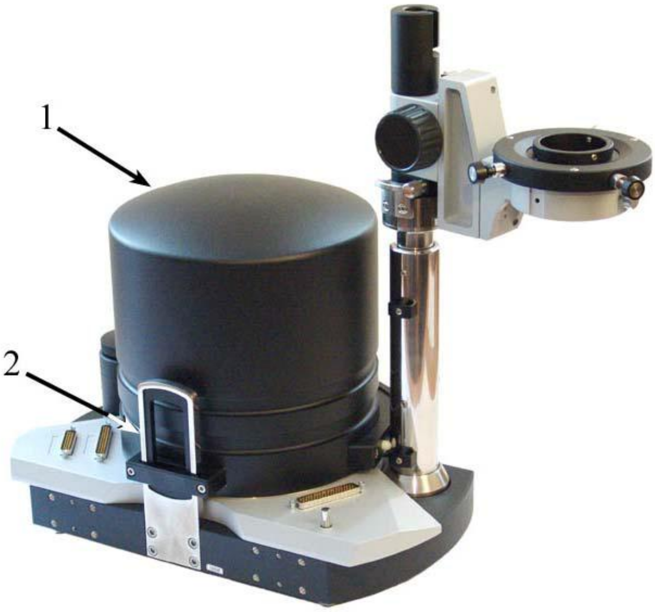

Figure A.4. Image of the AFM while performing measurements under vacuum conditions: 1) protective hood and 2) its frame (NTMDT/ User's manual).

A.2) Thermal control unit

The thermal control units developed at CETHIL to control the temperature of the Wollaston probe and KNT probe are based on balanced Wheastone bridge circuits. Figure A.5 presents a schematic of the units used in the measurements. It consists of a Wheatstone bridge and a feedback loop with a ratio between the two branches of the bridge of 5.

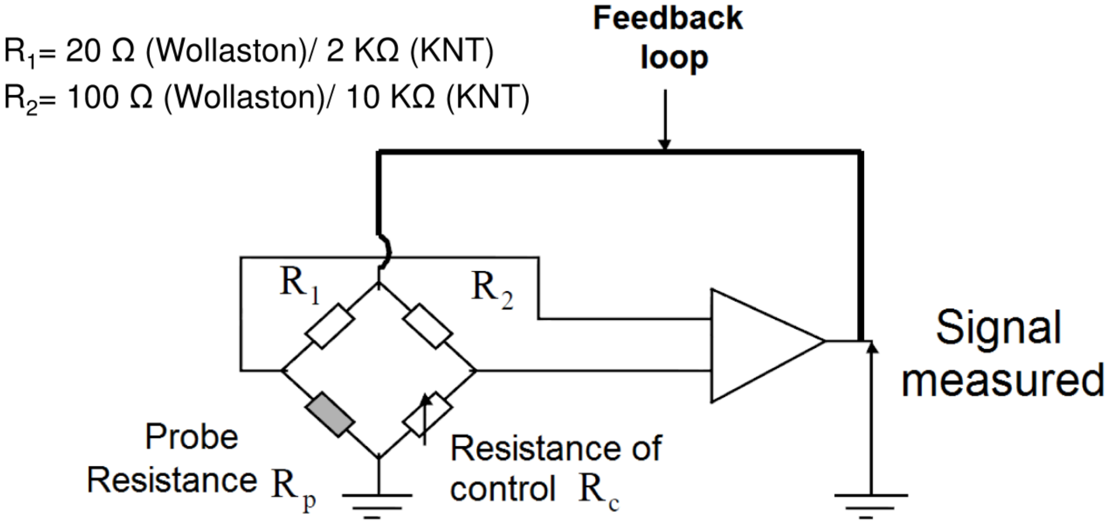

Figure A.5. Schematic of the Wheatstone bridge used in the measurements.

A.3) the NanoTA2

Figure A.6 shows an image of the "NanoTA2" with its main components. The power supply generates voltage across the controller and the CAL box. The controller serves for the communication with the AFM and ramping the voltage applied to the probe. The CAL box links to NanoTA2 to the probe and serves for measuring the applied voltage. In our case, the CAL box is set to the single probe mode that is illustrated in Figure A.7. This mode was used to apply the ramp of voltage to the probe during the calibration of the apex temperature as shown in chapter 4.

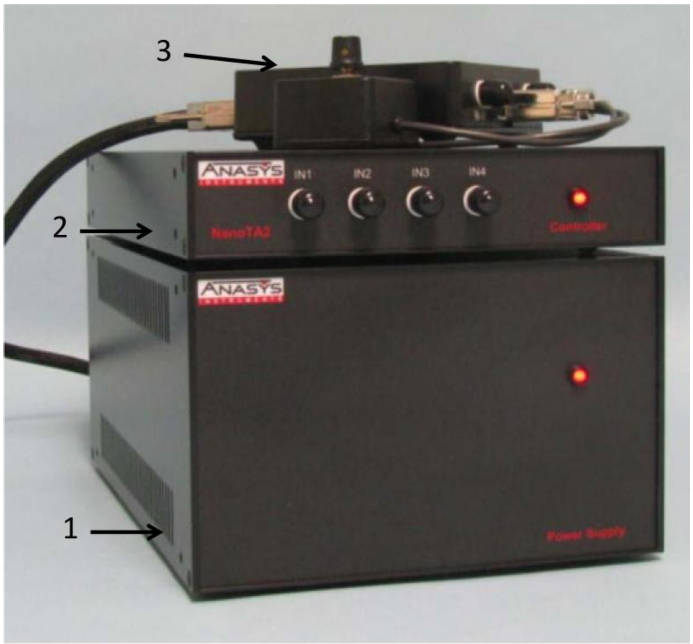

Figure A.6. The three parts of the NanoTA2: 1) Power supply, 2) Controller and 3) CAL Box.

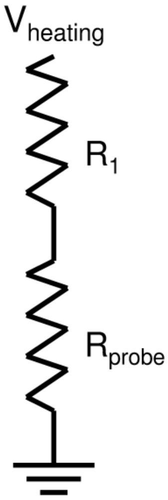

Figure A.7. Illustration of the single probe mode.

Appendix A: NTEGRA Probe Nanolaboratory, thermal control unit and the NanoTA2

Bibliography

1. Shakouri, A., *Nanoscale thermal transport and microrefrigerators on a chip.* Proceedings of the IEEE, 2006. **94**(8): p. 1613-1638.
2. Chandrakasan, A.P., W.J. Bowhill, and F. Fox, *Design of high-performance microprocessor circuits*. 2000: Wiley-IEEE Press.
3. Borkar, S. *Low power design challenges for the decade (invited talk)*. in *Proceedings of the 2001 Asia and South Pacific Design Automation Conference*. 2001. ACM.
4. Venkatasubramanian, R., *et al.*, *Thin-film thermoelectric devices with high room-temperature figures of merit.* Nature, 2001. **413**(6856): p. 597-602.
5. Snyder, G.J. and E.S. Toberer, *Complex thermoelectric materials.* Nature materials, 2008. **7**(2): p. 105-114.
6. Volz, S., *Microscale and nanoscale heat transfer*. 2007: Springer.
7. S. Gomès, A. Assy, P-O. Chapuis, *Scanning thermal microscopy : A review.* Physica Status Solidi (a). **Submitted**.
8. S. Gomès, A. Assy, P-O. Chapuis, *Thermometry at the nanoscale - Fundamentals and selected Applications*, ed. L.C.a.F. Palacio. 2014: Royal Society Publishing.
9. Williams, C. and H. Wickramasinghe, *Photothermal imaging with sub-100-nm spatial resolution*, in *Photoacoustic and Photothermal Phenomena*. 1988, Springer. p. 364-369.
10. Nonnenmacher, M. and H. Wickramasinghe, *Scanning probe microscopy of thermal conductivity and subsurface properties.* Applied Physics Letters, 1992. **61**(2): p. 168-170.
11. Goodson, K.E. and M. Asheghi, *Near-field optical thermometry.* Microscale Thermophysical Engineering, 1997. **1**(3): p. 225-235.
12. Gotsmann, B., *et al.*, *Nanoscale thermal and mechanical interactions studies using heatable probes.* Nanotechnology, 2010.
13. Lefèvre, S., S. Volz, and P.-O. Chapuis, *Nanoscale heat transfer at contact between a hot tip and a substrate.* International journal of heat and mass transfer, 2006. **49**(1): p. 251-258.
14. David, L., S. Gomes, and M. Raynaud, *Modelling for the thermal characterization of solid materials by dc scanning thermal microscopy.* Journal of Physics D: Applied Physics, 2007. **40**(14): p. 4337.
15. Dinwiddie, R., R. Pylkki, and P. West, *Thermal conductivity contrast imaging with a scanning thermal microscope.* Thermal conductivity, 1993. **22**: p. 668-668.
16. Tovee, P., *et al.*, *Nanoscale spatial resolution probes for Scanning Thermal Microscopy of solid state materials.* Journal of Applied Physics, 2012. **112**(11): p. 114317-114317-11.
17. Dobson, P.S., J.M. Weaver, and G. Mills. *New Methods for Calibrated Scanning Thermal Microscopy (SThM)*. in *Sensors, 2007 IEEE*. 2007. IEEE.
18. Despont, M., *et al.*, *VLSI-NEMS chip for parallel AFM data storage.* Sensors and Actuators A: Physical, 2000. **80**(2): p. 100-107.
19. Binnig, G., *et al.*, *Ultrahigh-density atomic force microscopy data storage with erase capability.* Applied Physics Letters, 1999. **74**(9): p. 1329-1331.
20. Gotsmann, B. and U. Dürig, *Thermally activated nanowear modes of a polymer surface induced by a heated tip.* Langmuir, 2004. **20**(4): p. 1495-1500.
21. Nelson, B. and W. King, *Measuring material softening with nanoscale spatial resolution using heated silicon probes.* Review of scientific instruments, 2007. **78**(2): p. 023702.

22. Lefèvre, S., *Modélisation et élaboration des métrologies de microscopie thermique à sonde locale résistive*. 2004, Université de Poitiers.
23. Gomès, S., *et al.*, *Characterization of the thermal conductivity of insulating thin films by scanning thermal microscopy.* Microelectronics journal, 2012.
24. Lefevre, S., *et al.*, *Thermal conductivity calibration for hot wire based dc scanning thermal microscopy.* Review of scientific instruments, 2003. **74**(4): p. 2418-2423.
25. Cahill, D.G., *Thermal conductivity measurement from 30 to 750 K: the 3ω method.* Review of Scientific Instruments, 1990. **61**(2): p. 802-808.
26. Lefèvre, S. and S. Volz, *3ω-scanning thermal microscope.* Review of scientific instruments, 2005. **76**(3): p. 033701.
27. Chapuis, P.-O., *Contribution à l'étude des transferts thermiques à l'échelle nanométrique: interaction pointe-surface*. 2007, Ecole Centrale Paris.
28. Puyoo, E., *Caractérisation thermique de nanofils de silicium pour des applications à la thermoélectricité.* 2010.
29. Prasher, R., *Predicting the thermal resistance of nanosized constrictions.* Nano letters, 2005. **5**(11): p. 2155-2159.
30. Watari, K., *et al.*, *Effect of grain size on the thermal conductivity of Si3N4.* Journal of the American Ceramic Society, 1999. **82**(3): p. 777-779.
31. Shivaprasad, S. and M. Angadi, *Temperature coefficient of resistance of thin palladium films.* Journal of Physics D: Applied Physics, 1980. **13**(9): p. L171.
32. Chen, G., *Phonon heat conduction in nanostructures.* International journal of thermal sciences, 2000. **39**(4): p. 471-480.
33. Nelson, B.A. and W.P. King, *Modeling and simulation of the interface temperature between a heated silicon tip and a substrate.* Nanoscale and Microscale Thermophysical Engineering, 2008. **12**(1): p. 98-115.
34. Swartz, E.T. and R.O. Pohl, *Thermal boundary resistance.* Reviews of Modern Physics, 1989. **61**(3): p. 605.
35. Guo, Z.-Y. and Z.-X. Li, *Size effect on microscale single-phase flow and heat transfer.* International journal of heat and mass transfer, 2003. **46**(1): p. 149-159.
36. Hu, X., A. Jain, and K.E. Goodson. *Investigation of the natural convection boundary condition in microfabricated structures*. in *ASME 2005 Summer Heat Transfer Conference collocated with the ASME 2005 Pacific Rim Technical Conference and Exhibition on Integration and Packaging of MEMS, NEMS, and Electronic Systems*. 2005. American Society of Mechanical Engineers.
37. Chapuis, P.-O., *et al. Heat transfer between a hot AFM tip and a cold sample: impact of the air pressure*. in *MRS Proceedings*. 2013. Cambridge Univ Press.
38. Lees, L. and C.-Y. Liu, *Kinetic-Theory Description of Conductive Heat Transfer from a Fine Wire.* Physics of Fluids, 1962. **5**(10): p. 1137-1148.
39. Taine, J. and J.-P. Petit, *Transferts thermiques*. 2003: Dunod.
40. Thiery, L., E. Gavignet, and B. Cretin, *Two omega method for active thermocouple microscopy.* Review of scientific instruments, 2009. **80**(3): p. 034901.
41. Kim, K.J. and W.P. King, *Thermal conduction between a heated microcantilever and a surrounding air environment.* Applied Thermal Engineering, 2009. **29**(8): p. 1631-1641.
42. Raphaël, O., *Contribution à la microscopie thermique à sonde locale en mode alternatif: Caractérisation de la réponse et de l'interaction sonde échantillon*. 2008, Reims.
43. Yovanovich, M. and E. Marotta, *Thermal spreading and contact resistances.* Heat Transfer Handbook, 2003. **1**: p. 261-394.

44. Majumdar, A., *Scanning thermal microscopy.* Annual review of materials science, 1999. **29**(1): p. 505-585.
45. Hinz, M., *et al.*, *High resolution vacuum scanning thermal microscopy of HfO2 and SiO2.* Applied Physics Letters, 2008. **92**(4): p. 043122-043122-3.
46. Kittel, A., *et al.*, *Near-field heat transfer in a scanning thermal microscope.* Physical review letters, 2005. **95**(22): p. 224301.
47. Narayanaswamy, A., S. Shen, and G. Chen, *Near-field radiative heat transfer between a sphere and a substrate.* Physical Review B, 2008. **78**(11): p. 115303.
48. Shen, S., A. Narayanaswamy, and G. Chen, *Surface phonon polaritons mediated energy transfer between nanoscale gaps.* Nano letters, 2009. **9**(8): p. 2909-2913.
49. Siria, A., *et al.*, *A scheme for solving the plane–plane challenge in force measurements at the nanoscale.* Nanoscale research letters, 2010. **5**(8): p. 1360-1365.
50. Grierson, D., E. Flater, and R. Carpick, *Accounting for the JKR–DMT transition in adhesion and friction measurements with atomic force microscopy.* Journal of adhesion science and technology, 2005. **19**(3-5): p. 291-311.
51. Johnson, K., K. Kendall, and A. Roberts, *Surface energy and the contact of elastic solids.* Proceedings of the royal society of London. A. mathematical and physical sciences, 1971. **324**(1558): p. 301-313.
52. Derjaguin, B., V. Muller, and Y.P. Toporov, *Effect of contact deformations on the adhesion of particles.* Journal of Colloid and interface science, 1975. **53**(2): p. 314-326.
53. Cappella, B. and G. Dietler, *Force-distance curves by atomic force microscopy.* Surface Science Reports, 1999. **34**(1): p. 1-104.
54. Schwarz, U.D., *A generalized analytical model for the elastic deformation of an adhesive contact between a sphere and a flat surface.* Journal of Colloid and Interface Science, 2003. **261**(1): p. 99-106.
55. Butt, H.-J., B. Cappella, and M. Kappl, *Force measurements with the atomic force microscope: Technique, interpretation and applications.* Surface Science Reports, 2005. **59**(1): p. 1-152.
56. David, L., *Développement de la microscopie thermique à sonde locale pour la détermination de la conductivité thermique de films minces Application aux céramiques pour le nucléaire*. 2006, INSTITUT NATIONAL DES SCIENCES APPLIQUEES DE LYON.
57. David, L., *Développement de la microscopie thermique à sonde locale pour la détermination de la conductivité thermique de films minces. Application aux céramiques pour le nucléaire.* 2006.
58. Gotsmann, B. and M. Lantz, *Quantized thermal transport across contacts of rough surfaces.* Nature materials, 2013. **12**(1): p. 59-65.
59. Luo, K., *et al.*, *Sensor nanofabrication, performance, and conduction mechanisms in scanning thermal microscopy.* Journal of Vacuum Science & Technology B, 1997. **15**(2): p. 349-360.
60. Shi, L. and A. Majumdar, *Thermal transport mechanisms at nanoscale point contacts.* ASME Journal of Heat Transfer, 2002. **124**(2): p. 329-337.
61. Thiery, L., *et al.*, *Thermal contact calibration between a thermocouple probe and a microhotplate.* Journal of Heat Transfer, 2008. **130**(9).
62. Gomès, S., N. Trannoy, and P. Grossel, *DC thermal microscopy: study of the thermal exchange between a probe and a sample.* Measurement Science and Technology, 1999. **10**(9): p. 805.

63. King, W.P. and K.E. Goodson, *Thermomechanical formation of nanoscale polymer indents with a heated silicon tip.* Journal of Heat Transfer, 2007. **129**(11): p. 1600-1604.
64. Chapuis, P.-O., *et al.*, *Heat transfer between a nano-tip and a surface.* Nanotechnology, 2006. **17**(12): p. 2978.
65. Bosse, J., *et al.*, *Nanothermal characterization of amorphous and crystalline phases in chalcogenide thin films with scanning thermal microscopy.* Journal of Applied Physics, 2014. **116**(13): p. 134904.
66. Juszczyk, J., M. Wojtol, and J. Bodzenta, *DC Experiments in Quantitative Scanning Thermal Microscopy.* International journal of thermophysics, 2013. **34**(4): p. 620-628.
67. Bhushan, B., *Nanotribology and nanomechanics of MEMS/NEMS and BioMEMS/BioNEMS materials and devices.* Microelectronic Engineering, 2007. **84**(3): p. 387-412.
68. Tas, N., *et al.*, *Stiction in surface micromachining.* Journal of Micromechanics and Microengineering, 1996. **6**(4): p. 385.
69. Rajagopalan, J., A. Tofangchi, and M.A. Saif, *Linear high-resolution bioMEMS force sensors with large measurement range.* Microelectromechanical Systems, Journal of, 2010. **19**(6): p. 1380-1389.
70. Bhushan, B., L. HUIWEN, and S.M. Hsu, *Adhesion and friction studies of silicon and hydrophobic and low friction films and investigation of scale effects.* Journal of tribology, 2004. **126**(3): p. 583-590.
71. Ogwu, A., T. Okpalugo, and J. McLaughlin, *The effect of PECVD plasma decomposition on the wettability and dielectric constant changes in silicon modified DLC films for potential MEMS and low stiction applications.* AIP Advances, 2012. **2**(3): p. 032128.
72. Puurunen, R., *et al.*, *Reducing stiction in microelectromechanical systems by rough nanometer-scale films grown by atomic layer deposition.* Sensors and Actuators A: Physical, 2012. **188**: p. 240-245.
73. Hurst, K.M., *et al.*, *Self-assembled monolayer-immobilized gold nanoparticles as durable, anti-stiction coatings for MEMS.* Microelectromechanical Systems, Journal of, 2011. **20**(2): p. 424-435.
74. Lantz, M.A., D. Wiesmann, and B. Gotsmann, *Dynamic superlubricity and the elimination of wear on the nanoscale.* Nature nanotechnology, 2009. **4**(9): p. 586-591.
75. Dinelli, F., *et al.*, *Ultrasound induced lubricity in microscopic contact.* Applied Physics Letters, 1997. **71**(9): p. 1177-1179.
76. Piner, R.D., *et al.*, *" Dip-pen" nanolithography.* Science, 1999. **283**(5402): p. 661-663.
77. Weeks, B., *et al.*, *Effect of dissolution kinetics on feature size in dip-pen nanolithography.* Physical review letters, 2002. **88**(25): p. 255505.
78. Ginger, D.S., H. Zhang, and C.A. Mirkin, *The Evolution of Dip-Pen Nanolithography.* Angewandte Chemie International Edition, 2004. **43**(1): p. 30-45.
79. Gonzalez-Angulo, A.M., B.T. Hennessy, and G.B. Mills, *Future of personalized medicine in oncology: a systems biology approach.* Journal of Clinical Oncology, 2010. **28**(16): p. 2777-2783.
80. Müller, D.J. and Y.F. Dufrene, *Atomic force microscopy as a multifunctional molecular toolbox in nanobiotechnology.* Nature nanotechnology, 2008. **3**(5): p. 261-269.
81. Li, Y., B.W. Maynor, and J. Liu, *Electrochemical AFM "dip-pen" nanolithography.* Journal of the American Chemical Society, 2001. **123**(9): p. 2105-2106.
82. Hu, J., X.D. Xiao, and M. Salmeron, *Scanning polarization force microscopy: A technique for imaging liquids and weakly adsorbed layers.* Applied Physics Letters, 1995. **67**(4): p. 476-478.

83. He, K.T., *et al.*, *Scanning Tunneling Microscopy Study and Nanomanipulation of Graphene-Coated Water on Mica.* Nano letters, 2012. **12**(6): p. 2665-2672.
84. Xu, L., *et al.*, *Wetting and capillary phenomena of water on mica.* The Journal of Physical Chemistry B, 1998. **102**(3): p. 540-548.
85. Gao, J., *et al.*, *Structured and viscous water in subnanometer gaps.* Physical Review B, 2007. **75**(11): p. 115415.
86. Zitzler, L., S. Herminghaus, and F. Mugele, *Capillary forces in tapping mode atomic force microscopy.* Physical Review B, 2002. **66**(15): p. 155436.
87. Guo, L., *et al.*, *Water adsorption behavior on metal surfaces and its influence on surface potential studied by in situ SPM.* Applied Surface Science, 2012. **258**(22): p. 9087-9091.
88. Gil, A., *et al.*, *Adsorption of water on solid surfaces studied by scanning force microscopy.* Langmuir, 2000. **16**(11): p. 5086-5092.
89. Santos, S., *et al.*, *Measuring the true height of water films on surfaces.* Nanotechnology, 2011. **22**(46): p. 465705.
90. Mate, C.M., M.R. Lorenz, and V. Novotny, *Atomic force microscopy of polymeric liquid films.* The Journal of Chemical Physics, 1989. **90**: p. 7550.
91. Hansson, P.M., *et al.*, *Influence of surface topography on the interactions between nanostructured hydrophobic surfaces.* Langmuir, 2012. **28**(21): p. 8026-8034.
92. Farshchi-Tabrizi, M., *et al.*, *On the adhesion between fine particles and nanocontacts: An atomic force microscope study.* Langmuir, 2006. **22**(5): p. 2171-2184.
93. Butt, H.-J. and M. Kappl, *Normal capillary forces.* Advances in colloid and interface science, 2009. **146**(1): p. 48-60.
94. Rabinovich, Y.I., *et al.*, *Capillary forces between surfaces with nanoscale roughness.* Advances in colloid and interface science, 2002. **96**(1): p. 213-230.
95. van Honschoten, J.W., N. Brunets, and N.R. Tas, *Capillarity at the nanoscale.* Chemical Society Reviews, 2010. **39**(3): p. 1096-1114.
96. Atkins, P. and J. de Paula, *Physical Chemistry Volume 1: Thermodynamics and Kinetics*. 2009: Macmillan Higher Education.
97. Israelachvili, J.N., *Intermolecular and surface forces: revised third edition*. 2011: Academic press.
98. Landman, U., *et al.*, *Atomistic mechanisms and dynamics of adhesion, nanoindentation, and fracture.* Science, 1990. **248**(4954): p. 454-461.
99. *Specification Scanning Thermal Microscope Option.* Topometrix Corporation (User's Manual Addendum), 1997.
100. Sirghi, L., *Transport Mechanisms in Capillary Condensation of Water at a Single-Asperity Nanoscopic Contact.* Langmuir, 2012. **28**(5): p. 2558-2566.
101. Crassous, J., E. Charlaix, and J.-L. Loubet, *Capillary condensation between high-energy surfaces. An experimental study with a surface force apparatus.* EPL (Europhysics Letters), 1994. **28**(1): p. 37.
102. Ge, Z., D.G. Cahill, and P.V. Braun, *Thermal conductance of hydrophilic and hydrophobic interfaces.* Physical review letters, 2006. **96**(18): p. 186101.
103. Crassous, J., E. Charlaix, and J.-L. Loubet, *Nanoscale investigation of wetting dynamics with a surface force apparatus.* Physical review letters, 1997. **78**(12): p. 2425.
104. Charlaix, E. and M. Ciccotti, *Capillary condensation in confined media. handbook of nanophysics: Principles and methods. ed. klaus sattler*. 2010, CRC Press.
105. Tovee, P., *et al.*, *Nanoscale spatial resolution probes for scanning thermal microscopy of solid state materials.* Journal of Applied Physics, 2012. **112**(11): p. 114317.

106. Gorbunov, V., *et al.*, *Probing surface microthermal properties by scanning thermal microscopy.* Langmuir, 1999. **15**(24): p. 8340-8343.
107. Assy, A., *et al.*, *Analysis of heat transfer in the water meniscus at the tip-sample contact in scanning thermal microscopy.* Journal of Physics D: Applied Physics, 2014. **47**(44): p. 442001.
108. Ata, A., Y.I. Rabinovich, and R.K. Singh, *Role of surface roughness in capillary adhesion.* Journal of adhesion science and technology, 2002. **16**(4): p. 337-346.
109. Halsey, T.C. and A.J. Levine, *How sandcastles fall.* Physical Review Letters, 1998. **80**(14): p. 3141.
110. He, M., *et al.*, *Critical phenomena of water bridges in nanoasperity contacts.* The Journal of Chemical Physics, 2001. **114**(3): p. 1355-1360.
111. Luna, M., J. Colchero, and A. Baró, *Study of water droplets and films on graphite by noncontact scanning force microscopy.* The Journal of Physical Chemistry B, 1999. **103**(44): p. 9576-9581.
112. Weeks, B.L., M.W. Vaughn, and J.J. DeYoreo, *Direct imaging of meniscus formation in atomic force microscopy using environmental scanning electron microscopy.* Langmuir, 2005. **21**(18): p. 8096-8098.
113. Greiner, C., *et al.*, *Controlling nanoscale friction through the competition between capillary adsorption and thermally activated sliding.* ACS nano, 2012. **6**(5): p. 4305-4313.
114. Pettes, M.T. and L. Shi, *A Reexamination of Phonon Transport Through a Nanoscale Point Contact in Vacuum.* Journal of Heat Transfer, 2014. **136**(3): p. 032401.
115. Wexler, G., *The size effect and the non-local Boltzmann transport equation in orifice and disk geometry.* Proceedings of the Physical Society, 1966. **89**(4): p. 927.
116. Chen, G., *Thermal conductivity and ballistic-phonon transport in the cross-plane direction of superlattices.* Physical Review B, 1998. **57**(23): p. 14958.
117. Prasher, R.S. and P.E. Phelan, *Microscopic and macroscopic thermal contact resistances of pressed mechanical contacts.* Journal of Applied Physics, 2006. **100**(6): p. 063538-063538-8.
118. Stoner, R. and H. Maris, *Kapitza conductance and heat flow between solids at temperatures from 50 to 300 K.* Physical Review B, 1993. **48**(22): p. 16373.
119. Stevens, R.J., A.N. Smith, and P.M. Norris, *Measurement of thermal boundary conductance of a series of metal-dielectric interfaces by the transient thermoreflectance technique.* Journal of Heat Transfer, 2005. **127**(3): p. 315-322.
120. Komarov, P.L., *et al.*, *Transient thermo-reflectance measurements of the thermal conductivity and interface resistance of metallized natural and isotopically-pure silicon.* Microelectronics journal, 2003. **34**(12): p. 1115-1118.
121. da Cruz, C.A., P. Chantrenne, and X. Kleber, *Molecular Dynamics simulations and Kapitza conductance prediction of Si/Au systems using the new full 2NN MEAM Si/Au cross-potential.* Journal of Heat Transfer, 2012. **134**(6): p. 062402.
122. Yang, N., *et al.*, *Thermal Interface Conductance between Aluminum and Silicon by Molecular Dynamics Simulations.* arXiv preprint arXiv:1401.5550, 2014.
123. Bejan, A., *Heat transfer. 1993.* 1971, New York: John Wiley & Sons.
124. Liñán, A. and V.N. Kurdyumov, *Laminar free convection induced by a line heat source, and heat transfer from wires at small Grashof numbers.* Journal of Fluid Mechanics, 1998. **362**: p. 199-227.
125. Zhang, Y., *et al.*, *A microprobe technique for simultaneously measuring thermal conductivity and Seebeck coefficient of thin films.* Applied Physics Letters, 2010. **96**(6): p. 062107-062107-3.

126. Pailhès, S., *et al.*, *Localization of Propagative Phonons in a Perfectly Crystalline Solid.* Physical review letters, 2014. **113**(2): p. 025506.

127. Majumdar, A. and P. Reddy, *Role of electron–phonon coupling in thermal conductance of metal–nonmetal interfaces.* Applied Physics Letters, 2004. **84**(23): p. 4768-4770.

128. Weber, W., *Adiabatic bond charge model for the phonons in diamond, Si, Ge, and α-Sn.* Physical Review B, 1977. **15**(10): p. 4789.

129. Pop, E., R.W. Dutton, and K.E. Goodson, *Analytic band Monte Carlo model for electron transport in Si including acoustic and optical phonon dispersion.* Journal of Applied Physics, 2004. **96**(9): p. 4998-5005.

130. Cahill, D.G., *et al.*, *Thermal conductivity of thin films: Measurements and understanding.* Journal of Vacuum Science & Technology A, 1989. **7**(3): p. 1259-1266.

131. Cahill, D.G., S.K. Watson, and R.O. Pohl, *Lower limit to the thermal conductivity of disordered crystals.* Physical Review B, 1992. **46**(10): p. 6131.

132. Duquesne, J.-Y., D. Fournier, and C. Frétigny, *Analytical solutions of the heat diffusion equation for 3ω method geometry.* Journal of Applied Physics, 2010. **108**(8): p. 086104.

133. Cahill, D.G., M. Katiyar, and J. Abelson, *Thermal conductivity of a-Si: H thin films.* Physical Review B, 1994. **50**(9): p. 6077.

134. Kim, J.H., A. Feldman, and D. Novotny, *Application of the three omega thermal conductivity measurement method to a film on a substrate of finite thickness.* Journal of Applied Physics, 1999. **86**(7): p. 3959-3963.

135. Borca-Tasciuc, T., A. Kumar, and G. Chen, *Data reduction in 3ω method for thin-film thermal conductivity determination.* Review of scientific instruments, 2001. **72**(4): p. 2139-2147.

136. Zhang, X. and C.P. Grigoropoulos, *Thermal conductivity and diffusivity of free-standing silicon nitride thin films.* Review of scientific instruments, 1995. **66**(2): p. 1115-1120.

137. Lu, L., W. Yi, and D. Zhang, *3ω method for specific heat and thermal conductivity measurements.* Review of scientific instruments, 2001. **72**(7): p. 2996-3003.

138. Bourgeois, O., T. Fournier, and J. Chaussy, *Measurement of the thermal conductance of silicon nanowires at low temperature.* Journal of Applied Physics, 2007. **101**(1): p. 016104-016104-3.

139. Heron, J., *et al.*, *Mesoscopic size effects on the thermal conductance of silicon nanowire.* Nano letters, 2009. **9**(5): p. 1861-1865.

140. Liu, W. and M. Asheghi, *Thermal conduction in ultrathin pure and doped single-crystal silicon layers at high temperatures.* Journal of Applied Physics, 2005. **98**(12): p. 123523.

141. Dames, C., *Measuring the thermal conductivity of thin films: 3 omega and related electrothermal methods.* Annual Review of Heat Transfer, 2013. **16**(16).

142. Ju, Y., K. Kurabayashi, and K. Goodson, *Thermal characterization of anisotropic thin dielectric films using harmonic Joule heating.* Thin Solid Films, 1999. **339**(1): p. 160-164.

143. Liu, W., *et al.*, *Anisotropic thermal conductivity of Ge quantum-dot and symmetrically strained Si/Ge superlattices.* Journal of nanoscience and nanotechnology, 2001. **1**(1): p. 39-42.

144. Jang, W., *et al.*, *Thickness-dependent thermal conductivity of encased graphene and ultrathin graphite.* Nano letters, 2010. **10**(10): p. 3909-3913.

145. Smakula, A. and V. Sils, *Precision density determination of large single crystals by hydrostatic weighing.* Physical Review, 1955. **99**: p. 1744-1746.

146. Watanabe, H., N. Yamada, and M. Okaji, *Linear thermal expansion coefficient of silicon from 293 to 1000 K.* International journal of thermophysics, 2004. **25**(1): p. 221-236.
147. Glassbrenner, C. and G.A. Slack, *Thermal conductivity of silicon and germanium from 3 K to the melting point.* Physical Review, 1964. **134**(4A): p. A1058.
148. Shanks, H., *et al.*, *Thermal conductivity of silicon from 300 to 1400 K.* Physical Review, 1963. **130**(5): p. 1743.
149. Parasuraman, J., *Vers des Métamatériaux Thermoelectriques à Base de Super-Réseaux Verticaux: Principes et Verrous Technologiques.* 2013.
150. Smith, A.N., J.L. Hostetler, and P.M. Norris, *Thermal boundary resistance measurements using a transient thermoreflectance technique.* Microscale Thermophysical Engineering, 2000. **4**(1): p. 51-60.
151. da Cruz, C.A., P. Chantrenne, and X. Kleber, *Molecular Dynamics simulations and Kapitza conductance prediction of Si/Au systems using the new full 2NN MEAM Si/Au cross-potential.* Journal of Heat Transfer, 2012. **134**(6).
152. Termentzidis, K., *et al.*, *Thermal conductivity and thermal boundary resistance of nanostructures.* Nanoscale research letters, 2011. **6**(1): p. 1-10.
153. Gundrum, B.C., D.G. Cahill, and R.S. Averback, *Thermal conductance of metal-metal interfaces.* Physical Review B, 2005. **72**(24): p. 245426.
154. Kijamnajsuk, P., *et al.*, *Photothermal Evidence of Laterally Inhomogeneous Interfacial Thermal Resistance in Copper-Coated Carbon Samples.* International journal of thermophysics, 2012. **33**(10-11): p. 2132-2138.
155. Ji, H., *et al.*, *In situ measurement of bond resistance varying with process parameters during ultrasonic wedge bonding.* Journal of Materials Processing Technology, 2009. **209**(1): p. 139-144.
156. Assy, A., *et al.*, *Investigation of the thermal properties of thin solid materials at different temperature levels using a set of microresistors.* Microelectronics Journal, 2014. **45**(5): p. 508-514.

FOLIO ADMINISTRATIF

THÈSE SOUTENUE DEVANT L'INSTITUT NATIONAL DES SCIENCES APPLIQUÉES DE LYON

NOM : ASSY

DATE de SOUTENANCE :
Le 03 Février 2015

Prénom : Ali

TITRE : Development of two techniques for thermal characterization of materials: Scanning Thermal Microscopy (SThM) and 2ω method

NATURE : Doctorat

Numéro d'ordre : _

Ecole doctorale : MEGA (Mécanique, Energétique, Génie civil, Acoustique)

Spécialité : Energétique

RESUME :

Deux techniques de caractérisation thermique des matériaux et d’analyse du transfert de chaleur aux micro- et nano- échelles ont été étudiées et sont présentées dans ce mémoire.
La première technique est la microscopie thermique à sonde locale (SThM). La pointe d’un microscope à force atomique intègre un élément résistif. Utilisée en mode contact, cette pointe, chauffée par effet joule, permet l'excitation thermique localisée de l’échantillon. La détermination des propriétés thermiques de l’échantillon nécessite l'analyse de la réponse de cette pointe avec un modèle du système sonde-échantillon et de son environnement. Un état de l'art général des études réalisées en SThM permet de poser les questions scientifiques actuellement traitées dans le domaine ainsi que les modèles utilisés pour analyser le système pointe-échantillon. Une attention particulière est accordée à l'interaction thermique sonde-échantillon. Sa compréhension nécessite d’être approfondie. L’étude ici présentée tient compte des propriétés thermiques, de la rugosité et de la mouillabilité de la surface de différents échantillons. Une nouvelle méthodologie est établie pour la spécification du transfert de chaleur échangée par conduction thermique au travers du ménisque de l'eau formé au contact sonde-échantillon. Cette méthodologie est basée sur l'analyse de la dépendance à la température de la sonde des courbes de force-distance obtenues à l'air ambiant. Elle est appliquée à trois sondes de taille, forme et constitution différentes: la sonde Wollaston, la sonde KNT et une sonde en silicium dopé. Quels que soient la sonde et l'échantillon, la contribution du ménisque d’eau à l'interaction est montrée être inférieure à celle de l'air. Par ailleurs, pour les sondes Wollaston et KNT, les paramètres d'une modélisation, basée sur une description du système sonde-échantillon avec un réseau de conductances thermiques, sont identifiés à partir de mesures effectuées à l’ambiante et sous vide. La conductance thermique au contact solide-solide est déterminée pour différents échantillons. Cela a permis d’identifier le coefficient de transmission de phonons dans le cas de la sonde KNT et des échantillons

non-métalliques. Nos résultats expérimentaux et de simulations numériques pour les mesures effectuées sous air démontrent que les paramètres utilisés pour décrire la conduction thermique via l’air dépendent fortement de la conductivité thermique de l'échantillon. Aussi des améliorations de la méthodologie actuelle d'étalonnage pour la mesure de la conductivité thermique sont proposées. Il est en outre montré que la variation de la rugosité de l'échantillon lors de l'étalonnage et de mesures doit être prise en compte. La sensibilité à la conductivité thermique pour les sondes Wollaston et KNT est part ailleurs montrée fortement réduite pour les matériaux de conductivité thermique supérieure à 10 et quelques W.m^{-1}.K^{-1} respectivement.

La seconde technique développée est une méthode d’analyse thermique moins locale nécessitant l’instrumentation de la surface de l’échantillon avec un réseau de sondes résistives filiformes. L’un des fils du réseau, chauffé par un courant alternatif à la fréquence f, a le rôle de source excitatrice continue et à la fréquence $2f$ de l’échantillon. Les autres fils sont des capteurs de la température (méthode «2ω»). Un modèle analytique 2D, basé sur le principe des ondes thermiques et développé pour identifier les propriétés thermiques d’échantillons anisotropes est présenté. Ce modèle peut être réduit à un modèle simplifié 1D dans le cas de matériaux homogènes et isotropes. Des simulations par éléments finis et avec ce modèle ont été utilisées pour dimensionner le montage expérimental et valider la méthode sur un échantillon de silicium pur. Les résultats obtenus à des températures de l’échantillon variant de l’ambiante à 500 K corroborent ceux de la littérature.

MOTS-CLÉS : méthodes thermiques, microscopie thermique à sonde locale, transfert de chaleur aux micro- et nano-échelles, conductance thermique, conductivité thermique, coefficient de transmission des phonons, méthode à fils résistifs déposés, ménisque d’eau

Laboratoire (s) de recherche : Centre d'Energétique et de Thermique de Lyon (CETHIL)

Directeur de thèse: Gomès Séverine

Président de jury : Volz Sebastian

Composition du jury : Weaver Jonathan (Rapporteur), Kolosov Oleg (Rapporteur), Volz Sebastian, Trannoy Nathalie, Bourgeois Olivier, Gomès Séverine, Lefèvre Stéphane, Vaillon Rodolphe